





Planet Mercury

More information about this series at http://www.springer.com/series/4097

Planet Mercury

From Pale Pink Dot to Dynamic World





David A. Rothery Department of Physical Sciences The Open University Milton Keynes, United Kingdom

ISBN 978-3-319-12116-1 ISBN 978-3-319-12117-8 (eBook) DOI 10.1007/978-3-319-12117-8 Springer Cham Heidelberg New York Dordrecht London

Library of Congress Control Number: 2014955656

© Springer International Publishing Switzerland 2015

This work is subject to copyright. All rights are reserved by the Publisher, whether the whole or part of the material is concerned, specifically the rights of translation, reprinting, reuse of illustrations, recitation, broadcasting, reproduction on microfilms or in any other physical way, and transmission or information storage and retrieval, electronic adaptation, computer software, or by similar or dissimilar methodology now known or hereafter developed. Exempted from this legal reservation are brief excerpts in connection with reviews or scholarly analysis or material supplied specifically for the purpose of being entered and executed on a computer system, for exclusive use by the purchaser of the work. Duplication of this publication or parts thereof is permitted only under the provisions of the Copyright Law of the Publisher's location, in its current version, and permission for use must always be obtained from Springer. Permissions for use may be obtained through RightsLink at the Copyright Clearance Center. Violations are liable to prosecution under the respective Copyright Law.

The use of general descriptive names, registered names, trademarks, service marks, etc. in this publication does not imply, even in the absence of a specific statement, that such names are exempt from the relevant protective laws and regulations and therefore free for general use.

While the advice and information in this book are believed to be true and accurate at the date of publication, neither the authors nor the editors nor the publisher can accept any legal responsibility for any errors or omissions that may be made. The publisher makes no warranty, express or implied, with respect to the material contained herein.

Cover Figure: Mercury at 90° rotation intervals, as seen by MESSENGER in exaggerated colour and put in front of a SOHO image of the Sun.

 ${\it Mercury\ Images\ Credit}.\ NASA/Johns\ Hopkins\ University\ Applied\ Physics.$

Background Image Credit: SOHO (ESA & NASA)

Printed on acid-free paper

Springer is part of Springer Science+Business Media (www.springer.com)

Preface

My acquaintance with Mercury goes back a number of years, long before we had intimate views of it like the one in Fig. 1. I first saw it as a schoolboy from my parents' home in Kings Norton, Birmingham, on 14 February 1974 (I still have my observing logbook). I had found out that Mercury was approaching elongation, and on a rare evening with no cloud on the horizon, I swept the sky with my trusty 7×50 binoculars above where the Sun had set about half an hour before. Eventually, there it was – way to the left of the Cadbury's chocolate factory and the more distant university clock tower, a rose-tinted speck of light just as described in

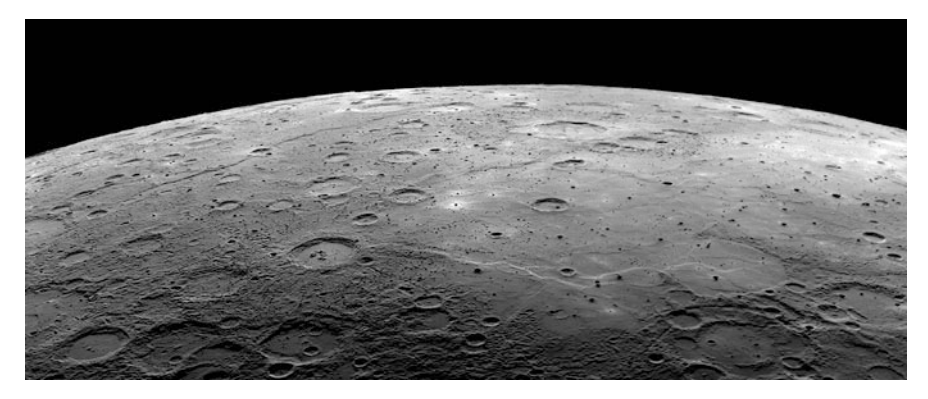


Fig. 1 A mosaic of MESSENGER NAC (Narrow-Angle Camera) images looking west across the limb of Mercury as seen during its approach to flyby 2 in July 2009. The Sun illuminates the terrain at a grazing incidence angle. This is as representative a view of Mercury's general terrain as you will find anywhere. The foreground and left are dominated by cratering and general impact architecture. On the right and extending across the background are lava plains, which have evidently flooded the cratered terrain. Wrinkle ridges and lobate scarps deform the lava plains. Shadowed impact craters as small as about 1 km in size show up as black specks scattered throughout. The peak-ring crater in the foreground at the extreme left (south) of this view is named Steichen and is about 180 km across (NASA/Johns Hopkins University Applied Physics Laboratory/Carnegie Institution of Washington)

vi Preface

Patrick Moore's books from which I had picked up my astronomy and, such as it was in those days, my planetary science. I was unable to make Mercury out with the naked eye before it sank into the murk, and having ticked it off my mental list, I did not see it again for a long time though I did manage brief glimpses of Mercury's silhouette projected using the Birmingham Astronomical Society's 12-in. reflecting telescope as it transited across the Sun in November of the same year.

All this took planning. Mercury is not a planet that draws attention to itself unlike Venus, Mars, Jupiter and even Saturn – all of which can be prominent bright objects high in a dark sky.

In 1978, about to graduate in geology and looking for a PhD position, I went to see John Guest at the University of London's Mill Hill Observatory. We spoke about a project on Mars, but on parting John gave me a copy of the June 1975 special issue of *Journal of Geophysical Research* containing the first lengthy papers arising from the first two Mariner 10 flybys of Mercury. I perused this with interest, but Mercury once again dropped below my radar as I began a PhD at the Open University (where I have been based ever since), using a mixture of satellite images and fieldwork to map part of the Oman mountains in Arabia.

Fast forward to May 1994, a few months before I was promoted to Senior Lecturer in Earth Sciences at the Open University. By then, I had a lot of terrestrial, and some martian, remote sensing under my belt. A team of scientists had submitted a proposal for a Mercury orbiter to the European Space Agency in 1993, and there was now to be a mission selection meeting at ESA headquarters in Paris. John Guest, who was one of the proposers, was unable to attend. The team felt the need of someone to present a geological case for renewed exploration of Mercury, and so I was recruited at short notice to fill the gap. I mugged up on Mercury (making liberal use of that *Journal of Geophysical Research* gift!), said my piece in Paris, and then stepped back out of the loop. It was not until 2000 that ESA gave approval for an ambitious 'Cornerstone' mission to Mercury named BepiColombo, consisting of two orbiters and a 44 kg lander. The lander was cancelled for budgetary reasons in 2003, by which time NASA had overtaken ESA and prepared a less ambitious single-orbiter mission called MESSENGER that was launched in 2004. This achieved orbit in 2011 and has provided most of the new data that justify this book.

In the meantime, in 2004 I found myself on a 'project peer review panel' convened by the relevant UK funding agency (in those days PPARC, the Particle Physics and Astronomy Research Council) to vet proposals from UK groups to ESA's call to provide instruments for BepiColombo. Our task was to recommend which, if any, should be funded.

We wanted to fund two instruments, but in the end only barely enough funding was forthcoming for one. This was the Mercury Imaging X-ray Spectrometer, MIXS, led by a team from Leicester University. It would be capable of measuring the abundances of elements on Mercury by mapping X-rays of characteristic energies fluoresced from the surface because Mercury's airless landscape is bathed in broadband X-rays emitted by the Sun.

For 2 years, I served on PPARC's BepiColombo oversight committee, whose job was to scrutinise expenditure and monitor progress, before I 'switched sides' and

Preface vii

joined the MIXS team as Lead Scientist. This gave me an entrée to ESA's BepiColombo science team, and I soon found myself leading ESA's Mercury Surface and Composition Working Group. Thanks to an attitude of mutual cooperation between NASA's MESSENGER team and ESA's BepiColombo team, I have also been able to attend various MESSENGER science team meetings.

Thus, I have had a ringside seat to observe much of the planning of two Mercury missions and the staggering unveiling of Mercury achieved by MESSENGER. BepiColombo is due for launch in 2016 and should return its first data from orbit in 2024. It will carry more, and generally more sophisticated, instruments than MESSENGER. We expect it to answer many of the questions left open by MESSENGER, but it will undoubtedly pose numerous new questions of its own. That is how planetary exploration progresses.

In the meantime, this is a good juncture at which to tell Mercury's story. I want to show that it is not a mere pink dot it the sky. Thanks largely to MESSENGER, it stands revealed as a world with a long and complex geological history, surrounded by a dynamic exosphere and magnetosphere, and with superbly sculpted and mysterious landscapes such as the one shown in Fig. 2.

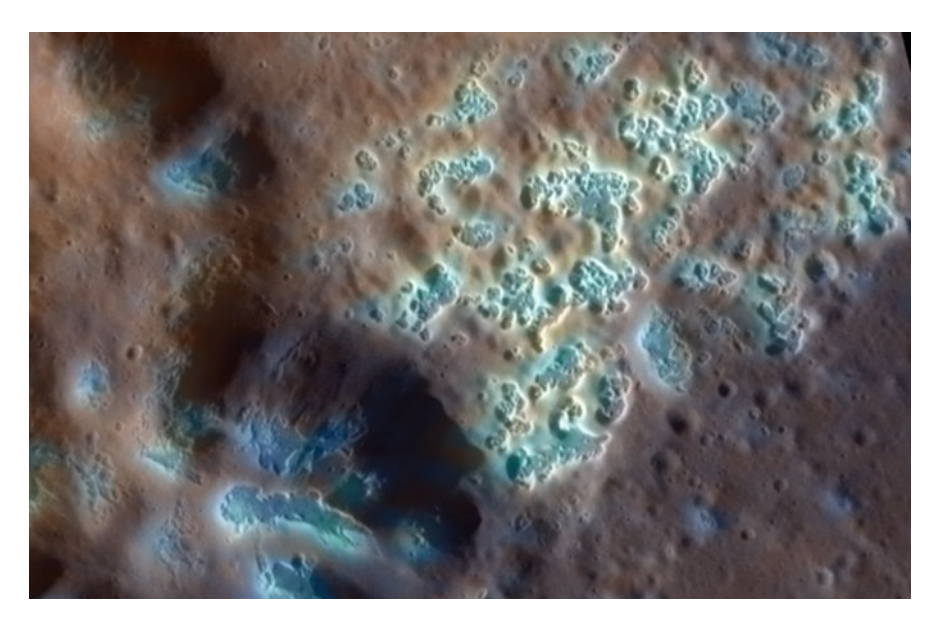


Fig. 2 This is a 18 km wide view of part of the floor and peak-ring structure of Mercury's Raditladi basin. It is a MESSENGER image in enhanced colour. Sunlight is shining from the left (west), casting shadows on the east-facing slopes of the peak ring. Circular, partly shadowed depressions are impact craters. What is most remarkable about the landscape here is the profusion of steep-sided flat-bottomed depressions a few tens of metres deep. These are known in the literature as 'hollows' and have complex outlines. Here, they have formed both on the peak ring and on part of the basin floor through the agency of some unknown process, possibly still active today, that has stripped away the top few tens of metres from Mercury's surface (NASA/Johns Hopkins University Applied Physics Laboratory/Carnegie Institution of Washington)

viii Preface

The hollows in Fig. 2 appear at lower resolution as 'bright crater floor deposits', but are revealed in this high-resolution colour image as high-albedo blue material intimately associated with hollowing. While filming for a BBC Sky at Night television programme broadcast in February 2008, Patrick Moore and I mused over the strangeness of these irregular bright patches on crater floors seen on images from MESSENGER's first flyby. Just about the only thing we got right about them was to agree that more detailed images from orbit would be needed before anyone could work out what they are.

I would probably have written this book anyway, but I would like to record here that in my last conversation with Patrick Moore, in November 2012, less than 3 weeks before he died, Patrick urged me (not for the first time!) to write a book about Mercury. I said that I would if he would promise to write a foreword for it, and so we reached agreement. I know Patrick would have kept his end of the bargain had he been spared.

It is not my intention to present a comprehensive account of the history of Mercury science, though I have traced in broad outline how ideas (and misconceptions!) about Mercury have arisen and progressed. Nor is this a blow-by-blow account of the unfolding of new insights during the MESSENGER mission. Instead, my main aim has been to present a 'snapshot' view of Mercury as understood in the year 2014 near the end of MESSENGER's extended mission in the light of knowledge gained from and ideas spawned by MESSENGER. It will be a decade before a comparable leap forward can be expected thanks to BepiColombo.

Citations

I have chosen not to litter the text with citations. This book is my own distillation (no doubt flawed or unbalanced in places) of what I have learned at conferences, in correspondence, in conversations and on websites, in addition to the peer-reviewed literature.

Citations are, however, included in the credits within figure captions, and in the appendix I give some pointers to finding the most relevant peer-reviewed publications.

Milton Keynes, United Kingdom

David A. Rothery

Acknowledgements

MESSENGER images in this book are courtesy of NASA/Johns Hopkins University Applied Physics Laboratory/Carnegie Institution of Washington. Many of the graphics have been redrawn based on information from a variety of sources. Others are acknowledged in the captions.

Many people have helped me in ways large or small on the journey that led to this book. With apologies to any whom I have inadvertently left out, those not mentioned above include the following:

On or associated with the MESSENGER team: Sean Solomon, Ralph McNutt, Jim Slavin, Nancy Chabot, Brett Denevi, Paul Byrne, Shoshana Weider, Christian Klimczak, Larry Nittler, Tom Watters, Deborah Domingue, Steve Hauck, Maria Banks, Miriam Riner, Laura Kerber, Jim Head, David Blewett, Caleb Fassett, Noam Izenberg, Rosemary Killen, Ron Vervack, Stan Peale, Bill Boynton, Kris Becker, Bill McClintock.

On or associated with the BepiColombo team: the late George Fraser, Johannes Benkhoff, Masaki Fujimoto, Shingo Kameda, Matteo Massironi, Gabriele Cremonese, Anna Milillo, Stefano Orsini, Adrian Martindale, James Carpenter, Jim Pearson, Helen Middleton, Jonathan McAuliffe, Harri Laakso, Jyri Näränen, Karri Muinonen, Juhani Huovelin, Jörn Helbert, Nick Thomas, Yves Langevin, Susan McKenna-Lawlor, Karl-Heinz Glassmeier, Harry Hiesinger, Frank Preusker, Jürgen Oberst, Manuel Grande.

PhD students who have worked on Mercury with me at the Open University: Rebecca Thomas, Emma Fegan, Valentina Galuzzi, Lorenza Giacomini.

From JPL: Chen-wan Yen.

From the team that proposed ESA's Mercury mission: André Balogh.

Contents

1	A P	ale Pink	K Dot	1
	1.1	Elusiv	e Planet	1
	1.2	Seeing	g Mercury	3
	1.3		and Transits	5
	1.4	Mappi	ng by Telescope, and Mercury's Rotation	7
		1.4.1	Early Telescopic Observations	7
		1.4.2	Schiaparelli and "Synchronous Rotation"	8
		1.4.3	Antoniadi's Map, and Later	9
		1.4.4	Not Synchronous After All	10
		1.4.5	A Day Twice as Long as a Year	12
		1.4.6	Hot Poles and Warm Poles	13
		1.4.7	An Explanation for 3:2 Spin:Orbit Coupling	15
	1.5	Mercu	ry's Size, Mass and Density	15
2	The	Marine	er 10 Era of Mercury Science	19
	2.1		uction	19
	2.2	Three	Flybys for the Price of One	19
		2.2.1	The Trajectory	19
		2.2.2	Limitations	22
	2.3	Marine	er 10's Instruments	23
		2.3.1	Television Science	23
		2.3.2	Infrared Radiometry	25
		2.3.3	Ultraviolet Spectroscopy	26
		2.3.4	Celestial Mechanics and Radio Science	26
		2.3.5	Magnetic Field	27
		2.3.6	Plasma Science	27
		2.3.7	Charged Particles	28
	2.4	Mappi	ng a New Planet	28
		2.4.1	Quadrangles	28
		2.4.2	Naming Features	28

xii Contents

	2.5	What	Mariner 10 Found	30
		2.5.1	Surface Characteristics	30
		2.5.2	Mercury Timescale and Stratigraphy	39
		2.5.3	The Magnetic Field	41
		2.5.4	The Interior	42
		2.5.5	Surface Composition	45
		2.5.6	Space Weathering	46
		2.5.7	The Exosphere	47
		2.5.8	Polar Ice?	49
	2.6	The C	Conundrum of Mercury's Origin	50
3	Higl	h Time	for Another Mission?	53
	3.1	Introd	uction	53
	3.2	Back t	to Mercury	54
	3.3	MESS	SENGER	56
		3.3.1	The Trajectory and Orbit	56
		3.3.2	The Spacecraft	60
		3.3.3	The Payload	62
	3.4	BepiC	Colombo	69
		3.4.1	The Trajectory and Orbit	69
		3.4.2	The Spacecraft	72
		3.4.3	The Payload	74
	3.5	Concl	usions	84
4	Mer	cury's	Surface as Seen by MESSENGER	85
	4.1	Introd	uction	85
	4.2	Crater	s and Terrain Types	86
		4.2.1	Crater Characteristics	86
		4.2.2	Global Overview in Colour	89
		4.2.3	Layer Upon Layer	97
	4.3	Surfac	ce Composition	99
		4.3.1	Elemental Abundances	101
		4.3.2	Minerals and Rock Types	103
	4.4	A Tou	ır of Mercury	105
		4.4.1	Global Topography	105
		4.4.2	The Oldest Terrain	107
		4.4.3	Compressional Tectonic Features	108
		4.4.4	Impact Basins	117
		4.4.5	Volcanism	127
		4.4.6	Hollows	135
		4.4.7	Polar Volatiles	139
		4.4.8	Mysteries	142

Contents xiii

5	Mei	rcury's Interior	147
	5.1	Inside a Planet	147
	5.2	The Core	147
		5.2.1 The Core's Size	147
		5.2.2 The Core's Composition	149
	5.3	Crustal Thickness	151
	5.4	The Lithosphere	153
	5.5	Mantle Composition	154
	5.6	Thermal Evolution	155
6	Mei	rcury's Magnetic Field and Exosphere as Seen	
		MESSENGER	157
	6.1	Above the Surface	157
	6.2	The Magnetic Field	157
		6.2.1 Strength and Asymmetry	157
		6.2.2 Dynamic Processes Related to the Magnetic Field	158
		6.2.3 Field Generation	163
	6.3	The Exosphere	163
7	Mo	re Questions than Answers?	167
	7.1	MESSENGER's Legacy	167
	7.2	How Did Mercury Form?	168
		7.2.1 Hit-and-Run	168
		7.2.2 Iron Sequestration into the Core	170
		7.2.3 Primary Crust	170
	7.3	Meteorites from Mercury?	171
	7.4	What Will BepiColombo Teach Us?	172
Αŗ	pend	lix A	173
-	A.1	Previous Publications About Mercury	173
	A.2	Mariner 10 Images	173
	A.3	MESSENGER Data	174
	A.4	BepiColombo Websites	174
	A.5	Seeing Mercury for Yourself	174
In	dex .		175

Chapter 1 A Pale Pink Dot

1.1 Elusive Planet

Unless you are in the tropics (or witness a total solar eclipse), you will never see Mercury in a completely dark sky, because when the Sun is far enough below the horizon for the sky to be dark, Mercury will be below the horizon too. You have to be in the right place at the right time to see it at all. Discounting total solar eclipses, which are extremely rare, the right place is anywhere with a clear, low horizon in the direction of either the sunset or the sunrise as appropriate. The right time is after sunset as the sky darkens, or, for early risers, before dawn. Even that will do you no good unless you have also chosen a date to coincide with Mercury's brief excursions far enough from the Sun for it to be sufficiently high above the horizon for it show itself in the brief interlude between daylight and full darkness. I have often glanced unawares at the sky and seen Venus shining high and bright in the evening or morning sky. You can hardly miss Venus when it's around, but I've never seen Mercury without deliberately setting out to look for it.

So what does Mercury look like? A pink star, that shows as no more than a pale pink dot through binoculars or any telescope to which you or I are ever likely to have access (Fig. 1.1). Disappointing in a way, but to see Mercury with your own eyes is to see our Solar System's smallest planet, and the one closest to the Sun. Congratulations if you have achieved this – you have seen the trickiest to locate of the five planets known in the ancient word: Mercury, Venus, Mars, Jupiter and Saturn. The great Copernicus himself, working for most of his life near the shores of the Baltic Sea, is reputed never to have managed to see it.

In the absence of street-lighting and tall buildings, Mercury would have been more obvious to dwellers in the ancient world, especially to those in lower latitudes where the ecliptic (the plane of Earth's orbit projected into the sky, to which all other planets lie close) makes a steeper angle to the horizon. The earliest known observations of Mercury are recorded on Assyrian clay tablets dated to 687 BC, but documenting observations made at least six centuries previously. The name given

1

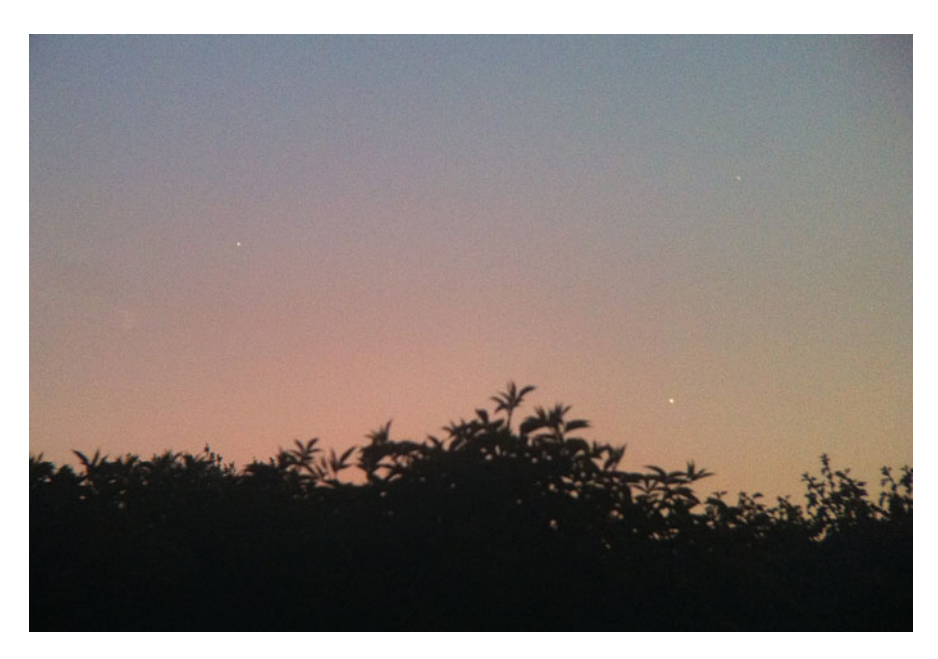


Fig. 1.1 The right place at the right time. A view westward from Yarnfield, Staffordshire, England 25 May 2013, showing Mercury, Venus and Jupiter. Venus is the brightest, *very low*, about to set just above the trees. Jupiter is *above left* of Venus. Mercury is the faintest of the three, *above* and slightly to the *right* of Venus. This is how it looked to the naked eye, but the picture was actually taken with an iPhone camera through one side of a pair of binoculars, balanced on a bollard for stability. For scale, the distance between Venus and Mercury was about 1°, or about two Moon diameters (Courtesy of Alastair Taylor)

to Mercury by the Assyrians translates as 'the jumping planet', perhaps a reflection of its rapidly changing position in the sky, and of how it can appear east and west of the Sun in fairly rapid succession. The Babylonians identified Mercury with Nabu and the Egyptians with Thoth, their deities associated with writing and who sometimes acted as the messenger of the gods. That was also the role of the ancient Greek Hermes and his Roman equivalent Mercury, though it took the Greeks a while to realise that morning and evening apparitions of Mercury were the same object. They were similarly confused over Venus.

To the imperial Romans, Wednesday was *dies Mercurii* (Mercury's day) and many languages descended from Latin preserve the name Mercury for the corresponding day in various forms: mercredi, mercoledi, miércoles, miercuri (French, Italian, Spanish, Romanian) and even Dydd Mercher (Welsh). The Norse/Germanic personification of Mercury was Odin/Wotan, from which English derives Wednesday (Woden's day), Dutch woensdag, and Danish, Norwegian and Swedish Onsdag. Although German preserves the names of gods in other days of the week, Wotansdag was replaced by the more prosaic Mittwoch ('Midweek') more than a 1,000 years ago, a convention also followed by Icelandic and most Slavic languages.

Oriental writings more than 2,000 years old recognise Mercury as Chen Xing ('the hour star') in China, and as Budha (god of merchandise) in Hindu mythology. In modern Chinese, Japanese, Korean and Vietnamese Mercury is literally 'the water star'.

The principal modern languages of the Indian subcontinent preserve the Budha element in their word for Wednesday, whereas in Chinese, Japanese and Korean Wednesday translates as 'water day': so all these preserve a link between the planet Mercury and Wednesday.

1.2 Seeing Mercury

The reason for Mercury's elusiveness is its closeness to the Sun. Even at aphelion, the point of its orbit furthest from the Sun, Mercury is only 0.47 AU (Astronomical Units) from the Sun, whereas at perihelion (closest to the Sun) the Sun-Mercury distance is only 0.31 AU. Given that the Earth, with a much less eccentric orbit than Mercury, is always about 1 AU (150 million km) from the Sun, a simple diagram (Fig. 1.2) shows that the greatest possible angular separation in the sky between Mercury and the Sun is 28°. This occurs when Mercury's aphelion coincides with the time of greatest elongation, which occurs when the line of sight from the Earth to Mercury is tangential to Mercury's orbit. The least favourable maximum elongation of 18° coincides with Mercury's perihelion.

Mercury's perihelion advances round the Sun at a rate of 1.56° per century. This slow progress means it has scarcely shifted in historic times, and for the purposes of discussing Mercury's observability it can be regarded as fixed.

Mercury's greatest elongation from the Sun in the morning sky occurs in April, whereas its greatest elongation from the Sun in the evening sky, is in August (Fig. 1.2).

The time of greatest possible maximum elongation is not quite the easiest date on which to spot Mercury, for two reasons. The first is that more of Mercury's disc is illuminated when it is on the far side of the Sun, and it is brighter overall then despite being further away. There is an observational trade-off between Mercury's brightness and its closeness to the Sun's glare, so Mercury is easiest to spot a few days before maximum eastern elongation (evening sky) or a few days after maximum western elongation (morning sky).

The second factor is Mercury's altitude above the horizon, which is controlled largely by the angle at which the ecliptic plane intersects the horizon. As seen from the northern hemisphere, the ecliptic at sunset strikes the horizon at its shallowest angle of the year at the September equinox, so even if Mercury is close to its greatest possible maximum elongation from the Sun it will already be low in the sky at sunset, and hard to see. Conversely, as seen from the southern hemisphere, at this time of year the ecliptic is at its steepest at sunset, and Mercury near maximum elongation is optimally placed for viewing. Southern hemisphere observers are luckier than northern observers when it comes to viewing Mercury near its greatest

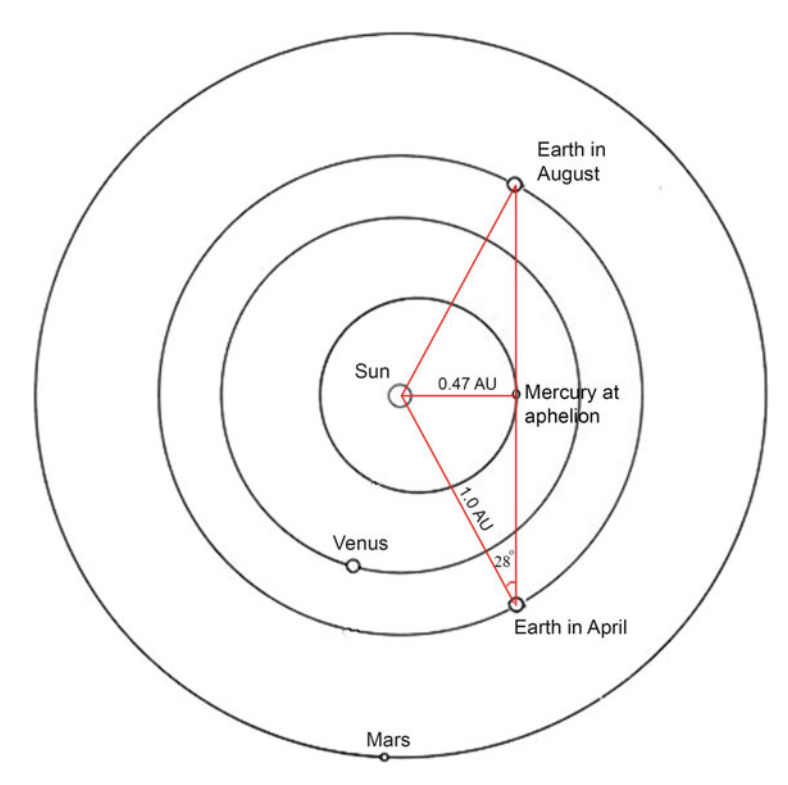


Fig. 1.2 The orbits of the inner planets to scale, showing Mercury at aphelion. This is when it is at its furthest from the Sun, a distance of 0.47 AU. If the Earth happens to be in the right part of its own orbit, this is when Mercury achieves its greatest possible maximum elongation (angular separation) of 28° from the Sun as seen in the Earth's sky. This can occur either in April, when Mercury is at its greatest possible maximum elongation west of the Sun and is visible in the morning sky before dawn, or in August, when Mercury is at its greatest possible maximum elongation east of the Sun and is visible in the evening sky after sunset. Shown here are greatest possible maximum elongation coincides with Mercury's aphelion. Maximum elongation occurs whenever the line of sight from Earth to Mercury is tangential to Mercury's orbit, and is as small as 18° when Mercury is at perihelion. Various other factors affect ease of visibility, so greatest possible maximum elongations are not necessarily the most favourable occasions to see Mercury

possible maximum western elongation too, because in April the ecliptic makes a steep angle with the southern hemisphere dawn horizon, whereas at that time of year the angle is shallow as seen from the northern hemisphere.

Thus whereas southern observers have the advantage of greatest possible maximum elongations more or less coinciding with steepest inclination of the ecliptic, for northern observers the two effects are never optimised at the same time. For them, the easiest time to see Mercury is when it is near maximum eastern elongation in March or April, when the ecliptic is steepest to the horizon, even though Mercury's angular separation from the Sun will then be closer to 20° than to 28°. However, it is perfectly possible to locate Mercury on other dates, as Fig. 1.1

1.3 Orbit and Transits 5

demonstrates, which was taken 17 days before maximum elongation and only 14 days after 'superior conjunction' when Mercury was on the far side of the Sun. At this time Mercury's elongation from the Sun was about 15°.

1.3 Orbit and Transits

Being so close to the Sun, Mercury's orbital speed is faster than that of every other planet, and because its orbit is smaller the time taken to complete an orbit is shorter still. Orbital period is related to average distance from the Sun (orbital semimajor axis) by Kepler's third law of planetary motion, which states that period (in years) squared = semimajor axis (in AU) cubed. Mercury's semimajor axis is the average of its perihelion (0.47 AU) and aphelion (0.31 AU) distances, working out at 0.39 AU, and its orbital period is thus 0.244 Earth years, or 88.0 Earth days.

Mercury's orbit has an eccentricity of 0.206, which, although it looks fairly circular when drawn (Fig. 1.2) is more eccentric (more strongly elliptical) than the orbit of any other planet. It is also more steeply inclined to the ecliptic than any other planet's orbit, at an angle of 7.0°. Mercury was north of the ecliptic when the image in Fig. 1.1 was taken, whereas Venus and Jupiter were closer to the ecliptic, which is why the three planets form a triangle rather than falling along a line.

Because the Earth is moving round the Sun too, the time between successive inferior conjunctions (when Mercury overtakes Earth on the inside track and passes between us and the Sun) is longer than a Mercury year, and happens every 3–4 months. The gaps between eastern elongation and inferior conjunction and between inferior conjunction and western elongation are significantly less than a quarter of this, and can be as little as 16 days, so no wonder the Assyrians called Mercury the 'jumping planet'!

Although Mercury passes between the Earth and the Sun at least three times a year, its orbital inclination is such that exact alignment is rare, and can happen only in May or November, when the Earth is close to one of the two points in its orbit where its orbital plane is intersected by the plane of Mercury's orbit. When the alignment is sufficiently exact, Mercury transits across the face of the Sun, though with an angular size of only about 12 s of arc (about 1/150th of the Sun's diameter) a magnified image is required to reveal it (Fig. 1.3).

The next transit of Mercury will happen on 9 May 2016. Its timing is ideal for viewing from western Europe, starting at 11:12 and finishing at 18:42 UT, which means that most of the transit will also be visible from North America. The one after that is less favourable for northern hemisphere viewers only because of the time of year: 11 Nov 2019 starting 12:35 and ending 18:04. There will then be a 13 year gap until the next transit on 13 November 2032, followed by 7 Nov 2039 and 7 May 2049.

Do not attempt to look directly at the Sun to see a transit, because there is a serious risk of blinding yourself (or setting fire to your camera!). If you have a telescope or binoculars, you can either project the Sun's image safely onto a shaded

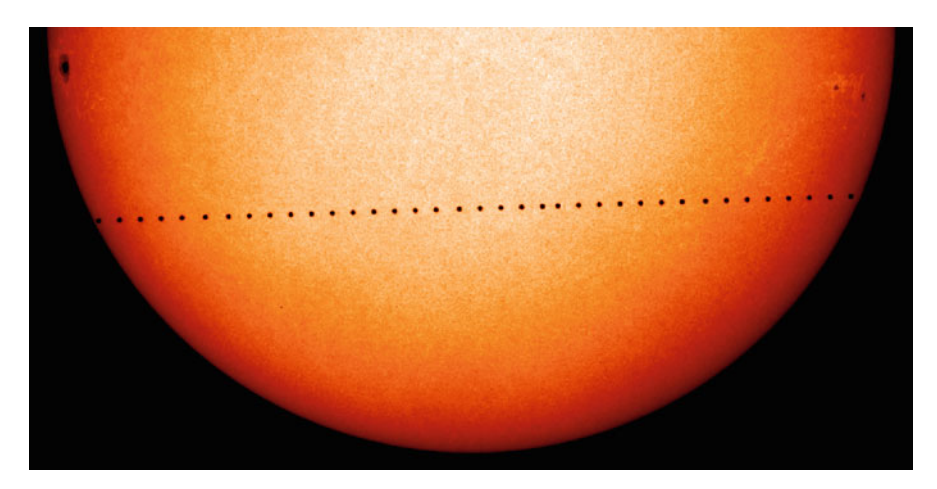


Fig. 1.3 Mercury's transit across the Sun 8 November 2006, compiled from a series of images recorded from near Earth by the ESA/NASA Solar and Heliospheric Observatory (SOHO) spacecraft. The total transit duration in this case was about 5 h (Credit: NASA)

card held at arm's length beyond the eyepiece, or observe it directly through the eyepiece only if you have a special solar filter fitted *in front* of your instrument and capable of blocking out 99.99 % of incoming sunlight at all wavelengths.

Transits of Mercury are more common than transits of Venus, and the first observation was achieved in 1631 by the French Jesuit astronomer Pierre Gassendi, thanks to a successful prediction by Johannes Kepler. There is no observational record of a transit of Venus until 1639, even though these can be seen by the naked eye.

Precise observation of planetary transits played a key role in determining the scale of the Solar System, and observing the 3 June 1769 transit of Venus from Tahiti was a primary scientific goal of Captain Cook's first voyage of circumnavigation on HMS Endeavour. Less well known is that the expedition's astronomer Charles Green, along with Cook himself who was also a capable observer, also observed a transit of Mercury on 9 November of the same year, from the shores of Mercury Bay in New Zealand. Green later fell ill, and died soon after putting out from Batavia (modern-day Jakarta) in 1771, but is credited with being the first to note that Mercury's crisp outline during transit demonstrates that the planet must have little or no atmosphere. Green was correct, but generations of later observers, some of them perhaps misled by dark or bright aureoles surrounding the transiting planet that can be caused by imperfect optics, adhered to the view that Mercury does have an atmosphere.

Details of the gradual advance (or precession) of Mercury's perihelion around the Sun, already noted, caused consternation for more than half a century. Precession of this nature is predicted by Newtonian dynamics, as a consequence of the gravitational pull of the other planets. The rate of precession is greatest for Mercury, because it is closer to the Sun than the other planets. However the observed rate of precession for Mercury is nearly 1 % too fast – a discrepancy of 43 s of arc per century. This was first noted in 1859 by the French mathematician Urbain Le Verrier, on the basis of his analysis of a series of precisely timed transits of Mercury from 1697 to 1848.

Le Verrier reasoned that the anomaly could be explained if there was an unknown planet, for convenience named Vulcan, orbiting closer to the Sun than Mercury. However, every observation of 'Vulcan' during total solar eclipses turned out to be merely a background star lying in almost the same direction as the Sun, and every black dot recorded on the Sun was explicable as a sunspot rather than Vulcan in transit. A transit of Vulcan predicted by Le Verrier on 22 March 1877 failed to materialise, and so did a 18 March 1879 transit predicted on the basis of revised orbital calculations by the Austrian astronomer Theodor von Oppolzer.

The mystery surrounding the advance of Mercury's perihelion remained until 1915 when Einstein published his General Theory of Relativity. He showed that Mercury's additional annual precession is exactly accounted for by treating the gravitational field within which Mercury moves as an effect of the curvature of spacetime in proximity to the Sun's large mass.

Thus a hypothetical Vulcan is not required to explain anything. On the contrary, given the neatness of Einstein's explanation, if Vulcan *did* exist then it would be hard to explain why it does *not* affect Mercury's perihelion advance, which is now perfectly accounted for. It is now certain that no planet-sized object exists closer to the Sun than Mercury. According to theory, small objects could exist in dynamically stable orbits at distances of 0.06–0.21 AU from the Sun, but searches for such a population of vulcanoid asteroids have yet to reveal anything. It now seems unlikely that there are any vulcanoids greater than about 6 km in size, and if there are any at all, statistics would suggest that fewer than a hundred of them are likely to be bigger than 1 km.

1.4 Mapping by Telescope, and Mercury's Rotation

1.4.1 Early Telescopic Observations

Through a telescope, Mars and Jupiter usually show clear features that enable their rotation periods to be measured. Saturn is trickier, but the occasional storm means that its rotation too can be worked out. The rotation of Venus remained undetermined until measured by radar in 1963, because its surface is hidden by permanent dazzling cloud. However, even the rotation of Mercury, which we now know to have a bare rocky surface, remained at first unknown, and then misinterpreted until as recently as 1965.

The first documented telescopic observations to show Mercury's phases were by the Italian Giovanni Zupus in 1639. Actual surface features are much more elusive. We now know that this is partly because of the lack of surface contrast across the

face of Mercury (it lacks the marked regional albedo contrasts seen on the Moon), but a more important factor is that Mercury cannot be observed under favourable conditions. If you catch Mercury in near-darkness it is always close to the horizon, so there is much more of the Earth's atmosphere between you and it than if it were high in the sky. The unsteadiness of the air and scattering of light conspire to make the image unsteady and the quality poor. Mercury can be located in a telescope in broad daylight, and you can choose a time of day when it is as high as you like, but the amount of scattered daylight in the foreground (if you like, the blueness of the sky between you and Mercury) severely reduces any contrast between areas of the planet's surface.

The Hanover-based Johann Schröter working between 1780 and 1815 inferred a mountain on Mercury 20 km high and deduced a rotation period for Mercury of 24 h 4 min. To his credit, Schröter's contemporary William Herschel, based in England, made no such claims despite persistent attempts to discern features through his own telescopes. Schröter's Mercury drawings are now discredited although he was an accomplished lunar observer.

1.4.2 Schiaparelli and "Synchronous Rotation"

As telescopes improved, visual observers, taking advantage of instants of 'good seeing' were able to discern features that would appear to be there on successive nights, and so gradually maps of Mercury were compiled. The first broadly credible map was by Giovanni Schiaparelli, observing by day and at twilight from Milan between 1881 and 1889 at first with an 8½ inch and then with an 18 in. refractor. Schiaparelli's map of one hemisphere of Mercury is shown in Fig. 1.4, and on the basis of his observations he announced that Mercury's rotation period is exactly the same as the period of its orbit about the Sun, with an observational uncertainty of about only 4 h either way. Schiaparelli also concluded that the tilt of its axis must be small; he was unable to measure it but concluded that it must be less than 8° (whereas the Earth's axis is tilted at 23°).

Synchronous rotation of the sort announced for Mercury by Schiaparelli is exactly what is exhibited by the Moon in its orbit about the Earth, and (as we now know) by most of the satellites of the giant planets. It is brought about by tidal forces, which drag on the orbiting body's tidal bulges and slow its rotation until it keeps the same face permanently towards the primary body.

If Mercury were in a state of synchronous rotation, an important consequence would be that it would keep the same face permanently towards the Sun. This would be intensely hot, whereas the 'dark side', facing always away from the Sun, would be very cold. There would be a narrow 'twilight zone' annulus where the Sun rested close to the horizon where the temperature might be conducive to life (a factor not lost on science fiction authors), though the eccentricity of Mercury's orbit would mean that near perihelion its orbital speed would be faster than its rotation whereas near aphelion it would lag behind. This 'libration' would cause sunrise and sunset

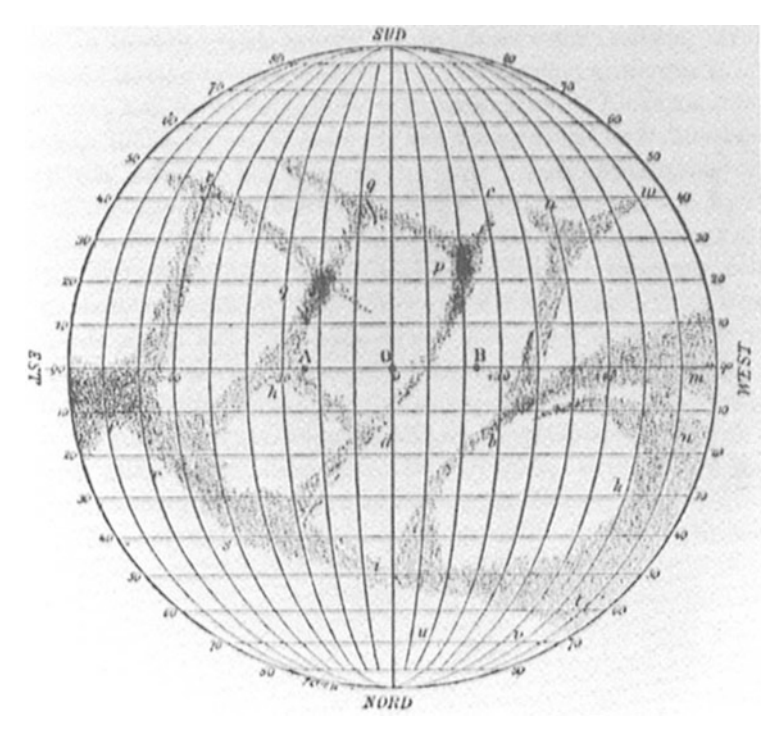


Fig. 1.4 Schiaparelli's 1889 map of Mercury, south at the top as seen through an astronomical telescope

above the *same* horizon across a narrow range of longitudes in the twilight zone during the course of an orbit.

Synchronous rotation seemed entirely plausible for Mercury, and was 'confirmed' by later observers. One such was the American Percival Lowell, who drew a network of lines on Mercury (1896), much as he did on Mars, though fewer of them. At least Lowell did not interpret these lines as artificially engineered irrigation canals (as it he did for Mars), but concluded that they were "best explained as the results of cooling."

1.4.3 Antoniadi's Map, and Later

Another adherent to the synchronous rotation view of Mercury, but on the basis of a more credible series of observations, was Eugène Antoniadi, a Greek working in France. He observed in daylight with the 83 cm Meudon refactor, and published a much more reasonable map, showing albedo features in 1934 (Fig. 1.5).

Antoniadi's map became the foundation for the work of subsequent visual and indeed photographic observers, such as Audoin Dollfus and colleagues based at the

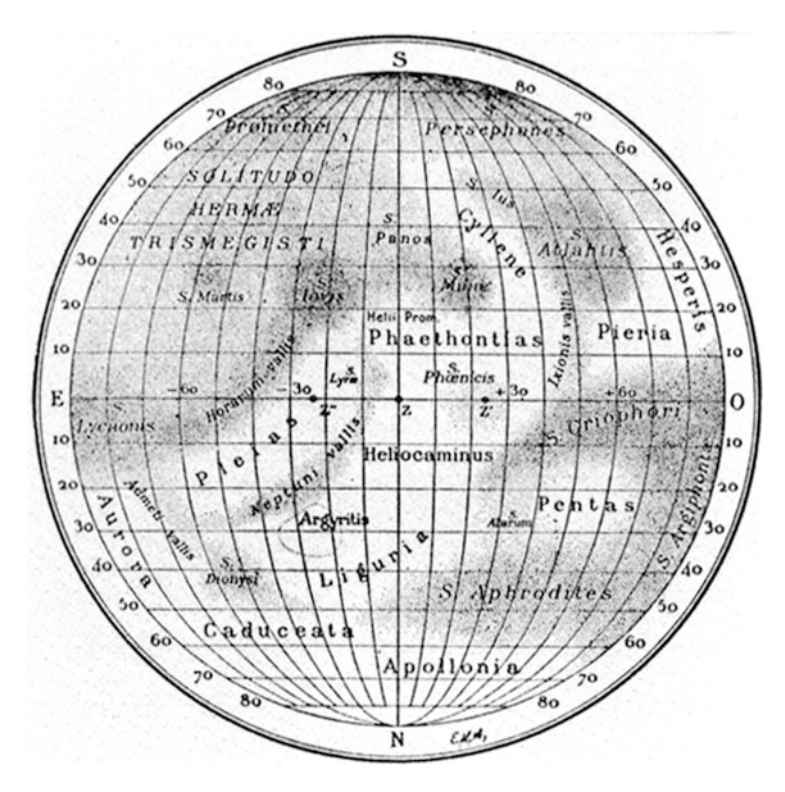


Fig. 1.5 Antoniadi's 1934 map of Mercury, south at the *top* as seen through an astronomical telescope

Meudon Observatory near Paris, but now observing at the Pic du Midi observatory in the French Pyrenees in the 1940s and 1950s. Names for regional albedo features named by Antioniadi and reobserved by Dollfus and his colleagues were adopted by the International Astronomical Union (Fig. 1.6) and became the basis for naming mapping quadrangles when the spacecraft (Mariner 10) obtained the first close-up images in 1974. Following Antoniadi's convention, names are of Latin form, dark area names being preceded by the descriptor term Solitudo, whereas light areas are designated by a Latin name alone.

However, a decade beforehand, Mercury's synchronous rotation had been shown to be a fiction. How then could Antoniadi's mapping have any value, when he had regarded it as proof of synchronous rotation?

1.4.4 Not Synchronous After All

The first hint that rotation could not be synchronous came in 1962 with the measurement of microwave radiation (representing 'black body' radiation, of

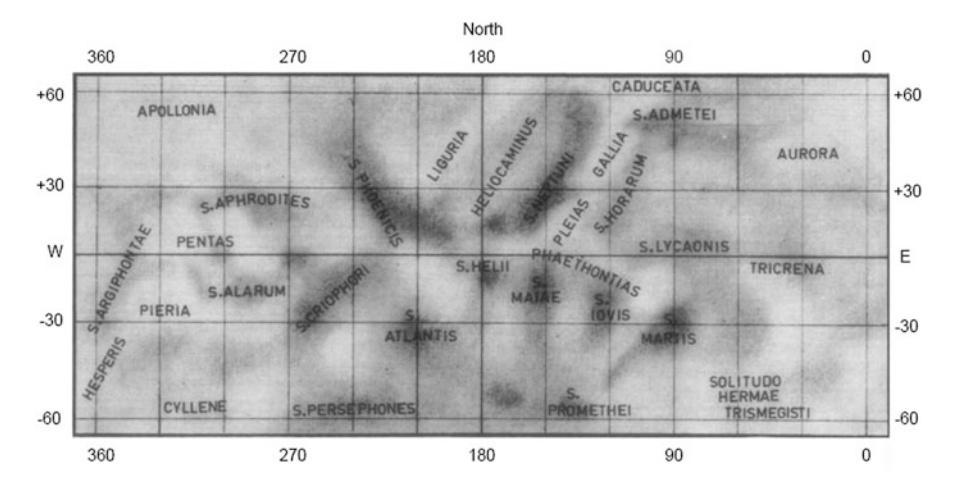


Fig. 1.6 1975 IAU nomenclature for albedo features on Mercury, on a 1972 telescopic map compiled from the best available visual and photographic data from Pic du Midi and New Mexico State Observatories. Solitudo is abbreviated S. Many of the features and names on Antoniadi's map (Fig. 1.5) can be seen, but beware that this map has north at the top and the prime meridian (zero longitude) has been redefined

thermal origin) from Mercury. This was achieved with the planet near maximum elongation by a team led by William Howard using the University of Michigan 26 m radiotelescope. Near maximum elongation, half of Mercury's Earth-facing hemisphere is sunlit and half is in shadow, but the measured microwave radiation was an average from the whole of this hemisphere. Calculations had suggested a temperature as low as 27 K on the permanent night-side of Mercury, far too cold to radiate any detectable microwave radiation. The measured flux, it was reasoned, could come only from the Earth-facing part of Mercury's dayside, but when Howard and his team did their sums on that basis, these seemed to show a temperature at the subsolar point in excess of 1,000 K. This was considerably higher than the expected value, which was 600–700 K, and no convincing explanation was forthcoming at the time.

With hindsight, it is easy to see that the explanation is that Mercury's rotation is not synchronous, so that the portion of the globe in darkness has been recently warmed by the Sun and is contributing to the total measured microwave flux. Therefore, only part of the total flux comes from the dayside, which is then consistent with a more reasonable temperature there, lower than the 1,000 K derived by Howard and colleagues.

The breakthrough came with a series of radar observations in April 1965 by Gordon Pettengill and Rolf Dyce, using the Arecibo telescope to bounce radar pulses off the surface of Mercury when close to inferior conjunction (lying between the Sun and the Earth). The limb-to-limb Doppler spread of the returned echo enabled Pettengill and Dyce to demonstrate that Mercury's rotation period must be somewhere in the range 55–64 days, rotating in a prograde direction. Stan Peale and

Tom Gold were then quick to point out the implausibility of Mercury having synchronous rotation as a result of tidal torque, writing in the same issue of *Nature* where Pettengill and Dyce announced their result:

For a planet on a circular orbit the final condition would ... be one of synchronous rotation like the motion of the Moon with respect to the Earth For a planet with a substantial orbital eccentricity the condition is different, however, and synchronous rotation with the orbital period need not be expected. (S J Peale and T Gold, *Nature*, v205, 19 June 1965).

Basically, Peale and Gold were saying that Mercury's orbit is too eccentric for synchronous rotation to be a stable state. Further radar observations soon pinned Mercury's rotation period down to 58.65 days, bang in the middle of Pettengill and Dyce's estimate, and *exactly* two-thirds of Mercury's orbital period. This is a state described as 3:2 spin:orbit coupling, and can be understood as a result of tidal friction acting on the planet, especially if there is a molten zone in its interior. It is also now known that the Mercury's spin axis is tilted at only 2 min of arc away from a right-angle to its orbital plane, so that Mercury experiences virtually no seasonal variations.

I will attempt to explain the reason for the 3:2 spin:orbit coupling shortly, but first let's see how this state of affairs fooled Schiaparelli and Antoniadi into misinterpreting their otherwise broadly valid observations as being proof of synchronous rotation

Mercury's most favourable elongations for observing occur about every 350 days. During that interval, Mercury will have rotated almost exactly six times (which takes 352 days to accomplish). This means that for many years in succession an observer's best observations will always show the same face of Mercury. Because Mercury's rotation is indeed slow, the amount of rotation during the optimal observing interlude is too small to notice. Furthermore, Antoniadi believed that Mercury has an atmosphere dense enough to support dust clouds, and attributed the mismatch between the surface features he could see at favourable and less-favourable elongations to be caused by local temporary obscuration by such clouds.

1.4.5 A Day Twice as Long as a Year

The 3:2 ratio between Mercury's rotation and orbital period has strange consequences other than the 'stroboscopic' favourable observing conditions, the weirdest of which is that Mercury's day (defined, for example, as the time between successive sunrises) is twice as long as its year. This 2:1 ratio between day-length and year-length may seem counterintuitive given the 3:2 ratio between rotation period and year length, until you realise that if Mercury were not rotating at all it would experience 1 day each year (with the Sun rising in the west and setting in the east!). If it were in synchronous rotation (1:1) its day would be infinitely long. How a 3:2

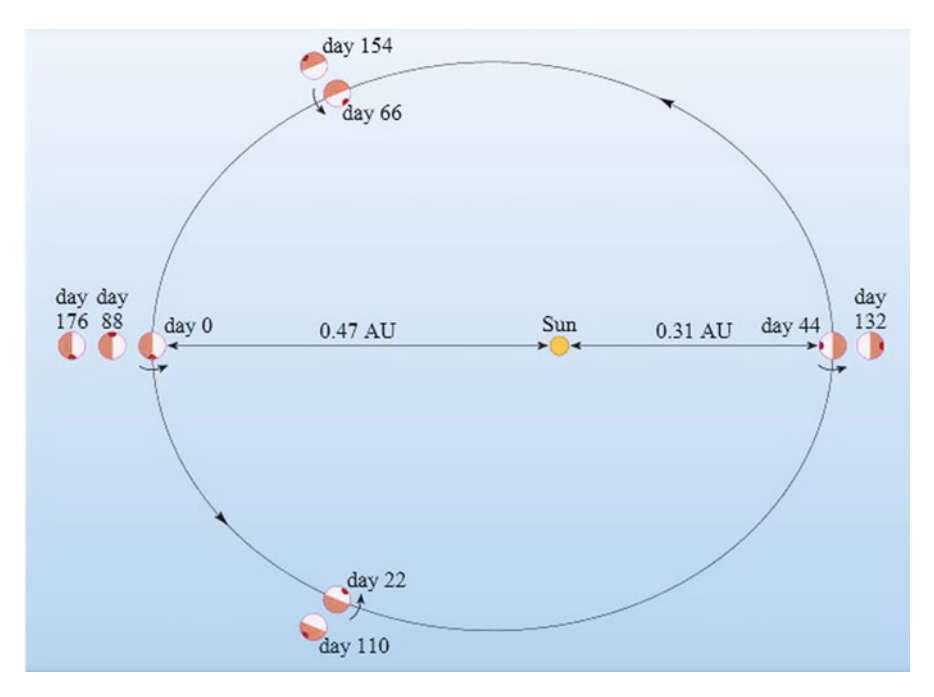


Fig. 1.7 The relationship between Mercury's rotation and orbit. Mercury's location and rotation are illustrated every quarter of an orbit, as the planet moves around two complete orbits, starting from aphelion on 'day 0', where 'day' refers to Earth days, as a convenient unit of time. The dot identifies a fixed point on Mercury's equator, which rotates three times during these two orbits in the direction indicated. On day 0 the dot is experiencing sunrise. On day 44 (perihelion) Mercury has completed $\frac{3}{4}$ of a rotation but the dot is only just experiencing noon. On day 88 Mercury has orbited the Sun once and completed $\frac{1}{2}$ rotations and the dot is experiencing its first sunset. Mercury needs to complete another orbit before the dot experiences sunrise, by which time a complete solar day will have occurred on Mercury -1 Mercury day lasting 2 Mercury years (To avoid superimposing pictures, Mercury has been drawn as if displaced outwards on successive orbits. Sun and Mercury not to scale)

spin:orbit ratio leads to a day-length twice as long as a year is best explained in a diagram (Fig. 1.7).

1.4.6 Hot Poles and Warm Poles

Fig. 1.7 can also be used to illustrate the concept of 'hot poles' on Mercury, which will become relevant when we look at Mercury's surface in detail in later chapters. Concentrate on the point marked by the dot on Mercury's equator. On day 0, when Mercury is at aphelion, this point is experiencing sunrise. Half an orbit (44 Earthdays) later Mercury has completed ¾ of a rotation but has travelled half-way round the Sun, and it is now solar noon at this point. Mercury is now at perihelion,

considerably closer to the Sun than at aphelion. The solid angle of Mercury's sky occupied by the Sun is proportional to the square of the distance, so the amount of solar radiation falling on the subsolar point on Mercury at perihelion (0.31 AU) is greater than at aphelion (0.47 AU) by a factor of $(0.47/0.31)^2$, or 2.3. Our marked point thus experiences more intense solar heating at local noon than places on the equator lying to east or west of it. Each time this point experiences noon, Mercury is at perihelion, so this is a permanent state of affairs. This point is called a 'hot pole', a slightly confusing term because Mercury does not rotate around it in any way – instead it just denotes the point of maximum noontime heating.

There are actually two hot poles on Mercury. The other one, not marked on Fig. 1.7, is on exactly the opposite side of the planet. This is the point on the equator experiencing sunset on day 0, midnight on Earth-day 44 and noon on Earth-day 132 (after $1\frac{1}{2}$ orbits). The two hot poles experience noon at alternate perihelia.

Mercury also has two 'warm poles', which are the places on its equator where noon occurs always at aphelion. One of these is at the subsolar point on day 0 (and again on Earth-day 176, after two orbits), and the other on Earth-day 88 (after one orbit). These are the points on the equator with the coldest noontime temperature, though not on the entire planet because the surface also cools towards the poles as a consequence of illumination becoming more oblique.

Noontime temperature at Mercury's hot poles is now known to be about 700 K, but only about 600 K at the warm poles. Night time temperatures drop to about 100 K just before dawn.

The hot pole effect is exaggerated by the interplay between the eccentricity of its orbit and its spin rate, because orbital speed is slowest at aphelion and fastest at perihelion. We have already noted the temporary to-and-fro migration of the apparent position of the Sun in Mercury's sky that would have been brought about by the eccentricity of its orbit if its rotation had indeed been synchronous. Although Mercury's actual rotation is faster, it is still outpaced by its orbital speed near perihelion, with similar consequences.

On Fig. 1.7 the dot representing the hot pole will experience a swift sunrise and the Sun will already be virtually overhead after about ¼ of an orbit (Earth-day 22), it stays there until about ¾ of an orbit has been completed (Earth-day 66) and then falls rapidly towards sunset. Thus the hot pole has the Sun almost overhead for far longer than you might expect. Moreover, Mercury's extremely rapid orbital motion near perihelion slightly outpaces its rotational speed, with the result that that shortly before perihelion, as seen from a hot pole, the Sun will pass overhead, reverse direction and pass overhead again backwards exactly at perihelion, and then reverse direction again to pass overhead for a third time. A corollary of this is that while the hot pole undergoes a 'triple noon', as seen from warm pole to its east the Sun will set, rise back into view a little, and then set for a final time whereas the other warm pole will see a sunrise, only to have the Sun set beyond the same horizon set before rising again.

1.4.7 An Explanation for 3:2 Spin:Orbit Coupling

Recognition of the long duration hot pole noons provides a way to appreciate how the 3:2 spin:orbit coupling is consistent with tidal forces. Over four billion years ago, soon after formation, Mercury would have been likely to have been spinning much faster than today, perhaps in just a few hours. Proximity to the Sun would stretch Mercury tidally, raising tidal bulges on the sunward and anti-sunward sides.

Tidal friction would slow the planet's rotation (so the bulges did not have to migrate round the globe so fast), but rather than slowing the rotation all the way into synchronicity with the orbital period, the orbit's eccentricity came into play (assuming it had a similarly large eccentricity then as now). Tidal forces are inversely proportional to the cube of distance, which means that the Sun's tidal effect on Mercury is about $3\frac{1}{2}$ times greater at perihelion than at aphelion.

Mercury's rotation has now settled into a stable configuration in which the Sun 'grabs' a tidal bulge before perihelion, and 'holds' it until after perihelion, throughout the portion of the orbit where orbital speed and rotation more or less keep pace so that there is little need for the bulge to migrate in order to stay lined up with the Sun. When Mercury nears aphelion, and the tidal force diminishes (and the bulge subsides), the Sun loses its grip on the bulge. However, it locks onto the opposite tidal bulge next time round. You can imagine the near-tidally-locked tidal bulges coinciding with hot poles between approximately day 22 and day 66 then again between approximately day 110 and day 154 on Fig. 1.7.

1.5 Mercury's Size, Mass and Density

Mercury's angular size can be measured well enough through a telescope. The radius of Mercury quoted in textbooks from the 1890s is 2,400 km, in good agreement with the currently accepted value of 2,440 km, which is correct to a precision of within 1 km.

Mercury has no moon, which would have made Mercury's mass straightforward to calculate. Instead, in 1841 the German astronomer Johann Encke measured Mercury's gravitational perturbation of the orbit of the short period comet that now bears his name. The mass he derived for Mercury was 4.1×10^{23} kg, about 20 % more than the correct value $(3.30 \times 10^{23}$ kg). Shortly after, Le Verrier estimated the mass of Mercury from tiny perturbations that its gravity causes to the Earth's orbit, to and came up with a value about 30 % too big. However, both were adequate to but adequate to demonstrate that Mercury's mass is less than a tenth of the mass of the Earth $(5.97 \times 10^{24}$ kg).

Further estimates for Mercury's mass, in the final decades of the nineteenth century, were sometimes higher, sometimes lower, but most were consistent with an important fact: dividing Mercury's mass by its volume reveals that it is a dense planet. As we now know, Mercury's density is 5.43×10^3 kg m⁻³. This is slightly

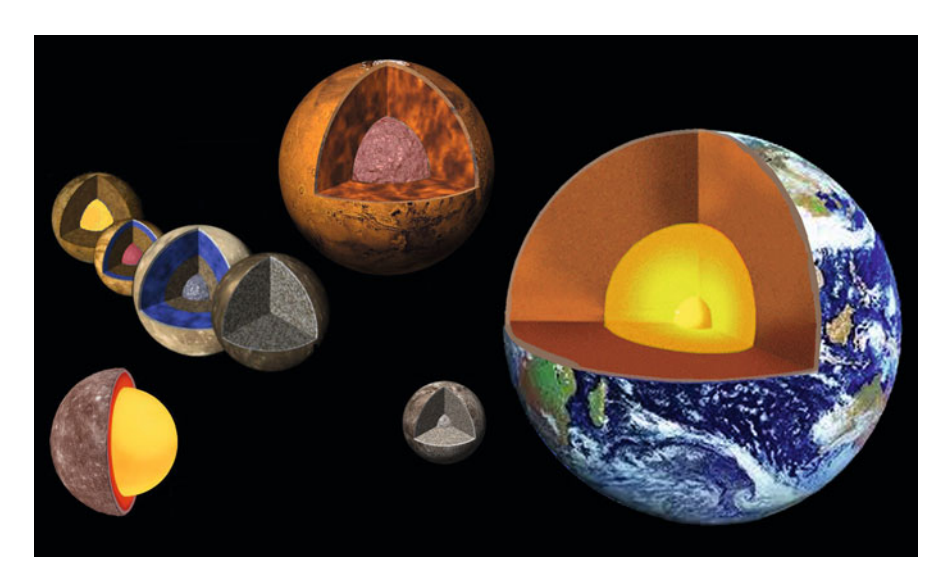


Fig. 1.8 Mercury and several other bodies shown to the correct relative scale, and cut away to reveal the sizes of their cores. Mercury is *lower left*, next to Jupiter's four Galilean satellites Io, Europa, Ganymede and Callisto. Mars is *top centre*, and on the *right* are the Moon and the Earth (showing inner and outer core). The likely temperature of each core is indicated qualitatively by its 'glow'. In the model shown here, Callisto is portrayed as broadly undifferentiated and lacking a discrete core (Modified from various sources)

less than the Earth's density ($5.51\times10^3~kg~m^{-3}$) and slightly greater than the density of Venus ($5.20\times10^3~kg~m^{-3}$).

Mercury's density being intermediate between that of Earth and Venus may seem unremarkable, but a more meaningful comparison can be made by taking into account the effect of each planet's gravity on its internal pressure, which will compress its interior. Mercury's much smaller mass results in weaker gravity, smaller internal pressure, and less internal 'self compression'. Allowing for this, the 'uncompressed density' of Mercury can be calculated as 5.3×10^3 kg m⁻³ as opposed to the Earth's uncompressed density of 4.0×10^3 kg m⁻³.

The only reasonable explanation for this is that Mercury has core that occupies a much greater fraction of its volume than is the case for the Earth, or indeed any other comparable body (Fig. 1.8).

Mercury's high density is not *proof* of a large core. Strictly, all that it shows is that Mercury has a greater proportion of dense matter than other planets. Bearing in mind the known composition of the Solar System (based on studies of the Earth, Moon and meteorites, and the abundances of elements in the Sun's photosphere) the only reasonable conclusion from this that Mercury has a relatively high proportion of metallic iron and a relatively small proportion of rocky (silicate) material. It is also entirely reasonable that the metallic material would have been able to segregate inwards to form a planetary core, with the silicates differentiated upwards to form the mantle and crust (defined in Box 2.1). These reasoned speculations are borne

Table 1.1 Basic physical parameters for Mercury, with the Earth for comparison

	Mercury	Earth
Orbit		
Period/Earth days	87.969	365.256
Semimajor axis/10 ⁶ km	57.91	149.60
Perihelion/10 ⁶ km	46.00	147.09
Aphelion/10 ⁶ km	69.82	152.10
Eccentricity	0.2056	0.0167
Inclination/degrees	7.00	0 (by definition)
Planet		
Rotation period/hours	1,407.6	23.9345
Axial inclination/degrees	0.0	23.44
Equatorial radius/km	2,439.7	6,378.1
Polar radius/km	2,437.2	6,371.0
Mass/10 ²⁴ kg	0.3301	5.9726
Density/kg m ⁻³	5,427	5,514
Uncompressed density/kg m ⁻³	5,300	4,000
Surface gravity/m s ⁻²	3.70	9.80
Escape velocity/km s ⁻¹	4.3	11.2

out by spacecraft data and other recent observations, as discussed in later chapters. The relatively large size of Mercury's core poses some perplexing questions about how Mercury formed, and these too will be addressed later, when other relevant data have been described.

Table 1.1 presents the currently accepted values for the various basic physical parameters for Mercury that have been covered in this chapter.

Chapter 2 The Mariner 10 Era of Mercury Science

2.1 Introduction

In this chapter I want to summarise what we found out about Mercury as a result of Mariner 10 and the ground-based observations (principally radar and spectroscopy) carried out until the first few years of the current century. It is thus a snapshot of Mercury knowledge in the immediate pre-MESSENGER era, when we had seen almost half of Mercury in close-up and had amassed a certain amount of geophysical data. I will try to avoid presenting as 'the truth' any Mariner 10 era interpretations that we now know to be incorrect.

Let's begin by looking at the Mariner 10 mission.

2.2 Three Flybys for the Price of One

2.2.1 The Trajectory

Mariner 10 (Fig. 2.1) was the first space probe to visit Mercury, and the seventh successful launch in NASA's Mariner series. The Mariner craft shared a common heritage, being based on a hexagonal or octagonal 'bus' housing the electronics and with components such as communications antennae, cameras, solar panels and thrusters attached. Mariners 1 (failed), 2 and 5 were Venus flyby missions, Mariners 3 (failed), 4, 5 and 6 were Mars flybys, and Mariners 8 (failed) and 9 were Mars orbiters. Mariners 11 and 12 had been planned as Mariner Jupiter-Saturn probes but were superseded by extensively redesigned probes that became Voyager 1 and Voyager 2.

At 502 kg, Mariner 10 was more than twice the mass of the first Mariners, but considerably less massive than the 998 kg Mariners 8 and 9. It was launched on 3 November 1973, spent 25 min in a parking orbit, and was then sent on its way toward Mercury powered by a hydrazine rocket capable of 222 N of thrust.



Fig. 2.1 Mariner 10 as it would have looked in flight. Each solar panel was 2.69 m long, and housed three pairs of orthogonal nitrogen gas reaction thrusters to control and stabilize the spacecraft's attitude. The arm extending to the left is the magnetometer boom, which was 5.8 m long. The flat white dish is the sunshade, through which the main engine's nozzle (invisible) projected. The steerable high-gain antenna for communications sticks out beyond the sunshade. The shorter arm houses the omnidirectional low gain antenna (NASA)

There was a scare after 10 days. Following a trajectory correction manoeuvre, the craft's star-tracker locked onto what is now presumed to have been a speck of paint that had flaked off the spacecraft, mistaking it for the guide star, Canopus. Fortunately this was rectified, and Mariner 10 continued on the correct path. In January 1974 the Mariner 10 team took advantage of an opportunity to make 15 days of continuous distant ultraviolet observations of the long-period comet Kohoutek, which had been discovered only 9 months before launch and was by now just past perihelion. On 5 February Mariner 10 made the closest yet flyby of Venus, at a range of less than 6,000 km. Its ultraviolet imaging of Venus revealed structure in the cloud deck that had hitherto seemed featureless, and its magnetometer showed that Venus has no significant magnetic field of its own.

Although the science that Mariner 10 achieved at Venus was important, the Venus flyby had an entirely different purpose. This was to use Venus's gravity to bend Mariner 10's trajectory so that it was now following a heliocentric orbit with a perihelion that would coincide with Mercury's position at the time of its coming encounter (Fig. 2.2). This had been timed to occur at Mercury's aphelion so that the spacecraft would not have to go any closer to the Sun than necessary, thereby reducing the risk of overheating.

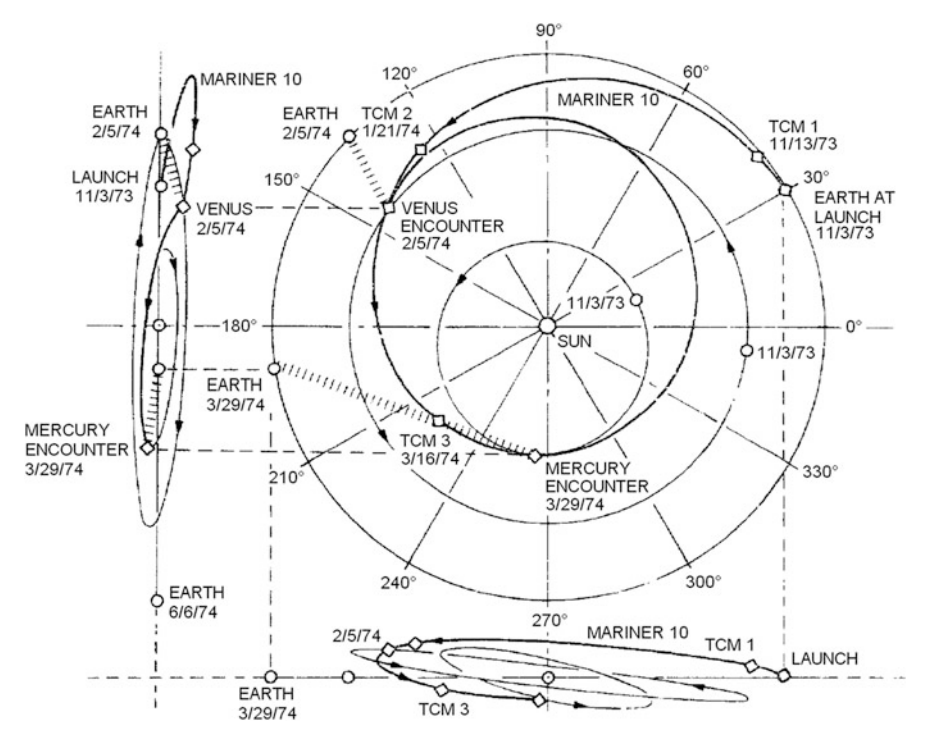


Fig. 2.2 A diagram copied from a 1976 NASA technical manual, illustrating the trajectory of Mariner 10. The main graphic shows a plan view of the orbits of Earth, Venus and Mercury plus the position of each planet at launch (with dates expressed in the American month/day/year format: 11/3/73 for 3 November 1973). Also shown are positions of three planned trajectory correction manoeuvres (TCM), the positions of Earth and Venus during Mariner 10's Venus flyby, and the positions of Earth and Mercury during Mariner 10's first Mercury flyby. Graphics at side and bottom show projections of the trajectory viewed side-on to Earth's orbital plane (the ecliptic), reminding us that Mariner 10 had to escape from this plane to accomplish its flybys of Mercury (NASA)

Mariner 10's swing past Venus was the first ever execution of a 'gravitational slingshot manoeuvre', also known as a 'gravity assist trajectory'. This is a technique now widely used in missions to both the inner and outer parts of the Solar System. By accelerating a spacecraft into a more suitable trajectory, it enables a spacecraft to fly with less fuel so that it can carry a greater mass of scientific instruments.

The precise gravity assist trajectory chosen for Mariner 10 did more than merely setting up a flyby of Mercury at the right time. Giuseppe (known as 'Bepi') Colombo, Professor of Applied Mechanics at the University of Padua, Italy (Fig. 2.3), had made an insightful suggestion at a conference on the Earth-Venus-Mercury mission held in Pasadena in 1970. As a result of this, the gravity assist from its first Mercury encounter was used to place Mariner 10 in an orbit about the Sun with a period exactly twice that of Mercury. With no further expenditure of rocket fuel (which was by now pretty much exhausted anyway), Mariner 10 would orbit the Sun and return to the same point 176 days later to find Mercury, having gone twice round the in the meantime, there again.



Fig. 2.3 Two people whose insights made missions to Mercury feasible. *Left*: Giuseppe Colombo, who proposed the 2:1 probe:Mercury resonant solar orbit achieved by Mariner 10. *Right*: Chenwan Yen, who found a low-cost trajectory to get a probe into orbit about Mercury, as used by MESSENGER and BepiColombo (Left courtesy of ESA, right courtesy of Chen-wan Yen)

In fact Mariner 10 made three successful flybys of Mercury. The first, 29 March 1974, passed at closest only 704 km above Mercury's surface. The second, 21 September 1974, was at a more distant 48,069 km but allowed the south polar region to be imaged. The third, 16 March 1975 at a closest altitude of 327 km, was achieved only after recovery from another temporary loss of star tracking (probably another floating speck of paint), and tilting of the solar panels to control the roll of the spacecraft so as to conserve precious attitude-control gas. The gas became totally depleted 9 days after the third fly-by. Mariner 10 then began slowly to tumble uncontrollably. There being no means to correct this, commands were sent to the spacecraft to turn off its transmitter. This ended Mariner 10's contact with Earth forever, though presumably it still passes close to Mercury at every perihelion of its lonely orbit.

2.2.2 Limitations

Despite achieving three flybys for the price of one, Mariner 10 data acquisition was not without its problems. The onboard tape recorder failed soon after the first flyby, which meant that data from subsequent flybys had to be transmitted to Earth in real time. This required the use of multiple tracking station antennae in parallel to overcome the noise problems inherent in such weak signals transmitted at the necessary data rate. During the third flyby, Mercury was below the horizon, and so unobservable, from the Goldstone tracking station in California. Only the Canberra Deep Space Network station could see Mercury, but this developed a problem with a cooling system that had been intended to reduce receiver noise. To make the best of

the situation, Mariner 10 had to be instructed to transmit only narrow strips of images, rather than full frames of the high resolution targeted images that had been selected on the basis of the most interesting areas seen in the first flyby.

Further limitations to Mariner 10's study of Mercury's surface had nothing to do with hiccups in the technology. These relate to Mercury's 3:2 spin orbit coupling. Because Mercury completed exactly two orbits of the Sun between flybys, it had meanwhile rotated exactly three times and so experienced exactly 1 solar day (Fig. 1.7). Therefore the same hemisphere was in darkness during each flyby, and so could not be seen at all. In total about 40–45 % of the globe was imaged well enough to attempt mapping, using a total of about 2,800 images.

For mapping, and even simply to understand the surface features, the position of the Sun in the sky is important. At high 'Sun angle', when there is a large angle between the Sun and the local vertical, the Sun is fairly close to the local horizon, so the sunlight strikes the ground obliquely. This casts shadows that can reveal subtle topographic features with great clarity. It is the preferred illumination condition for many purposes, though of course you can see nothing inside the shadows and so most geologists would prefer to complement this with a second high Sun angle pass with the sunlight coming from the opposite side. On the other hand, when the Sun is high in the sky (described as conditions of low Sun angle, because there is only a small angle between the Sun and the local vertical) the whole of the ground is bathed in sunlight, revealing differences in surface reflectivity that are suppressed under high Sun angle conditions. However, in the absence of shadows or subtleties of shading brought about by such illumination, the topography can be very indistinct. Figure 2.4 shows an example of the different information revealed according to Sun angle.

2.3 Mariner 10's Instruments

Mariner 10 did more than just send back images from Mercury. It carried a total instrument payload of 79.4 kg, designed to contribute to seven scientific experiments. These are listed in Table 2.1 and described below.

2.3.1 Television Science

The now rather quaint-sounding 'Television science' experiment was so-named because it used what were effectively TV cameras (vidicons) to obtain its images. The imaging system was mounted on a steerable scan platform to allow accurate pointing and construction of image mosaics without having to re-orient the whole spacecraft. Long focal length fore-optics (the telescopes) were fitted because for the first and third flybys the closest approach to the planet would be on the night-side. High magnification was therefore needed to achieve high-resolution (detailed) images while the sunward part of the globe was in view, before and after the closest stages of the inward and outward legs of the flyby (Fig. 2.5).

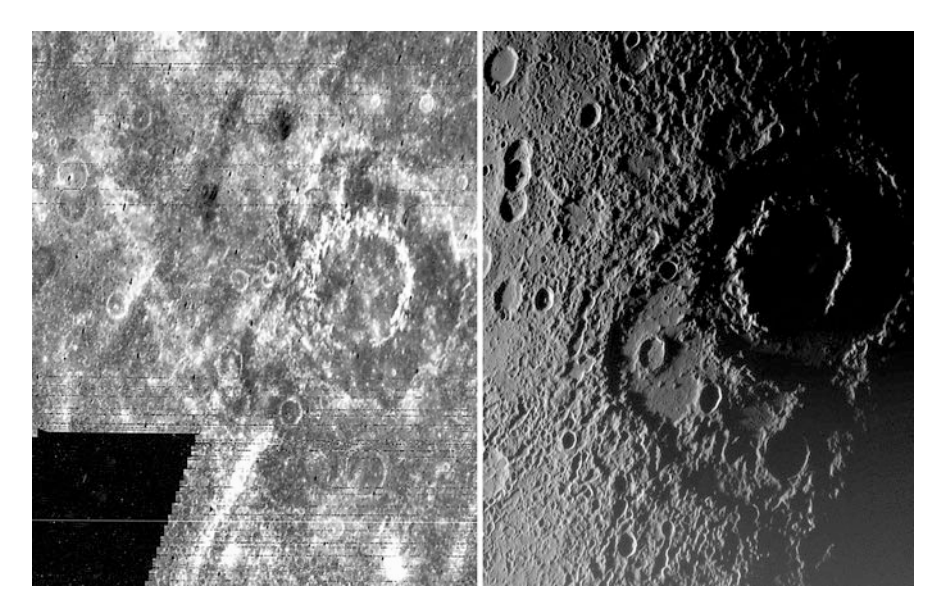


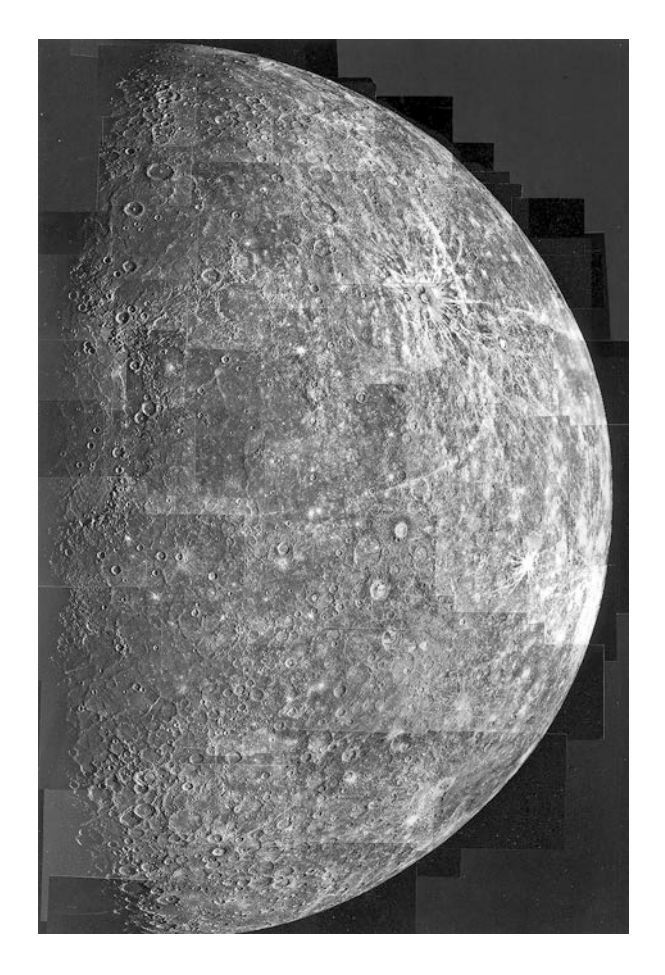
Fig. 2.4 Mariner-10 (*left*) and MESSENGER (*right*) views of the same area of Mercury. The 200 km diameter peak-ring crater Vivaldi is prominent on the right of each image. Mariner-10 saw this area with the Sun nearly overhead (low Sun angle) so albedo features are prominent, but topography is suppressed. The bright streaks are mostly ejecta rays: the one in the lower left (adjacent to the missing data) is from Vivaldi itself, but others can be traced to craters as distant as 2,000 km. The MESSENGER image, acquired during its first flyby in 2008, shows the same area shortly before sunset (high Sun angle) so topography is clearly seen. This comparison does Mariner 10 somewhat of an injustice, because high Sun angle Mariner 10 images (not available at this longitude) are almost as attractive as MESSENGER high Sun angle images (NASA)

Table 2.1 Mariner 10's seven scientific experiments and the relevant instruments

Experiment	Instrument
Television science	Vidicon cameras fitted to twin 1.5 m focal length telescopes
Infrared radiometry	Infrared radiometer
Ultraviolet spectroscopy	Airglow spectrometer and occultation spectrometer
Celestial mechanics and radio science	X-and S-band radio transmitters
Magnetic field	Two triaxial fluxgate magnetometers
Plasma science	Scanning electrostatic analyser and electron spectrometer
Charged particles	Charged particle telescopes

The spatial resolution in the images used for Fig. 2.4 was 2–4 km, but resolution as high as about 100 m was achieved for small areas at about 30 min either side of closest approach. The second flyby passed over the south polar region, acquiring images that enabled the inbound and outbound image sequences from the first flyby to be fitted together with cartographic accuracy.

Fig. 2.5 Photomosaic of the hemisphere of Mercury seen by Mariner 10 outbound from its first flyby. I have adjusted the contrast to reveal detail near the terminator without saturating the more brightly-lit region near the limb. The sunlit half of the Caloris basin straddles the equator on the terminator (NASA)



A full image frame consisted of 700 scan lines of 832 pixels each, and could be recorded through any of five filters, which were mounted on a filter wheel deployed between the telescope and the vidicon. Filters were 'clear', ultraviolet (UV, central wavelength 355 nm), blue (central wavelength 475 nm), 'minus-ultraviolet' (MUV, central wavelength 511 nm) and orange (central wavelength 575 nm). There was also a polarizing ultraviolet filter used only at Venus. Colour information obtained at Mercury was poor, and generally has to be inferred from the orange albedo and the UV/orange ratio.

2.3.2 Infrared Radiometry

The main purpose of this experiment was to measure infrared radiation emitted from the surface of Mercury, and thus to determine surface temperature. It was based on two 2.5 cm aperture telescope radiometers, one sensitive to $8.5{\text -}14~\mu m$ and the other to $34{\text -}55~\mu m$ radiation. Unlike the television science experiment, this was not steerable but was mounted on the spacecraft so as to allow nearly perpendicular viewing onto the night side of Mercury plus the inbound and outbound terminators. This was not an imaging experiment, but merely recorded radiation as the radiometers' $0.5{\text -}1^\circ$ fields of view tracked across the planet.

During the first flyby, the two radiometers measured how temperature varied along a near-equatorial line beginning shortly before local sunset and extending through midnight to end well after dawn (approximately 1700 to 0900 'local time' on the surface). The experiment determined that Mercury's surface physical properties controlling its rate of day-night heating-cooling were essentially indistinguishable from those of the Moon.

2.3.3 Ultraviolet Spectroscopy

The airglow spectrometer searched for UV emission at discrete energies associated with specific gas species. In the event, it was able to measure H, He and O (atomic hydrogen, helium and oxygen), and placed upper limits on the possible abundances of Ne, Ar and C (neon, argon and carbon).

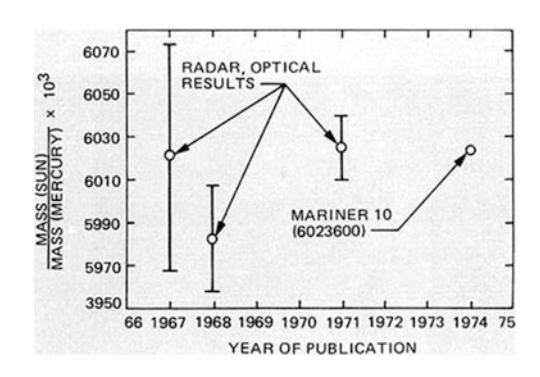
The occultation spectrometer was designed to look at the Sun in the 30–95 nm region (a part of the spectrum where any gases would scatter/absorb sunlight most strongly) as it was occulted by Mercury's limb, to search for absorption by any atmospheric gases. In the event, no measurable absorption was found, placing an upper limit on Mercury's atmospheric density.

2.3.4 Celestial Mechanics and Radio Science

This experiment was designed to extract scientific information from the dual-frequency X-band and S-band radio transmissions from Mariner 10 that were used to send data to Earth. The celestial mechanics part of the experiment was based on determining slight Doppler shifts in the received wavelengths while the spacecraft was accelerated by the competing gravitational tugs of Mercury and the Sun. This measured the mass of the planet to far greater precision than ever before (Fig. 2.6), and gave some hints about its internal mass distribution.

The radio science part of the experiment considered the signals as Mariner 10 passed behind Mercury as seen from the Earth. This provided a check on the planet's size, and together with the celestial mechanics data confirmed Mercury's density at the currently accepted value. In addition, the lack of attenuation of the signal when the line of sight approached the planet put upper limits on the electron density in any ionosphere and on the surface atmospheric pressure.

Fig. 2.6 Published values of the ratio between the Sun's mass and Mercury's mass as measured by radar and optical methods, with error bars, and the much more precise determination by the Mariner 10 celestial mechanics experiment, published in 1974 (NASA)



2.3.5 Magnetic Field

Before Mariner 10, it was widely assumed that Mercury was too small for any zone in its core to be hot enough to be molten, because the higher surface-to-volume ratio of a smaller planet allows it to lose more of its internal heat than a larger planet. It was further reasoned that Mercury's rotation is too slow to stir any molten core into the kind of motion necessary to generate an Earth-like magnetic field. With these considerations in mind, Mariner 10's magnetic field experiment was expected to observe the interaction between Mercury and the solar magnetic field, and the extent to which the charged particles in the solar wind were able to induce a secondary magnetic field inside the planet.

Mariner 10 carried two magnetometers, one halfway along and one at the end of its magnetometer boom to allow any spacecraft-induced secondary magnetic fields to be identified and eliminated. These were triaxial fluxgate magnetometers, each capable of measuring the strength and direction of the local magnetic field in three orthogonal directions. By summing the three measurements, this gave the strength and direction of the field in three-dimensional space.

Strong hints of a powerful, internally-generated magnetic field during the first flyby of Mercury, which were confirmed in the third flyby, provided a major surprise, especially after none had been found at Venus. Mariner 10 did not pass inside Mercury's magnetosphere during its more distant, and dayside polar, second flyby.

2.3.6 Plasma Science

This experiment comprised an ion and electron analyser scanning in the sunward direction (the electrostatic analyser) and an electron spectrometer looking in the antisun direction. Unfortunately the electrostatic analyser failed, so no data about the ion population were acquired. However, useful data came from the electron spectrometer, which measured the flux of electrons at a variety of energies (effectively the rate at which electrons of different energies were encountered). This showed dramatic step-like changes when Mariner 10 crossed boundaries between

the ambient solar wind environment and the region of space close to Mercury controlled by its magnetic field.

2.3.7 Charged Particles

This experiment used two charged particle telescopes to detect high-energy particles (mainly electrons, but also protons and helium nuclei). These were copies of the instruments that had been launched shortly before on Pioneer 10 in March 1972 and Pioneer 11 in April 1973 to fly past Jupiter (Jan 1974 and Jan 1975) and Saturn (Oct 1979). They complemented the Magnetic Field and Plasma Science experiments in revealing phenomena associated with Mercury's magnetic field.

2.4 Mapping a New Planet

2.4.1 Quadrangles

Before Mariner 10 arrived, preparations were made for mapping Mercury's surface. Images from the television science experiment were to be used as a basis for both pictorial terrain maps and interpreted geological maps. The prime meridian (0° longitude) of Mercury had already been defined as the longitude where the Sun was overhead when Mercury passed through its first perihelion in the year 1950. A glance back at Fig. 1.7 shows that this must coincide with one of the planet's 'hot poles'.

The surface of a planet or a large moon is conveniently divided into 'quadrangles' for mapping purposes. For Mercury, the Astrogeology Branch of the United States Geological Survey devised a system of five equatorial quadrangles to be mapped on Mercator projections, four northern and four southern quadrangles to be mapped on Lambert projections, and two polar sheets to be mapped on polar stereographic projections (Fig. 2.7). The quadrangles are numbered H-1 to H-15 (where H is a prefix to signify Mercury, from the Greek Hermes). Original IAU-approved names for each of these quadrangles were taken from the albedo features on the Dollfus-Antoniadi map (Fig. 1.6). However, it was found that these albedo features are not apparent in close-up images, so new names were devised for the quadrangles taken from the name of a prominent feature in each quadrangle revealed by Mariner 10, once such features had been named.

2.4.2 Naming Features

The naming of specific features on a planet that no one is likely to visit is a far from pointless exercise. It is much more convenient to have names that all concerned

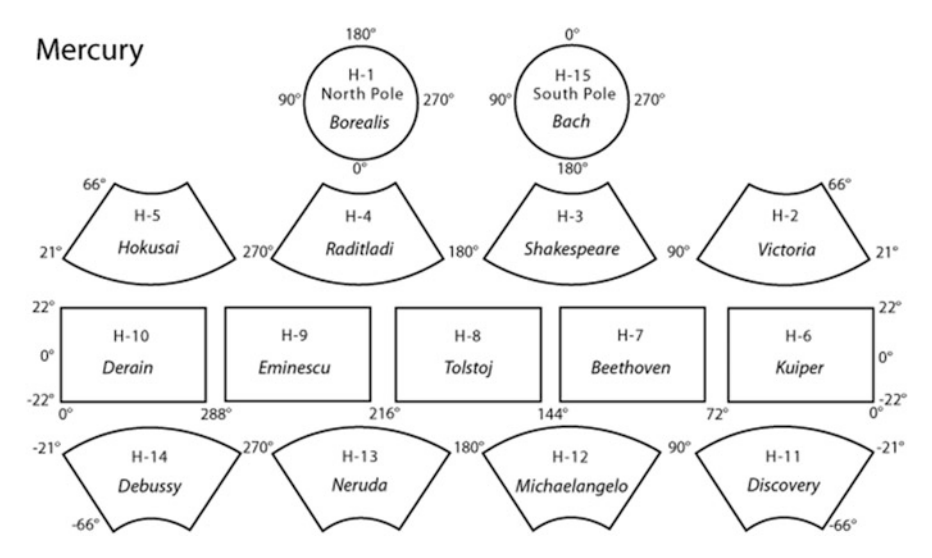


Fig. 2.7 The mapping quadrangles for Mercury, showing the currently-agreed names. Mariner 10 did not image the six westernmost quadrangles, so until MESSENGER images became available these still went by their pre-Mariner 10 names of Apollonia, Liguria, Pieria, Solitudo Criophori, Cyllene, and Solitudo Persephones

recognise than it would be if features could be referred to only by their co-ordinates. A present-day use for names unforeseeable in the Mariner 10 era is that if you want to find out what has been published about a particular feature, then its name is the most useful term to feed into an online search engine.

Surface nomenclature is overseen by the IAU, with two principal aims. First, to allocate non-controversial names that achieve a balance representing all the world's cultures, across the Solar System as a whole and, to the extent possible, also on individual bodies. Second, to indicate what class a feature belongs to, but without implying how it formed. The first is intended to avoid names being contentious, and the second tries to avoid names becoming obsolete or inapplicable as a result of new data or reinterpretation.

Following a convention previously established for the Moon and Mars, craters on Mercury are simply given a one part name according to a theme for crater names agreed for the planet. Other features are given two part name: the name itself (according to the theme for each particular kind of feature) plus a descriptor term. The descriptor term denotes the morphological characteristics of the feature, and is derived from Latin. If this seems complicated, Table 2.2 should help.

Craters are by far the commonest named features, with over 370 names allocated to individual craters by late-2014. The next most common named features are Rupes (scarps), of which 30 had been named by late-2014, when there were seven named Planitiae. The only two named Dorsae were Antoniadi Dorsum and Schiaparelli Dorsum, both named on the basis of Mariner 10 images. The descriptors

Type of feature	Theme for name	Descriptor term (plural in brackets)
Crater	Famous deceased artists, musicians, painters, authors	(None used)
Chain of craters	Radio telescope facilities	Catena (Catenae)
Ridge	Astronomers who made detailed studies of Mercury	Dorsum (Dorsa)
Long, narrow depression	Significant works of architecture ^a	Fossa (Fossae)
Mountain	Words for "hot" in various languages	Mons (Montes)
Low-lying plain	Names for Mercury (the planet or the god) in various languages	Planitia (Planitiae)
Scarp	Ships of discovery or scientific expeditions	Rupes (Rupes)
Valley	Abandoned cities/settlements of antiquity ^a	Vallis (Valles)

Table 2.2 The IAU-approved naming convention for features on Mercury

Montes and Fossae had each been allocated once only, both in the plural form. Caloris Montes denotes the uplifted rim-wall fringing the Caloris basin (which is more properly referred to as Caloris Planitia), and Pantheon Fossae denotes a system of radial fractures in the centre of the Caloris Basin that was not recognised until MESSENGER arrived.

There are only a few exceptions to the naming themes. Borealis Planitia means literally Northern Plain and is inherited from the old Borea albedo province, from which the Borealis quadrangle takes its name. Caloris Planitia was so-named ('Hot Plain') because it sits astride one of Mercury's hot poles. The most prominent young bright (high albedo) crater seen by Mariner 10 was named Kuiper, after Gerard Kuiper (1905–1973), a famous Dutch-American planetary astronomer who had been a member of the Mariner Venus-Mercury imaging team but who died shortly after launch.

Most re-named quadrangles are named after a large or otherwise prominent crater that falls within them. The only exceptions other than Borealis are Victoria and Discovery, which are both named after Rupes.

2.5 What Mariner 10 Found

2.5.1 Surface Characteristics

Fast orbital speeds at Mercury's close distance from the Sun result in typical impact speeds of nearly 90 km s^{-1} for comets and about 34 km s^{-1} for asteroidal material hitting Mercury, as opposed to $50 \text{ and } 17 \text{ km s}^{-1}$ respectively for comet and

^aIndicates themes allocated only after MESSENGER images had been acquired

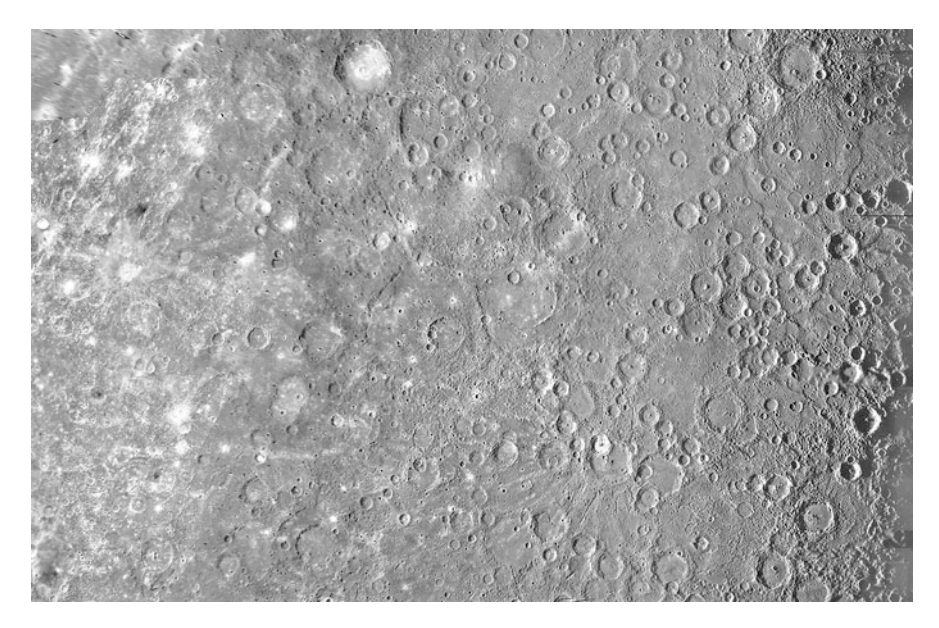


Fig. 2.8 Most of the Kuiper quadrangle, seen in a seamless computer-generated mosaic of Mariner 10 images displayed in a Mercator projection. The area shown is about 2,700 km from east to west. The bright-floored crater in the lower right is Kuiper itself, from which the whole quadrangle takes its name (NASA)

asteroid impacts on the Moon and Earth. It was no surprise that Mariner 10 revealed Mercury as a heavily-cratered planet, given that it was already known to lack sufficient atmosphere to protect its surface. In fact, some larger craters had been seen using Earth-based radar several years before Mariner 10. Figure 2.8 is an overview of the Kuiper quadrangle, where much of the terrain is particularly heavily cratered, though smoother 'plains' areas are apparent between craters.

Note how the appearance of craters changes across the wide range of longitudes covered in this view. The eastern edge is on the terminator, experiencing local sunset (very high Sun angle) so craters and various other surface irregularities show up well. The western edge was nearly at local noon (low Sun angle), and there are no shadows. The youngest craters, which are surrounded by high-albedo ejecta, show up as white spots, and they have bright rays radiating from them. Kuiper is probably the youngest crater of its size in this quadrangle and is now known to have rays emanating from it in all directions. However under the Mariner 10 illumination conditions the rays to its west can be discerned only faintly, and those to its east do not show up at all.

Figure 2.9 is a somewhat more detailed view of the northwestern quarter of the Shakespeare quadrangle. This shows wide expanses of plains more clearly than the previous image, and you can also see that the large basins Van Eyck and Shakespeare itself are shallow and have flat floors occupied by smooth, plains-like material (with some smaller, younger craters superimposed).

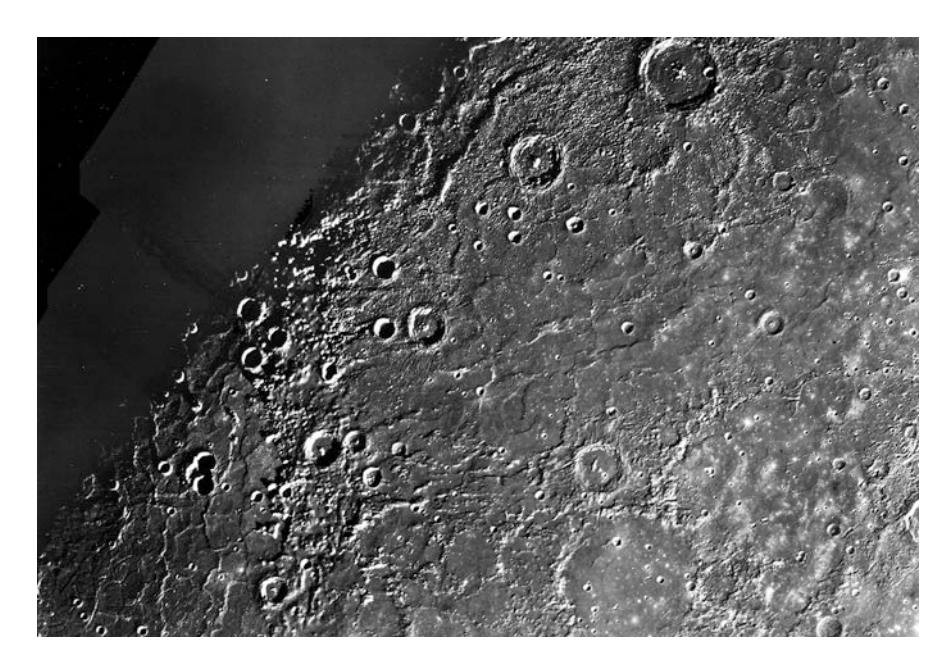


Fig. 2.9 The northwest quarter of the Shakespeare quadrangle, seen in a seamless computer-generated mosaic of Mariner 10 images displayed in a Lambert projection. The area shown is about 1,400 km from east to west. Shakespeare crater, from which the whole quadrangle takes its name, is in the lower right corner, with the more obvious 270 km crater Van Eyck slightly overlapping its southwestern edge. Part of the Caloris basin is seen on the terminator at the lower left (NASA)

Telescopic studies of Mercury's brightness at different phases, and the thermal properties measured by Mariner 10's infrared radiometry experiment, showed that Mercury's surface across virtually the entire globe is powdery, with very little exposed solid bedrock. The surface is thus covered by a metres-thick regolith, consisting of fragments of rock generated and dispersed by impacts on all scales from basin-forming down to micrometeorite impacts. Greater impact speeds on Mercury would tend to result in a smaller average grain size than on the Moon, but essentially Mercury's surface is probably very lunar in appearance (Fig. 2.10). Chuming of the regolith by small impacts is one reason why crater rays fade into the background with age.

The single most famous feature on Mercury has to be the Caloris basin (more formally known as Caloris Planitia, though technically this refers only to its interior plains), which is a large impact basin situated at one of Mercury's hot poles, from which it derived its name. It can be seen in the low resolution outbound mosaic in Fig. 2.5, and more clearly in the mosaic of higher resolution frames in Fig. 2.11a. It was estimated on the basis of Mariner 10 images to be about 1,300 km across, but complete imaging by MESSENGER has now shown it to be 1,550 km in diameter. It is both the largest and one of the youngest impact basins on Mercury.

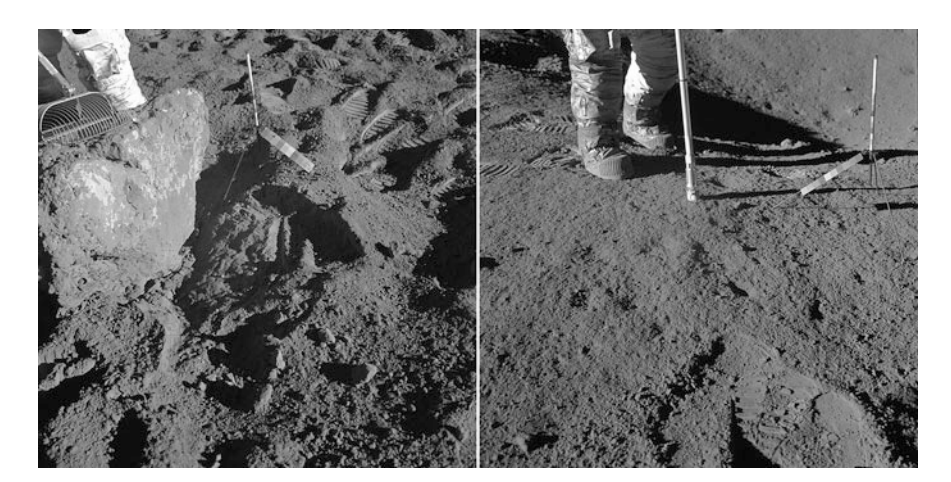


Fig. 2.10 Two Apollo 15 photographs of the lunar regolith. This consists of rock fragments and impact-generated glass on a variety of scales. Particles only tens of micrometres in size make it cohesive enough to retain footprints, but larger fragments are scattered throughout. Mercury's surface would look pretty much the same as this (NASA)

The Caloris basin was clearly formed by a major impact into Mericry, by an impactor that must have been at least 100 km across. It has an uplifted basin rim (Caloris Montes), outside of which much of the terrain has been radially sculpted by what appears to be a mixture of depositional and erosional/abrasional processes during dispersal of ejecta from the impact site. Comparable radial sculpture is associated with some of the impact basins on the Moon, such as Imbrium and Nectaris. The circum-Caloris radial sculpture is overlain by younger plains material, which in places buries it completely. The interior of the basin is completely floored by plains materials, bearing a complex pattern of ridges and troughs, seen clearly in the high-resolution frame in Fig. 2.11b. The fracturing within Caloris is interpretable as a result of uplift of the basement in an isostatic (buoyancy-driven) response to the removal of the excavated material, plus consequences of cooling, contraction and subsidence following emplacement of the basin-filling plains material.

All these features are overprinted by younger impact craters, whose density suggests an age of 3–4 billion years for Caloris itself (during an episode known as the late heavy bombardment, well known from studies of the Moon) to judge from the density of superimposed craters on the Caloris Montes. The Caloris and circum-Caloris plains, which have a lower density of craters, must be younger by up to several 100 million years.

Many scientists working in the Mariner 10 era were happy to accept that the plains associated with Caloris and elsewhere on Mercury (such as Fig. 2.8) are a result of flooding by volcanic lava flows. However, mindful of a recent faux pas when the crew of Apollo 16 visited the supposed volcanic plains of the lunar Cayley Formation in 1972 and found them to be an ejecta sheet, some remained sceptical.

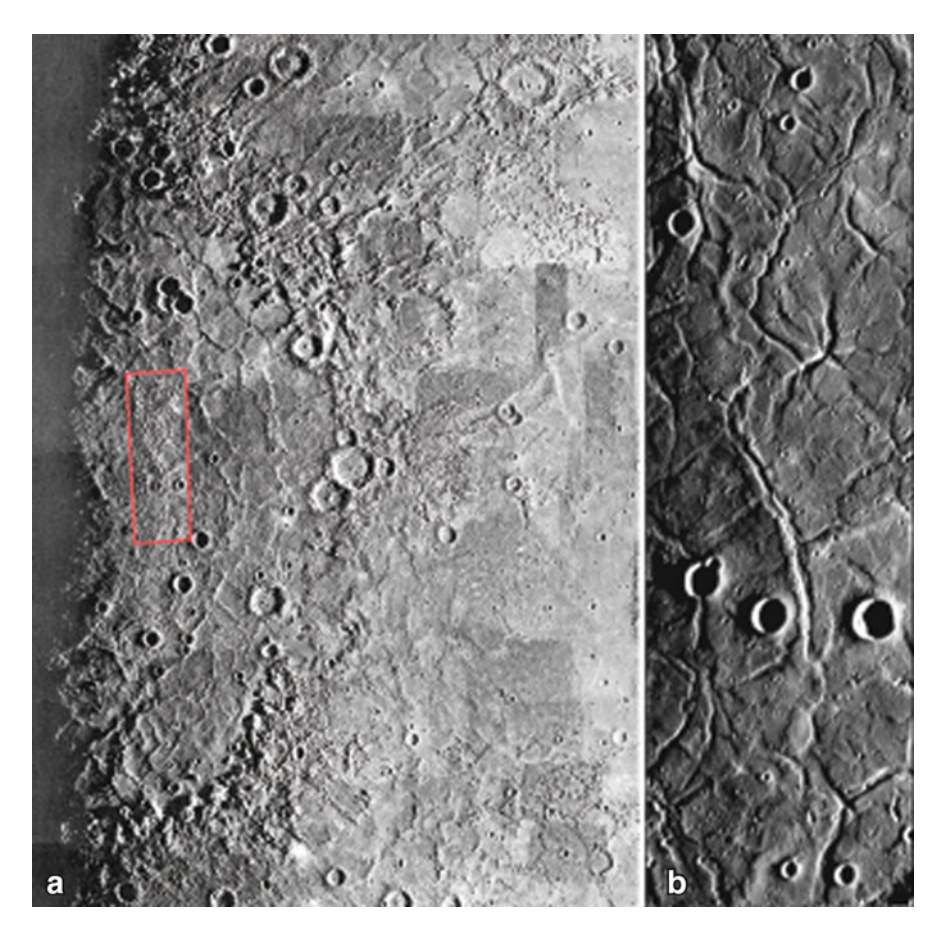


Fig. 2.11 (a) A mosaic of Mariner 10 first flyby outbound images, with most of the individual frames discernible because of incomplete photometric correction between them. The area shown is about 1,100 km across, and the eastern part of the Caloris basin (Caloris Planitia) sits near the terminator at the western edge of the area. The *rectangle* denotes the area shown in (b). (b) High-resolution targeted image strip acquired during Mariner 10's third flyby. The area shown is about 125 km across (NASA)

Smooth plains of impact ejecta remained a defensible interpretation of Mercury's plains until fuller and more detailed imaging by MESSENGER resolved the issue firmly in favour of a volcanic origin.

Like the lunar maria, the plains-forming lavas on Mercury are significantly younger than the basins that they occupy (and beyond which they often extend). The age difference means that eruption cannot be explained simply as a consequence of escape of quantities of pre-existing magma up fractures caused by a large impact. However, unlike the lunar maria, which are significantly darker (lower in albedo) than the lunar highland crust that they overly (Fig. 2.12), Mercury's lava plains do not contrast strongly with the underlying terrain. This was a (fairly weak)

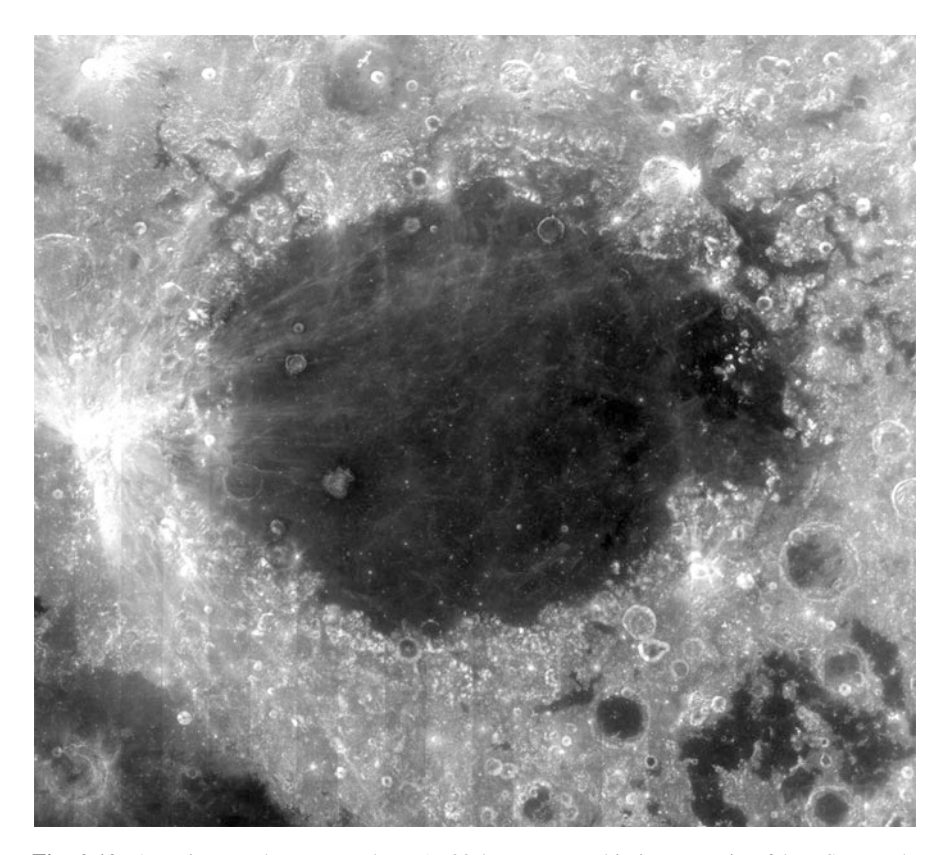


Fig. 2.12 A region on the Moon, about 1,700 km across. This is a mosaic of low Sun angle Clementine images of Mare Crisium and the surrounding region (cylindrical projection). The strong albedo contrast between lunar lava plains (maria) and the older, more heavily-cratered, highland crust is obvious. Such a relationship is absent on Mercury, even at similar low Sun angles (NASA/USGS)

argument in favour of them being composed of the same material, redistributed as ejecta sheets from (unimaged/unidentified) impact sites.

Because the Caloris basin was on the terminator of the Mariner 10 outbound view, the part of the globe exactly opposite, its antipode, was on the opposite terminator, and was seen in Mariner 10's inbound view. The terrain here is unlike anything elsewhere on Mercury, and consists of a jumble of hills up to 1.8 km high (Fig. 2.13). This was dubbed 'hilly and lineated' terrain (though it is more hilly than lineated), and is generally accepted to result from shock waves generated by the basin-forming impact that travelled both through Mercury's interior and round its surface before converging and interfering at the opposite point on the globe. Somewhat similar terrain was recognised about the same time on the Moon, antipodal to the Imbrium and Orientale basins and was explained in the same way.

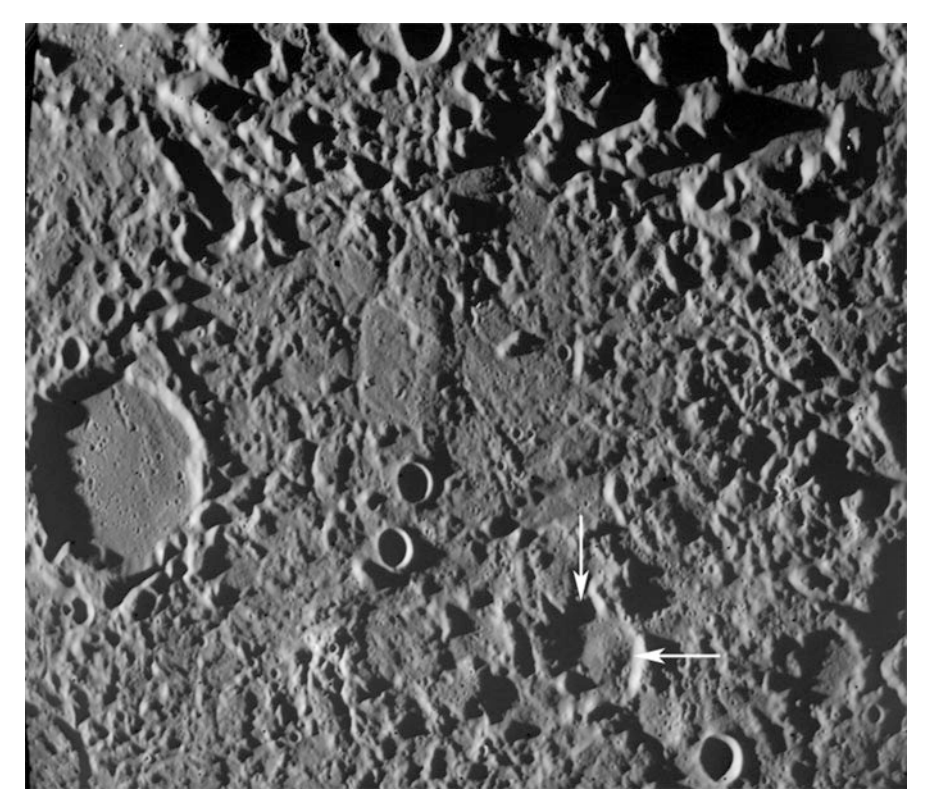


Fig. 2.13 A Mariner 10 first flyby inbound image, 130 km across, which captured 'hilly and lineated terrain', antipodal to the Caloris basin. *Arrows* indicate the partially-disrupted rim of a 15 km crater that pre-dates the surface disruption (NASA)

One class of feature revealed on Mariner 10 images that has no analogue (at such a large scale) on the Moon is exemplified by Discovery Rupes in Fig. 2.14, which is named after HMS Discovery – one of the two ships in Captain Cook's third, and fatal, voyage to the Pacific (1776–1779). The rupes on Mercury are scarps, which is to say steps in the terrain, up to about 2 km high and tens of hundreds of km in length. They are sinuous rather than straight, hence their common description as 'lobate scarps'.

Lobate scarps cut across all terrain units, and no Mariner 10 image showed plains units embaying any of them. Clearly lobate scarps must be relatively young features, though not so young that they have escaped overprinting by some younger impact craters. Because lobate scarps displace the terrain, they were readily accepted as tectonic features, and specifically as the surface expressions of faults. Moreover, because in plan-view they are lobate rather than straight, it was fairly simple for geologists to recognise them as thrust faults, whose shallow dip intersecting gently rolling topography would naturally result in a wavy line (Fig. 2.15). In some cases there is a measurable shortening of 1–2 km across craters

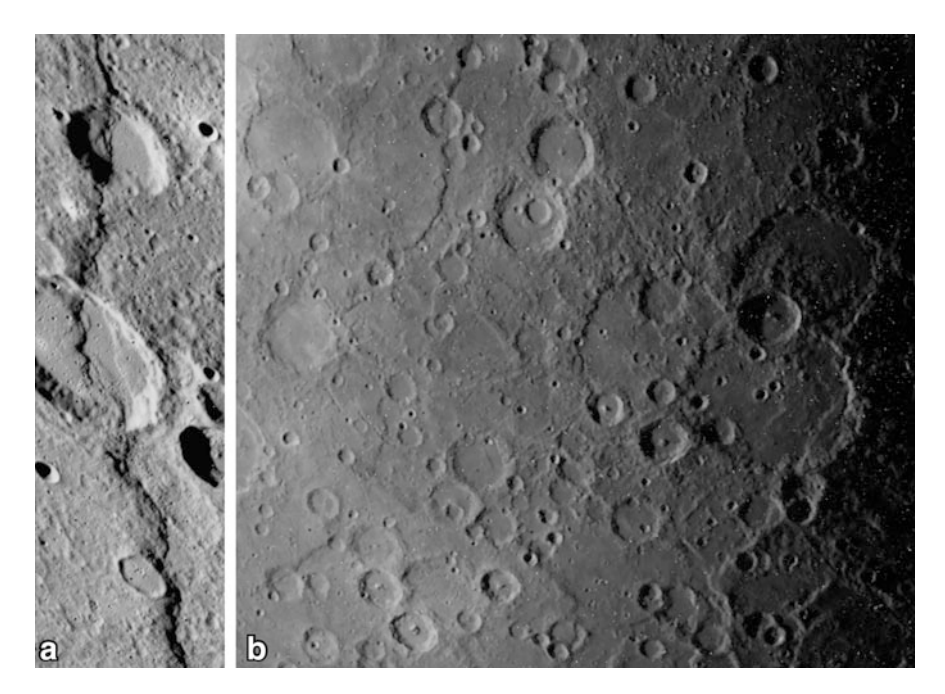


Fig. 2.14 (a) Mariner 10 third flyby high resolution targeted image of Discovery Rupes, which is at about 55° S. The crater Rameau, cut by Discovery Rupes in the centre of the strip, is 31 km across. Note the 8 km crater superimposed on the scarp near the south end of the image strip, whose overprinting relationship shows it to be younger than the scarp. (b) Mariner 10 second flyby inbound image, showing the regional setting of Discovery Rupes. The area covered is about 1,000 km across (NASA)

cut by a lobate scarp, which is consistent with this interpretation. The amount of displacement across a lobate scarp thrust fault is much smaller than for the major thrusts on the Earth associated with continental collision and mountain building, for example in the Alps or the Rockies, where displacement of tens or hundreds of km are known.

In common with faults on the Earth, the displacement across a lobate scarp is presumed to decrease towards the fault-tip at either end of the scarp, and this is consistent with Discovery Rupes becoming less prominent towards its southern tip as is seen in Fig. 2.14b.

Mariner 10 found lobate scarps at a wide range of latitudes, with named Rupes occurring between 49° N and 65° S. There are other tectonic features on Mercury, but I will leave these aside for a fuller discussion in the light of MESSENGER data.

So, what caused Mercury's lobate scarps to form? Before tidal despinning slowed Mercury's probably much faster early rotation to its present 3:2 spin:orbit coupled state, Mercury must have had an equatorial bulge. For example the Earth's equatorial radius is 21 km greater than its polar radius, because of its relatively rapid spin. However, polar and equatorial radii differ by less than 1 km for Mercury today. The collapse of Mercury's former equatorial bulge would have caused a

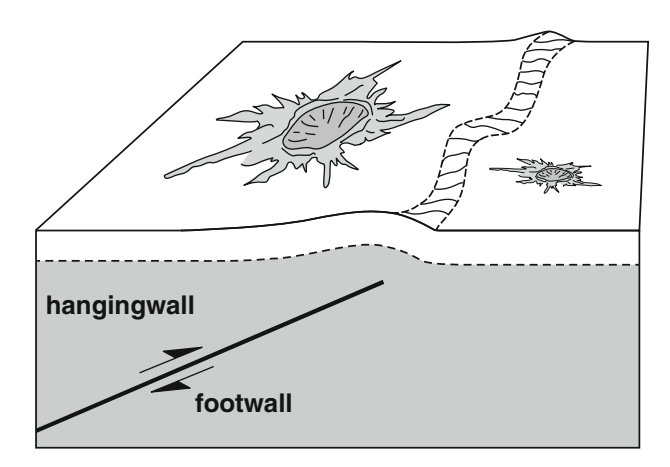


Fig. 2.15 Sketch cross-section to illustrate how a shallow-dipping compressional fault (a thrust fault) can create a lobate scarp at the surface. A steeper fault would result in a more linear topographic feature. The terms 'footwall' and 'hangingwall' refer respectively to the block of terrain that has been over-ridden by the fault movement and to the over-riding block

reduction in equatorial circumference that would be expected to lead to east—west shortening at low latitudes. However, unless the planet's total volume decreased, there would have to have been a simultaneous expansion of the polar circumference that should have caused extensional faulting in the polar regions (and strike-slip, sideways, fault movements a little further from the poles). This is inconsistent with the pattern of faulting revealed by Mariner 10, and so it was concluded that tidal despinning must have occurred too early in Mercury's history to leave such clear traces on its present surface, so another explanation was sought for the lobate scarps.

The overwhelming propensity of tectonic features on Mercury to be compressional in nature led scientists of the Mariner 10 era to conclude that Mercury has been a shrinking planet at all latitudes. Lobate scarps are best seen at high Sun angles, and particularly when the Sun's direction is such that the downhill side of the scarp casts a shadow. This makes them hard to identify in about half of the region imaged by Mariner 10, and of course none could be seen on the night-side of the globe. However, assuming that the lobate scarps visible on suitable Mariner 10 images are representative of the globe as a whole, they were taken to demonstrate a global contraction in radius of 0.5–1 km.

If a planet is becoming smaller, without losing mass, this requires its density to increase. There are two ways for this to happen, both being consequences of falling internal temperature. One is simple thermal contraction: most solids, including rock, contract as they cool. The other involves internal phase changes, particularly freezing of the core (the solid part of the core growing at the expense of the liquid part of the core), that would cause Mercury's interior to become denser. In either case,

the rigid rocky outer layer would then be too big to fit over the interior, and it would behave rather like the skin of a desiccating apple, except that it developed mostly asymmetric scarps rather than simple wrinkles.

It is likely that both causes of contraction have operated, and it is possible that late tidal despinning may have had some influence over scarp development too. We will defer further discussion until the MESSENGER data are considered.

2.5.2 Mercury Timescale and Stratigraphy

Those working with Mariner 10 images were quick to follow the recent lead of lunar mappers in looking for evidence to define relative ages of features in Mercury. Relative dating is done using the geologically well-established 'principle of superposition', which recognises that overlying or overprinting features are younger than the underlying or overprinted features. The degradation states of the impact craters was also used, on the basis that younger craters would retain their pristine morphology, whereas progressively older craters would lose definition as a result of various processes such as impact gardening (local churning of regolith by small impacts) and partial burial by ejecta from neighbouring younger craters.

Absolute ages of terrains were estimated by counting the density of superimposed craters, and applying the radiometrically-calibrated lunar cratering timescale, after correction for Mercury conditions.

The resulting timescale and stratigraphy, divided by convention into named 'systems' (each of which is intended to encompass features and surfaces formed within a specific time bracket) are summarised in Table 2.3. Beware that absolute ages may be significantly in error.

The youngest two systems defined on Mercury were based on isolated craters rather than on extensive surface units. The youngest class of craters in Mercury is typified by the crater Kuiper: morphologically fresh and with associated rays of

System	Major units	Age of base/ billions of years
Kuiperian	Fresh craters with rays	1.0
Mansurian	Fresh craters without surviving rays	3.0-3.5
Calorian	Caloris basin and its ejecta	3.8-3.9
	Plains inside and outside Caloris. Partially degraded craters	
Tolstojan	The Tolstoj basin, its ejecta, and associated plains. More heavily degraded craters	4.0
Pre- Tolstojan	Intercrater plains and multiring basins older than Tolstoj. Most heavily degraded craters	>4.0

Table 2.3 Mercury timescale and stratigraphy, as understood from Mariner 10 data

Tolstoj is named after the Russian author conventionally spelt 'Tolstoy', and is usually pronounced that way. Approximate lunar equivalents are (youngest to oldest): Copernican, Eratosthenian, Imbrian, Nectarian, pre-Nectarian

ejecta. Craters like this are probably 1.0 billion years old or younger, and these and any other features of demonstrably similar age are assigned to the Kuiperian system.

The next-oldest system is defined by craters that are still morphologically fresh in respect of the structure of their walls and central peaks. They are surrounded by recognisable ejecta deposits, but lack surviving visible ejecta rays. The crater Mansur is apparently the oldest such example, and the ejecta from Mansur defines the base of the Mansurian system, which began about 3.0–3.5 billion years ago. Mariner 10 showed no surface units of regional extent to which a Mansurian age could be attributed, though the floors of some Mansurian craters have become occupied by smooth material (which must therefore be Mansurian or Kuiperian in age).

Prior to the Mansurian, it is possible to recognise units of regional extent. The youngest of these are assigned to the Calorian system, which begins with the excavation of the Caloris basin (about 3.9 or 3.8 billion years ago) and continues with the smooth plains both inside and outside Caloris that can be shown to post-date the basin. The rims and any internal terraces of impact craters of Calorian age are degraded, and smooth crater-fill is often present. Proximal ejecta deposits can still be seen surrounding Calorian craters. Most of the region covered in Fig. 2.9 is plains of Calorian age.

The next oldest system is the Tolstojan, which begins with the formation of the 510 km diameter Tolstoj basin (Fig. 2.16), about 4.0 billion years ago. This may have been as little as 0.1 billion years before the Caloris basin, so the Tolstojan

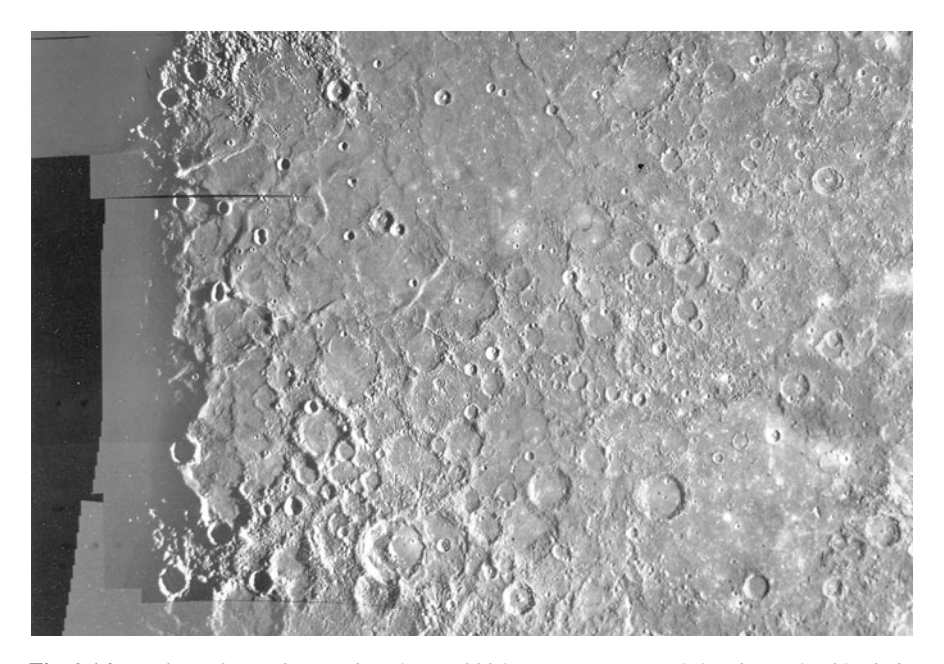


Fig. 2.16 Mariner 10 mosaic covering about 1,200 km east to west, and showing Tolstoj basin in the southeast. The surrounding plains are pre-Tolstojan intercrater plains, except for some Calorian plains in the northwest corner (which lies southeast of the Caloris basin) (NASA)

represents relatively short period of time, but one during which there was a lot of impact cratering (it was during the inner Solar System's late heavy bombardment episode) as well as plains formation. Craters of Tolstojan age have smooth fills, degraded rims, and no surviving proximal ejecta deposits.

Everything older than this is described as pre-Tolstojan. This includes many poorly-preserved impact basins. Whatever early crust these basins were formed in has been largely buried by 'intercrater' plains of pre-Tolstojan age, now generally accepted to be volcanic plains old enough to have been liberally peppered by subsequent impacts. Much of the region shown in Fig. 2.8 is of this type. Nowhere on Mercury is so heavily cratered as the lunar highlands, and the nature of the very oldest crust of Mercury remains a mystery.

2.5.3 The Magnetic Field

Mariner 10 made just two passes through Mercury's magnetosphere (the zone within which the paths of charged particles are controlled by the planet's own magnetic field father than the Sun's), and both were on the night-side of the planet. Despite the limitations of such restricted coverage, a credible general model for Mercury's magnetic field was developed by combining data from the Magnetic Field, Plasma Science and Charged Particles experiments (Fig. 2.17). The total

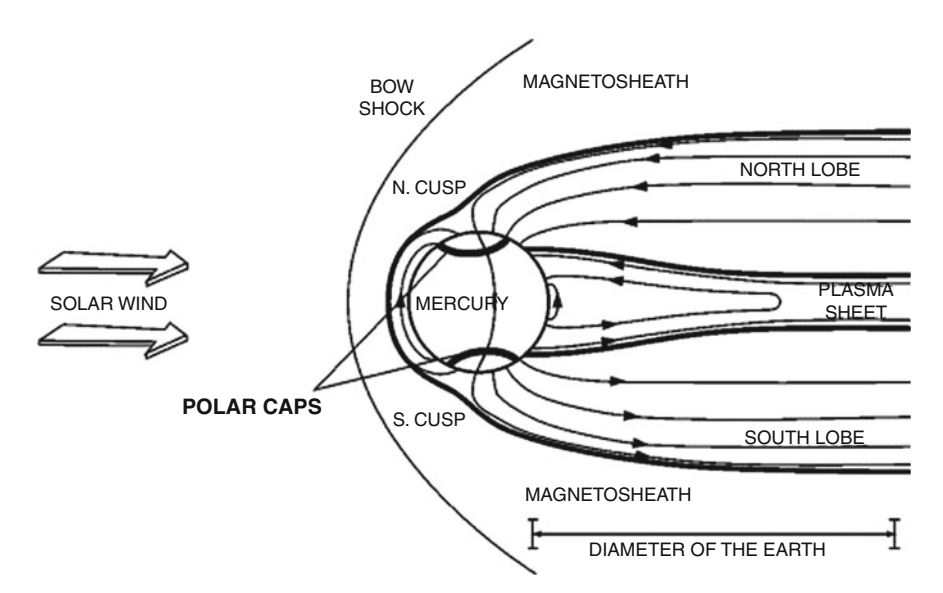


Fig. 2.17 A post-Mariner 10 model of Mercury's magnetosphere, showing magnetic field lines and labeled regions. This model is still reasonably valid, except that MESSENGER revealed a north–south asymmetry, such that that the field is displaced northward of Mercury's equator by about one-fifth of the planetary radius (Modified from Grad, E., and Balogh, A., *Planetary & Space Science*, v.49, pp.1395–1407, 2001)

strength of the field is about 1 % of the Earth's, with which it shares many characteristics except that the solid body of Mercury occupies a much greater proportion of its magnetosphere than the Earth does.

Essentially Mercury's magnetic field resembles that of a giant bar magnet, aligned along the planet's spin axis, described as a dipole. It is distorted because of the overpowering influence of the solar wind, which consists of charged particles (mainly electrons and protons) streaming away from the Sun at hundreds of kilometres per second. The magnetopause is the boundary where the pressure from the planetary magnetic field is balanced by the pressure from the solar wind, or, in other words, where the field lines of the Sun's magnetic field are held at bay by the field lines of the planet's own magnetic field. Based on the two Mariner 10 passes through the magnetosphere, the magnetopause was assumed to be only about half a planetary radius above the (unvisited) day-side, but to extend much further on the night-side in a 'magnetotail' where a sparse flow of charged particles is able to be channelled 'upstream' along the magnetic field lines in the opposite direction to the solar wind. Mariner 10 passed through the plasma sheet, in the equatorial part of the magnetotail, where the field is weak but the density of charged particles is much higher. It was speculated that at times of high solar activity, the day-side magnetopause would probably be forced down to the planetary surface.

The outer limit of the magnetosphere is the bow shock, where solar wind particles experience sudden deceleration (from supersonic to subsonic) as they approach the magnetopause. Between bow shock and magnetopause lies the magnetosheath, marked by slow (subsonic) solar wind mixed with some plasma from the magnetosphere.

2.5.4 The Interior

Of course there is not actually a giant bar magnet inside Mercury. Nor is its iron core 'magnetised' in any way – the internal temperature must be far too hot for any kind of 'permanent magnet' (the Curie temperature of iron, above which it cannot retain a magnetic field, is 770 °C). The only known way for a terrestrial planet to generate its own magnetic field is by motion within a liquid, electrically conducting layer, which acts as a self-sustaining dynamo. This is fairly well understood in the case of the Earth, where seismic data clearly show that the outer core is liquid (molten). Mariner 10's discovery of Mercury's intrinsic magnetic field showed that it was likely to have a liquid shell in its core too, although it had been unexpected and there was no other compelling evidence for the size, or the location, of the molten zone in Mercury's core.

Confirmation that Mercury's outer core is indeed liquid came in 2007, with the publication by Jean-Luc Margot and colleagues of their analysis of simultaneous radar observations from California, West Virginia and Puerto Rico during 2002–2006. Matching up the speckled pattern of the radar echo from Mercury's Earthfacing hemisphere at two different receivers enabled tiny variations in Mercury's spin rate to be measured, revealing libration of Mercury's surface amounting to a

few hundred metres of side-to-side wobble during each orbit. This may seem tiny, and it was a remarkable feat to detect it, but it is a much greater libration than could occur if Mercury were solid throughout. However, it is entirely consistent with the solid rocky part of the planet being decoupled from the main body of the core by a liquid shell occupying the outer core. Modelling suggests that such a liquid shell could be prevented from freezing if it contained a few percent of sulfur. Motion in this shell is likely to be maintained not so much by Mercury's rotation but by convection as metal freezes onto the top of the inner core, making the residual outer core progressively richer in sulfur and so more buoyant.

As established in Chap. 1, the rocky part of Mercury surrounding its core is relatively thin – accounting for the outer 25 % of Mercury's radius (so about 600 km thick according to pre-MESSENGER models) and 58 % of the its volume. In contrast, Earth's rocky part occupies the outer 44 % of its radius and 84 % of its volume. Mariner 10 provided no data on the structure of the rocky zone, but by analogy with the Earth it was expected that the majority would be classifiable as 'mantle', made of silicate rock of a composition broadly similar to the rock known on Earth as peridotite (with a chemical composition of approximately 45 % SiO₂, 38 % MgO, and the remainder mostly oxides of iron, calcium and aluminium). Overlying this, in a surface shell a few tens of km deep, would be Mercury's crust, composed of silicate rock poorer in MgO than the mantle, but correspondingly richer in the other common oxides. The crust would be naturally slightly lower in density than the mantle, having been extracted from it by a variety of possible processes soon after the birth of the planet. These processes could include crystallization from a global magma ocean, and volcanic eruption and igneous intrusion after the mantle had solidified. Figure 2.18 illustrates the internal layered structure of Mercury as understood after Mariner 10. Box 2.1 defines terms in general use to denote layers within a planet.

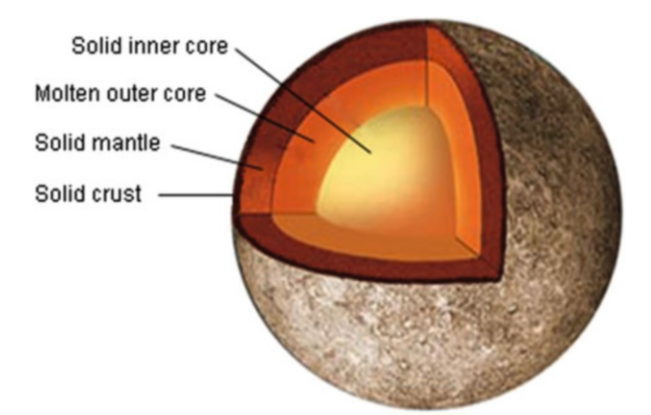


Fig. 2.18 The basic internal structure of Mercury, as understood after Mariner 10. The inner core is probably mostly iron with a few percent nickel, whereas the molten outer core must contain also a lighter element such as sulfur, capable of suppressing the freezing temperature. The mantle and crust are rocky, being composed of silicate minerals

Box 2.1. Terminology for Planetary Interiors

Planetary scientists use a small number of terms to denote layers within a planetary body. These are defined here for the benefit of readers who may be unfamiliar with them.

Core: a compositionally distinct dense inner part. In the case of terrestrial planets the core is thought to be metallic: mostly iron with a few percent nickel. If the outer part of the core is liquid (as in the case of the Earth and Mercury) this is believed to occur because of the presence of a lighter element, such as sulfur, capable of reducing the melting temperature. Earth and Mercury thus have a solid inner core and a liquid outer core.

Mantle: whatever surrounds the core. In the case of a terrestrial planet this is made largely of silicate minerals, based around silicon atoms each bonded to four oxygen atoms, SiO_4^{4-} , with the charge balance maintained by the presence of ions of various metallic elements, chiefly Mg, but also Fe, Ca, Al, Ti, Na, K (magnesium, iron, calcium, aluminium, titanium, sodium, potassium).

Crust: a differentiated, and potentially heterogeneous, layer enclosing the mantle, from which it has been extracted by various processes. In terrestrial planets the crust tends to be richer than the mantle in all the elements listed above except Mg, which is much less abundant in crust than in mantle. Crust can form by flotation of low-density crystals in a magma ocean (primary crust, like the lunar highlands) or be supplied by volcanic eruption and igneous intrusion of magmas extracted from solid mantle by partial melting (secondary crust, like the lunar maria and the Earth's oceanic crust). Partial melting does not fractionate Fe strongly, so secondary crust has only slightly higher Fe content than the mantle from which it was extracted.

Whereas core, mantle and crust are defined on the basis of compositional differences, it is also useful to recognize mechanical layering too. The elastic outer layer of a planetary body is its **lithosphere**. In the case of the Earth this comprises the crust and the uppermost part of the mantle jointly comprising a rigid shell that is 20–50 km thick in the oceans and about 150 km thick in the continents. The lithosphere can be defined by its rigidity in response to stress (it appears thicker for faster stress rates) or as a conductive lid (where heat is transferred purely by conduction) above a more mobile, convecting interior.

Below the lithosphere, the mantle although essentially solid is capable of flow at rates of a few cm per year. In this part of a planetary interior, heat is carried outwards by convection. The convecting part of the Earth's mantle is weakest immediately below the lithosphere and this is described as the **asthenosphere**. Other planets appear to lack an equivalent especially weak zone, but for many purposes the whole of the convecting part of a mantle can be treated as asthenosphere.

2.5.5 Surface Composition

None of the instruments in Mariner 10's experiment suite were tailored towards determining the composition of Mercury's surface. Measurements of how the brightness of sunlight reflected by the surface varies at different phase angles (the angle between the Sun, the surface, and the observer) by Mariner 10 and by Earth-based telescope instruments suggested that the topmost millimetre of Mercury's regolith is finer and more translucent than the lunar regolith, and probably contains more agglutinate particles (tiny fractured grains stuck together by impact-glass). The small particle size and the amount of agglutinates are plausible consequences of the higher impact energies at Mercury, whereas the degree of translucency is consistent with the surface paucity in iron that is inferred by other means (as described shortly).

Mariner 10's airglow spectrometer showed that Mercury's albedo (the fraction of incident sunlight reflected) is a few percent lower than the Moon's in the extreme ultraviolet. Mercury's albedo in the visible part of the spectrum is also slightly lower than the average for the lunar near-side. However, Mercury's reflectance rises more steeply with wavelength than the Moon's, so that Mercury is more reflective than the Moon at near-infrared wavelengths. Another way of putting this is to say that Mercury is slightly redder than the Moon, though this is too subtle an effect to be the main reason behind Mercury's 'pale pink dot' visual appearance.

Reflected light spectroscopy and emitted infrared spectroscopy (both of which can be attempted with telescopes) were among the few techniques, prior to MES-SENGER, capable of giving information on the mineralogic composition of Mercury's surface. Most notably, iron in silicate minerals will absorb light in the 900–1,100 nm region as the result of electron transitions (between energy states) in iron atoms bonded to oxygen. The wavelength of the deepest part of the absorption depends somewhat on the size and shape of the crystal lattice surrounding the iron atom, and so if the depth and central wavelength of this feature can be identified it places constraints on both the amount of iron in silicates and on the species of minerals in which most of the iron occurs. In the event, this iron feature proved elusive, and the consensus arrived at prior to MESSENGER was that FeO in silicates could not be more than about 3 % by weight (wt%). Hints of an absorption feature near 1,100 nm suggested that such iron as is present occurs mostly within the mineral clinopyroxene. Mid-infrared spectra, obtained from the summit of Mauna Kea in Hawaii to minimise absorption by atmospheric water vapour, showed some regional variations across Mercury's surface and were consistent with 3-5 wt% FeO. Untangling the possible mixtures of minerals that could be responsible for the spectrum was fraught with uncertainties, but feldspars and magnesium-rich, iron-poor pyroxenes of the clino- (Ca-bearing) and ortho-(Ca-poor) varieties seemed likely.

Disc-resolved microwave imaging provided a further insight by measuring Mercury's 'dielectric loss tangent', which constrained the total FeO + TiO_2 content of the surface to be <6 wt%. In the 1990s this was misinterpreted as indicating that

most of Mercury was covered by feldspar-dominated rocks, possibly anorthosite analogous to the lunar highland crust, whereas it became clear thanks to MESSENGER that much of Mercury's surface is Mg-rich (and very Fe-poor) lavas made largely of pyroxenes plus 20–30 % of feldspar.

2.5.6 Space Weathering

The very limited colour imaging by Mariner 10 showed some regional variations, but was useful chiefly to demonstrate that the spectral properties of Mercury's surface change over time in a manner similar to that already understood for the Moon, though probably faster because of Mercury's more extreme environment. These changes are a result of 'space weathering', a blanket term encompassing a variety of processes affecting the physical and chemical (and hence the optical) properties of any airless body (Fig. 2.19).

Meteorite and micrometeorite bombardment vaporises some of the target, pulverises more of it, and embeds particles in glass-welded agglutinates, as previously mentioned. High energy cosmic rays and solar ultraviolet light can break vulnerable chemical bonds (a process called 'photon-stimulated desorption'), and release atoms into space, thus changing the surface composition. Solar wind particles (electrons and ions) can also eject atoms (a phenomenon described as sputtering), but they can also become trapped (implanted) into the surface, changing the

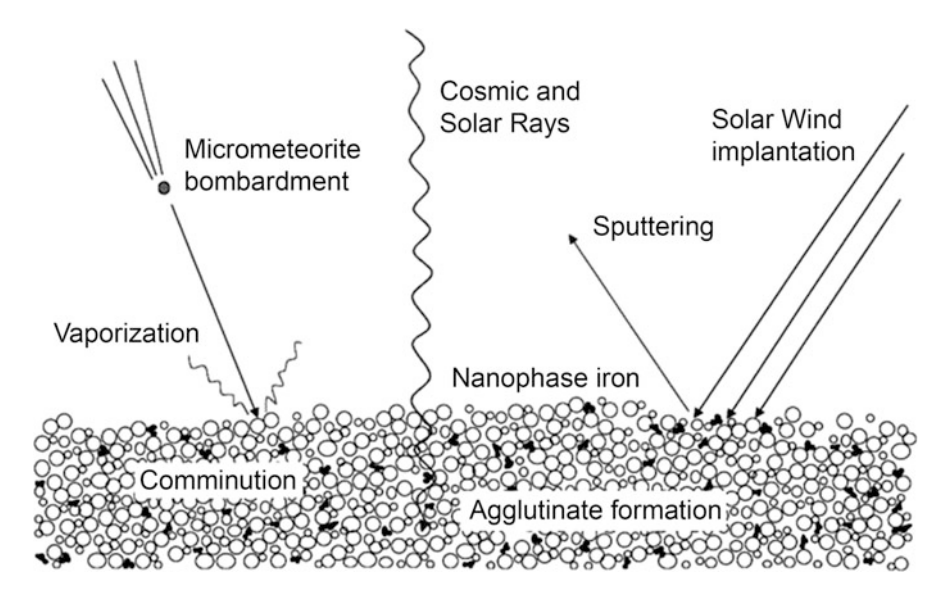


Fig. 2.19 The different components of apace weathering (Modified after: Sarah Noble, creative commons)

composition by addition as well as by subtraction. The mixing of meteoritic material into the regolith will also change its composition over time.

A major result of space weathering on the Moon is to break iron-oxygen bonds and embed particles of metallic iron within the agglutinates and on exposed surfaces of minerals. These particles are typically a few nanometres in size, and so they are described as nanophase iron. Nanophase iron has the effect of darkening and reddening the overall spectral response of the regolith. On the other hand, increasing abundance of spectrally neutral opaque minerals, such as ilmenite (FeTiO₃), is found to darken the material but also to make it less red.

A plausible reason why Mercury is darker (has a lower albedo) than the Moon could be that the regolith is rich in ilmenite, which is why the upper limit on the total FeO + TiO₂ provided by microwave measurements was important, and showed that a different explanation must be sought.

2.5.7 The Exosphere

Mercury's gravity is too weak and its day-side temperature too high to enable it to retain a dense atmosphere. Although does have some atoms gravitationally bound to it, these are too few and far between to collide with each other, so they just bounce around on large, parabolic ballistic trajectories. At their furthest from the planet, they are vulnerable to being swept away by the solar wind or simply by the pressure exerted by solar radiation. The same situation prevails in the outer part of the Earth's atmosphere, in the zone known as the exosphere. However, unlike the Earth, Mercury's exosphere extends right down to the surface, so it is described as a 'surface-bounded exosphere'.

Mariner 10 provided the first data on Mercury's exosphere, when measurements by its UV airglow spectrometer were used to calculate the density of atomic oxygen, helium and hydrogen (O, He and He) to be about 44,000, 6,000 and 230 atoms per cubic cm at the planetary surface, respectively. What was actually measured was the column density of each species (the total number of atoms along a line of sight), which was then modelled down to the surface assuming hydrostatic equilibrium.

Mercury's ground-level density of oxygen atoms at 44,000 per cubic cm might seem like a lot, but the density of molecules at the base of the Earth's atmosphere is more than 10^{18} per cubic cm, or at least 10^{13} times greater than on Mercury. Another useful comparison is given by the atmospheric pressure at the surface. Mercury's surface atmospheric pressure is about only 10^{-15} of the Earth's.

The most straightforward way to account for the exospheric H and He detected by Mariner 10 is capture from the solar wind, though inevitably some He must also leak from the surface as a result of radioactive decay. On the other hand the O seemed likely to have been liberated from silicate minerals at the surface by charged particle sputtering.

Table 2.4 Atoms in
Mercury's exosphere as
known prior to the
MESSENGER mission

Column abundance/atoms per cm ²
5×10^{10}
2×10^{13}
7×10^{12}
2×10^{12}
1×10^{10}
1×10^{9}

To the three species detected by Mariner 10, ground based spectroscopy added sodium (Na) and potassium (K) in the 1980s and calcium (Ca) in 1998. Na was found to have a surface density almost as great as O, whereas K and Ca seemed to be about a hundred and a thousand times less abundant, respectively. These data also revealed the first asymmetries and temporal variations in Mercury's exosphere, with both Na and K varying by an order of magnitude between different observations of the same region of the planet. A dawn-dusk asymmetry was noted, whereby Ca and K are more abundant near the dawn terminator than near the dusk terminator, and Na is more abundant near the poles than near the equator. Ground based spectroscopy also revealed that Mercury has a sodium tail, consisting of atoms stripped out of the exosphere by the pressure of solar radiation and traceable for 50,000 km down-Sun from the planet.

The inventory of Mercury's exosphere as understood before MESSENGER is summarized in Table 2.4, in the form of column abundance (or column density) of the six known species. This is the total number of atoms in a column all the way down to the surface, and the relative values do not compare directly with surface density because of the different scale heights (the rate at which density falls off with height) for species of different atomic masses.

To maintain the exosphere in an approximately steady-state, species must be being removed at a time-averaged rate equivalent to that at which they are supplied. Maybe churning of the regolith is adequate to refresh the supply of rocky material that has not yet lost a significant proportion of the vulnerable elements. Maybe many of the exospheric atoms get reimplanted back into the surface.

Neither the sources nor the sinks of the non-solar wind species were resolved prior to MESSENGER. Photon stimulated desorption, electron stimulated desorption and ion sputtering (during interludes when the magnetosphere fails to adequately protect the surface), thermal desorption and impact vaporization (mainly from micrometeorite impacts) were all suggested as source mechanisms. At least half the loss can be accounted for by photoionization, whereby solar UV ionizes the neutral atoms, some of which are then swept away in the magnetospheric and solar wind currents, whereas others are recycled to the surface and neutralized.

2.5.8 Polar Ice?

To complete the pre-MESSENGER survey we turn again to ground-based radar. As previously mentioned, radar imaging, chiefly using the Arecibo dish, is able to image some of Mercury's craters, and it became apparent that there is something strange about the craters near both of the planet's poles (Fig. 2.20).

The floors and pole-facing walls of craters near the poles reflect an anomalously strong fraction of the incident radar signal, with polarization properties indicative of 'volume scattering', meaning backscatter within a medium rather than specular reflection from a surface. It was quickly suggested that the most likely cause of this was grains of ice (specifically water-ice) within the local regolith. These 'radar bright' locations coincide with permanently shadowed areas (remember that

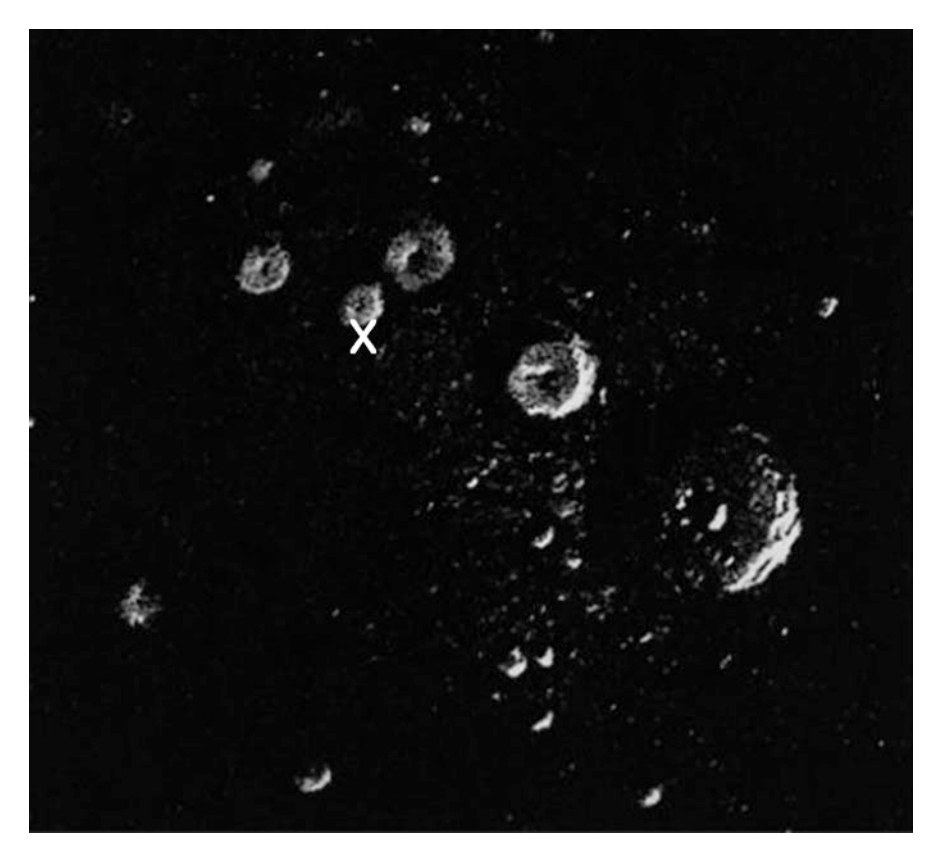


Fig. 2.20 An Arecibo radar image including Mercury's north pole, captured in July 1999. The pole is indicated by the superimposed X. The largest crater in the lower right is 90 km across. Note the bright radar returns on the floors and particularly the pole-facing walls of the craters (From J.K. Harmon et al., *Icarus*, v.149, 1–15, 2001)

Mercury's spin axis has no measurable tilt), so they act as 'cold traps'. When a comet hits Mercury and is vaporised, water molecules will bounce around until dissociated into H and O. However a few molecules will find their way into such a cold trap before they are dissociated, where the very low surface temperature absorbs their kinetic energy upon impact so that they stick rather than bouncing away.

Sulfur has sufficiently similar properties to be indistinguishable from water-ice based on these radar observations alone, and it was not until MESSENGER arrived that the identity of the radar-bright material was confirmed as water-ice.

2.6 The Conundrum of Mercury's Origin

The knowledge gained about Mercury during the Mariner 10 era left us with many conundrums about Mercury's origin. Mercury stood revealed as denser than the other terrestrial planets, with a disproportionally large core relative to its silicate outer layers. How could such a planet form? Was its crust really so deficient in iron as the data seemed to suggest? If so, how could that be reconciled with the enormous amount of iron needed to form its core?

Three kinds of model emerged during the 1970s and 1980s seeking to explain Mercury's high core:silicate ratio. 'Selective accretion' models proposed an oxidation gradient during condensation of the solar nebula that led to more metallic iron and less oxidized iron close to the Sun. This sunward enrichment in metallic iron could have been enhanced by the effectiveness of gravitational and drag forces being different on dust grains of different densities, such that lower-density silicate grains were preferentially removed from the zone where Mercury formed.

Alternatively, 'post-accretion vaporisation' appeals to intense radiation (electromagnetic and solar wind particles) from the young Sun as a cause of vaporisation and loss of silicates from Mercury's exterior after the planet had formed. This process could have worked equally well at an earlier stage, stripping away part of the silicate mantle from differentiated planetary embryos that would later collide and coalesce to form Mercury.

The third kind of model called for the proto-Mercury to have been struck catastrophically by a planetary embryo in a giant impact that stripped away any early crust and part of its mantle (Fig. 2.21). Models of magma ocean crystallization for a planet the size of Mercury suggest that Fe and Ti would be enriched in the upper part of the resulting mantle, and so removal of the uppermost mantle would seem to be consistent with Mercury's crustal deficiency in those two elements, which is probably symptomatic of almost equally low Fe and Ti in the current mantle.

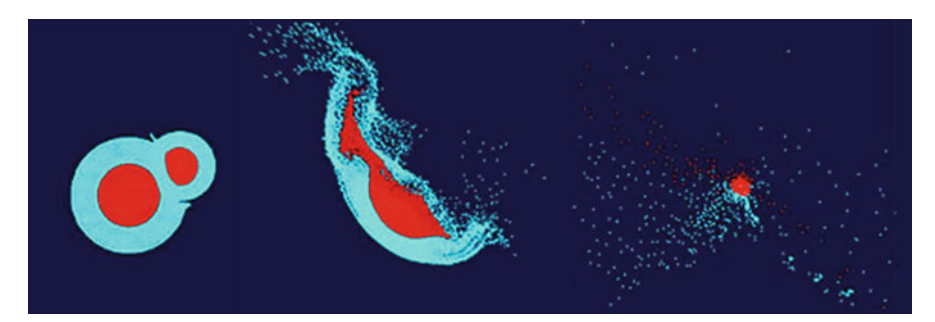


Fig. 2.21 Snapshots of a computer simulation of a Mercury-forming giant impact. *Left*: 2 min after first contact between two colliding planetary embryos, seen in cross-section. Before collision, both were differentiated into iron core (*red*) and silicate mantle (*blue*). *Middle*: the same two bodies 6 min later. *Right*: 2 h later, and shown at half the scale, the core of the target body has been stripped of most of its mantle, only some of which will re-accrete. Most of the dispersed material of dust-size will spiral towards the Sun (From W. Benz et al., *Space Sci Rev*, v.132, 189–202, 2007)

Deciding between these competing models required more data than was available in the pre-MESSENGER era. Indeed, in revealing Mercury's surface to be rich in volatiles, MESSENGER has blown holes in all three models. We will return to this later, but first the next chapter looks at how a new generation of missions to Mercury came about.

Chapter 3 High Time for Another Mission?

3.1 Introduction

It was nearly 30 years after the demise of Mariner 10 in March 1975 before the next mission to Mercury was launched. Such a delay is excusable given that the last quarter of the twentieth century saw major progress in other aspects of Solar System science including Venus landings and mapping from orbit by radar, the first orbital exploration of the Jupiter system, the dawn of a new era of Mars exploration, and the launch of the Cassini mission to Saturn.

Most planetary scientists joining the profession during that period would have had some justification in regarding Mercury as a small, Moon-like body of less interest than somewhere like Mars that could host life, or Io that has erupting volcanoes, or the Moon that is our nearest neighbour. However, once some of the higher priority targets had been explored in a little more depth, there was bound to come a time when attention would return to Mercury. After all, less than half of the planet had been mapped by Mariner 10, and with a fairly limited suite of instruments. There were bound to be surprises when we looked in more detail, but already the issues surrounding Mercury's composition, structure and origin suggested that learning more about Mercury would also cast light on planet-formation and Solar System evolution in general. Burgeoning discoveries of exoplanets (planets of other stars) in the new century added an extra facet – the easiest exoplanets to find were those closest to their stars, so discovering more about how proximity to the Sun has affected Mercury should help us to understand the conditions affecting them too.

The logical way to improve significantly on what Mariner 10 had achieved was to put a probe into orbit about Mercury, thereby avoiding the many observational limitations of flybys. However, a crucial factor contributing to the delay in returning to Mercury was the problem of how to overcome the constraints posed by celestial mechanics before a probe can be placed into orbit about the planet. The change in velocity, or ΔV (delta-V), required by a probe arriving directly from Earth so it can

match Mercury's velocity sufficiently closely to be captured into orbit would require an unfeasible amount of propellant.

Fortunately, in 1985, Chen-wan Yen a theoretical physicist who went on to specialize in optimizing interplanetary trajectories at NASA's Jet Propulsion Laboratory (Fig. 2.3), provided a solution as elegant as had been Giuseppe Colombo's to the earlier problem of multiple flybys. She showed that by using a number of Venus and Mercury flybys, a trajectory can be designed that reduces the eventual ΔV requirement enough to make a Mercury orbiter mission affordable.

Early on in Chen-wan Yen's model, Venus gravity assists are used to decrease the energy required for a probe to reach Mercury and also to achieve much of the 7° tilting of the probe's orbital plane needed to match Mercury's orbital plane. Once the perihelion of the probe's orbit has been lowered enough to reach Mercury, a series of gravity assists from Mercury flybys can commence. Each of these to helps to lower the probe's aphelion from near Venus down to near Mercury's orbit. At the same time, these successive Mercury gravity assists nudge the spacecraft into 2:3 then 3:4 then 4:5 (and so on, if required) orbital resonance with Mercury. After three or four Mercury flybys the shape of the probe's orbit about the Sun is close enough to Mercury's orbital shape for the probe to be captured into orbit about the planet for only a small expenditure of ΔV .

3.2 Back to Mercury

With Yen's conceptual breakthrough having shown that a Mercury orbiter was feasible, a NASA Science Working Team held workshops in 1988–1989 and published a feasibility report in 1990. Seven competing proposals for a Mercury mission (some flyby, some orbital) were submitted for consideration in NASA's low-cost Discovery programme in 1993. Two of these received funding for mission definition studies. Neither was eventually approved, but a lively US community of Mercury advocates had now formed, and they continued to lobby and to study mission scenarios.

Across the Atlantic, also in 1993, a team of 19 interested scientists submitted a proposal for a Mercury orbiter to the European Space Agency (ESA). I myself was co-opted the following year to help to make the geological case for renewed exploration of Mercury at a mission selection meeting held at ESA headquarters in Paris, but deserve little credit for my role, because, as described in the Introduction, this was my sole appearance on the Mercury scene for a decade. Further assessment showed that this project would exceed the cost of a 'medium-size mission', but in the year 2000 ESA's Science Programme Committee gave approval for an ambitious 'Cornerstone' mission to be named BepiColombo, in honour of Giuseppe Colombo, who had died of pancreatic cancer in 1984.

As initially announced, BepiColombo was to consist of two orbiters and a 44 kg lander, with launch provisionally set for 2009. Two orbiters were possible because the Japan Space Exploration Agency (JAXA) joined the project, and would provide

a Mercury Magnetospheric Orbiter (MMO), whereas ESA was to provide the Mercury Planetary Orbiter (MPO) and the Mercury Surface Element (MSE), which was the lander. Both orbiters would be in polar orbits, with similar periapsis (closest orbital point to the planet, alternatively known as periherm), but the MMO would have a more eccentric orbit to explore the depths of the magnetosphere, whereas the MPO would stay closer to the planet. The MSE was to be equipped with a camera, a seismometer and instruments for determining the elemental composition and physical properties of the regolith. To avoid extremes of temperature, the MSE would land near one of the poles where it was expected to operate for at least a week, whereas the nominal mission for the orbiters would last a year.

In the meantime, NASA had accepted for further study a proposal from the 1997 round of Discovery program proposals, for a 'Mercury Surface, Space Environment, Geochemistry and Ranging' mission (MESSENGER), which would be a single orbiter designed and built largely at the Johns Hopkins University Applied Physics Laboratory in Maryland. The mission received final approval in July 1999, with launch set for spring 2004.

Once approved, MESSENGER was always fated to beat BepiColombo to Mercury, and in fact was launched on 3 August 2004. After three Mercury gravity-assist fly-bys in 2008–2009, it arrived in orbit about Mercury in March 2011. MESSENGER is a simpler and cheaper mission, initially costed at \$286 million as opposed to BepiColombo's 550 million euros (\$673 million), which has subsequently risen to 970 million euros. MESSENGER's instrument payload has a mass amounting to a little more than 40 kg, which is about one third of BepiColombo's (MPO plus MMO) instrument payload.

While MESSENGER design, build, launch and cruise were proceeding pretty much on schedule, the BepiColombo project had to contend with various delays and disappointments. A Ministerial Conference in 2001 drastically reduced ESA's science budget, and consequently two years later ESA's Science Programme Committee took the hard decision to cancel a stellar photometry mission called Eddington (which would have searched for exoplanets) and to scale back on BepiColombo, most notably by cancelling the lander (MSE). As the mission's thermal and power design progressed it became clear that the volume and mass would be too great for it to be launched by a Soyuz-Fregat as previously intended, and in 2008 it was decided that the launch would have to be switched to a more expensive Ariane 5. The BepiColombo launch date is now likely to be July 2016 or soon after, with orbital science operations at Mercury beginning in May 2024.

The rest of this chapter describes the MESSENGER and BepiColombo missions in more detail. Later chapters will assess what has been learned about Mercury after three years of MESSENGER orbital science.

3.3 MESSENGER

3.3.1 The Trajectory and Orbit

MESSENGER was launched on a Delta II rocket (Fig. 3.1), and made its way to Mercury via a series of gravity assists that facilitated its eventual capture into planetary orbit.

3.3.1.1 The Cruise and Flybys

Figure 3.2 shows MESSENGER's trajectory as far as Mercury orbit insertion. It made one circuit of the Sun before an Earth flyby on 2 August 2005, followed by two Venus flybys, and then three Mercury flybys, using gravity assists after the manner that had been suggested by Chen-wan Yen. Thrusters where used for five main propulsive corrections to the trajectory, known as Deep Space Manoeuvres



Fig. 3.1 *Left*: MESSENGER attached to its payload assist module, 14 July 2004. The flat panels are solar arrays stowed in their launch positions, and the stowed magnetometer boom can be seen between them. The sunshade is on the far side. *Right*: The launch of MESSENGER from Cape Canaveral, at 06:15:56 UTC on 3 August 2004 (Both from Solomon et al., *Space Sci Rev*, v131, 3–39, 2007)

3.3 MESSENGER 57

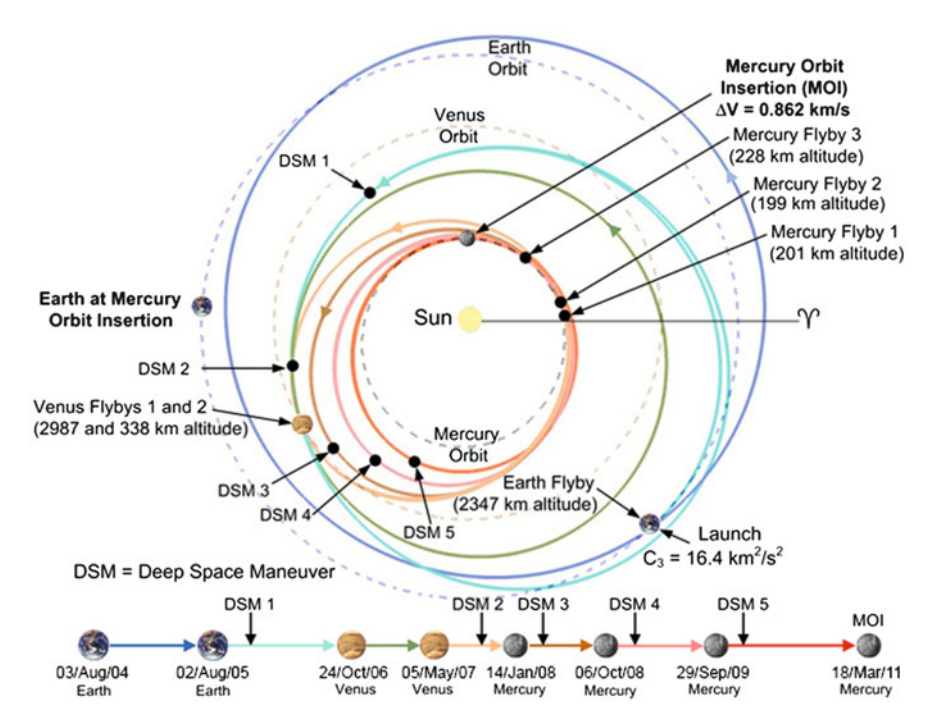


Fig. 3.2 MESSENGER's trajectory from Earth to Mercury Orbit Insertion. The trajectory is shown as a coloured line, with a colour change at each planetary gravity assist. The symbol Υ marks a standard reference direction, which is a line between the Sun and the Earth at the spring equinox. The bottom element is a time-line, showing dates of each encounter (NASA/Johns Hopkins University Applied Physics Laboratory/Carnegie Institution of Washington)

(DSM), of which DSM 1 was the largest, imparting a ΔV of 315.6 m s⁻¹. DSM 5 was the burn to target Mercury sufficiently precisely for orbital insertion 4 months later and required a ΔV of 177.75 m s⁻¹. There were also dozen secondary manoeuvres (not indicated in the figure) to make minor course adjustments, of which all but two were for ΔV of less than 5 m s⁻¹.

The Earth flyby was used to calibrate some of the instruments, but there was no science during the first Venus flyby because it occurred on the far side of the Sun from the Earth, precluding any communication. However a large dataset was collected during the second Venus flyby, notably making measurements of particles and fields simultaneously with ESA's Venus Express that was operating in orbit about Venus.

The Mercury flybys in January and October 2008 and September 2009 provided a wealth of science, complementing and exceeding what had been achieved by Mariner 10. For example, after the third flyby, 98 % of Mercury had been imaged, the magnetic field had been confirmed as pretty much the same as when Mariner 10 visited, and seasonal changes had been observed in the exosphere (such as Mercury's tail of neutral sodium being reduced at the time of the third flyby).

Each flyby passed within 200 km of the surface (on the night side), considerably closer than Mariner 10.

A problem occurred during the third flyby 4 min before closest approach when, flying in Mercury's shadow and reliant on battery power, the spacecraft systems went into 'safe mode', thereby losing the data collection opportunity that the outbound leg would have provided. The fault was swiftly understood and rectified, but even if MESSENGER had become permanently inoperable, the mission could still have been counted as a partial success given the advances made over Mariner 10.

3.3.1.2 Orbiting Mercury

MESSENGER used about 31 % of its propellant to achieve the 861.6 m s⁻¹ reduction in velocity required for capture into Mercury orbit upon its fourth encounter with the planet. Figure 3.3 shows the arrival trajectory, the location of Mercury Orbit Insertion (MOI) and the initial orbit. MESSENGER's nominal

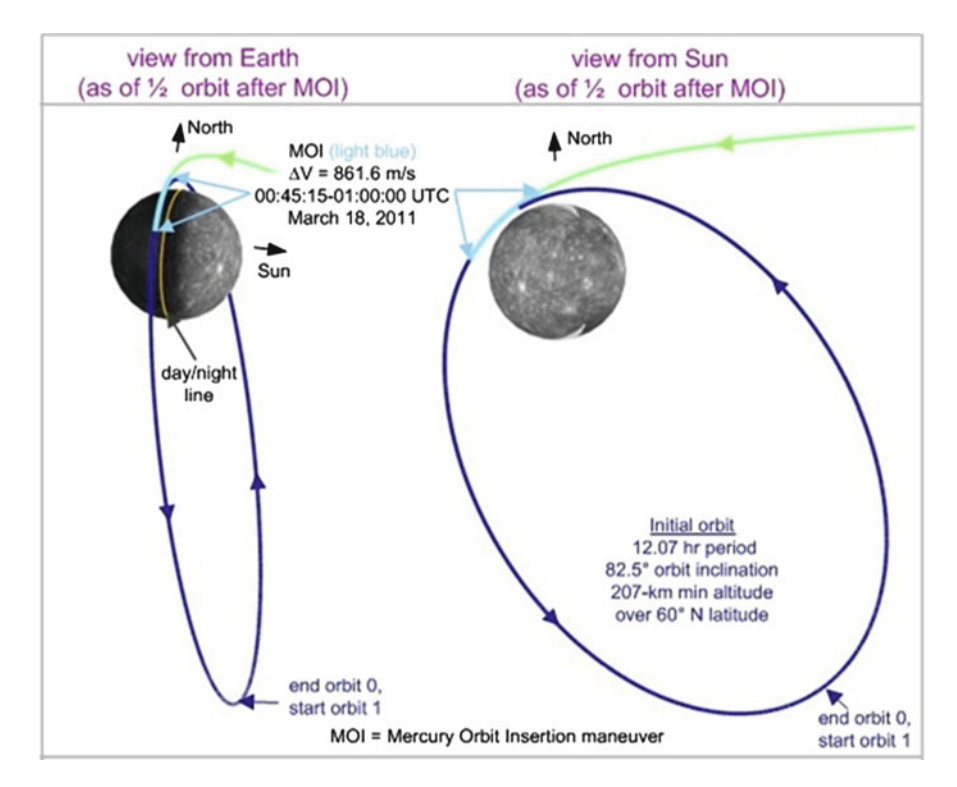


Fig. 3.3 MESSENGER's Mercury Orbit Insertion (MOI) and its initial orbit. The MOI burn lasted nearly 15 min (NASA/Johns Hopkins University Applied Physics Laboratory/Carnegie Institution of Washington)

3.3 MESSENGER 59

mission was scheduled to last one Earth year, but in the event it was extended to 4 years.

The initial orbit was highly eccentric, about 200 km above the surface at its nearest point (periapsis) and nearly 15,200 km above the surface at its furthest point (apoapsis), with an orbital period of 12.07 h. The orbit was inclined at 82.5° to Mercury's equator, and periapsis occurred at 60° N. The orbital plane was stable in inertial space, while Mercury slowly rotated beneath it, meaning that in 22 days (a quarter of an orbit) the orbital plane migrated from the dawn-dusk line to the noon-midnight line. The dawn-dusk orbits were chosen to occur at perihelion, so that the spacecraft would never pass over either 'hot pole' at local noon.

The main reason for such an eccentric orbit was to limit the time that MESSEN-GER spent close to the 700 K planetary surface. This was good for some of the science experiments (for example it meant that MESSENGER toured various depths of the magnetosphere) but it reduced the surface resolution (or even placed the surface out of range) for downward-looking experiments over southern latitudes.

In the absence of any further propulsive corrections, small forces, notably the gravitational attraction of the Sun and departures of Mercury's gravitational field from spherical symmetry, would slowly change MESSENGER's orbit. Periapsis would drift further away during the first two (Earth) years and drift closer to the planet after that. During MESSENGER's first Earth year in orbit, Orbit Correction Manoeuvre (OCM) thruster burns were therefore made each Mercury year to lower the periapsis altitude back down to 200 km (requiring a ΔV of 20–30 m s $^{-1}$), and there were a couple of smaller burns (ΔV of 4 m s $^{-1}$) to nudge the orbital period back up to 12 h.

During this time, gravitational forces were causing the angle between MES-SENGER's northward crossing of Mercury's equator and the latitude at which periapsis occurs to decrease from an initial value of 119°, until it passed below 90° on 6 March 2013. After that the forces' combined effect became such as to decrease the orbital inclination and to *decrease* the periapsis altitude. MESSENGER's 'nominal mission' was for a single Earth year of orbital operations, but at the end of this time it was still in perfect working order and plenty of new science goals had emerged, NASA gave approval (and funding for) a 1 year extended mission beginning on 18 March 2012, and subsequently allowed an 'extended extended mission' to continue.

Two thruster burns in April 2012 were used to lower the apoapsis altitude and to place the craft in an 8 h orbit with periapsis at 278 km and apoapsis at 10,314 km above the surface. Periapsis continued to drift lower, dipping to 114 km in June 2014 and likely to hit the surface 2 months later (Fig. 3.4). To save the mission, a thruster burn was made to boost periapsis back up to 155 km. This enabled an extended 'low altitude campaign' (defined as periapsis below about 200 km, including some occasions below 50 km), when data could be collected at particularly high spatial resolution. With little propellant remaining, three more orbital correction 'boost-up' burns were planned. The final burn in January 2015 would exhaust the remaining propellant but would keep MESSENGER operational until

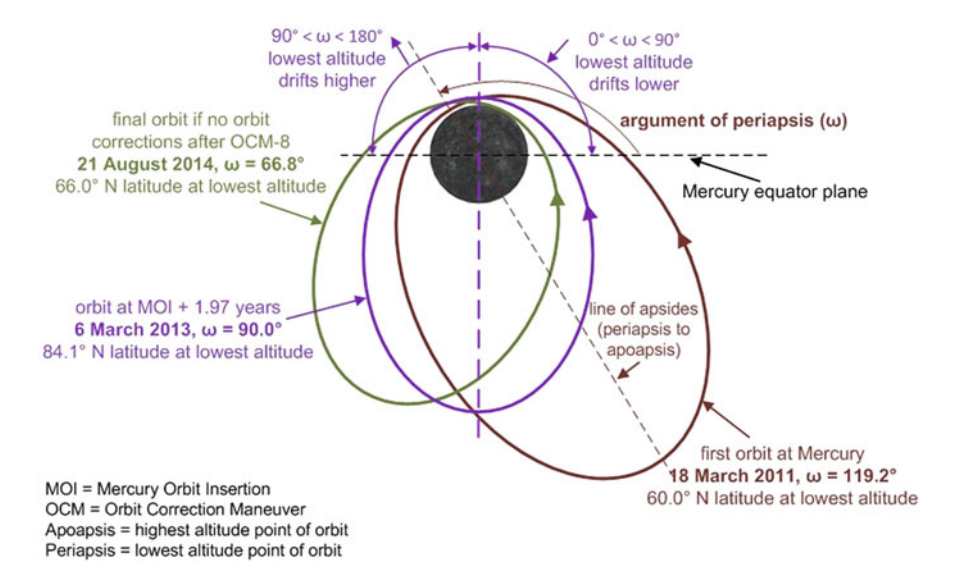


Fig. 3.4 MESSENGER's initial orbit, the orbit established for the extended mission in March 2013, and the August 2014 orbit if there had been no further orbit corrections. The diagram indicates how the angle between the northward orbital crossing of the equator and the periapsis (the 'argument of periapsis') decreased over time because of external forces, and how the drift in periapsis altitude changed from becoming higher to becoming lower once the argument of periapsis had decreased to less than 90°, making eventual impact onto Mercury's surface inevitable when all propulsive opportunities had been exhausted (NASA/Johns Hopkins University Applied Physics Laboratory/Carnegie Institution of Washington)

the inevitable impact onto Mercury's surface at the end of March 2015, probably somewhere near 55° E, 54° N.

3.3.2 The Spacecraft

MESSENGER's launch mass was 1,107 kg, of which 599 kg was propellant. Most of the remainder of the mass was taken up by the physical structure of the craft, even though this was made mostly of lightweight composite materials. Excluding propellant, MESSENGER's total mass was very similar to that of Mariner 10, though the mass of its instrument payload, 42.4 kg, was little over half that of Mariner 10's.

3.3.2.1 Thrusters

Whereas Mariner 10 had used a 'monopropellant' fuel for its thrusters (simple hydrazine decomposed by a catalyst), MESSENGER's main thruster was a

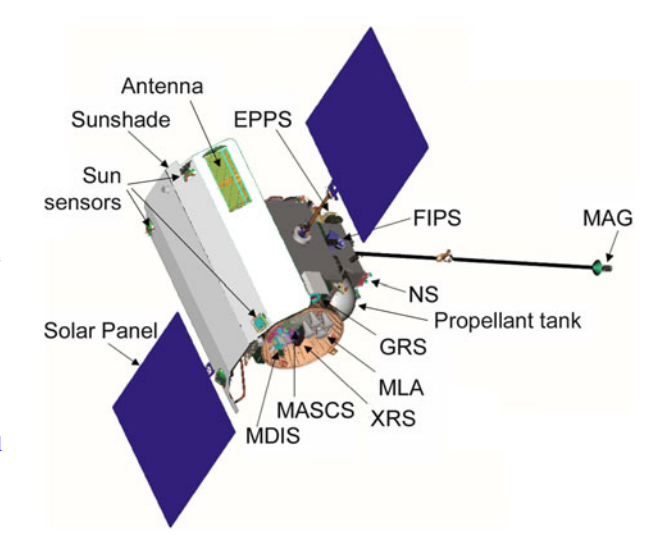
3.3 MESSENGER 61

bipropellant device (in which hydrazine was mixed with nitrogen tetroxide to act as an oxidizer) capable of 600 N (newtons) of thrust. It also had four 22 N hydrazine monopropellant thrusters used for small course corrections and to steady the craft during main engine burns, plus a dozen 4.4 N hydrazine monopropellant thrusters for small course corrections and to serve as backup for attitude control in situations where the craft's four spinning reaction wheels were unable to cope.

3.3.2.2 Thermal Design

The basic layout of MESSENGER is illustrated in Fig. 3.5. Its sunshade is a particularly notable feature, and draws attention to the thermal issues that must be overcome for a spacecraft that has to operate in orbit about Mercury. Thermal design, after the trajectory had been solved, was the main technical obstacle to designing a viable orbital mission. MESSENGER's sunshade consisted of front and back skins of ceramic cloth enclosing multi-layer insulation. At Mercury's perihelion distance from the Sun, the intensity of solar radiation is nearly 11 times that at Earth, and the sunshade was required to protect the craft from direct solar heating at all times. The shaded side of the craft was fitted with radiators to get rid of excess heat, which was carried out from the innards of the craft by diode (one-way) heat pipes. When low over the day-side of Mercury any orbiter is also baked by heat radiated from the 700 K surface that occupies much of the anti-sunward part of the sky, so MESSENGER was placed in an eccentric 12-h orbit spending less than half an hour at low altitude on the day-side at high northern latitudes (Fig. 3.4).

Fig. 3.5 A schematic diagram of MESSENGER. The sunshade was 2.5 m long. The Sun sensors (of which there were six) were a backup for the star trackers (not shown) whose role was to ensure that the spacecraft was always oriented behind the sunshade as seen from the Sun. The experiments are labelled by their standard abbreviations; see Table 3.1 (Johns Hopkins University Applied Physics Laboratory)



3.3.2.3 Communications and Data Storage

MESSENGER was in communication with the antennas of NASA's 'Deep Space Network' for 8 h each day. Signal strength, and thus the rate at which data could be successfully downlinked, varied with distance from Earth. Therefore during periods of the orbital mission when Mercury was far from Earth, MESSENGER stored most of its data in its 1 gigabyte solid-state recorders, for transmission when the two planets were closer together.

3.3.3 The Payload

MESSENGER's payload consisted of seven instruments plus a radio science experiment. It carried no equivalent of Mariner 10's Infrared radiometry experiment. However its Gamma-Ray, Neutron, and X-Ray Spectrometers, its Visible and Infrared Spectrograph and its Laser Altimeter provided totally new kinds of Mercury data, and its other instruments offered significant advantages over their Mariner 10 counterparts. MESSENGER's instruments are summarized in Table 3.1 and are discussed briefly below.

3.3.3.1 Mercury Dual Imaging System, MDIS

This was a 8.0 kg instrument consisting of a wide-angle camera (WAC) and a narrow-angle camera (NAC). They were mounted on a pivoting platform to allow pointing for optical navigation, for planetary mapping during flybys, and for stereoscopic imaging from orbit. This was MESSENGER's only instrument with pointing capability independent of spacecraft attitude. It was a significant improvement over Mariner 10's Television science experiment.

The detector for each camera was a $1,024 \times 1,024$ array of charge-coupled devices (CCDs), with 12-bit intensity resolution (routinely compressed to 8 bits). To minimize sensor noise, the CCDs had to be maintained at between -10 and $-40\,^{\circ}\text{C}$.

The WAC had a 10.5° field of view, and was equipped with a filter wheel to allow the compilation of colour images (one band at a time). One filter was 'clear', allowing the passage of light across the full 395–1,040 nm sensitivity range of the CCDs, and the others were narrow-band filters (20 nm wide or less) centred at a range of wavelengths from 430 nm (violet) to 1,010 nm (near-infrared). The NAC had a 1.5° field of view, and collected monochrome images at 700–800 nm (very near-infrared). When at MESSENGER's lowest nominal altitude of 200 km, each WAC pixel measured 36 m across, whereas NAC pixels were just over 5 m across.

Flyby objectives for MDIS were to complete near-global coverage at about 500 m/pixel and to begin multispectral imaging at about 2 km/pixel. Orbital objectives were: to produce a nadir-looking monochrome mosaic at 55–75° solar

3.3 MESSENGER 63

Table 3.1 MESSENGER's seven scientific instruments and the radio science experiment

Instrument/experiment	Description
Mercury Dual Imaging System, MDIS	Wide-angle Camera (WAC) with 11 filters, and a single channel Narrow-angle Camera (NAC)
Gamma-Ray and Neutron Spectrometer, GRNS	Gamma-Ray Spectrometer (GRS) to measure gamma rays emitted by the nuclei of atoms near the surface struck by cosmic rays (H, Mg, Si, O, Fe, Ti, Na, Ca) and from radioactive K, Th, U. Neutron Spectrometer to map local variations in abundance of neutrons of different energies (especially relevant to the presence of polar ice)
X-Ray Spectrometer, XRS	Three downward-looking gas-filled detectors to measure X-rays from the planet's surface (specifically Mg, Al, Si, S, Ca, Ti and Fe) and a Sun-pointing silicon solid-state detector to calibrate the incoming X-ray flux
Magnetometer, MAG	Triaxial fluxgate magnetometer to map strength and direction of Mercury's magnetic field
Mercury Laser Altimeter, MLA	Near-infrared laser transmitter/receiver to map and measure topography and to measure forced libration. Combined with Radio Science data to map Mercury's gravitational field
Mercury Atmospheric and Surface Composition Spectrometer, MASCS	Measurement of the abundance of exospheric gases using an Ultraviolet and Visible Spectrometer (UVVS), and identification of minerals in surface materials using a Visible and Infrared Spectrograph (VIRS)
Energetic Particle and Plasma Spectrometer, EPPS	Measurement of the mix and characteristics of the charged particles in and around the magnetosphere using an Energetic Particle Spectrometer (EPS) and a Fast Imaging Plasma Spectrometer (FIPS)
Radio Science, RS	Tracking via the spacecraft's X-band communications system, primarily to study Mercury's gravitational field

incidence angle and 250 m/pixel or smaller sampling; to compile a similar but 25° off-nadir mosaic to reveal topography in stereo; to complete the multispectral mapping begun during the fly-bys; to collect high-resolution (20–50 m/pixel) targeted images across representative geological units and structures. The flybys would thus fill in the large blank area left by Mariner 10 and begin to map in colour, whereas the orbital campaign would achieve much higher spatial resolution and yield global colour mosaics.

To bring the high data volume below the threshold imposed by constraints of onboard storage and data transmission rate, there was an option for 2×2 binning of pixels (to make a 512×512 image). Furthermore although monochrome data were acquired in 8-bit mode and multispectral data in 12-bit mode, both were compressed losslessly before onboard storage.

3.3.3.2 Gamma-Ray and Neutron Spectrometer, GRNS

The Gamma-Ray Spectrometer (GRS) had a cryocooled germanium detector operating at <70 K capable of measuring gamma rays in the energy range 60 keV to 9 MeV expected to be emitted by the nuclei of atoms (notably H, Mg, Si, O, Fe, Ti, Na, and Ca) struck by cosmic rays, and by radioactive decay of long-lived isotopes of K, Th, and U. The emitted gamma rays have energies characteristic of each source element, and the flux at each energy can be used to determine the elemental concentration. The GRS was surrounded by an 'anticoincidence shield' (a borated plastic scintillator) to detect, and thus enable elimination of, the continuum background.

The gamma rays detectable from orbit come from the top few tens of cm of the regolith, and so sample more deeply than other geochemical remote sensing methods that are sensitive to only the uppermost surface layer (<1 mm). For most purposes, useful GRS data could be collected only when the spacecraft was less than about 2,000 km from the surface, and allowed coarse mapping with ground resolution of about 1,000 km. The GRS was the first of MESSENGER's instruments to malfunction. In June 2012 its cryocooler failed so that gamma ray spectra could no longer be recorded. However this provided an opportunity to re-purpose the anticoincidence shield, by uploading new software that turned it into a neutron and electron detector.

The Neutron Spectrometer (NS) used scintillation detectors enriched in ⁶Li to measure the flux of neutrons ejected from Mercury as a result of cosmic ray interactions. Conventionally, three neutron energy ranges are distinguished: thermal (up to 1 eV), epithermal (1 eV to 500 keV) and fast (500 keV to about 7 MeV). The chief science goal of the NS was to map the hydrogen (and hence water) abundance over the northern hemisphere, taking advantage of the fact that epithermal neutrons are slowed down to become thermal neutrons by collisions with hydrogen nuclei (which of course have almost the same mass as a neutron) whereas fast neutrons lose only insignificant fractions of their energy in collisions. Epithermal neutrons bounce off massive nuclei without much loss of momentum, so it is really only hydrogen that has this effect.

3.3.3.3 X-Ray Spectrometer Spectrometer, XRS

This was an improved version of the XRS previously flown on the Near Earth Asteroid Rendezvous (NEAR) mission. It was designed to detect X-rays fluoresced from the top mm of Mercury's regolith when atoms are excited by incident solar X-rays. This is a technique that can be used for any airless body. The closer to the Sun the better because of the stronger incident flux, though solar X-ray flux varies by orders of magnitude according to the solar activity cycle.

The XRS planetary sensor used 'gas proportional counters' capable of measuring X-rays across an energy range of 1–10 keV. The energy resolution of these

3.3 MESSENGER 65

devices was several hundred eV, too coarse to distinguish between the key low-energy X-ray emissions from Mg (1.25 keV), Al (1.49 eV) and Si (1.74 eV). To get round this problem, three identical counters were used. One had no filter, and allowed all X-rays to reach the counter, but the second had a Mg foil over the entrance window to eliminate incoming X-rays fluoresced by Mg on the planet, and the third had a Al foil filter to eliminate incoming X-rays fluoresced by Al on the planet. By comparing counts from all three detectors, ambiguities could be removed. Elements with distinguishable X-ray fluorescence lines expected to occur in sufficient concentration to be detectable were Mg, Al, Si, S, Ca, Ti and Fe. S was expected to be of interest because it was an alternative candidate to waterice for the radar-bright polar crater deposits. In the event MESSENGER confirmed those to be water-ice, but the XRS found an unexpectedly high sulfur content across Mercury's surface globally.

The XRS was a non-imaging system. The field of view was 12° , corresponding to about 50 km from 200 km altitude, but the integration time of many tens of seconds needed to collect sufficient signal even from the strongest X-ray lines meant that the achievable spatial resolution was much coarser than this. Because fluorescent X-ray flux varies according to the state of the Sun, it was necessary to measure the solar X-ray flux to avoid misinterpretation, so MESSENGER carried a solid-state solar X-ray monitor mounted on the sunshield, with a 42° field of view to keep the Sun on the detector at all anticipated spacecraft pointing angles. The beryllium foil covering the aperture was expected to exceed 500 °C in orbit, whereas the detector just 4 cm behind was kept at -45 °C.

3.3.3.4 Magnetometer, MAG

MESSENGER carried a single triaxial fluxgate magnetometer, on a 3.6 m carbon-fibre boom behind its own small conical sunscreen (Fig. 3.1) to protect it on the occasions when it was expected emerge from the shadow of the main sunscreen while the spacecraft was tilted for operational purposes required by some of the other experiments. The basic design was similar to that used on many previous missions, including Mariner 10. However on MESSENGER any spacecraft-induced secondary magnetic fields were minimized by shielding and compensation magnets, so a single magnetometer was sufficient for the task of determining the planetary field.

Repeated passages through the magnetopause as MESSENGER orbited would obviously give a more reliable picture of Mercury's magnetic field than could be inferred from Mariner 10's two relevant flybys. The sampling rate for measurements was every 50 ms when close to magnetospheric boundaries, decreasing to once per second in less dynamic regions.

3.3.3.5 Mercury Laser Altimeter, MLA

The laser altimeter determined the height of the spacecraft above Mercury's surface by measuring the duration between transmission of laser pulses and receipt of the reflection (the round-trip time of laser pulses). Laser pulses of 1,064 nm wavelength were transmitted eight times per second, providing altitude measurements with 30-cm precision. When at 200 km altitude, the laser footprint was a spot about 16 m across. During design it became clear that the reflecting telescopes used for the receiver optics on previous planetary laser altimeter experiments would not perform well in the Mercury thermal environment, and so a set of four refracting telescopes with sapphire objective lenses (equivalent to a single 25 cm lens) was used.

Because the strength of the reflection from the surface would fall off with at least the inverse square of the distance, MLA was capable of recording data only when the range was less than about 1,200 km, and so was planned to operate for about only 30 min close to periapsis. This meant that from the nominal orbit it could map the northern but not the southern hemisphere. Spacing between spot measurements along a track was typically a few hundred m, and by the end of the mission the accumulation of tracks was such that spacing between tracks was tens of km near the equator and less at higher northern latitudes. Figure 3.6 shows some of the results of the first 2 years of MLA orbital operations.

A secondary objective of MLA was to measure and map the surface reflectivity at 1,064 nm, and in addition to sunlit areas this was achieved within permanently-shadowed craters where it revealed high-albedo exposures of ice and also some low-albedo patches presumed to be organics of cometary origin.

MLA data were used in combination with radio science data to improve on the ground-based radar determinations of Mercury's forced libration in order to refine models of the state and structure of the planet's core.

3.3.3.6 Mercury Atmospheric and Surface Composition Spectrometer, MASCS

MASCS was an instrument for measuring properties of both the surface and the exosphere. It was mounted with its telescope optical axis aligned with the spacecraft's Z-axis. This facilitated limb-scanning, but required rotation of the craft in order to make surface observations.

The Ultraviolet and Visible Spectrometer (UVVS) and the Visible and Infrared Spectrograph (VIRS) shared a single 50 mm aperture reflecting telescope. The diffraction grating feeding the UVVS spectrometer sampled light across the 115–600 nm range using three photomultiplier tubes (115–190, 160–320 and 250–600 nm) with a spectral resolution of 0.3–0.7 nm. The spectral range was chosen to be sensitive UV emission from previously known species H, O, Na, K and Ca with the intention of mapping their exospheric temperatures and density. It would also search for previously unknown but predicted species Si, Al, Mg, Fe, S and

3.3 MESSENGER 67

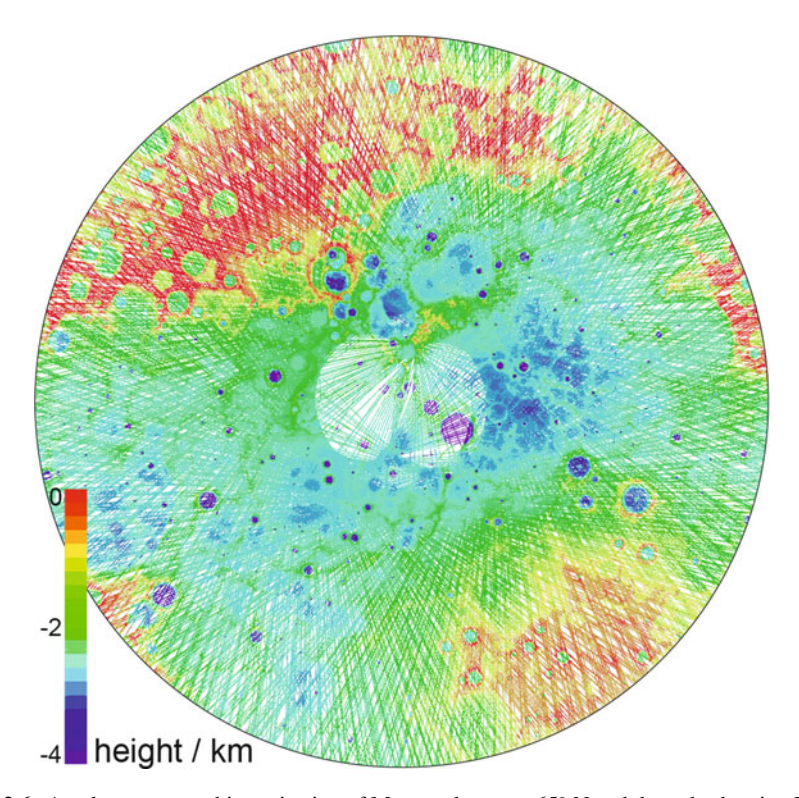


Fig. 3.6 A polar stereographic projection of Mercury between 65° N and the pole showing MLA data collected during MESSENGER's first two complete years in orbit. At this scale, along-track gaps are invisible, but gaps between tracks become apparent at lower latitudes and in some regions near the pole as a result of orbit adjustments. Height is colour-coded relative to a reference sphere of 2,440 km radius. The generally below-zero altitude reflects the low-lying terrain of the northern plains rather than being symptomatic of polar flattening of the globe (NASA/Johns Hopkins University Applied Physics Laboratory/Carnegie Institution of Washington)

OH. Its altitude resolution was 25 km when scanning Mercury's limb to observe exospheric UV emission.

Light for VIRS was fed from the telescope's focal plane by a fibre optics link to a pair of solid-state array detectors measuring 'visible' (300–1,050 nm) and near-infrared (850–1,450) wavelengths with a spectral resolution of 4.7 nm. Between them, UVVS and VIRS were to able measure surface reflectance from middle ultraviolet through visible to near-infrared wavelengths with the intention of searching for minerals containing ferrous iron (Fe²⁺) by means of characteristic absorptions near 1,000 nm and broad-band absorption near 250 nm, and Fe- and Ti-bearing glasses (features near 340 nm). This was a non-imaging system, providing data along lines with a best spatial resolution of about 3 km in the along-track direction.

3.3.3.7 Energetic Particle and Plasma Spectrometer, EPPS

This was an experiment to identify the species of charged particles in and around Mercury's magnetosphere, and to determine their energy distribution. The Energetic Particle Spectrometer (EPS) and Fast Imaging Plasma Spectrometer (FIPS) each included a time-of-flight mass spectrometer. Such devices pass incoming charged particles through an electric field, which sorts them according to their velocity and mass-to-charge ratio.

The EPS was sensitive to ions between 10 keV and about 3 MeV per nucleon and to electrons up to 400 keV. It had a field of view of 160° by 12°, divided into six segments of 25° each. FIPS provided nearly full hemispheric coverage and combined an electrostatic analyzer plus time-of-flight mass spectrometer to measure low-energy ions coming from Mercury's surface, ionized exospheric atoms picked up by the solar wind, and solar wind particles themselves.

The EPS was mounted on the rear of the spacecraft enabling it to concentrate on ions and electrons accelerated in the magnetosphere, whereas FIPS was on the side of the spacecraft, from where it could observe the plasma over a wide range of pitch angles (which is the angle between a particle's velocity and the local magnetic field).

3.3.3.8 Radio Science, RS

MESSENGER's telecommunications system consisted of two opposite-facing high-gain phased-array antennas (one of which is visible in Fig. 3.5) in place of a steerable antenna such as that carried by Mariner 10, two fanbeam medium-gain antennas, and four low-gain antennas. These received uplinked data transmitted by NASA's Deep Space Network (DSN) at 7.2 GHz and communicated back to the DSN at 8.4 GHz. Both frequencies are in the X-band part of the spectrum, whereas Mariner 10 had used both X- and S-band.

Precise observations of the Doppler frequency shifts of received transmissions were used to determine spacecraft accelerations and hence local variations in Mercury's gravity field, and, in conjunction with MLA, to track libration. The times of occultation of the spacecraft's radio signal (when the line of sight from Earth was interrupted by the planet) were used to determine local variations in Mercury's radius, of particular value in the southern hemisphere which was mostly beyond the range of the MLA.

3.4 BepiColombo

3.4.1 The Trajectory and Orbit

BepiColombo is scheduled to be launched on an Earth-escape trajectory in July 2016 on an Ariane 5 rocket. Science operations in orbit about Mercury are due to commence in May 2024, even if launch is several months late. The nominal mission is 1 year, with a possible extension for at least one further year.

BepiColombo's two orbiters, the European Mercury Planetary Orbiter (MPO) and the Japanese Mercury Magnetospheric Orbiter (MMO), will be transported to Mercury by a Mercury Transfer Module (MTM). This will provide all the propulsive capability required en route (a total ΔV of about 5.6 km s⁻¹) after separation from the Ariane 5 launcher (Fig. 3.7). During cruise, the European Space Operations Centre (ESOC) in Darmstadt, Germany, will coordinate the operation of the full composite spacecraft by using the Cebreros 35 m antenna in Spain. MMO operations will be taken over by the ISAS/JAXA Sagamihara Space Operation

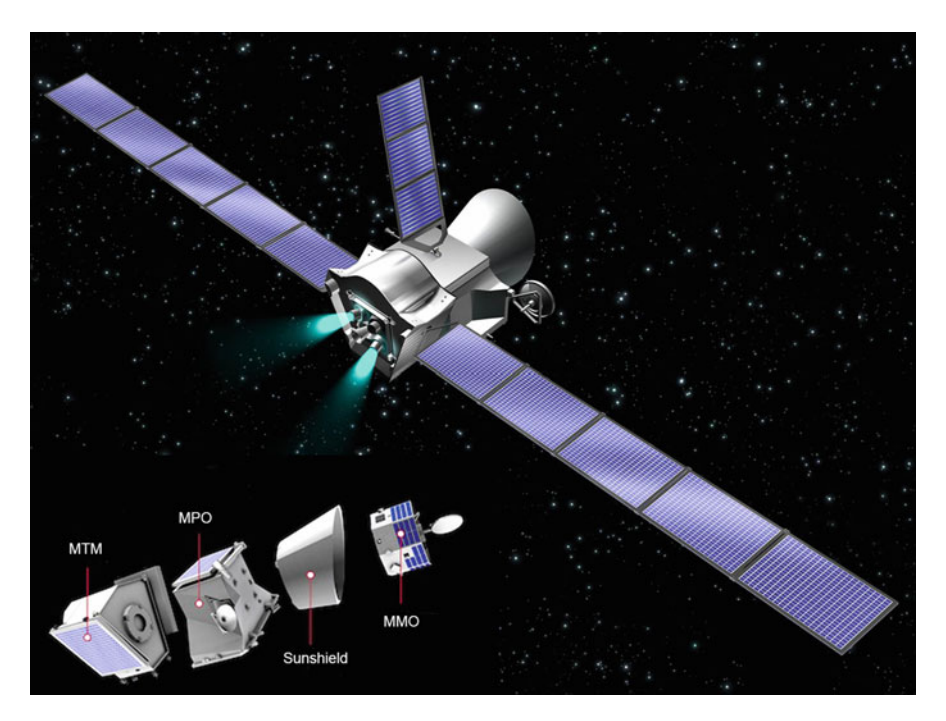


Fig. 3.7 BepiColombo as it will look during cruise to Mercury. The inset at the lower left shows an exploded view of the modules, with extendable components stowed (as necessary to fit within the launch housing). MMO is not visible in the main view, because it sits within the Sunshield. The solar panel arrays deployed on either side on the MTM are each about 12 m long (Modified from ESA sources)

Centre, via the Usuda 64 m antenna in Japan, once it is in independent orbit around Mercury, while ESOC will remain in charge of MPO.

3.4.1.1 The Cruise and Flybys

The first flyby of the cruise will be a gravity-assist manoeuvre past the Earth after 1 year. This will be followed by two Venus flybys to reduce the perihelion down to Mercury's orbit, and then four Mercury flybys (passing through 3:2, 4:3 and 5:4 resonance) until, on the fourth encounter, capture into orbit about Mercury occurs almost passively without the need for a major orbit insertion burn.

Although the cruise will operate along the principles established by Chen-wan Yen, an important difference with respect to MESSENGER is that propulsive manoeuvres during cruise are to be made by solar-powered electric propulsion (described later) operating over episodes of up to several months each, rather than by short bursts from more powerful chemical thrusters. For example, after the third Mercury flyby the relative velocity between the spacecraft and the planet will be about 1.8 km s $^{-1}$, but solar-powered electric propulsion sustained for most of the time between then and the final encounter will lead to final arrival with such slight velocity difference that capture into orbit will be almost passive.

Another difference to MESSENGER is that the cruise configuration of the spacecraft will not allow operation of the science experiments. Therefore there no data will be gathered during flybys, except for radio science.

The MTM will be jettisoned 2 months prior to final arrival at Mercury, with the craft already in a weakly-bound highly elliptical orbit. Stronger Mercury Orbit Insertion will be established with the aid of the MPO thrusters.

3.4.1.2 Orbiting Mercury

After Mercury Orbit Insertion, a series of three MPO thruster burns will be used to achieve a polar orbit with periapsis 480 km above the surface fairly close to the equator, apoapsis at about 12,000 km, and an orbital period of 9.3 h. MMO is a spin-stabilized craft and will be spun up by a spring-release mechanism before being detached into this orbit. The shape of the MMO orbit will be not dissimilar to that of MESSENGER's initial 200 and 12,200 km periapsis and apoapsis orbit, but there is an important difference in that periapsis will be close to the equator.

MPO will then jettison the Sunshield (and the associated interface structure) that had been needed to protect MMO during cruise. Twelve more thruster burns will lower MPO's apoapsis to 1,500 km by April 2024, by which time a ΔV of 950 m s⁻¹ will have been achieved. The orbit will have a period of about 2.3 h, and be co-planar with MMO's orbit.

Because MPO and MMO periapses will be almost the same, the two craft will pass within 200 km of each other many times during the first year of operations, and will pass within 20 km several times if the mission continues into a second year. These close passages will allow cross-scale measurements of local irregularities or

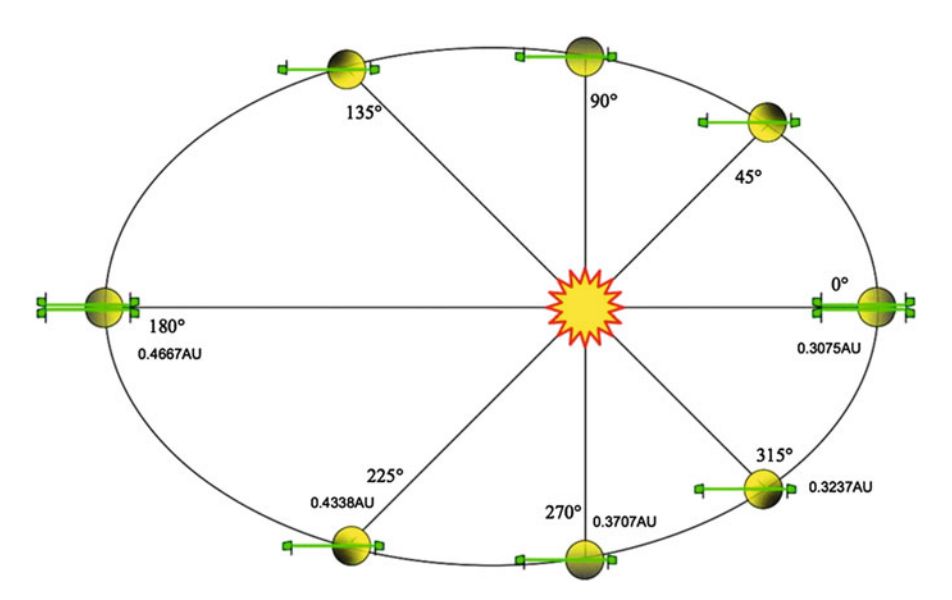


Fig. 3.8 The relationship between the MPO orbit about Mercury, and Mercury's orbit about the Sun. This is a view looking southward showing the MPO orbital plane as a green line. This is fixed in space, such that periapsis occurs at noon at aphelion and at midnight perihelion. The diagram also indicates 'flip-over' at perihelion and aphelion, where MPO will be rotated 180° for thermal reasons (ESA)

short-term events in the magnetosphere. The orbits will be inertially fixed, with periapsis coinciding with noon when Mercury is at aphelion, and with midnight when Mercury is at perihelion (Fig. 3.8).

Initially, MMO's orbital period will be slightly more than exactly four times longer than MPO's. However, once in their science operations orbits, they will be subject to the same forces as those experienced by MESSENGER, but MPO will be the more strongly affected. Insights into Mercury's gravity field gained from MESSENGER have been fed into BepiColombo planning, and it is expected that slight north—south asymmetry in Mercury's gravity field (its so-called J3 gravity field coefficient) will cause MPO's periapsis to decrease and apoapsis to increase, while the latitude at which periapsis occurs will creep northward too. The rate of drift depends on the latitude of periapsis. Optimisation studies are still underway, but one likely solution is to set the initial latitude of periapsis to 2° S. After 25 months this would have drifted to about 6° N. During this time, MPO periherm would have decreased from 480 to 300 km and apopherm increased from 1,500 to 1,680 km, whereas MMO periherm would have decreased to about 345 km.

3.4.2 The Spacecraft

The entire BepiColombo ensemble, illustrated in Fig. 3.7, will have a mass of 4,100 kg, including propellant. This is nearly four times greater than MESSEN-GER's launch mass.

3.4.2.1 Transfer Module

The Mercury Transfer Module employed to deliver BepiColombo into Mercury orbit, before being jettisoned, houses the main propulsion system. This consists of four individually pointable ion thrusters mounted on the same face (two of them are firing in Fig. 3.7). These provide thrust by solar-electric propulsion, which is a form of ion drive. MTM's large solar panels will generate electricity, providing up to 13.5 kW of power. This will be used to ionize xenon (which 580 kg will be carried) and accelerate a stream of xenon ions across an electrical grid and thence out via the thruster nozzles. The reaction as the jets exit the nozzles will provide ΔV for the spacecraft. Ion propulsion will operate at intervals totalling more than half the duration of the cruise, pushing against the direction of travel to counteract the acceleration experienced as the craft falls sunwards.

The MTM will also have an array of bipropellant thrusters for navigation manoeuvres and attitude control, with a 150 kg fuel supply. To avoid overheating, much of the MTM surface will be covered by radiator panels, linked to its innards by heat pipes.

3.4.2.2 MPO

MPO measures about $1.6 \text{ m} \times 1.7 \text{ m} \times 1.9 \text{ m}$ and will be an autonomous free-flier during science operations (Fig. 3.9), but before that has the task of delivering MMO into its operational orbit. MPO's 'dry mass' will be 1,147 kg but it will also carry 650 kg of fuel for hydrazine/nitrogen tetroxide bipropellant thrusters used for orbit adjustments, and hydrazine thrusters used during reaction wheel unloading and to assist in attitude control. A steerable solar array will provide power during cruise (for telecommunications) and during the orbital mission. The power generated in orbit will be about 1,000 W (with the solar array being slanted to a low solar incidence angle to avoid overheating, rather than aiming for full face-on illumination), and there will be a battery capable of a similar supply for about an hour.

Telecommunications will be via two fixed low-gain X-band antennas, a steerable medium-gain X-band antenna, and a steerable one metre diameter high gain dual-band antenna. The low gain antennas are primarily to receive commands during any emergencies. The medium gain antenna will be used mainly during cruise and be available orbit MPO goes into 'safe mode'. The high gain antenna will be used during science operations for X-band uplink and downlink and K-band downlink.

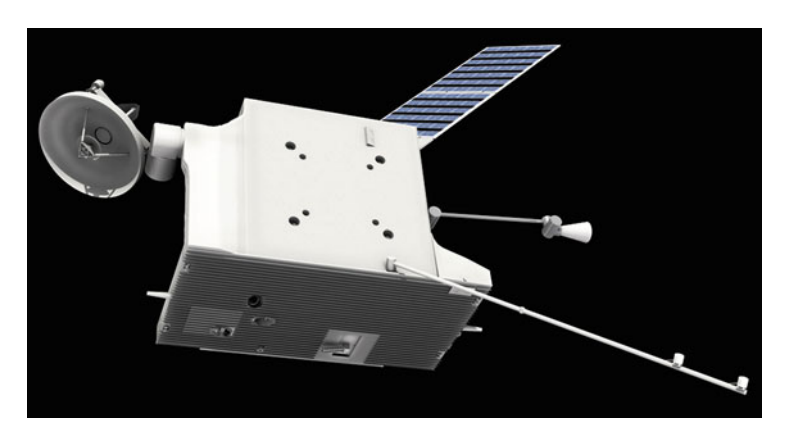


Fig. 3.9 MPO deployed for orbit about Mercury. The lower face is the 3.7 m long radiator panel, which will always face the planet and never be allowed to receive direct sunlight (ESA)

The rate of data transmission to Earth will vary according to the Earth-Mercury distance and the visibility of ground stations, so MPO will have an onboard solid state mass memory capable of storing up to 384 gigabits of data. The total amount of data downlinked is expected to be about 1,550 gigabits per year.

In order to cope with the thermal environment in Mercury orbit, MPO will be well insulated and penetrated by heat pipes feeding a 2 m \times 3.6 m radiator panel. This forms the face of MPO that will be kept permanently directed down towards the planet, and will be protected by a set of coated louvres whose function is to prevent infrared radiated from the planet striking the radiator surface while still allowing heat to escape from it to space. The radiator would not be able to function if direct sunlight were to fall on it, so this will be avoided by flipping MPO through 180° at every perihelion and aphelion, with the aid of four internal reaction wheels. The flip-over will be performed while MPO is in eclipse, on the night-side of Mercury.

3.4.2.3 MMO

The body of MMO is in the shape of an octagonal prism, 0.9 m tall and measuring 1.8 m between opposite faces (Fig. 3.10). It is thus less bulky than MPO and has a total mass, excluding fuel, that is less than a quarter of MPO's mass.

MMO will be spun up to 15 rpm before separation from MPO, with its spin axis almost perpendicular to Mercury's orbital plane. Having left the shelter of the cruise Sunshield, this spin will prevent overheating as well as stabilizing the craft.

Sunlight will never fall on the top and bottom faces, but the eight side faces will see the Sun in turn and will carry solar panels delivering about 350 W of power. The 0.8 m high-gain antenna will be de-spun to remain in communication with Japanese ground stations, and there is a medium-gain antenna as backup. Total data volume is expected to be about 160 gigabits per year.

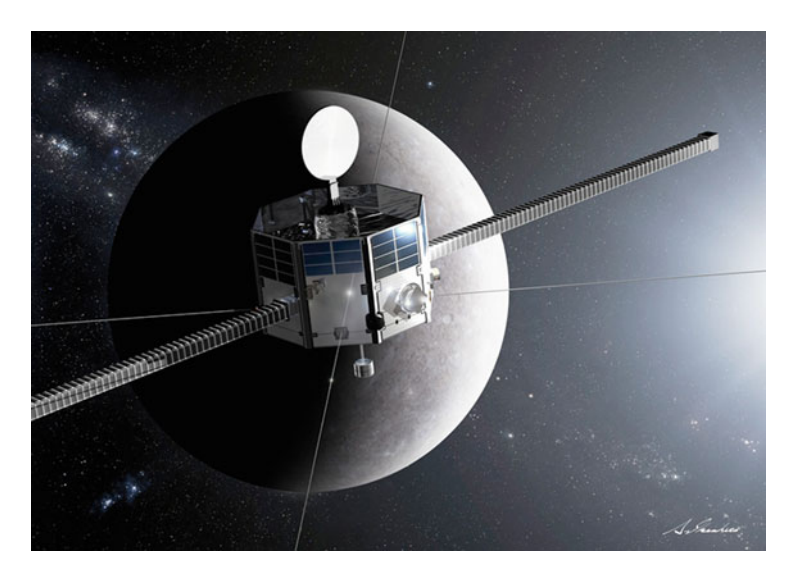


Fig. 3.10 MMO deployed for orbit about Mercury. It will be spinning about the axis that runs up through the high-gain antenna (*above*) and the medium-gain antenna (*below*). The fine lines are four 15 m long wire antennas for electric field and radiowave measurements, deployed by the craft's spin, and the two bulkier projections are 5 m long magnetometer booms (JAXA)

Once separated, MMO will be an autonomous mission under Japanese control. It will have six cold nitrogen gas jet thrusters for attitude control, but these will be incapable of making significant adjustments to the orbit.

3.4.3 The Payload

The MPO spacecraft will weigh 1,140 kg, including 80 kg of instruments summarized in Table 3.2. The MMO spacecraft will weigh about 275 kg, including 45 kg of scientific instruments summarized in Table 3.3. Their design and purpose are discussed briefly below.

3.4.3.1 BepiColombo Laser Altimeter, BELA (MPO)

Like MESSENGER's MLA, this will use a 1,064 nm laser, but pulsing at ten times per second rather than eight. It is a heavy instrument massing about 15 kg, and requiring about 30 W of power. The aims of the experiment are to map the global shape of Mercury, to map the topography relative to that shape, to determine the tidal deformation of the surface, and to study surface roughness, local slopes and albedo variations. Using BELA data in conjunction with radio science data (MORE) will place constraints on Mercury's internal structure.

 Table 3.2
 BepiColombo MPO's 11 scientific instruments

Instrument/experiment	Description
BepiColombo Laser Altimeter, BELA	Near-infrared laser transmitter/receiver to characterize and measure the figure, topography, and surface morphology of Mercury. It will provide absolute topographic height and position with respect to a Mercury centred coordinate system
Italian Spring Accelerometer, ISA	Three-axis spring accelerometer to measure acceleration of the MPO structure, giving insights into Mercury's internal structure and providing a test of Einstein's theory of General Relativity
Mercury Polar Orbiter Magnetometer, MPO/MAG (MERMAG)	Two triaxial fluxgate magnetometers to map strength and direction of Mercury's magnetic field
Mercury Radiometer and Thermal Infrared Spectrometer, MERTIS	Thermal infrared imaging spectrometer and radiometer. Global mapping at 500 m resolution in the 7–14 µm spectral range at 90 nm spectral resolution
Mercury Gamma ray and Neutron Spectrometer, MGNS	Gamma ray spectrometer and a set of four neutron sensors to count thermal, epithermal and high-energy neutrons
Mercury Imaging X-ray Spectrometer, MIXS	Collimated (MIXS-C) and focussed (MIXS-T) mapping of X-ray fluoresence; Si, Ti, Al, Fe, Mg, Na, Ca, P, Mn, K, S, Cr, Ni and O,
Mercury Orbiter Radio science Experiment, MORE	Precise tracking via MPO's K-band digital transponder
Probing the Hermean Exosphere by Ultraviolet Spectroscopy, PHEBUS	Extreme, far and near UV spectrometers to characterise the structure, composition and dynamics of the exosphere
Search for Exosphere Refilling and Emitted Neutral Abundance, SERENA	ELENA (Emitted Low-Energy Neutral Atoms) to measure <20 eV-5 keV neutral particles; STROFIO (Start from a Rotating Field Mass Spectrometer) to measure cold, 0 to a few eV, exospheric gas; MIPA (Miniature Ion Precipitation Analyser) 10 eV-15 keV ion spectrometer; PICAM (Planetary Ion Camera) 1 eV-3 keV ion mass spectrometer
Spectrometers and Imagers for MPO BepiColombo Integrated Observatory System, SYMBIO-SYS	Stereo Channel (STC) for imaging the whole planet at 50 m per pixel or better, in panchromatic and colour stereo. High Spatial Resolution Imaging Channel (HRIC) for 5 m per pixel mapping from periapsis in three colours and a broad panchromatic band. Visible and near-Infrared Hyperspectral Imaging channel (VIHI), imaging in 256 narrow 400–2,000 nm channels at 100 m per pixel at periapsis
Solar Intensity X-ray and particle Spectrometer, SIXS	SIXS-X to measure solar X-rays and SIXS-P to measure energetic particles from the Sun

Instrument/experiment	Description
Mercury Magnetospheric Orbiter Magnetometer, MMO/MGF (MERMAG)	Two triaxial fluxgate magnetometers to map strength and direction of Mercury's magnetic field
Mercury Plasma Particle Experiment, MPPE	Seven sensors to study the plasma/particle environment: two electron energy spectrum analyzers (MEA1, MEA2), ion mass spectrometer (MSA), ion energy spectrum analyszer (MIA), high energy particle and high energy ion instruments (HEP-ele and HEP-ion), energetic neutrals analyzer (ENA)
Mercury Plasma Wave Instrument, PWI	Measurement of intensity, waveforms and the fre- quency spectra of electric and magnetic fields, using wire- and boom-mounted instruments
Mercury Sodium Atmospheric Spectral Imager, MSASI	Fabry-Perot elaton for detailed analysis of 589 nm sodium emission
Mercury Dust Monitor, MDM	Piezoelectric sensors to record impact of dust particles

 Table 3.3
 BepiColombo MMO's five scientific instruments

The MPO orbit will allow BELA to operate equally well over both hemispheres, whereas MESSENGER's MLA could collect data only in the north.

3.4.3.2 Italian Spring Accelerometer, ISA (MPO)

The main goal of ISA is to measure the subtle non-gravitational accelerations that MPO is expected to experience in the strong radiation environment of Mercury, principally from solar radiation and radiation reflected and emitted by the planet. Accelerations will be tracked with an accuracy of 10^{-8} m s⁻² over the course of an orbit. Isolation of non-gravitational accelerations, in conjunction with radio science data (MORE), will enable gravitational effects to be determined more precisely. These are relevant to planetary structure and can also act as a test of General Relativity.

ISA has a mass of about 7 kg and will require about 12 W of power.

3.4.3.3 Mercury Polar Orbiter Magnetometer, MPO/MAG (MERMAG)

The MPO and MMO magnetometers form an experiment consortium sharing the common name of MERMAG. The MPO experiment, MPO/MAG, is a triaxial fluxgate magnetometer mounted on a 2.8 m boom plus an identical instrument on the same boom but 0.5 m closer to the spacecraft. Using these in tandem enables compensation for the magnetic field induced by the electric currents within the spacecraft. The instrument is based on similar examples flown on Rosetta and Venus Express, and will measure field strength with a precision of 2 picoteslas.

The MPO/MAG instruments have a mass of only 2 kg and consume about 13 W of power.

The main objective is to take advantage of MPO's close orbit to measure all terms associated with Mercury's internal fields up to octopole (the component, superimposed on the dipole field, that can be likened to the combined effect of eight magnetic poles). Simultaneous measurements by MMO's magnetometer will permit allowance to be made for any effects of electric currents in the magnetosphere on the MPO measurements.

Secondary objectives include study of the interaction of the solar wind with Mercury's magnetic field and with the body of the planet, which are expected to cause highly dynamic magnetospheric currents.

3.4.3.4 Mercury Thermal Infrared Spectrometer, MERTIS (MPO)

MERTIS will use common optics with a 10 cm diameter primary mirror to supply infrared radiation to a push-broom grating spectrometer (for spectral imaging, 78 channels 7–14 μ m) and to a radiometer (two channels, 7–40 μ m). Detector performance depends on its temperature, so this will be stabilized by a thermo electric cooler to ensure thermal stability of better than 0.05 °C per minute within a permissible operational range of 20–40 °C. The package has a low mass of little more than 3 kg, drawing about 13 W of power.

MERTIS will be nadir-pointing and its 4° field-of-view will enable imaging ground-tracks to overlap by about 10% at the equator. The nominal mission will allow global mapping with a pixel size of 500 m, with 5-10% of the planet imaged in more detail.

MERTIS data will be of a kind that neither Mariner 10 nor MESSENGER obtained, and are likely to be especially valuable because the 7–14 μ m spectral range covers diagnostic spectral features that allow feldspar minerals to be detected and characterized, and is also useful for detecting pyroxenes, olivines and elemental sulfur. Laboratory studies of minerals under simulated Mercury thermal and vacuum conditions performed in preparation for MERTIS have already shown that heating to Mercury's day-time temperature can lower their albedo, by poorly-understood structural (mineral lattice) changes, so MERTIS data may help us to understand Mercury's low albedo.

Other science objectives to which MERTIS will contribute include: characterization of Mercury's surface composition, identification of rock-forming minerals in the regolith, and mapping of surface mineralogy. The radiometer and spectrometer will be used to determine thermal inertia (relevant to composition and physical nature of the regolith) and surface temperature variations.

3.4.3.5 Mercury Gamma-ray Neutron Spectrometer, MGNS (MPO)

This 5.2 kg, 6 W, package uses an innovative lanthanum bromide scintillation sensor to map gamma ray emissions in 4,096 channels spanning 0.3–10.0 MeV. It is much less massive than MESSENGER's equivalent germanium detector because it does not require specialist cryocooling.

The neutron detectors are three ³He proportional counters most sensitive to thermal and epithermal neutrons (up to 500 keV) and a scintillation counter based on a crystal of stilbene (diphenylethene) to count high-energy neutrons (16 energy channels, 0.3–10.0 MeV).

MGNS will map elements including Na, Mg, Al, Si, O, Ca, Ti, Cr, Mn, Fe, K, Th and U with a spatial resolution of about 400 km, and will be able to study polar volatiles at both poles.

Instrument design was to have been refined according to experience from a similar package flown on the Russian Phobos-Grunt spacecraft, but sadly the November 2011 launch of that mission was a failure.

3.4.3.6 Mercury Imaging X-ray Spectrometer, MIXS (MPO)

This 11 kg, 20 W, package is a major advance over MESSENGER's X-ray spectrometer in terms of both spatial resolution for mapping and energy resolution for element detection. It will map X-ray emission from Mercury's surface across an energy range of 0.5–7.5 keV.

MIXS is a two-component instrument, each fed by its own 'microchannel plate' (MCP) optics in which X-rays are reflected internally as they are channelled along 20 μm wide square pores in an array. A collimated collector, (MIXS-C) will collect X-rays across a 10° field-of-view, whereas telescope optics (MIXS-T) will use front and rear curved MCP arrays to produce a focused image. The achievable spatial resolution will be 70–270 km for MIXS-C and as small as 10 km for MIXS-T during solar flares.

In contrast to the gas proportional counters of MESSENGER's XRS, which really only give ratios between line intensities, MIXS will measure line intensities directly. MIXS-C and MIXS-T will each send their collected X-ray photons to its own 64×64 array of field-effect transistors. Each element of the array will count and record the energy of each incident X-ray photon. The energy resolution will initially be about 100 eV, degrading to about 200 eV after 1 year of operations.

Elements detectable and discriminable by MIXS will be Si, Ti, Al, Fe, Mg, Na, Ca, P, Mn, K, S, Cr, Ni and O, of which less than half were seen by MESSENGER's XRS. As well as studying X-ray fluorescence induced by solar X-rays, MIXS will look out for particle-induced X-ray fluorescence – for example where solar wind protons strike the night-side or polar regions.

3.4.3.7 Mercury Orbiter Radio Science Experiment, MORE (MPO)

Knowledge of precisely where MPO is at any time (to a precision of about 20 cm) thanks to MORE in conjunction with other experiments, such as BELA and ISA, will contribute to mapping of Mercury's shape, topography and gravity field. It will also test General Relativity and alternative theories of gravity by measuring time-delay and Doppler shift of radio waves, and by improving the precision of our knowledge of the rate of advance of Mercury's perihelion.

3.4.3.8 Probing the Hermean Exosphere by Ultraviolet Spectroscopy, PHEBUS (MPO)

This 7.7 kg instrument will collect data across a wider spectral range than MES-SENGER's MASCS, and will concentrate on the exosphere rather than the surface. It has an extreme UV (EUV) device to detect emission lines at 25–155 nm and a far UV (FUV) device to cover 145–315 nm. Both will have a spectral resolution of better than 1 nm. A near UV (NUV) detector will monitor at 404 and 422 nm in order to observe Ca and K.

PHEBUS will aim to determine the composition and vertical structure of the exosphere, between the surface and 1,500 km with a vertical resolution of about 20 km. It will characterise exospheric dynamics, in particular day-night circulation, transport between active and inactive regions, and interchange of species with the exosphere. PHEBUS will be able to scan only within MPO's orbital plane. This will enable all latitudes to be sampled, whereas longitude will migrate with the orbit.

There will be three modes of operation. 'Grazing sounding mode' at twilight will point from the dark side towards the limb, using the obscured Sun as a source of UV excitation and will be particularly useful for measuring the exosphere at low altitude. 'Vertical scanning mode' will also operate when the spacecraft is in shadow, and will scan up to about 1,000 km altitude. 'Along-orbit sounding mode' will look ahead or at a fixed angle below the direction of travel avoiding the surface of the planet.

Detectable species include the already-known atoms Na, K, Ca, Mg, O, H and He, and others such as Si, Fe, C, N, S, H₂O, H₂, OH, CO, Ar, Ne, He⁺, Na⁺, Mg⁺, S⁺ and C⁺. It will also be possible to search for reflection from the nightside surface, illuminated by the interplanetary hydrogen Lyman-alpha glow at 121.6 nm. This may, for example, reveal signatures of volatiles such as H₂O, SO₂, N₂ or CO₂ in polar craters.

3.4.3.9 Search for Exospheric Refilling and Emitted Natural Abundances, SERENA (MPO)

SERENA is an 8.8 kg suite of instruments (Table 3.2) that will measure neutral and ionized atoms in situ, thus complementing the global exospheric mapping of PHEBUS. The low energy neutral atoms detected by ELENA and STROFIO are expected to be chiefly those escaping from the planet's surface, whereas MIPA and PICAM will be sensitive to species that have dwelt longer in the exosphere or that are arriving in the solar wind.

The ELENA sensor is nadir-pointing and samples a wide field of view orthogonal to MPO's orbital plane, whereas STROFIO provides no directional information. PICAM will sample charged particles arriving from the whole visible hemisphere of sky and will determine the three dimensional velocity distribution and mass spectrum for species as heavy as xenon (132 amu). MIPA is optimized to detect ions (up to 50 amu, but most importantly protons) precipitated into Mercury's exosphere from the solar wind from a variety of directions.

The goals of the SERENA suite include: identifying and localizing the sources and sink processes of neutral and charged particles, and determining the efficiencies with which they operate; determining the composition, energy spectrum and altitude profiles for neutral and charged particles of exospheric species; and elucidating the dynamics of the neutral and ionized exosphere, including exchange with the magnetosphere.

3.4.3.10 Spectrometer and Imagers for MPO BepiColombo Integrated Observatory System, SIMBIO-SYS

SIMBIO-SYS is a suite of three devices for imaging and spectroscopic imaging of the surface (Fig. 3.11). At nearly 14 kg and drawing at least 25 W, after BELA it is

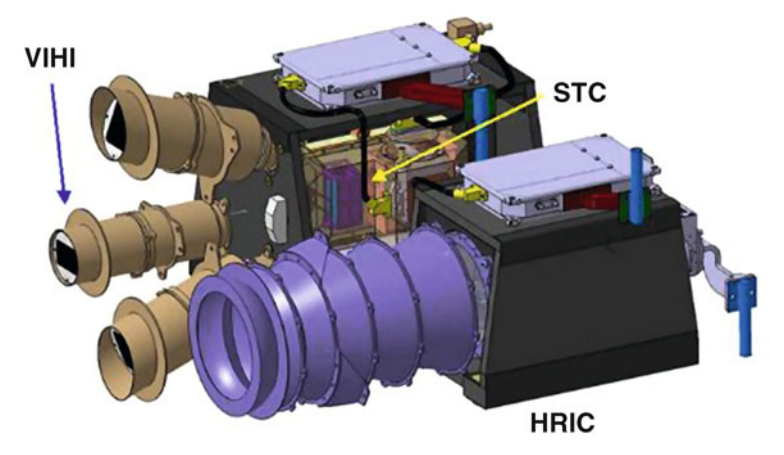


Fig. 3.11 Overall view of SIMBIO-SYS. HRIC and VIHI are nadir-viewing, whereas the two STC cameras point forward and aft to achieve stereo (ESA)

the second largest of MPO's experiments. Its Stereo Channel (STC) has the goal of imaging the whole planet at 50 m per pixel or better in panchromatic stereo (700 \pm 100 nm) and in four colour channels (420 \pm 10 nm, 550 \pm 10 nm, 700 \pm 10 nm, 920 \pm 10 nm). Its High Spatial Resolution Imaging Channel (HRIC) will achieve 5 m per pixel mapping when at 400 km altitude in three colours and a broad panchromatic band (550 \pm 20, 750 \pm 20, 880 \pm 20, and 650 \pm 230 nm). Its Visible and near-Infrared Hyperspectral Imaging channel (VIHI) will image in 256 narrow channels across the 400–2,000 nm range with a pixel size of 100 m at periapsis and 375 m at apoapsis.

SIMBIO-SYS will thus provide higher resolution imaging in colour and stereo than MESSENGER's MDIS for most of the planet, especially in the southern hemisphere thanks to BepiColombo's near-equatorial periapsis. VIHI will provide spectral imaging at nearly as good spectral resolution as MESSENGER's non-imaging MASCS, missing some UV but gaining some near-infrared, and with pixels more than ten times narrower.

3.4.3.11 Solar Intensity X-ray and Particle Spectrometer, SIXS (MPO)

Because the intensity and energy spectrum of X-rays and high-energy solar wind particles are highly variable, both of these must be measured at all times so that the fluorescent X-ray line intensities measured by MIXS can be turned into estimates of elemental abundance. This is the same logic as behind MESSENGER's solar X-ray monitor, but SIXS-X consists of three identical detectors (sensitive to 1–20 keV with 300 eV resolution) each with a 100° field-of-view and mounted so that at least one can see the Sun for all operational MPO orientations.

SIXS-P is a scintillation detector viewing about ¼ of the whole sky, providing low angular resolution, low energy resolution mapping of charged particles. Electrons will be detected across an energy range of 0.1–3 MeV and protons across a range of 1–30 MeV. As well as being required for calibration of any particle-induced X-ray fluorescence detected on Mercury's night-side, these data will also contribute to exospheric and magnetospheric studies by SERENA, PHEBUS and some MMO instruments.

If you have become lost in the names of MPO instruments, many of which are rather laboriously contrived acronyms to make words of dubious pronunciation and meaning, console yourself that MIXS and SIXS make sense, at least if you are Finnish. The SIXS team is Finnish, whereas the MIXS team is led by a British group. As explained, MIXS needs SIXS in order for its data to be calibrated, and the MIXS and SIXS teams worked together closely during design and construction. If you say 'mixs?' it sounds like a Finnish dialect expression 'miks?' meaning 'why?', to which the dialect reply meaning 'that's why!' is 'siks!'.

3.4.3.12 Mercury Magnetospheric Orbiter Magnetometer, MMO/MGF (MERMAG)

This is MMO's half of the MERMAG experiment consortium. It consists of an outboard triaxial fluxgate magnetometer at the tip of a 4.4 m-long boom and a second one situated 1.6 m inboard of this. Tandem operation enables compensation for the magnetic field induced by electric currents within the spacecraft. Field strength will be determined to a precision of 3.8 picoteslas.

MMO/MGF will map Mercury's magnetic field in its own right, but also, in combination with MPO/MAG, will be able to distinguish between temporal fluctuations and spatial variations. A notable topic will be 'magnetic reconnection' involving the interaction of the solar wind both upstream and downstream of Mercury. When on Mercury's dayside, MMO will spend considerable time beyond the magnetopause, where it will be able to study the role of magnetic field fluctuations in heating and accelerating the solar wind. As well as studying Mercury's magnetospheric bow shock each time it crosses the magnetopause, it will also be well-placed to study interplanetary shocks initiated by major solar flares.

3.4.3.13 Mercury Plasma Particle Experiment, MPPE (MMO)

MPPE is complex package that is MMO's answer to MESSENGER's EPPS. It will be sensitive to ions from 5 eV up to 1.5 MeV and to electrons from 5 eV to 700 keV, extending to lower energies than sensed by EPPS. It will provide the first simultaneous three-dimensional measurements of the flux of low to high energy ions and electrons around Mercury, and will also measure neutral species for which MESSENGER carried no instrument.

In total, MPPE will cast light on: magnetospheric structure, dynamics and physical processes (including the solar wind contribution to magnetospheric plasmas), and the interactions between surface, exosphere and magnetosphere. It will also be used study the physics of collisionless shocks in the inner heliosphere, of interest because the local interplanetary magnetic field is about five times greater than near Earth and the solar wind density about 32 times greater.

3.4.3.14 Mercury Plasma Wave Instrument, PWI (MMO)

PWI is an innovative package, collecting data of a type not sought by Mariner-10 or MESSENGER. It will measure electric fields, plasma waves and radio waves, to provide information about plasma transport and acceleration in Mercury's magnetosphere. The wires visible in Fig. 3.10 are dipole antennas to measure the electric field, and will be the first wire antennas to be deployed in orbit about another planet.

PWI also includes boom-mounted magnetic field sensors to measure the strength of alternating magnetic fields (rather than the total field intensity recorded by MERMAG). In total, PWI will measure intensity, waveforms and the frequency spectra of the electric field ranging from the direct current to 10 MHz alternating current, and of the magnetic field from 0.1 Hz to 640 kHz.

3.4.3.15 Mercury Sodium Atmospheric Spectral Imager, MSASI (MMO)

MSASI will map changes in density and velocity distribution of exospheric sodium, in order to understand the dominant release mechanism from the surface, the nature and details of the dawn-dusk asymmetry, and processes in Mercury's sodium tail.

It is an instrument specialised for mapping the distribution of exospheric sodium, by concentrating on sodium D2 emission at 589 nm. It will be able to obtain images of the whole disc as often as every 85 s during a 3 h 25 m interval between periapsis and apoapsis. Spectral resolution will be 0.007 nm, achieved by a 'Fabry-Perot etalon', which measures wavelengths by means of interference effects produced by multiple reflections between two highly reflective parallel surfaces. This is an approach not previously attempted on planetary missions.

MSASI's very high spectral dispersion (spreading out the wavelengths of light) will enable sodium emission to be distinguished even against the background of the sunlit surface (which MESSENGER's MDIS was unable to achieve). Such data added to the vertical distribution profiles of sodium and other species to be obtained by MPO's PHEBUS should ensure that BepiColombo gives a much more detailed insight than MESSENGER into Mercury's exosphere.

3.4.3.16 Mercury Dust Monitor, MDM (MMO)

MDM will directly measure the dust environment around Mercury, which neither Mariner 10 nor MESSENGER attempted. Four ceramic piezoelectric sensors will be mounted on one MMO's side plates. The strength of each signal will give the momentum imparted by each impact, and the approximate direction can be inferred from knowledge of the facing direction of the sensor as MMO rotates.

The results will show the flux and momentum distribution of interplanetary dust, casting light both on the effectiveness of dust (micrometeorite) impacts on Mercury as a source of exospheric species and on the processes of dust particle generation (release from comets and asteroids) and acceleration (the Poynting-Robertson effect, which causes interplanetary dust grains to spiral slowly towards the Sun).

3.5 Conclusions

MESSENGER has taught us a lot about Mercury, and also raised many new questions for BepiColombo and other projects to answer. Placing a more diverse suite of better instruments into orbit than carried by Mariner 10 during its flybys is what is largely responsible for our current state of knowledge about Mercury. The next chapters summarise what we know about Mercury after nearly 4 years of MESSENGER orbital science.

Chapter 4 Mercury's Surface as Seen by MESSENGER

4.1 Introduction

As the first flyby on 14 January 2008 drew near, it was with mounting anticipation that I, and doubtless many others, repeatedly refreshed my browser for updates to the MESSENGER website. The first image to appear, captioned 'MESSENGER Readies for Its Encounter with Mercury' was acquired by the NAC on 9 January and showed merely a distant crescent. Subsequent daily images showed a slightly bigger view of the same thing, but little detail. The most interesting thing about them was how successive captions used different words to say the same thing: 'MESSENGER Closes in on Mercury', 'MESSENGER Nears Mercury' and 'MESSENGER Has Mercury in Its Sights'. However the 5th image, acquired 36 h before closest approach 'Countdown to MESSENGER's Closest Approach to Mercury' revealed recognisable features at last (Fig. 4.1).

The inbound images showed part of the globe already seen by Mariner 10, though under different illumination conditions (Fig. 2.4). However a large part of the sunlit area in the outbound view was previously unimaged terrain, including for example the whole of the Caloris basin. Figure 4.2 illustrates the quality of the flyby views, and includes an example of one of the highest-resolution NAC flyby images.

It is not my purpose to recount the incremental unveiling of Mercury by the flybys, or during the first months of orbital science as the full payload of instruments commenced routine operation. Instead, I attempt to summarise the overall picture in the state to which it had evolved by the final year of MESSENGER operations. In this chapter I describe Mercury's surface: its physiography, its composition, the tectonic and volcanic processes that have left their marks, and the actions of volatile substances. Finally, I draw attention to some features that have so far defied explanation. The next two chapters deal with the interior, and then with the magnetosphere and exosphere. You will see that many of the findings were unexpected – but then that's one of the reasons why space exploration is so fascinating.

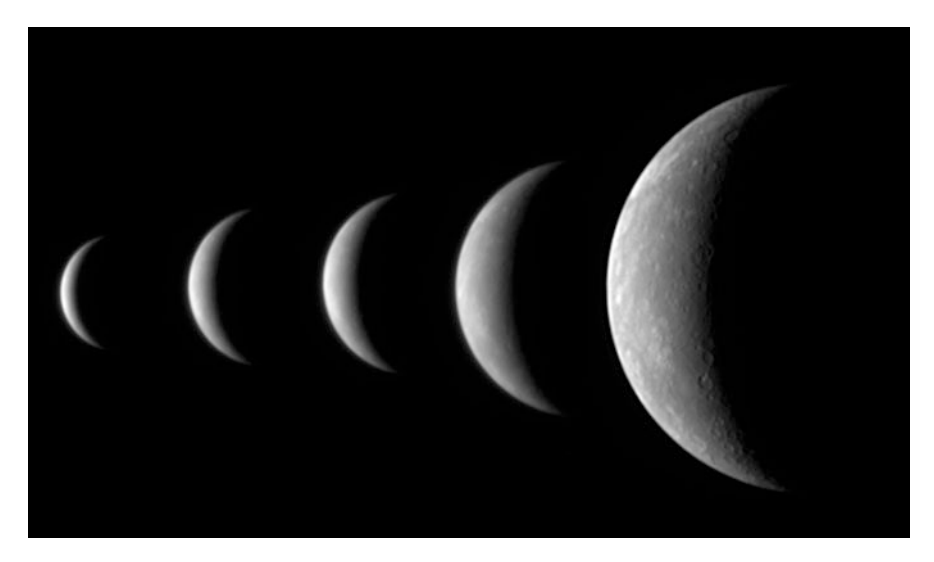


Fig. 4.1 A sequence of five NAC images acquired during the inbound leg of MESSENGER's first flyby in January 2008. Vivaldi crater (Fig. 2.4) can be discerned just north of the equator near the terminator in the fifth view, acquired from a range of 760,000 km. Closer images revealed much more detail (NASA/Johns Hopkins University Applied Physics Laboratory/Carnegie Institution of Washington)

4.2 Craters and Terrain Types

4.2.1 Crater Characteristics

Mercury's general timescale and stratigraphy deduced from Mariner 10 data (as summarised in Chap. 2) remains broadly valid, including the observation that Mercury lacks any extensive terrain so densely-cratered as the lunar highlands. In more detail, it is now clear that even the most densely-cratered regions of Mercury are deficient in craters of less than 100 km diameter compared to lunar highlands (Fig. 4.3). For craters of about 100–500 km the density of craters on the two bodies is similar, but for large basin sizes of >500 km the spatial density on Mercury once again falls behind that on the Moon.

The simplest and most plausible explanation is that Mercury experienced globewide resurfacing that began just after the onset of the Late Heavy Bombardment about 4.0–4.1 Ga ago and continued until its tail-end 300–400 million years later (some smaller areas were resurfaced more recently). During this time, most pre-existing <100 km craters were buried (by volcanic lavas, as argued below). However the 100–500 km craters were too big to be hidden in this way which is why the crater-density in this size range is similar on Mercury and the Moon. Mercury's relative deficiency in >500 km basins is probably a consequence of other differences between the two bodies, controlled by surface gravity and the thickness and strength of the early lithosphere. For example, local conditions on

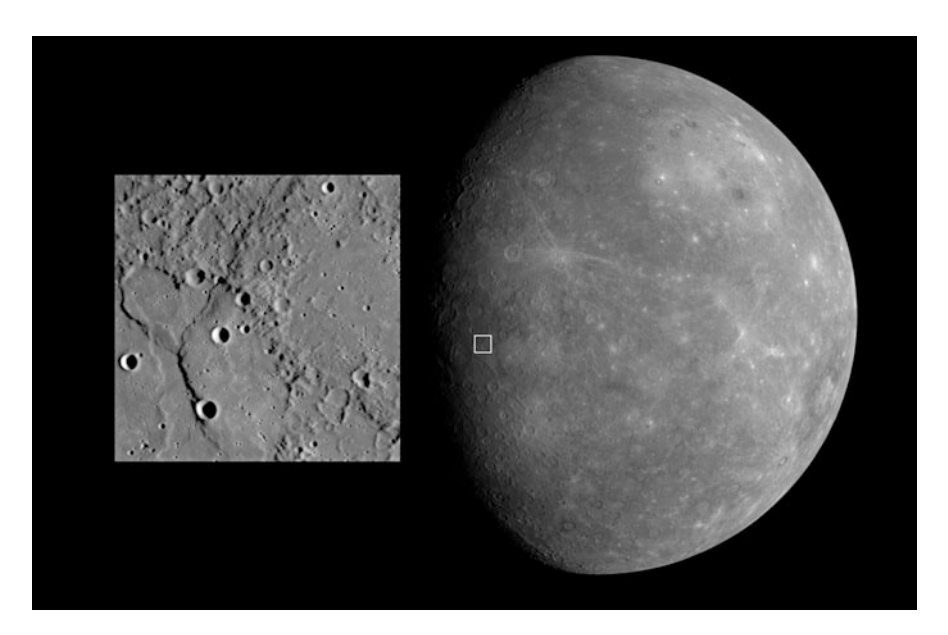


Fig. 4.2 Global view: a MESSENGER WAC image acquired 80 min after closest approach on flyby 1, from a range of 27,000 km. The Caloris basin is the large area of moderately high albedo in the upper right, largely surrounded by a belt of lower-albedo plains. The *box* indicates the area covered by the view on the left, which is a NAC image acquired 18 min after closest approach from a range of 5,000 km. The area shown is about 200 km across, and features as small as 400 m in size can be made out. It shows lobate scarps cutting lava-flooded impact basins. Note one scarp overprinting an older scarp within the triangle defined by the three most prominent shadow-filled impact craters (NASA/Johns Hopkins University Applied Physics Laboratory/Carnegie Institution of Washington)

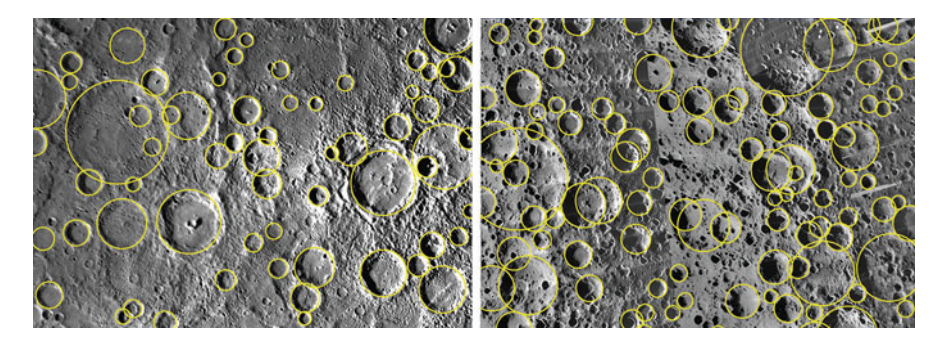


Fig. 4.3 700 km-wide views of the most densely cratered terrain on Mercury (*left*) and the Moon (*right*). The rims of craters >20 km diameter are circled. On Mercury, crater density is lower and smooth terrain between craters is more evident. These are symptoms of emplacement of intercrater plains on Mercury, most likely as lava flows (Modified from Fassett et al. *Geophysical Research Letters*, v38, L10202, 2011)

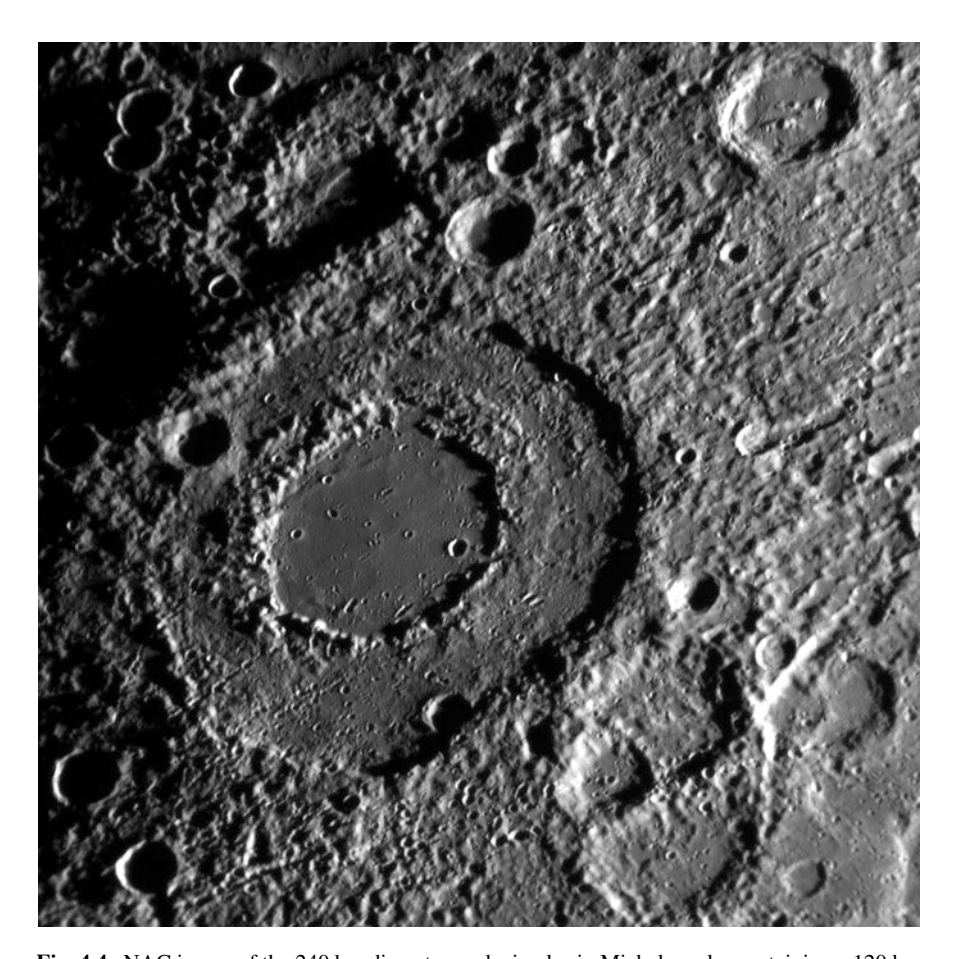


Fig. 4.4 NAC image of the 240 km diameter peak-ring basin Michelangelo, containing a 120 km peak ring. The smooth floor within the peak-ring is probably impact melt. Chains of mostly km-size secondary craters running diagonally across the area were probably formed by ejecta from Hawthorne, a younger 127 km peak-ring basin whose centre is 330 km to the southwest of Michelangelo's centre (NASA/Johns Hopkins University Applied Physics Laboratory/Carnegie Institution of Washington)

Mercury could have caused basins to form with fewer concentric rings, and allowed basin topography to become more quickly subdued.

Another notable contrast between lunar and mercurian cratering is that peak-ring basins (like Vivaldi, Fig. 2.4, and Michelangelo, Fig. 4.4) are five times more common on Mercury. This is a consequence of the minimum size at which peakring basins form on Mercury being only 84 km, whereas they do not occur on the Moon at less than about 320 km. The main controlling factor appears to be impact speed (twice as fast at Mercury), and the likely explanation is that this encourages formation of impact melt within a central cavity in the transient crater, which collapses to form a peak-ring before the crater stabilizes.



Fig. 4.5 MESSENGER exaggerated WAC colour view, centred near 180° E. The Caloris basin is the orange area of 'high-reflectance red plains' in the upper left, and can be seen to be bordered by 'low reflectance blue plains' to the south and west. At a similar latitude to the Caloris basin in the upper right is Sobkou Planitia, which is similarly filled by 'high-reflectance red plains' and partially surrounded by 'low reflectance blue plains'. Below right of centre, the smaller basin Tolstoj has a similar plains fill but is made prominent by a ring of much darker blue 'low-reflectance material'. Crater rays and the ejecta blankets of the youngest craters are bright blue (NASA/Johns Hopkins University Applied Physics Laboratory/Carnegie Institution of Washington)

4.2.2 Global Overview in Colour

As a starting point for summarizing the complete globe of Mercury as revealed by MESSENGER, Figs. 4.5, 4.6, 4.7 and 4.8 show exaggerated colour renderings of a global WAC colour mosaic projected to show views at 90° intervals around the



Fig. 4.6 MESSENGER exaggerated WAC colour view, centred near 270° E. Sobkou Planitia is now in the upper left (NASA/Johns Hopkins University Applied Physics Laboratory/Carnegie Institution of Washington)

equator. The colours are rendered according to what became a standard product among the MESSENGER team, and are derived in part from a principal components transformation of the nine narrow-band WAC channels (Box 4.1).



Fig. 4.7 MESSENGER exaggerated WAC colour, centred near 000° E. The prominent rayed crater in the south centre, situated on 'low-reflectance blue plains', is Debussy, and the one in the high north, on 'high-reflectance red plains', is Hokusai. To the NNE of Debussy, the 170 km crater Derain is prominent thanks to the presence of dark blue 'low-reflectance material' on much of the outer part of its floor, spectrally similar to that which surrounds Tolstoj in Fig. 4.5 (NASA/Johns Hopkins University Applied Physics Laboratory/Carnegie Institution of Washington)

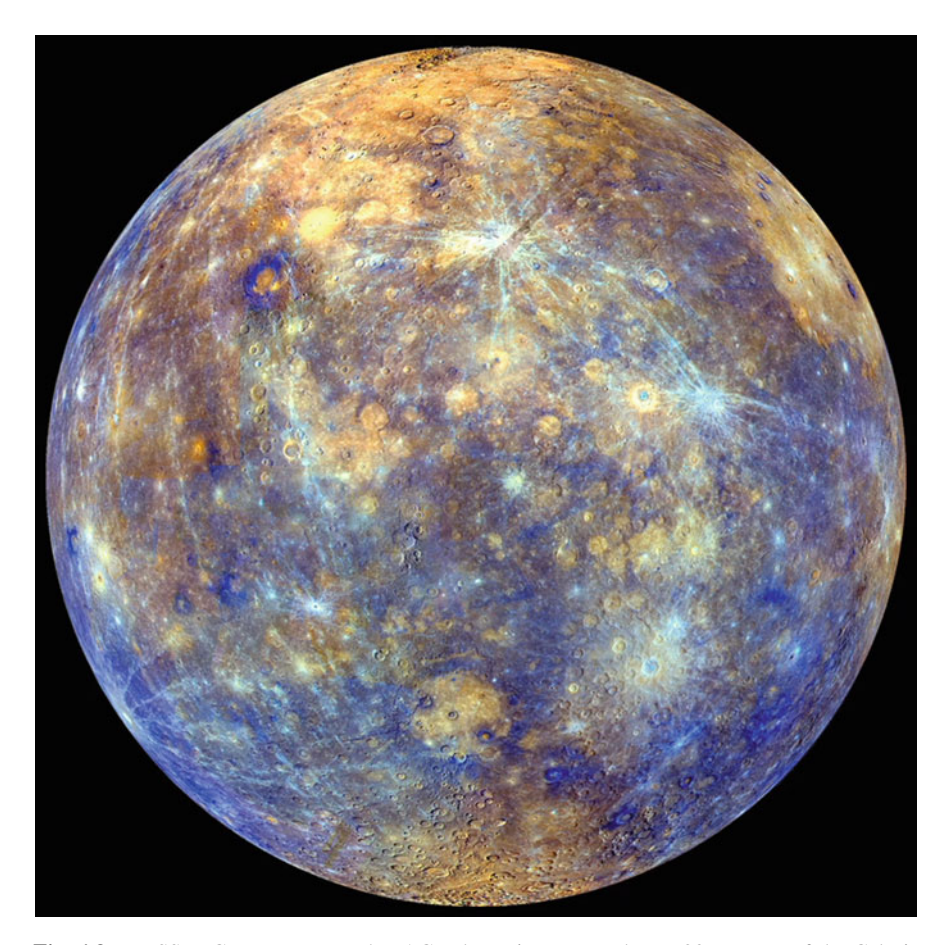


Fig. 4.8 MESSENGER exaggerated WAC colour view, centred near 90° E. Part of the Caloris basin is visible on the limb at the upper right. In the south centre can be seen Rembrandt basin, whose floor is composed of 'high-reflectance red plains' similar to those in Caloris and Sobkou (Fig. 4.5). 'High-reflectance red plains' in the far north, also visible at high northern latitudes in Figs. 4.5, 4.6 and 4.7, are best seen in this view (NASA/Johns Hopkins University Applied Physics Laboratory/Carnegie Institution of Washington)

Box 4.1 Principal Components Transformation and the Standard MESSENGER Exaggerated Colour Rendering

Our eyes can distinguish between mixtures of only three colours of light in a displayed image (mixing red, green and blue in different proportions and brightnesses). Principal components transformation provides way to maximise the displayable information in a colour image for which *more* than three channels of data were collected, by concentrating information into specific

(continued)

Box 4.1 (continued)

display channels. In the standard MESSENGER exaggerated colour rendering, red, green and blue display channels correspond respectively to: the negative of the second principal component of all the WAC channels (this corresponds to the largest spectral differences), the first principal component of all the WAC channels (this correlates very strongly with brightness), and the 430 nm WAC channel divided by the 1,000 nm WAC channel (essentially a ratio between blue and near-infrared).

This may sound confusing, and it is not intuitively obvious how to interpret the resulting colours. However, the beauty of this product in the case of Mercury is that usually the colour relationships look pretty much the same as if you had taken a natural colour image and exaggerated the colour saturation, with the additional advantage that data from WAC's full spectral range are used, capturing differences that could have been missed in an image based on only three channels. This means that surfaces that look red or blue truly are redder (having a steeper than average upward spectral slope from short to long wavelength) or bluer (having a less-steep than average upward spectral slope from short to long wavelength), respectively, than the average Mercury surface (which, recall, judged against a neutral grey standard would be slightly reddish). Thus, colour descriptions given below generally apply equally well to appearance on these exaggerated colour renderings or to subtle differences from the mean surface colour that would be slightly discernable on a simple three-channel colour composite.

An important basic inference that can be drawn from these global colour views is that Mercury *does* have spectrally diverse terrains, and that recognizable units recur all across the globe. This was an important demonstration by MESSENGER, given the poor and geographically restricted colour information obtained by Mariner 10. I will delay discussion of the chemical and mineralogic composition of the units until a later section, and concentrate for now on qualitative descriptions.

On the basis of morphology and colour characteristics, the MESSENGER team defined five major units on Mercury, as follows:

- High-reflectance red plains: the most conspicuous smooth plains on Mercury, with albedo up to 20 % higher than the global mean and a red colour. They typically have sharp boundaries with surrounding terrain, which they generally overlie.
- Low-reflectance blue plains: similar morphology to high-reflectance red plains, but blue and with albedo about 15 % below the global mean.
- Intermediate plains: similar morphology to high-reflectance red plains, but colour and albedo both similar to the global mean.
- Intermediate terrain: higher crater density than the three smooth plains units, and usually corresponding to intercrater plains. Colour and albedo both similar to the global mean, but more variation than within the intermediate plains.

 Low reflectance material: albedo as much as 30 % below the global mean, looking dark blue in exaggerated colour. Can occur across broad regions or be localised in ejecta or uplifted centres of some craters. Lacks distinct surface morphology. Most would be classified as intermediate terrain if not for its colour.

The southern two-thirds of the inset in Fig. 4.2 is plains (in fact intermediate plains), whereas the northern third is intermediate terrain.

Three other spectrally distinct units that occur in many places across the globe, but in individually much smaller patches than the major units, are worth pointing out at this stage:

- Fresh impact ejecta: rays and proximal ejecta blankets associated with the freshest (Kuiperian age) impact craters having high albedo and somewhat blue colour. It doesn't seem to matter to which of the five main spectral types the substrate belongs, the fresh ejecta looks similar in each case until space weathering has blended it back into the background.
- Red spots: patches typically up to a 100 km or so across with diffuse outer edges and (on exaggerated colour views) orange colour. The largest example is in the upper left of Fig. 4.8 (looking yellow rather than orange), but there is a more typical orange example further south close to the equator. Similar spots can be seen on Figs. 4.5, 4.6 and 4.7 too. These are interpreted as volcanic ejecta dispersed from explosive vents (which can usually be discerned in the centre of each spot using high resolution NAC images).
- Bright crater floor deposits. The bluest material on Mercury, with a high albedo. Typically as patches on the floors of a certain craters (revealed at high resolution to be associated with a landform described as 'hollows', which I will illustrate in detail later).

Fresh impact ejecta and red spots can be made out on the global views (especially Fig. 4.5), but bright crater floor deposits are not readily apparent at this scale. However clear examples of all three small-area units show up in the exaggerated colour view from flyby 1 shown in Fig. 4.9.

Smooth plains cover about 27 % of Mercury's surface, excluding isolated patches within <100 km craters that are likely to represent impact melt. Because of polar foreshortening, the equatorial global views in Figs. 4.5, 4.6, 4.7 and 4.8 obscure a rather notable north–south asymmetry, which is that high reflectance red plains are extensive in Mercury's far north, whereas smooth plains of any variety are scarce south of about 40° S. This is clarified by the map projection used in Fig. 4.10.

The northern high reflectance red plains cover a contiguous area occupying about 6 % of Mercury, constituting a more extensive Borealis Planitia than was revealed by Mariner 10's incomplete mapping. Figure 4.11 shows part of the edge of the northern plains in more detail. It can be deduced from this that the plains overlie bluer and more densely cratered 'intermediate terrain'. Craters that had already been formed on the intermediate terrain can be seen in various states of

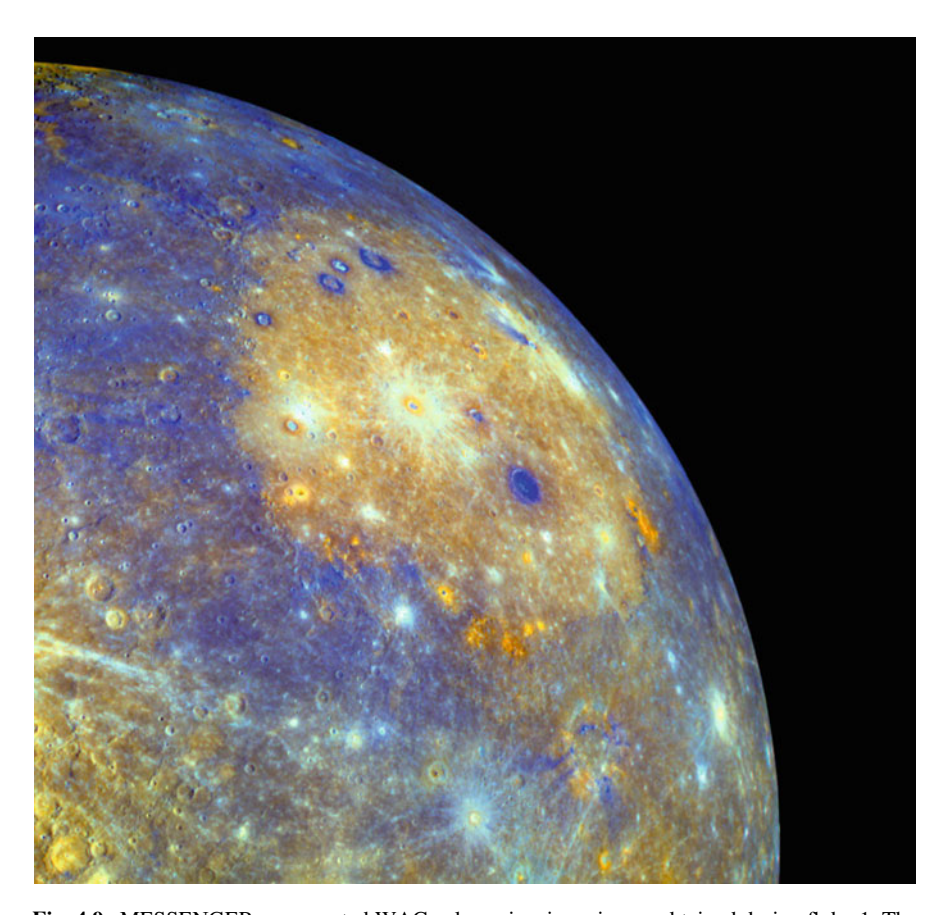


Fig. 4.9 MESSENGER exaggerated WAC colour view in an image obtained during flyby 1. The Caloris basin is prominent in the upper right thanks to its fill of high reflectance red plains. Note several 'red spots' near its southern rim, and the cyan colour inside two craters in the north and west of the basin that represents bright crater floor deposits. The dark blue outlines of the craters either side of the northern bright crater floor deposit occurrence are low reflectance material uplifted into crater rims. Bluish-white fresh impact ejecta can be seen around young craters both within and outside of the Caloris basin (NASA/Johns Hopkins University Applied Physics Laboratory/Carnegie Institution of Washington)

flooding by the plains lavas. In particular, about one third of the southern rim of the crater Monteverdi (and the rough ejecta outside it) survives beyond the extent of the plains, but the whole of its floor has been infilled by lava. The trace of the northern part of its rim can be made out, but it is largely buried. It is visible mainly because shrinkage and subsidence of the emplaced lava (through degassing and thermal contraction) was less over the shallowly-buried rim than over the more deeply-buried crater floor or the ground beyond the crater.

There are several prominent craters smaller than Monteverdi that were formed on the plains after they had been emplaced, but if you look carefully you can also

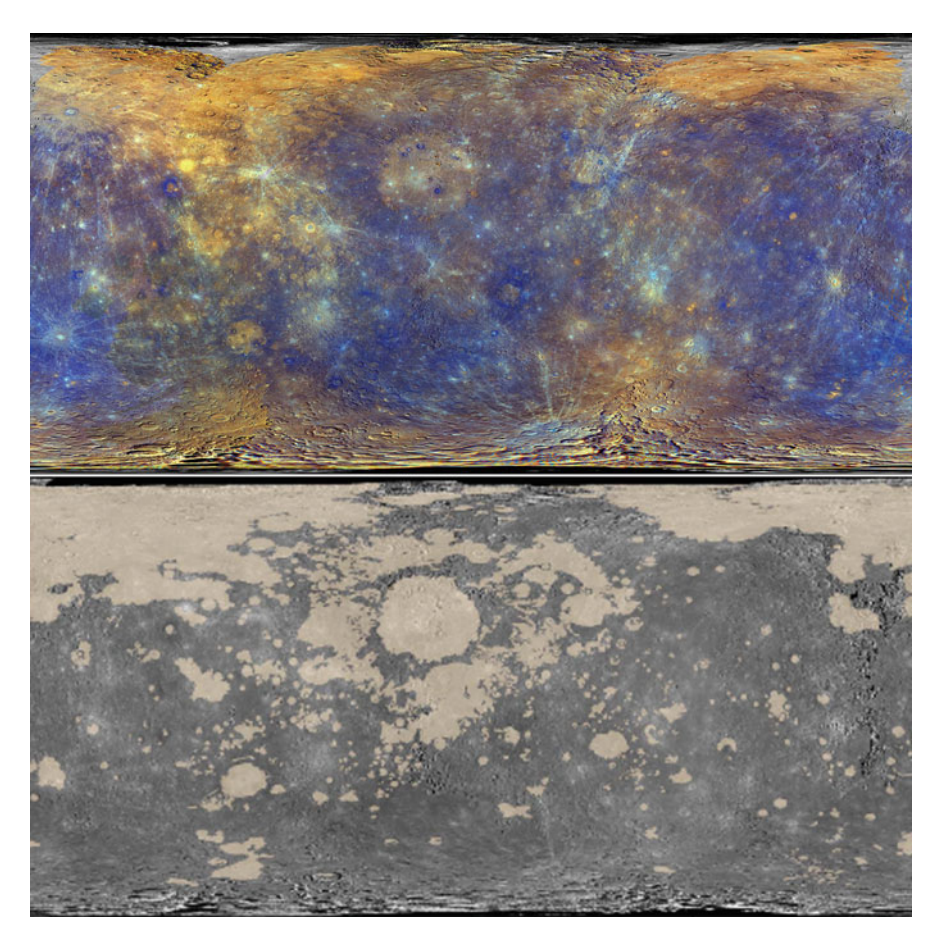


Fig. 4.10 A simple cylindrical map projection of Mercury, centred at 180° E. *Top*: standard exaggerated WAC colour view (NASA/Johns Hopkins University Applied Physics Laboratory/ Carnegie Institution of Washington). *Bottom*: the extent of smooth plains (as mapped by Denevi et al. *Journal of Geophysical Research*, v.188, 891–907, 2013)

make out the buried rims of several craters that, unlike Monteverdi, were completely flooded. These are referred to as 'ghost craters', and are a class of feature already well-known on the Moon and Mars.

Ghost craters are easier to see in Fig. 4.12, which is part of a NAC mosaic of a 320 km basin named Goethe, whose southern half can be seen in the upper right of Fig. 4.11. Apart from the widespread evidence for flooding during plains formation, other evidence that the plains were emplaced as lava is provided by wrinkle ridges. As their name implies they are wrinkle-like features, and are at least partly a consequence of surface subsidence as the lava cooled and degassed. A nice example occurs in the southwest of the inset to Fig. 4.2.

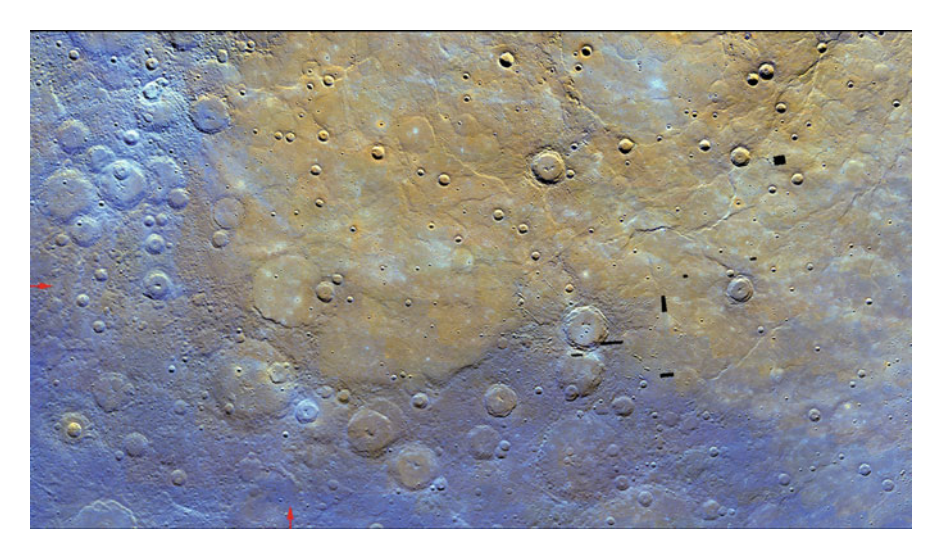


Fig. 4.11 Standard exaggerated WAC colour view of part of the margin of the northern plains, centred at 73° N, 300° E. The area shown is about 1,700 km across, and is shown as a polar stereographic projection. The northern plains are 'high reflectance red plains', and overlie 'intermediate terrain' which is exposed at the surface in the east and south of this view. *Arrows* at left and bottom point towards the partly-flooded 134 km crater Monteverdi. This is a mosaic of several WAC images (with a few data gaps in the east) (NASA/Johns Hopkins University Applied Physics Laboratory/Carnegie Institution of Washington)

Smooth plains occur both within basins and beyond basins, as exemplified by the northern plains and other examples that will crop up later. The intercrater plains are less obviously volcanic but wrinkle ridges can sometimes be made out, and ghost craters may be abundant, as in the example shown in Fig. 4.13 where, in addition to ghost craters some other older craters in the 50–70 km size range appear to have been externally flooded nearly to the top of their rims but without the flood material having found its way inside them.

4.2.3 Layer Upon Layer

While Mercury's crust assuredly does *not* consist of discrete layers of global extent, we can see units that extend for hundreds of kilometres at the surface, and infer units of similar extent below them. Figure 4.14 shows an example. The smooth dark orange plains unit in most of the central part of this area occupies an unnamed 390 km diameter degraded basin and the floor of the 120 km crater Rudaki to its east, and has been known as the Rudaki plains since the time of Mariner 10. This unit is an occurrence of intermediate plains, and is the youngest major unit in this area.

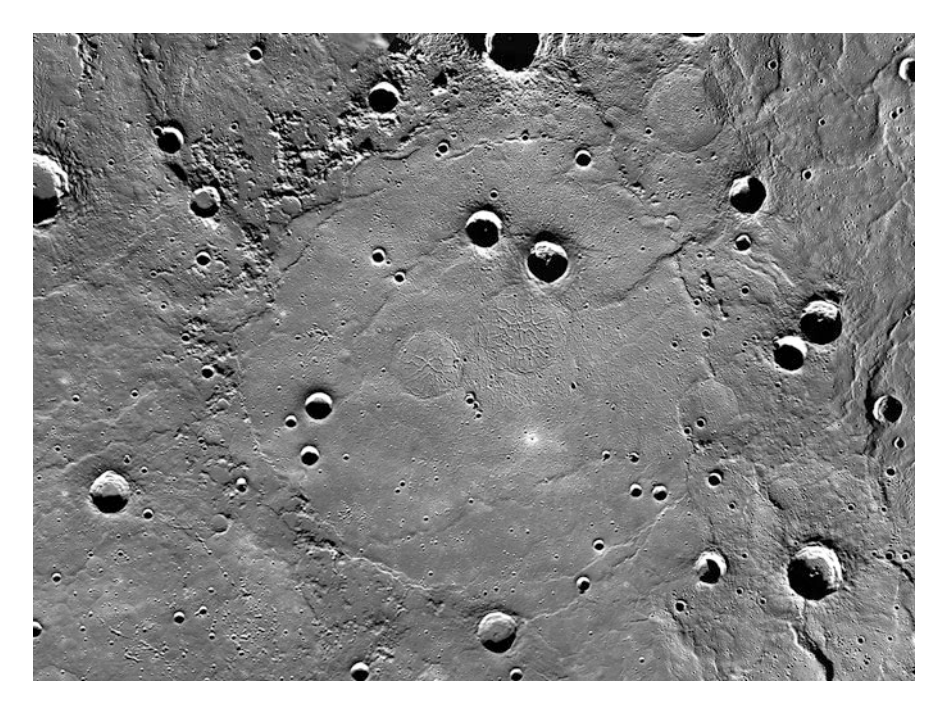


Fig. 4.12 MDIS orbital NAC mosaic including the 320 km Goethe basin. Two ghost craters are visible near the centre, about 40 and 50 km across. The area is 580 km wide, centred at 54° E, 81° N and is shown on a Transverse Mercator projection. (NASA/Johns Hopkins University Applied Physics Laboratory/Carnegie Institution of Washington)

The walls and proximal ejecta of Calvino expose material that is spectrally indistinguishable from high-reflectance red plains, and it can be inferred that high-reflectance red plains underlie the intermediate plains here, and probably beyond the basin too. An even deeper unit is brought to the surface in Calvino's central peak. Spectrally this is low-reflectance material, and similar-looking material also occupies the surface surrounding the degraded basin. This appears to be impact ejecta composed of low-reflectance material thrown out when the basin was excavated, so we can infer low-reflectance material at depth below the whole basin (and probably beyond). However the 16 km crater WSW of Calvino is not deep enough to exhume either low-reflectance material or high-reflectance red plains, allowing us to deduce that the intermediate plains fill of the basin must be least 1.2 km thick. In the extreme northeast of the image, intermediate plains flood across the lowest lying part of the basin's low-reflectance material ejecta, beyond which low-reflectance blue plains occur at the surface.

What I have just described is a purely local stratigraphy. Low-reflectance material (exposed by impact) and intermediate terrain (inferred from regional context) are deeper, and older. The three smooth plains units are younger, but the older-to-younger order exhibited here of low-reflectance blue plains first, then high-reflectance red plains, and then intermediate plains is not a general rule.

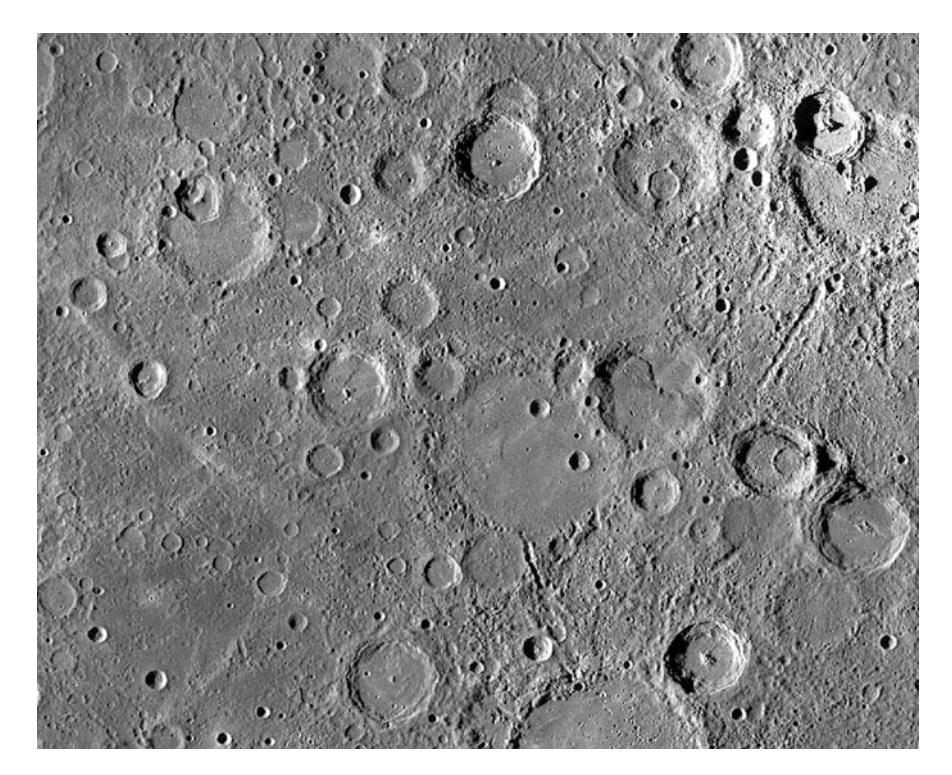


Fig. 4.13 NAC mosaic covering a 510 km-wide region of Mercury showing intermediate plains. The image is centred at 322° E, 18° S. The crater Kuiper is visible at the upper right. Other young craters and ghost craters up to about 70 km across occur throughout much of the rest of the image. This area is in the centre of the lower edge of the Mariner 10 mosaic in Fig. 2.8. (NASA/Johns Hopkins University Applied Physics Laboratory/Carnegie Institution of Washington)

Furthermore, in many cases (including the whole area of Fig. 4.14) low-reflectance material might never have constituted a surface layer. It could have originated as a layer formed at depth within the crust, for example injected as an igneous intrusion, being brought to the surface only locally by excavation (in ejecta) or uplift (in central peaks) or be impact melt generated in the basin-forming impact.

4.3 Surface Composition

Before discussing in more detail the MDIS imaging of some of Mercury's individual provinces and features, let's pause to take stock of the new insights into the elemental and mineralogical composition of Mercury's surface that MESSENGER revealed. Recall that previously there were no measurements at all of the abundance of individual elements, and that mineralogical information was ambiguous and derived mostly from ground-based observations. MESSENGER was equipped to measure various elements using its Gamma-Ray Spectrometer (GRS) and its

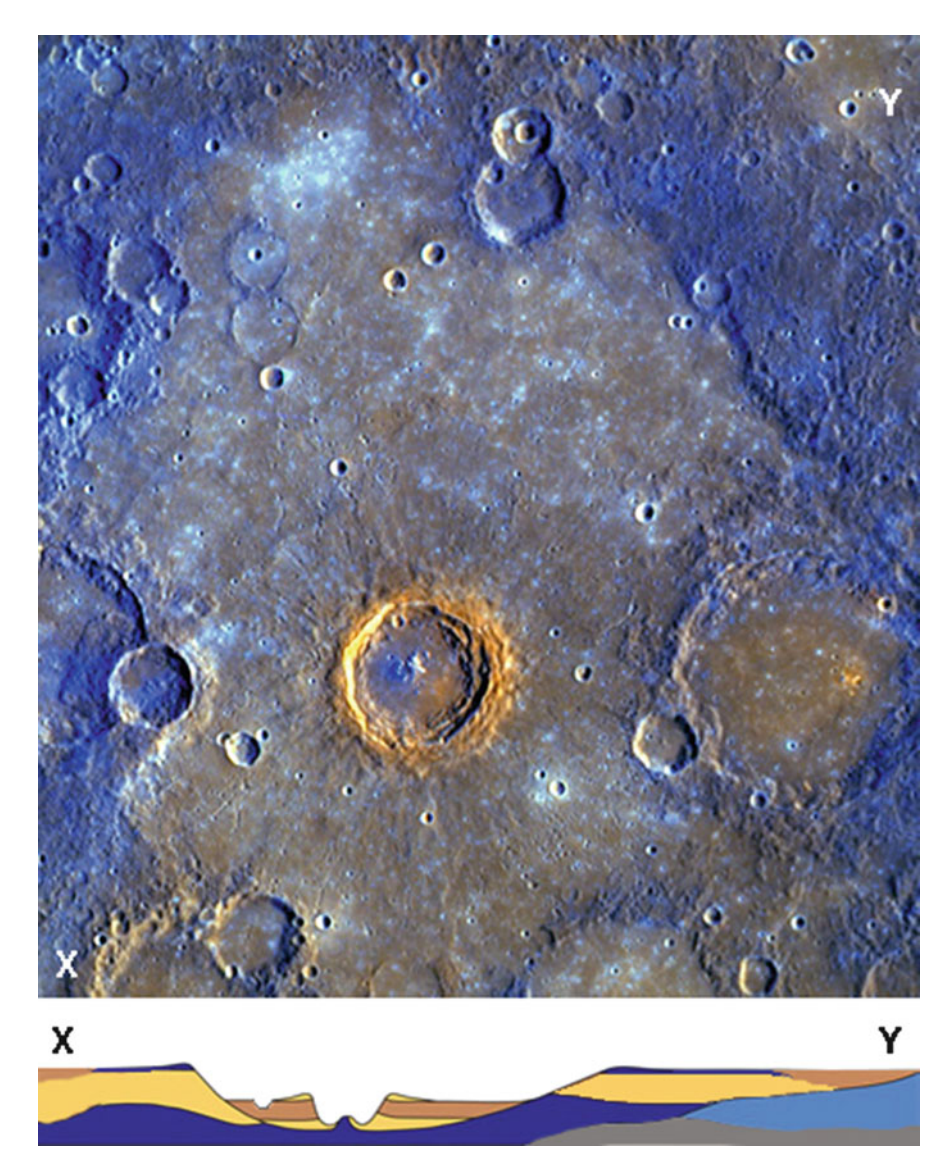


Fig. 4.14 *Top:* Standard exaggerated WAC colour view of a 350 km wide region including the 68 km cater Calvino (3.9° S, 304° E), made prominent by its rim of uplifted high reflectance red plains. *Bottom:* Schematic cross section along the line XY. Key: *yellow* high-reflectance red plains, *orange* intermediate terrain, *light blue* low reflectance blue plains, *dark blue* low-reflectance material, *grey* intermediate terrain (Reinterpreted from an earlier version by NASA/Johns Hopkins University Applied Physics Laboratory/Arizona State University/Carnegie Institution of Washington)

X-Ray Spectrometer (XRS), and to study mineralogy by means of visible and infrared spectroscopy, principally from the non-imaging spectrometer, MASCS, but also by means of MDIS colour images.

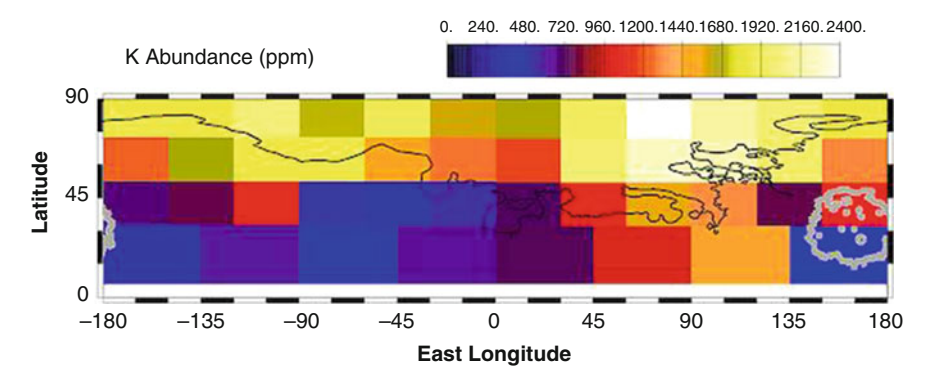


Fig. 4.15 Map of potassium abundance in Mercury's northern hemisphere from GRS data, in parts per million. For reference, the outlines of the northern plains and of the Caloris interior plains are shown as back and grey lines, respectively (Credit: P. N. Peplowski et al., *J. Geophysical Research*, v.117, E00L04, 2012)

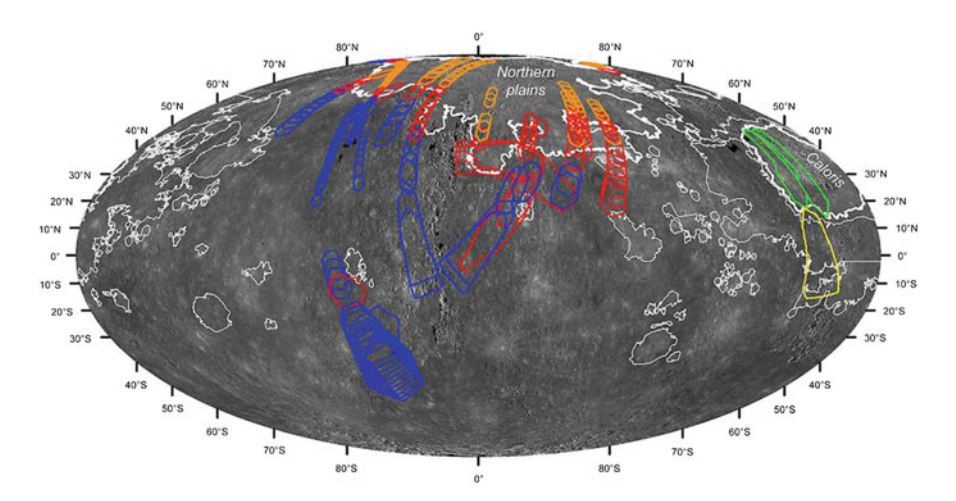


Fig. 4.16 Not data, but the footprints of orbital XRS data collected during 16 solar flares prior to 2012. White outlines show smooth plains. Footprints are coloured according to the terrain type within each: blue intermediate terrain, orange northern smooth plains, red mixture of the two previous types, green Caloris interior smooth plains, yellow circum-Caloris low-reflectance blue plains (Credit: S. Weider et al., J. Geophysical Research, v.117, E00L05, 2012)

4.3.1 Elemental Abundances

MESSENGER provided GRS data on elemental abundances in the northern hemisphere with a resolution of about 1,000 km (Fig. 4.15), whereas the XRS provided considerably finer resolution during solar flares when the incoming X-ray flux (and hence the fluoresced X-ray flux) was greatest (Fig. 4.16). In the case of elements that were detectable by both techniques (such as calcium, iron, aluminium and

sulfur), there was good agreement between the concentrations derived by each, which inspires confidence. Moreover, given that X-ray fluorescence occurs in only the top mm whereas detectable gamma-rays come from the top few tens of cm, it also indicates that Mercury's regolith is homogenized at least down to a depth of tens of centimetres.

XRS data fairly swiftly confirmed the paucity of iron (in any form) at Mercury's surface that had been expected from most ground-based observations. Solar flares allowed XRS detection of titanium too, with the result that Mercury's surface Ti:Si ratio is now known to be in the range 0.007–0.02 whereas Fe:Si is in the range 0.02–0.10. The upshot of this is that the maximum abundances of Ti and Fe are about 0.6 and 3 wt%, respectively, whereas their average abundances are about 0.3 wt % and 1.5 wt %. This pretty much rules out iron and titanium oxides from being the main causes of Mercury's low albedo.

For other major elements, the XRS showed that Mercury has a higher Mg:Si ratio but lower Al:Si and Ca:Si ratios than terrestrial (continental or oceanic) and lunar (highland or mare) crusts. Assuming a reasonable value of 24.6 wt% for the abundance of Si, the approximate average crustal abundances of the other major elements are Ca 5.9 wt%, Mg 12 wt%, Fe 1.9 wt%, Na 2.9 wt%, Al 7.1 wt%, Mn 0.1 wt %, Cr 0.1 wt %. There some notable regional variations for some elements, especially magnesium, that are discussed in the next section.

XRS data also unexpectedly showed sulfur present across the globe in concentrations in the range 2–5 wt%, which is an order of magnitude greater than the sulfur abundance in the bulk silicate fraction of the Earth, Moon, Mars and differentiated asteroids. If Mercury's high surface sulfur concentration is symptomatic of a high internal sulfur content too, this would be hard to reconcile with models previously invoked to explain Mercury's large core:silicate ratio, such as post-accretion vaporization or catastrophic impact, because these would be expected to have preferentially stripped away volatile elements such as sulfur. The form in which Mercury's sulfur occurs cannot be directly determined, but the XRS showed calcium and magnesium abundances rising and falling in step with sulfur, whereas there is no correlation between iron and sulfur abundance. The sulfur therefore does not reside in iron sulfide, but may be largely in (Ca,Mg)S, a mineral known as oldhamite.

GRS confirmed the sulfur abundance, and also showed a northern hemisphere K:Th ratio of $6,600 \pm 2,800$, which is similar to that of Mars but about ten times greater than for the volatile-depleted Moon. The significance of this ratio is that potassium is more volatile than thorium, so the ratio can be used a proxy for volatile retention during a planet's formation and evolution. GRS also detected two other volatile elements: Na (about 2.9 wt%, about the same as K) and Cl (about 0.14 wt%), the latter being about a hundred times its terrestrial abundance. Like the sulfur argument, the unexpectedly high abundance of these three volatile elements suggests that Mercury did not suffer the degree of volatile loss predicted by some models for its early evolution, unless it somehow formed with initially abnormally high concentrations of volatile elements. However, they are also enhanced towards

the north pole (presumably the south pole too, where there are no GRS data), so there may also be other processes at play, as discussed in Sect. 4.4.7.

If you have tried adding up the elemental percentages listed above you will find that they fall well short of a hundred. The remaining element is assumed to be oxygen, which is the species that forms the anions (negatively charged ions) to balance the positively charged metal ions (the cations) in silicate minerals. MES-SENGER'S XRS could not detect oxygen, so we will have to wait for data from BepiColombo's more capable X-ray experiment (MIXS) for confirmation. There could also be some carbon, in particular in the low reflectance material, where there were plans to search for it by looking for a related change in the ratio of thermal to fast neutrons in neutron spectrometer data collected during the low-altitude campaign near the end of the mission.

4.3.2 Minerals and Rock Types

MASCS data from the first flyby suggested that iron (as Fe²⁺) in Mercury's surface silicates is present at no more than 2–3 wt% thanks to a detectable absorption in the ultraviolet combined with lack of a corresponding absorption near 1,000 nm (this is consistent with the XRS data on total iron abundance). There are few other data relating directly to mineralogy of the surface, nor will there be until BepiColombo returns spectra further into the near-infrared from VIHI and especially in the thermal infrared from MERTIS.

The identity of the rock types present on Mercury therefore has to be inferred from elemental abundances. If we are willing make the assumption that the composition of the regolith at each point corresponds to a single igneous rock type that crystallized under equilibrium conditions, standard petrological models can be used to deduce the mixture of minerals that should be present. That's a big 'if', for several reasons. The shapes and sizes of the pixels, or fields-of-view, in which different elements are measured are usually different, and their centre-points do not necessarily coincide, so unless Mercury's crust is homogeneous on a scale of many tens of km, MESSENGER compositional remote sensing will never see a single rock type. The surface is regolith, rather than exposed bedrock, and so is inevitably a mixture, but the fact that there are spectrally distinct units in WAC images, and often with fairly sharp boundaries, indicates that compositional measurements obtained from areas that do not straddle such a boundary will reflect bedrock composition. This does not get round the problem that the bedrock could consist of two or more intimately-mixed rock types, or that some igneous rocks can consist of assemblages of minerals that formed under non-equilibrium conditions, or that rapidly quenched lavas can be largely glassy with few distinct crystals, or that space weathering could lead to regional changes in the extreme surface abundance of volatile elements.

We are thus left with defining rock types on the basis of the detectable, major, elements (this is a common practice for igneous rocks on Earth, where, however we

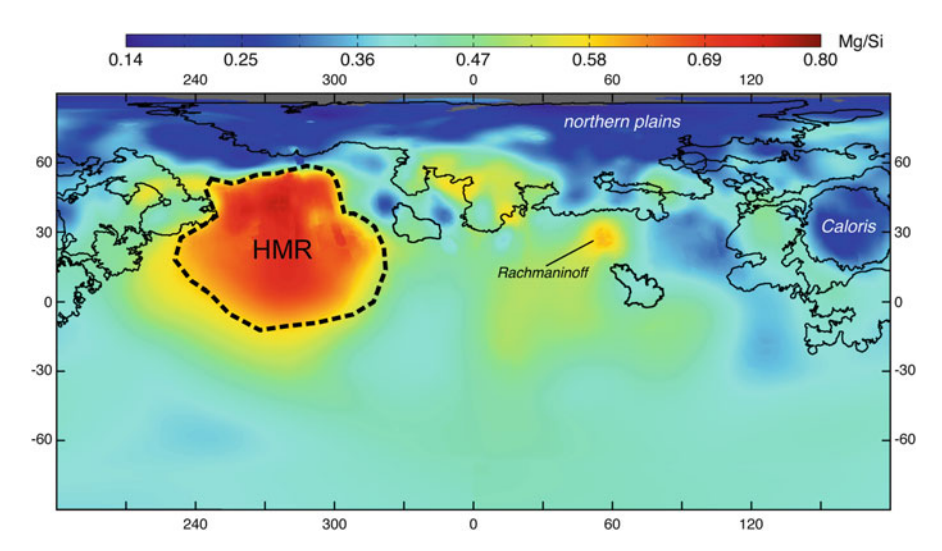


Fig. 4.17 MESSENGER XRS measurements of magnesium:silicon ratio, smoothed according to the effective resolution of the measurements. HMR = high-magnesium region (see text). A smaller region of elevated magnesium:silicon ratio labelled Rachmaninoff may reflect ejecta surrounding the Rachmaninoff impact basin (Credit: S. Weider et al., LPSC, 2014)

can be confident that only one rock type has been sampled) and assuming the likely mineralogy. A rather simple but very important inference that can be drawn from the GRS and XRS elemental abundance measurements (showing low Al and Ca abundances) is that Mercury has no extensive unit dominated by feldspar minerals, and hence there is no evidence of a lunar-like anorthosite highland crust, which had been a plausible suggestion based on the low total $FeO+TiO_2$ content deduced from pre-MESSENGER studies.

Instead, the high Mg abundance seen everywhere is compatible with Mercury being surfaced by a rock-type similar to a terrestrial magnesium-rich basalt, poorer in Fe than is usual on Earth, and likely to be composed mainly of Mg-rich orthopyroxene and calcium-rich plagioclase, which when erupted as lava would have a lower viscosity and higher temperature than most terrestrial basalts. Intermediate terrain (the intercrater plains) is richer than the average in magnesium, calcium and sulfur, but lower in aluminium and sodium. This composition verges on that of an ultramafic rock-type called komatiite, and implies a greater than average degree of partial melting to have extracted it from a mantle source. The equilibrium mineralogy of intermediate terrain would be 58 % orthopyroxene, 28 % plagioclase, 8 % quartz, 3 % sulfides, 2 % olivine and about 1 % spinel. Some regional variation is discernable among the intermediate terrain (Fig. 4.17), notably a 'high-magnesium region' at 60–120° W that is best interpreted as representing an especially high degree of partial melting having occurred when it was extracted from the mantle.

The less Mg-rich smooth plains are best explained as derived by a lower degree of partial melting. The mineralogy of the northern volcanic plains has been

modelled as approximately 41 % orthopyroxene (slightly poorer in magnesium and richer in iron than in the intermediate terrain), 24 % plagioclase (slightly poorer in calcium but richer in sodium than the intermediate terrain), maybe about 22 % of quartz and nepheline (the latter being strongly-dependent on quite how much Na there is, though GRS suggests Na enrichment here), 2 % sulfides, 2 % olivine and 5 % spinel. The Caloris interior plains are similar to the northern volcanic plains, except for probably having calcium-rich plagioclase and being poorer in potassium. It is not clear whether the latter reflects original composition, or loss of volatile-potassium as a consequence of especially high noontime temperatures. Beyond showing that the circum-Caloris low-reflectance blue plains are higher in Mg, the data are not adequate to demonstrate compositional differences among numerous smaller expanses of smooth plains, or to suggest reasons for the spectral differences visible on WAC and MASCS data.

4.4 A Tour of Mercury

It is impossible to give a comprehensive account of the surface of an entire planet in a single chapter. What follows is a representative review of the most important types of terrain features. It is intended to be fairly comprehensive in scope, though it clearly does not mention every example.

4.4.1 Global Topography

MESSENGER provided two ways to map Mercury's topography: laser altimetry from MLA and stereo imaging by MDIS (Fig. 4.18a, b). The eccentricity of MESSENGER's orbit means that MLA data become unusable a little way south of the equator, but the excellent correspondence between the two data products in the northern hemisphere inspires confidence.

The northern plains are generally low-lying, but there is little other relationship between topography and independently-mapped terrain units (for example, even the Caloris basin is far from obvious). Instead there are a number of 'quasi-linear rises' such as those that run from west-south-west to east-north-east from near the western edge of Fig. 4.18 (two in the northern hemisphere and either one or two in the southern hemisphere). The northernmost can be traced for at least 7,000 km, crossing the Caloris basin without deflection with its crest running parallel to its neighbour about 1,300 km so the south. There is also a north-south rise, branching into two northwards, that straddles the edge of the map. Gravity studies (in the northern hemisphere only) suggest that these quasi-linear rises correspond to belts of thickened crust, and are so are at least partly supported isostatically (i.e., by their own buoyancy), and are not likely to simply be lithospheric flexures imposed by

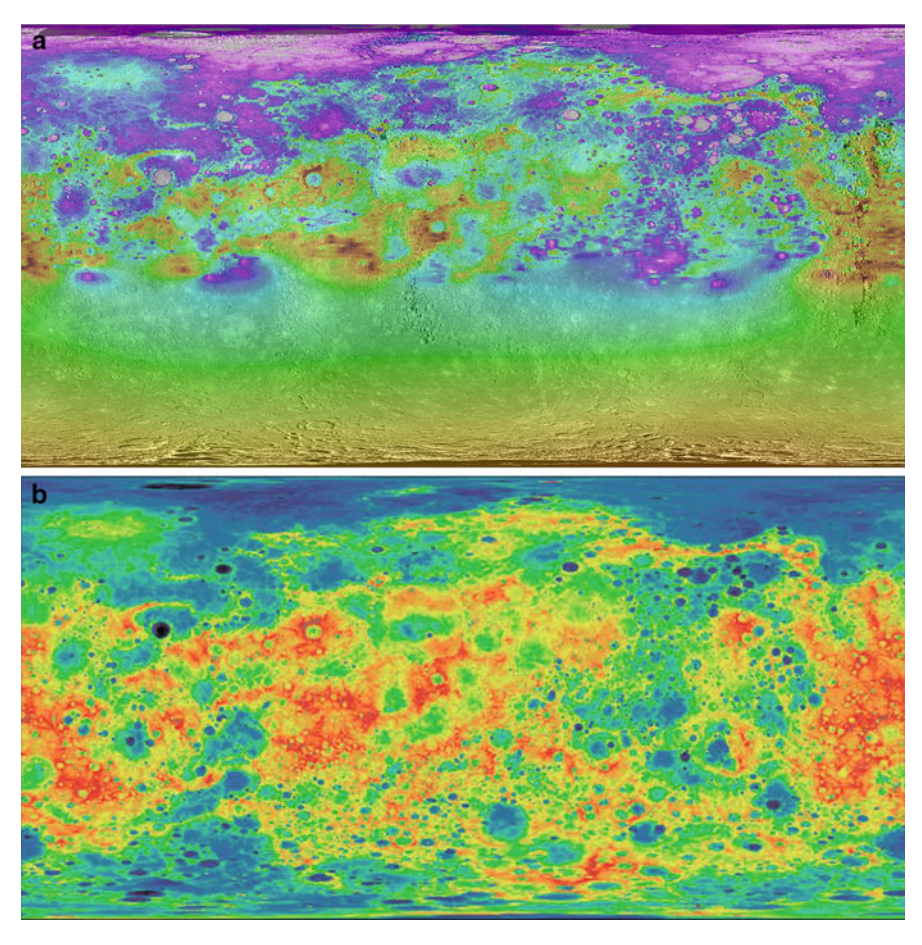


Fig. 4.18 (a) MLA topography as mapped up to April 2013, shown on a similar map projection to Fig. 4.10, centred at 180° E. The data are colour-coded with red about 2 km above datum and purple about 3 km below datum. Colours are transparent to allow an underlying MDIS mosaic base-map to show through. Floors of deep craters outside this altitude range are uncoloured. The Caloris basin is just above left of centre, but does not dominate the local topography. The apparent smoothness of the southern hemisphere is illusory, and is an artefact of the lack of MLA data (Derived from QuickMap PDS11, data courtesy of MESSENGER team). (b) Topography based on MDIS stereo imaging, based on a control-point network up to June 2013 (Courtesy of NASA/Johns Hopkins University Applied Physics Laboratory/Carnegie Institution of Washington/United States Geological Survey)

global contraction. Whatever their explanation, these rises clearly post-date the plains volcanism, because they have flexed the Caloris basin-fill.

Some less elongated, more dome-like rises can be noted too, such as the one in the northern plains close to the western edge of Fig. 4.18. These seem not to correlate with crustal thickness (as deduced from gravity studies) and may be situated where the underlying mantle is anomalous.

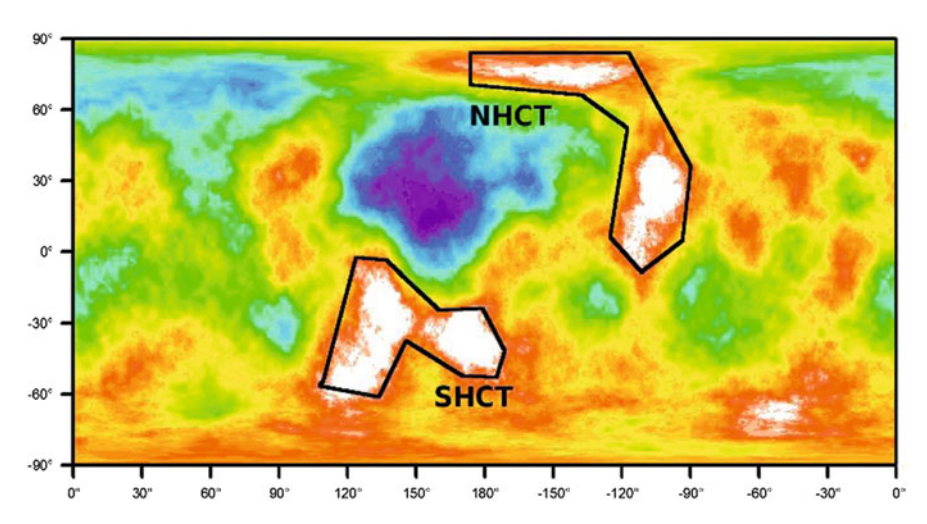


Fig. 4.19 Density of craters >25 km diameter on Mercury. *Purple* lowest density, *white* highest density. The two most heavily-cratered regions are indicated as NHCT, northern heavily cratered terrains, and SHCT, southern heavily cratered terrain. The region of lowest crater density, situated between these, is Caloris and its surrounding plains (Reprinted by permission from Macmillan Publishers Ltd: *Nature* v499, 59–61, S. Marchi et al., © 2013)

Turning to more local scale topography, the floors of Kuiperian and Mansurian craters are deep, and can often be picked out on Fig. 4.18. For example a purple spot (in Fig. 4.18a) in the southeast of Caloris coincides with the 110 km crater Atget whose floor is about 2 km below the surrounding plains, and the 230 km Mozart crater, 200 km beyond the southern rim of Caloris, is prominent thanks to its bluegreen floor (on the colour scale used in both products) being about 3 km lower than the surrounding red-yellow highlands of one of the quasi-linear rises. In the southern hemisphere, Rembrandt, Tolstoj, Beethoven and several larger, un-named, lava-filled basins are apparent as topographic lows.

4.4.2 The Oldest Terrain

Crater counts based on MESSENGER imaging suggest that the oldest surviving surfaces on Mercury date from about 4.0 to 4.1 billion years ago, just after the start of the Late Heavy Bombardment. The most extensive examples (Fig. 4.19) are the northern heavily cratered terrains, in the Beethoven quadrangle and extending north across the eastern part of the Shakespeare quadrangle, and the southern heavily cratered terrain that dominates the Neruda quadrangle.

An area of the southern heavily cratered terrain is shown in Fig. 4.20. Parts of this figure contain adjacent or overlapping craters, but even here tracts of cratered plains intervene between some craters, and some of the craters have subdued rims and shallow depths that show them to be ghost craters, from which we can infer volcanic flooding of parts of the area while the Late Heavy Bombardment was still in progress.

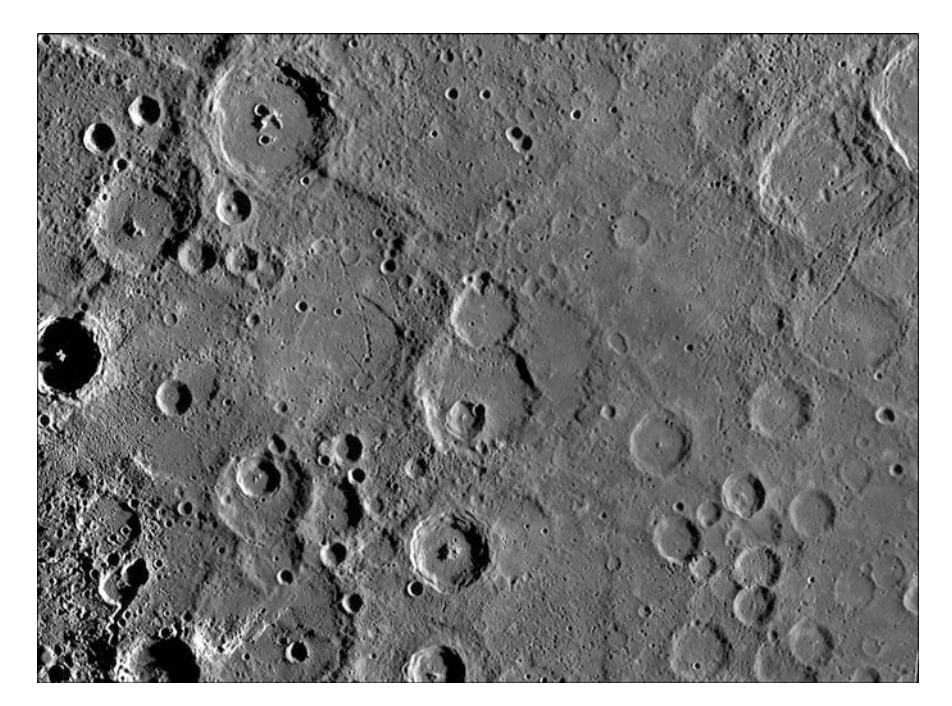


Fig. 4.20 670 km wide view of part of the southern heavily cratered terrain, 162–179° E, 23–34° S. This is from a mosaic of MDIS images acquired under a variety of illumination conditions. The ancient 90 km crater near the middle, with a 30 km diameter central-peaked crater on its southern floor, is Sarmiento (NASA/Johns Hopkins University Applied Physics Laboratory/Carnegie Institution of Washington)

4.4.3 Compressional Tectonic Features

MESSENGER images enabled much more comprehensive mapping of lobate scarps and related tectonic features than was possible on Mariner 10 data. Global analysis taking account of the shortening that can be inferred from larger-scale (lobate scarps and associated ridges) and smaller-scale (wrinkle ridges) features suggests contraction of Mercury's radius by about 7 km. This is several times greater than could be demonstrated on Mariner 10 imaging, but is in line with some predictions based on models of global cooling and contraction. The quasilinear rises identified in Sect. 4.4.1 could represent compressional lithospheric flexure, but if so their additional contribution would be negligible.

Between latitudes 60° N and S, the orientations of observed structures cluster strongly about the N-S direction, but there is a more even spread of orientations at latitudes greater than 60°. Lighting geometry would make E-W structures harder to detect at low latitudes, and it is not clear how strong any latitude-dependent N-S preference truly is. The consensus view is that the main driver for Mercury's compressional tectonics has been global contraction, though some (including myself) would argue that there is a genuine preference for N-S orientations among the most significant structures at low- and mid-latitudes, and that this

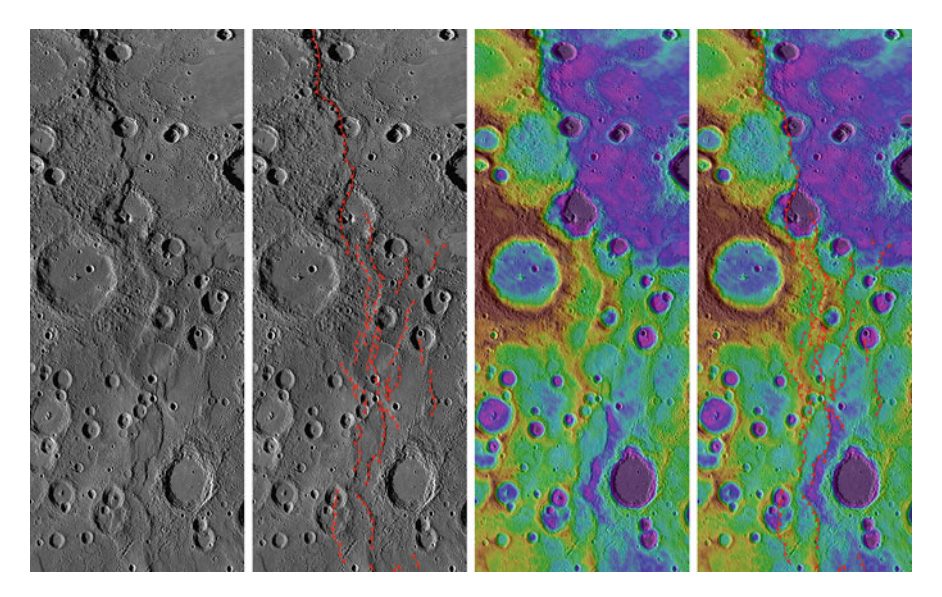


Fig. 4.21 Victoria Rupes (in the north) and Endeavour Rupes (in the south). From left to right: MDIS mosaic, MDIS mosaic with interpretation, stereo-derived topography, stereo-derived topography with interpretation. Thrusts are shown (according to convention) as lines with solid triangles on the hanging wall (i.e. on the terrain that has been thrust over the adjacent terrain). The area shown is 500 km wide and centred at 328° E. It extends from about 35° N to about 55° N. Interpretation and compilation courtesy of Valentina Galluzzi (NASA/Johns Hopkins University Applied Physics Laboratory/Carnegie Institution of Washington)

provides evidence for either collapse of an equatorial bulge during relatively late tidal despinning or strong influence of convection in the mantle upon the crustal fault pattern.

Extensional tectonics on a broad scale is observed only in the plains lava fill of many of Mercury's larger basins. It manifests itself as extensional fractures that can be attributed to isostatic adjustments, and is discussed in Sect. 4.4.4. Here I show examples of compressional structures. It has become apparent that simple, isolated scarps like Discovery Rupes (Fig. 2.14) are rare, and instead most are components of linked fault systems, in which as the displacement on one scarp dies away near a fault-tip it is transferred to displacement on an adjacent fault.

4.4.3.1 Victoria and Endeavour Rupes

Victoria Rupes gives its name to the Victoria quadrangle (Fig. 2.7), and was named after the only ship in Ferdinand Magellan's 1520 expedition to complete the first circumnavigation of the globe. To its south, Endeavour Rupes is named after Captain Cook's ship on his third, and fatal, Pacific voyage of 1768–71. Each was recognized and named on the basis of Mariner 10 images, but MESSENGER images show that they are part of a single continuous system of faults (Fig. 4.21).

Figure 4.21 shows Victoria Rupes and the northern part of Endeavour Rupes in detail, allowing you to compare the structures on MDIS images and on stereoderived topography. For most of its length, Victoria Rupes is a single east-facing scarp, suggesting east—west compression with the hanging wall transported eastwards. In structural geology parlance this is described as eastward vergence. As originally defined, Victoria Rupes ends near the southern rim of the 150 km crater containing a strange 40 km pit.

The MESSENGER data allow us to see that the structural trend is continued southwards by an array of mostly west-facing scarps for about 300 km before predominantly east-facing scarps take over in a wider and more complicated array of faults which are Endeavour Rupes. It is fortunate that the term Rupes has identical singular and plural forms, because there are certainly several lengths of scarp that could lay claim to the name Endeavour Rupes if it had to refer to just a single feature.

The sector with the west-facing scarps that connects Victoria Rupes to Endeavour Rupes was apparently not recognized to be significant on the Mariner 10 images, and went unnamed. Today we can appreciate that the Victoria-Endeavour fault system is a part of single array, the whole of which is consistent with east—west compression. Some thrusts have opposite-verging back-thrusts in their hanging walls, but there is a clear impression of dominantly eastward vergence in Victoria and Endeavour Rupes and dominantly westward vergence in the intervening sector. South of Endeavour Rupes, beyond the coverage of Fig. 4.21, the structure simplifies into a 40 km wide north—south ridge, presumably bounded by outward-verging thrusts on either side, mapped on Mariner 10 images as Antoniadi Dorsum, reaching 500 km south of Fig. 4.21. In total the Victoria-Endeavour-Antoniadi fault array extends for about 2,000 km.

When a pre-existing impact crater has been cut by a thrust fault, as occurs twice in the northern half of Fig. 4.21, one part of the crater has been shunted over another and the trace of the crater's rim is no longer circular. This can be measured on the images. In addition, there is a mismatch between the altitude of the crater rim on opposite sides. This can be measured on the stereo-derived topography. Combining both measurements for deformed craters in the Victoria-Endeavour system suggests thrust dips in the range $15-20^{\circ}$ and displacements in the range 3-6 km.

4.4.3.2 Beagle Rupes

Beagle Rupes (Fig. 4.22) was prominent on MESSENGER flyby 1 outbound images and became the first newly-discovered lobate scarp to be named. It commemorates the ship on which Charles Darwin served as a naturalist (1831–1836) when he made the observations that led him to develop his theory of evolution. It is hard to think of a more influential voyage of scientific discovery, so it is strange that the name had not been used for any of the Mariner 10 scarps. However, thanks to MESSENGER the name was awarded in time for the bicentenary of Darwin's birth and the 150th anniversary of his publication of *On the Origin of Species*.

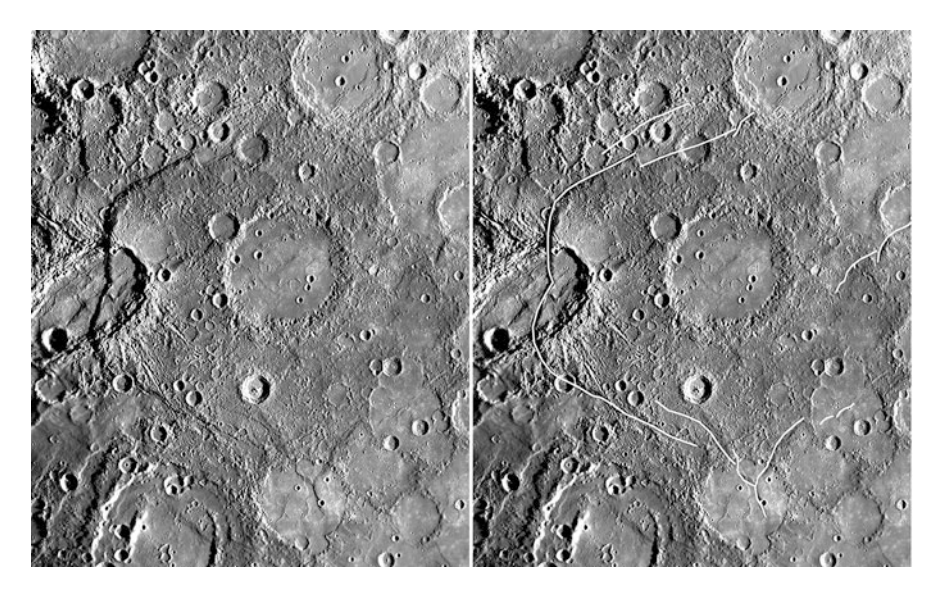


Fig. 4.22 Beagle Rupes, without (*left*) and with (*right*) interpretation. The main faults are indicated, but triangles to indicate the hangingwall of thrusts (as in Fig. 4.21) have been omitted. An MDIS mosaic based on flyby 1 images is shown here, because the high Sun angle reveals landscape features to good effect, though orbital images were also used in the interpretation. The elongated basin that Beagle Rupes crosses is Sveinsdottir, which is a rare example of a crater apparently formed by a very oblique impact on Mercury. The plains in the lower right and most flooded crater floors are occupied by high reflectance red plains. The area shown is 610 km wide and is centred at 106° E, 2° S (NASA/Johns Hopkins University Applied Physics Laboratory/ Carnegie Institution of Washington)

The classic Discovery Rupes-type scarp and the individual scarps in the Victoria-Endeavour array can be explained by the model shown in Fig. 2.15, in which a dipping, essentially planar, thrust dies out at depth. However Beagle Rupes differs in that the trace of the gently lobate north—south scarp of its frontal thrust bends back by about 60° at either end, to make a bow-shape. The north—south portion appears to be a westward directed thrust, with about 2 km of westward transport demonstrable where the hangingwall has overthrust a 17 km crater in the footwall to the north of the elongated Sveinsdottir basin. A little thought shows that if the displacement is westwards across the frontal thrust, and thus at right-angles to it, the displacement has to be largely sideways ('transcurrent') but partly compressional across the oblique structures at either end. A structural geologist would describe such displacement as 'transpressional'. In further terminology used by structural geologists on Earth, these oblique structures are equivalent to transpressional 'sidewall ramps' bounding a thrust sheet.

The terrain inside the bent trace of Beagle Rupes (the hangingwall terrain) cannot have been displaced unless the frontal thrust and sidewall ramps that we can see at the surface join up at depth. In order to achieve this, although the dip of the frontal thrust could be nearly 30° where it reaches the surface it must soon

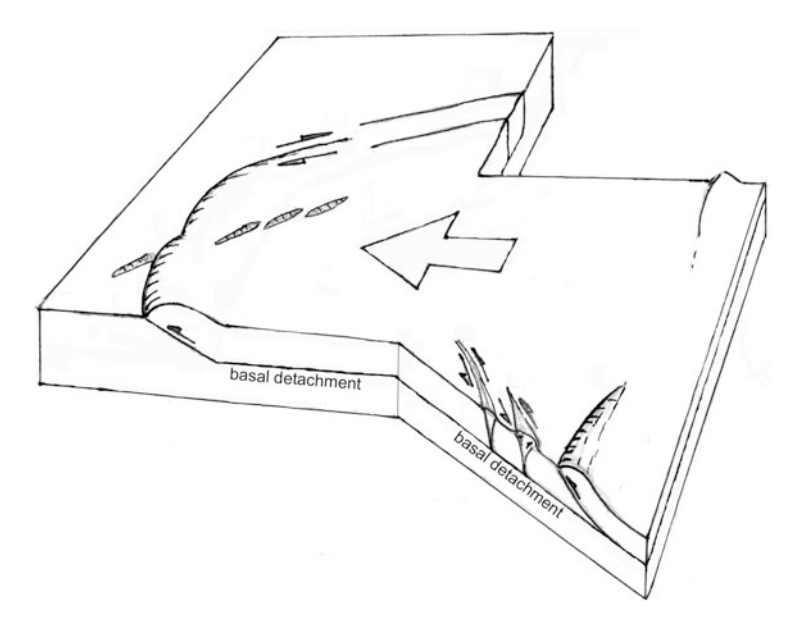


Fig. 4.23 A sketch interpretation of Beagle Rupes in three-dimensions. This imagined view is looking northwards across the region shown in Fig. 4.22, with some terrain made invisible to reveal the underground structure. An en echelon array of surface ridges (visible but not marked on Fig. 4.22) on both sides of the frontal thrust, like wrinkles on a tablecloth, is consistent with the same regional stress regime in operation before the thrust system developed. The total distance along the two nearside faces of the model is about 550 km (Modified from D. A. Rothery & M. Massironi, *Icarus*, v.299, 256–261, 2010)

become much shallower, perhaps even horizontal. This is illustrated in Fig. 4.23, which shows the dip of the frontal thrust shallowing to become a basal detachment surface below the displaced hangingwall terrain.

Another important aspect of Fig. 4.22 is that the southern sidewall ramp becomes less distinct as it is traced away from the frontal thrust, but near where it dies out a shorter length of scarp (probably an oblique thrust) seems to take over. This in turn is cut across by two more successively younger thrusts. There are some wrinkle ridges on the lava-fill of the 130 km flooded basin at the southeast end of the Beagle Rupes system, but those are confined within the basin and are thus of less significance (they appear to be older, and unrelated).

The successive thrusts are shown in Fig. 4.23. One way to interpret this is that motion on the frontal thrust ceased while the compressional tectonic regime was still strong enough to cause deformation. With the front of the structure somehow 'locked', a new thrust propagated towards the surface from further back in the hangingwall thrust sheet. This in turn became 'locked' and a new thrust developed further back, and so on.

On Earth, thrust stacks tend to propagate forwards by detaching successive slices of the footwall, but so called 'out of sequence' thrusts, as suggested here for the Beagle Rupes system, do occur in some circumstances.

Irrespective of the detailed interpretation, it is geometrically implausible for the basal detachment surface of the Beagle Rupes system to be deeper than about 30 km (which is the depth suggested by the sketch in Fig. 4.23). Parts of the Earth's continental crust contain weak sedimentary layers that tend to serve as the bases of thrust sheets, and the Beagle Rupes basal detachment surface is likely to occur at a weak layer too.

Section 4.2.3 showed evidence that Mercury's crust is layered in some regions. It is not likely that any of the recognized terrain units would be intrinsically weak, but maybe the detachment surface follows the interface between two layers. This would be facilitated if the upper layer was lavas burying a regolith-covered lower layer, because the buried regolith would be relatively weak. On the other hand, if the depth of the detachment layer is in the region of 30 km, then an alternative plausible explanation is that this depth marks where the temperature is sufficient for a structurally dominant mineral phase to become ductile, and hence weak.

4.4.3.3 Paramour Rupes

Paramour Rupes (Fig. 4.24) lies 2,000 km east of Beagle Rupes, in the low-reflectance blue plains that surround much of the Caloris basin. The name was approved in 2014, and commemorates the Paramour, a Royal Naval vessel that spent 1698–1700 quartering the Atlantic ocean to chart how magnetic declination (the difference between true north and magnetic north) varied with position, which

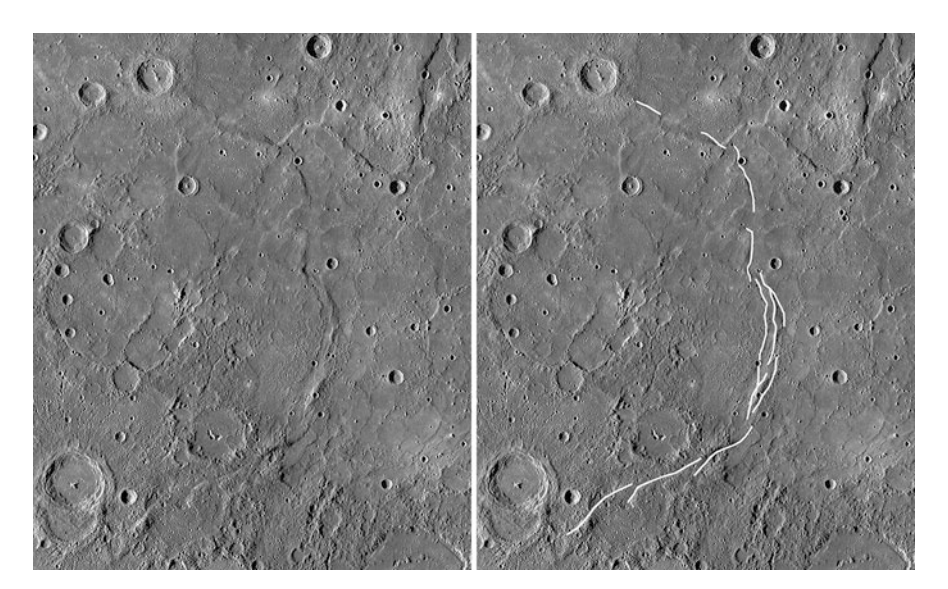


Fig. 4.24 Paramour Rupes, without (*left*) and with (*right*) the main faults indicated, on an MDIS mosaic based on orbital images. The shadowed scarp in the upper right is Alvin Rupes. This is at the same scale as Fig. 4.22. It is 610 km wide and centred at 146° E, 0° N (NASA/Johns Hopkins University Applied Physics Laboratory/Carnegie Institution of Washington)

was intended to be an aid to navigation. The Paramour was commanded by no less a person than Edmund Halley (later of comet fame), who also made most of the necessary observations. The name is trebly appropriate for Mercury, because as well as honouring a scientific expedition/voyage of discovery (the essential criterion) it has a link to a famous astronomer and to planetary magnetism.

The Paramour Rupes system is an array of linked faults. The shortening direction here is once again east—west, but this time the movement of the hangingwall terrain over the footwall would have been towards the east. This makes it a sort of mirror image of the Beagle Rupes system, but the frontal thrust scarp is less prominent. This is partly because of the lighting, but also because part of it branches into an array reminiscent of Endeavour Rupes. The sidewall structures are different too, the southern one being best interpreted as a set of en echelon transpressive ridges (developed where there is a 'restraining bend' on the sidewall structure), with no indication of backwards (out of sequence) thrust propagation. However, using the same argument as for Beagle Rupes, the whole terrain within the fault-bounded bow-shaped region must have been transported, which requires the faults to be linked at some depth within the crust by a sub-horizontal weak layer.

It would be premature to claim that Beagle and Paramour are components of a single, tectonically-linked system. Their spatial relationship is shown in Fig. 4.25,

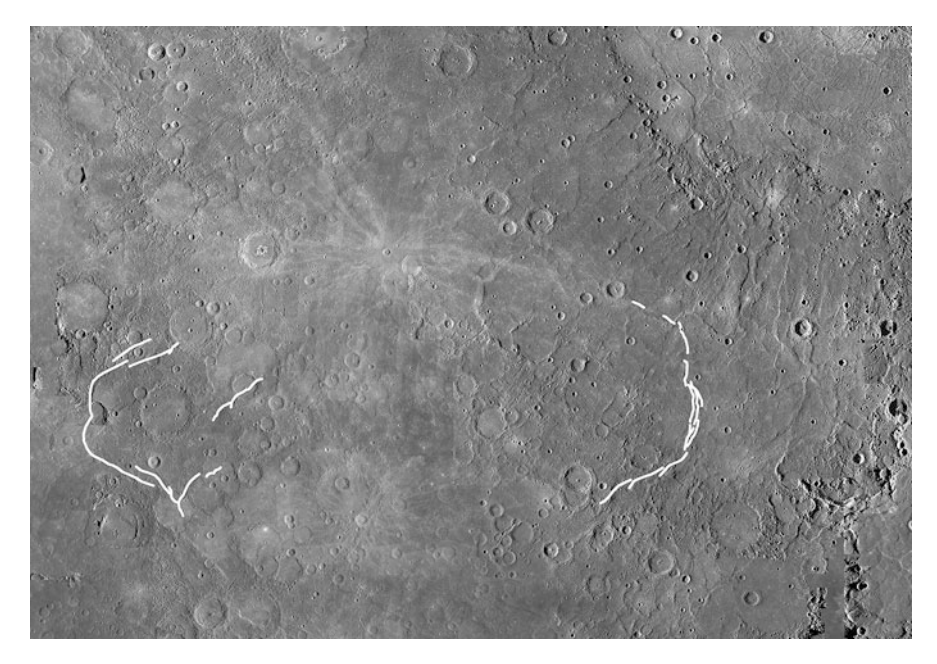


Fig. 4.25 Beagle Rupes (*left*) and Paramour Rupes (*right*) on an MDIS mosaic based on orbital images, to show their geographic relationship. Other faults within this area have been omitted. The southwest quarter of the Caloris basin can be seen in the upper right. The area shown is 2,500 km wide and is centred at 130° E, 5° N (NASA/Johns Hopkins University Applied Physics Laboratory/Carnegie Institution of Washington)

and the most that can safely be said is that they each provide clear evidence of predominantly east—west shortening in this part of Mercury's equatorial region.

4.4.3.4 Enterprise Rupes

The scarp that was given the name Enterprise Rupes came to attention during MESSENGER's second flyby (Fig. 4.26), because it cuts through part of the newly discovered Rembrandt basin. I am sorry to disappoint any Star Trek fans, but the name commemorates (officially at least) a more prosaic maritime USS Enterprise, being a sail-assisted steamship that surveyed the mouths of the Mississippi and Amazon 1877–8 and completed a round the world hydrographic survey 1883–1886.

The Enterprise Rupes system consists of an almost continuous southeast facing scarp, which is probably the main thrust, with a number of discontinuous scarps facing in the opposite direction 20–80 km behind it, which are probably backthrusts. It thus has the form of a ridge, though the regional terrain is distinctly lower on the southeast side. It cuts across part of Rembrandt (at 715 km diameter one of the largest basins on Mercury) and is younger than the lava-fill of the basin and some of the large craters on its floor.

The main scarp is bent back by about 40° just inside Rembrandt's southwestern rim. Displacement appears to be left-lateral transpression on the portion of the scarp north of the bend, but right-lateral transpression on the portion of the scarp southwest of the bend. Examination of the discontinuous scarps behind the southwest part of the main scarp west suggests that they have been formed by uplift of 'pop-up' blocks on restraining bends. About 3 km of oblique right-lateral slip can be calculated on geometric grounds, which tallies with the offsets of the rims of three 60–75 km diameter craters (two inside and one outside Rembrandt) that are cut by main thrust. Taking all these factors into consideration, the shortening across the Enterprise Rupes system is towards the southeast as indicated by the arrow in Fig. 4.26. Both halves of the scarp are oblique sidewall ramps, and there is no frontal thrust except at the apex of the curve where the two meet.

4.4.3.5 Ages of Movement

Some compressional features such as Discovery and Victoria Rupes are entirely within intermediate terrain, but others such as Beagle, Paramour and Endeavour Rupes cut through smooth plains of various kinds. A fault must be younger than any surface that it displaces, so we can say that much of the global contraction post-dates the Late Heavy Bombardment. But by how much?

Some faults have Kuiperian, Mansurian (Beagle and Paramour Rupes) or even Calorian craters superimposed on them, which places an oldest limit on the date of the most-recent movement on each fault. One the other hand, some faults displace Mansurian craters (Enterprise Rupes), and even some fresh-looking <3 km craters

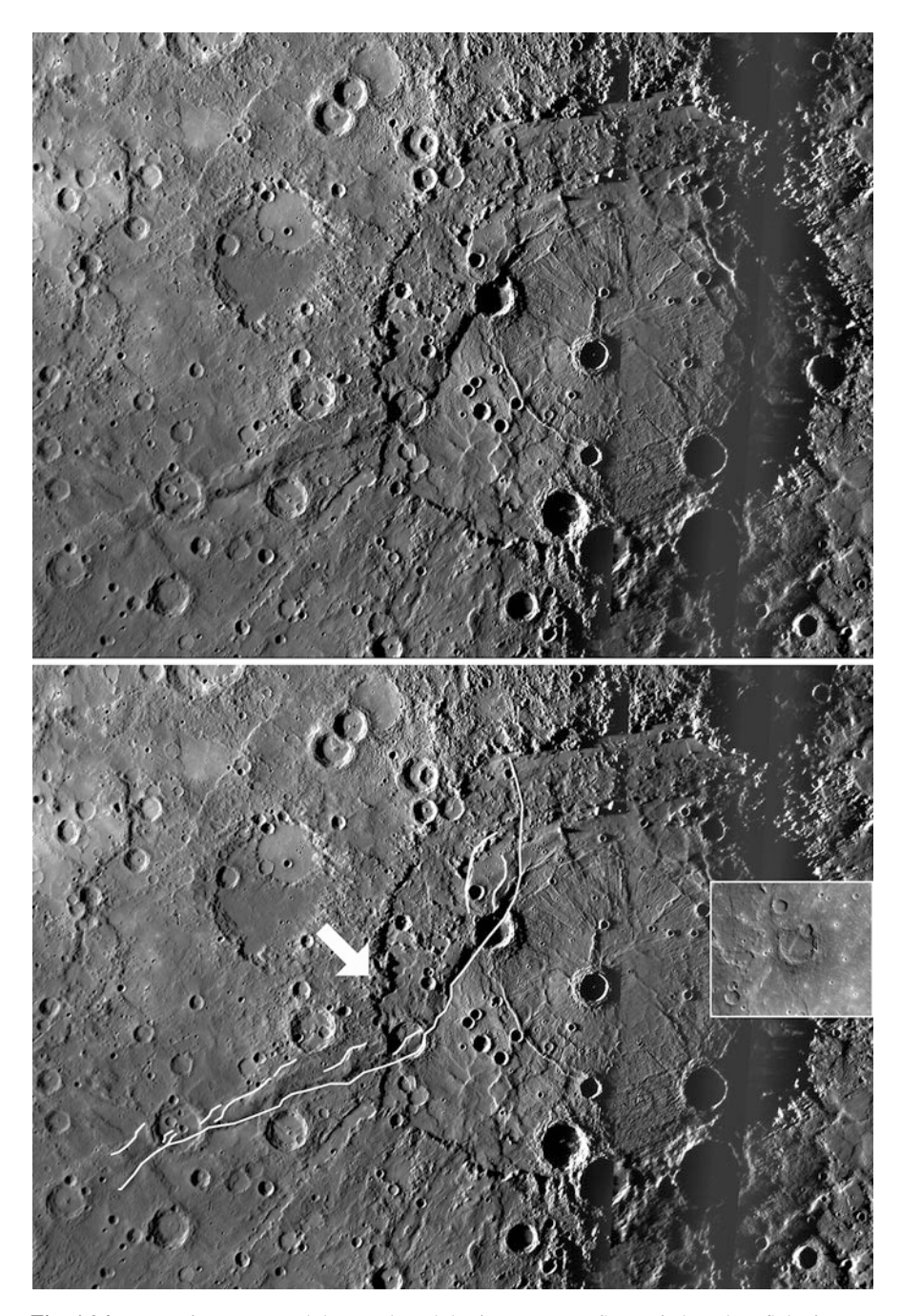


Fig. 4.26 Enterprise Rupes and the Rembrandt basin on an MDIS mosaic based on flyby images (the change in illumination direction in the east of the basin marks a join between the flyby 1 outbound sunrise terminator and the flyby 2 inbound sunset terminator). Lines on the copy below indicate scarps belonging to the Enterprise Rupes array, and the *arrow* is the inferred direction of transport. Unmarked ENE- and WSW-facing scarps in the upper left are not linked with the

that are probably of Kuiperian age, and so must have moved more recently. To try to be more quantitative, one approach is to use crater statistics, for example by counting how many craters are superimposed on a fault but not displaced by it, and so must be younger than the fault movement. However, because a fault is a linear feature it crosses relatively few craters, so the statistical uncertainty is much greater than for dating of a large area of terrain. Another approach is to look at the floors of craters on the hangingwall terrain close behind the fault, where the ground surface has been tilted away from the scarp. The floors of craters that were formed before the displacement will share this tilt, whereas craters that were formed after the fault-related tilting will tend to have horizontal floors.

Taking all kinds of evidence into account, the picture that emerges is of demonstrable compressional tectonics dating back to the Late Heavy Bombardment (evidence of likely older tectonics has been lost). Some scarps show no displacement since that epoch, but reactivation of existing scarps and initiation of some new ones continued into the Kuiperian.

4.4.4 Impact Basins

There is no formal size definition of 'impact basin'. I use the term here to mean craters more than a couple of hundred km in diameter. They are notable on Mercury for their variety.

Section 4.2.1 reported that 100–500 km craters on Mercury are as common as on the Moon, but that there are fewer examples than might be expected greater than 500 km in diameter. Figure 4.26 showed Rembrandt, which like almost all basins on Mercury has been largely flooded by lava but is exceptional in being transected by a lobate scarp that lies partly beyond the basin. Now let's take a look at some of the others, presented in order of decreasing size. Except where noted, the basin-filling lavas are of Calorian age, dated by crater-counting at 3.55–3.9 billion years ago.

4.4.4.1 Caloris

At 1,550 km in diameter, this is the largest basin on Mercury (Fig. 4.27), but strictly speaking it has no name. The plains within it are Caloris Planitia, and the uplifted eastern rim, which is the only part that was visible in Mariner 10 images, is named Caloris Montes (the sole use of the descriptor term Montes yet made on Mercury). However, at the time of writing the name Caloris does not feature in the IAU list of

Fig. 4.26 (continued) Enterprise system. The *small inset box* shows a sunlit view from orbit of the main scarp crossing the crater that was shadow-filled in the fly-by images. The area is 1,330 km wide, centred at 82° E, 32° S and is shown on a Transverse Mercator protection (NASA/Johns Hopkins University Applied Physics Laboratory/Carnegie Institution of Washington)

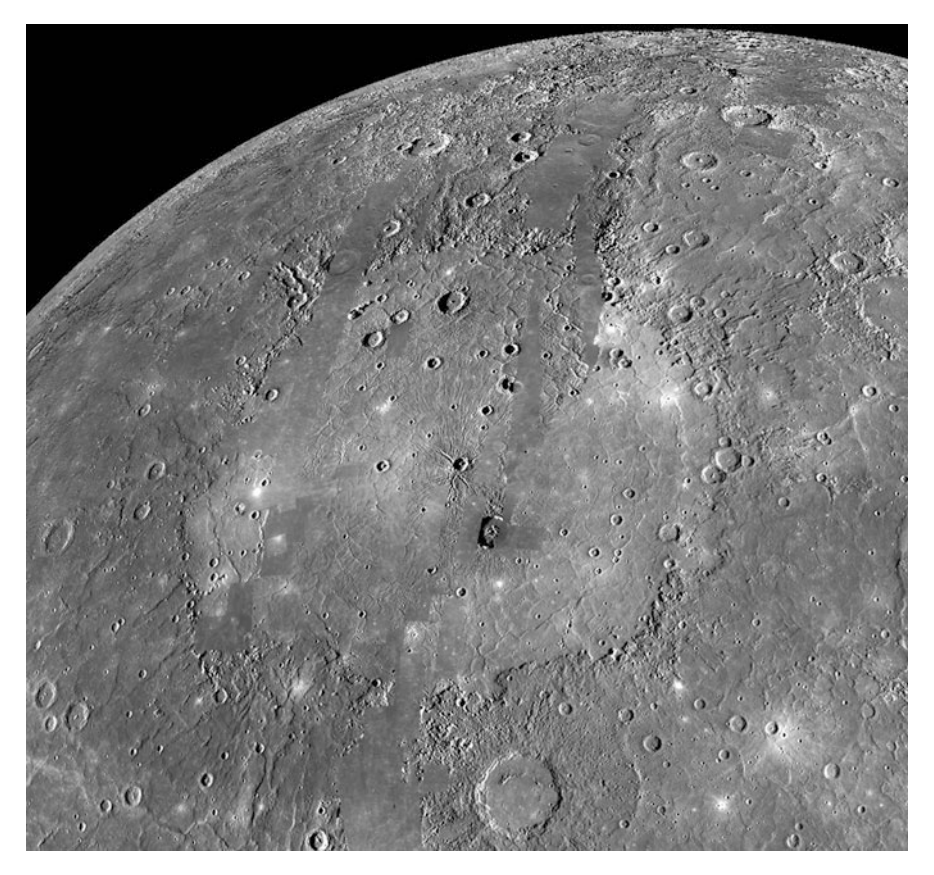


Fig. 4.27 Projected view of an MDIS orbital mosaic showing the Caloris basin. The 240 km smooth plains-flooded peak-ring basin Mozart to the south is younger (NASA/Johns Hopkins University Applied Physics Laboratory/Carnegie Institution of Washington)

impact basins (craters), though no one seriously doubts that it is such a basin. The plains within Caloris are 'high reflectance red plains' (Sect. 4.2.2), and their origin as basin-filling lavas is no longer in doubt. Crater counting suggests an age of about 3.7 billion years.

Mariner 10 had showed circumferential wrinkle ridges on the outer part of the Caloris floor giving way to a somewhat rectilinear fracture pattern further inwards (Fig. 2.11). MESSENGER was able to confirm that this pattern persists around the whole basin, and revealed that the centre of the basin is dominated by a radial fracture pattern. This can be discerned on Fig. 4.27, but is much clearer on Fig. 4.28.

This radial pattern is so striking that it was named Pantheon Fossae, so far the only use of the fossa/fossae descriptor term on Mercury, though there is a somewhat similar radial fracture pattern in the central part of Rembrandt too. The Pantheon Fossae radial fractures are manifested as troughs from one to a few km wide, and a few hundred metres deep. They seem to be converging towards the basin centre, but

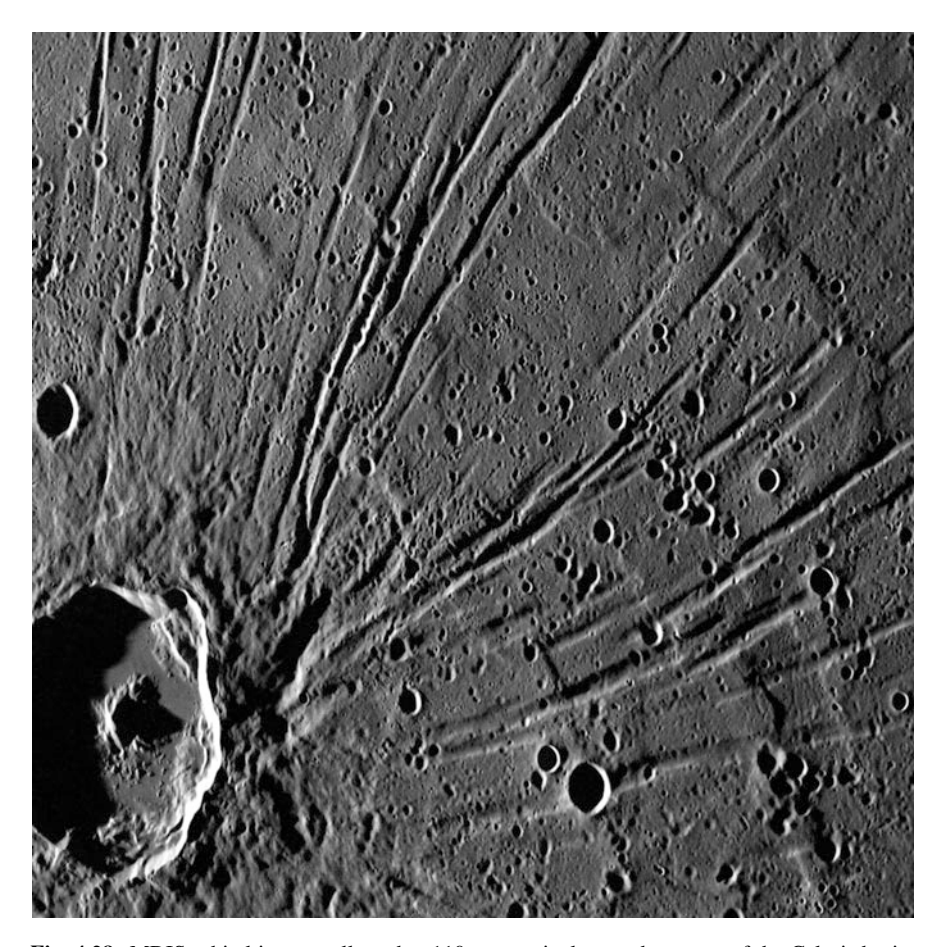


Fig. 4.28 MDIS orbital image collected at 110 m per pixel, near the centre of the Caloris basin. Apollodorus crater at the lower left is 42 km across (NASA/Johns Hopkins University Applied Physics Laboratory/Carnegie Institution of Washington)

are there obscured by the 40 km crater Apollodorus and its ejecta. This crater is unlikely to have been the cause of the fracture pattern, and seems to have been a near bulls-eye impact long after the pattern had been established. The troughs are probably grabens overlying radial dykes (vertical curtain-like igneous intrusions) or representing radial fracturing in response to doming of the Caloris floor. The latter could be an isostatic response to the crustal thinning when the basin was excavated, but if so it clearly post-dates the partial infilling of the basin by lavas that ought to have counteracted this tendency.

We will revisit Caloris in the context of volcanic vents later.

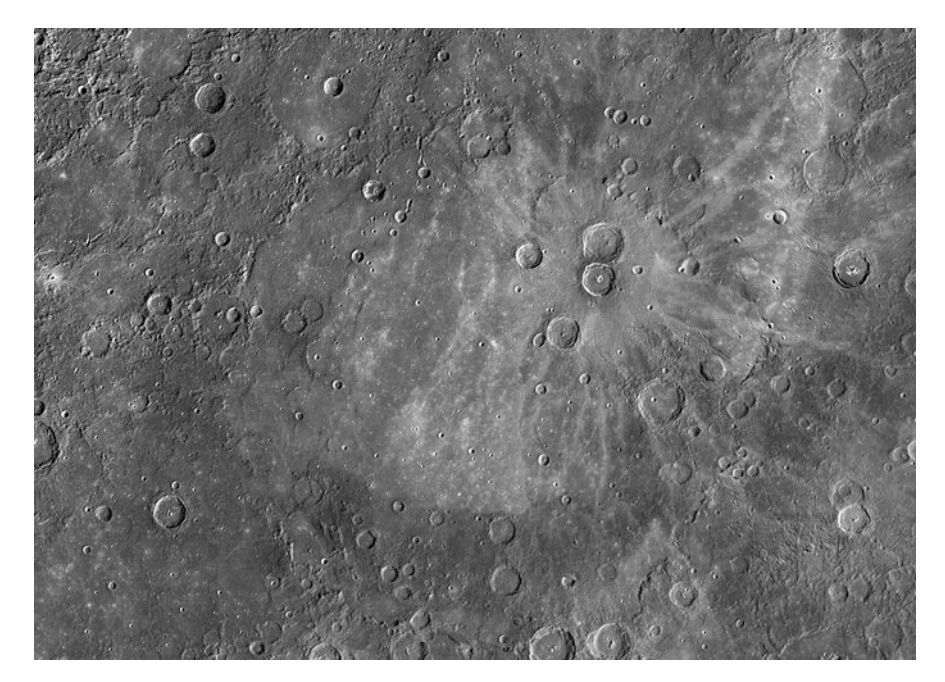


Fig. 4.29 MDIS orbital mosaic including Sobkou Planitia. The area is 1,400 km wide, centred at 130° W, 35° N and is shown on a Transverse Mercator protection. Rays from the 55 km Kuiperian crater Degas within the basin cross its floor and the plains to the east. The apparent albedo change in the east of the basin floor is an artefact (NASA/Johns Hopkins University Applied Physics Laboratory/Carnegie Institution of Washington)

4.4.4.2 Sobkou

Sobkou (770 km diameter) was recognized as a pre-Tolstojan basin on Mariner 10 images on the basis of its degraded and cratered rim, though (as for Caloris) strictly speaking the name is given to Sobkou Planitia rather than to the basin itself. In keeping with the convention for most planitiae on Mercury (Table 2.2), Sobkou takes its name from the ancient Egyptian messenger god, which was probably also their name for the planet Mercury.

WAC exaggerated colour shows that the basin floor is occupied by high-reflectance red plains. Figure 4.29 shows that these generally embay the basin rim (and have breached it in the north and also at the eastern extremity to merge into the adjacent plains). However in the far west of the basin, just north of where an ancient 80 km crater cuts the rim, the junction between basin-fill and basin-rim has become a westward-facing lobate scarp. This is an instance of the tectonisation of basin edges, a widespread phenomenon that we will discuss after you have seen some more dramatic examples.

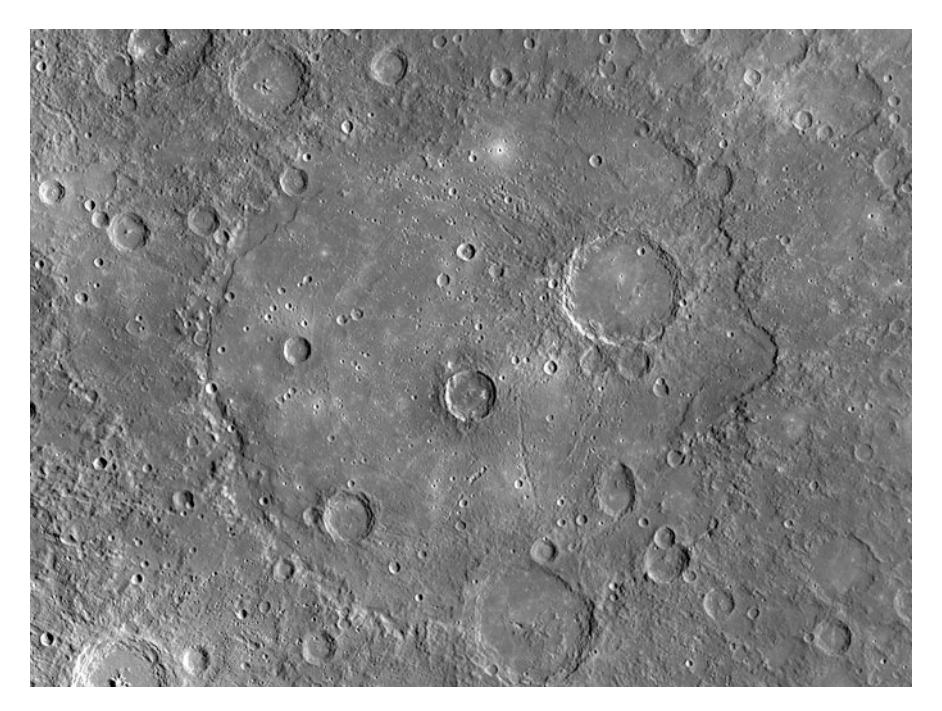


Fig. 4.30 MDIS orbital mosaic including Beethoven. The area is 930 km wide, centred at 123° W, 21° S and is shown on a Transverse Mercator protection (NASA/Johns Hopkins University Applied Physics Laboratory/Carnegie Institution of Washington)

4.4.4.3 Beethoven

Beethoven (630 km diameter) appears to be a more ancient basin than Caloris (probably late Tolstojan), having the 140 km crater Sayat Noya superimposed across its southern rim and the equally large crater Bello on its floor (Fig. 4.30). Beethoven's floor is flooded by lavas that embay the scarp formed by its uplifted rim on the east. Bello is clearly younger than these plains lavas because its ejecta blanket and trains of secondary craters traceable to it have been superimposed. In contrast to Caloris and Rembrandt, there is no sign of a radial fracture pattern near the basin centre, but there are hints of circumferential ridges about 150 km in from its western rim.

Just inside Beethoven's western rim, the basin fill has been thrust westwards against the rim to form a 700 km long scarp, in an arc of nearly 120°. This is much more dramatic than the similarly situated scarp in the Sobkhou basin, and is named Duyfken Rupes, after the Dutch ship captained by Willem Janszoon that made the first European landfall in Australia in 1606.

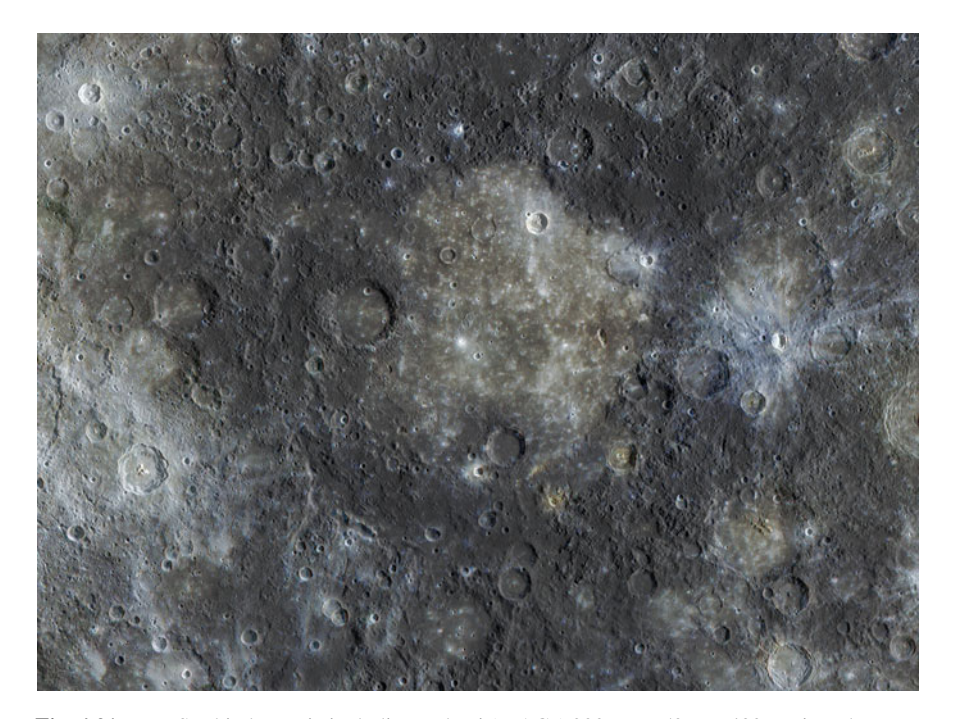


Fig. 4.31 MDIS orbital mosaic including Tolstoj (WAC 1,000 nm, 750 nm, 430 nm in red, green, blue superimposed on a NAC base). The area is 930 km wide, centred at 165° W, 16° S and is shown on a Transverse Mercator protection. This area is approximately the lower-right quarter of Fig. 2.16 (NASA/Johns Hopkins University Applied Physics Laboratory/Carnegie Institution of Washington)

4.4.4.4 Tolstoj

Tolstoj (490 km diameter) was prominent in Fig. 4.5 thanks to low reflectance blue material surrounding high reflectance red plains. The higher resolution colour view in Fig. 4.31 shows that the plains-fill is off-centre, leaving a >100 km wide belt of low reflectance blue material exposed on the west and south of the floor (possibly impact-melt from the basin-forming event), whereas most of the low reflectance blue material to the north and east is ejecta excavated by the impact. This is one of the oldest moderately well-preserved basins on Mercury (it defines the base of the Tolstojan system) and is one of the least lava-filled, both of which make its rim hard to see. The western rim passes about 80 km west of the 95 km crater Liszt, which is the largest crater on Tolstoj's floor.

4.4.4.5 Aneirin

This 430 km diameter basin (Fig. 4.31) has a prominent 140 km crater across its western rim that was named Dario (after a Nicaraguan poet) on the basis of Mariner

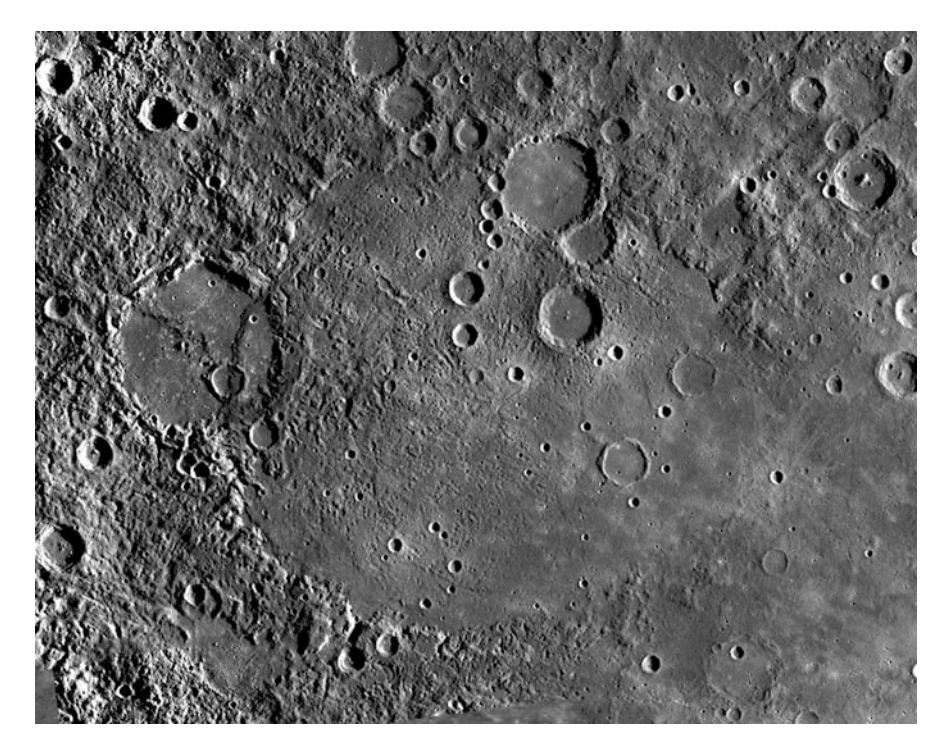


Fig. 4.32 MDIS orbital mosaic including Aneirin. The area is 750 km wide, centred at 3° W, 27° S and is shown on a Transverse Mercator protection (NASA/Johns Hopkins University Applied Physics Laboratory/Carnegie Institution of Washington)

10 images. These had Dario on the dawn terminator, whereas the larger basin was in darkness. It remained unsuspected until revealed by MESSENGER and eventually named Aneirin, after a sixth century Welsh poet. The basin is pretty-much brim-full with lava, and in fact the easternmost part of its rim has been flooded over to merge with plains lavas that extend hundreds of km further east.

A sequence of events can be deduced by consideration of relationships visible in Fig. 4.32. The basin was formed by impact, and there was time for subsequent impacts to make at least two 40 km craters on the east of its floor before the whole basin was flooded by lavas, leaving their rims visible as ghost craters. Dario is clearly younger than the Aneirin, but it is unclear whether Dario's ejecta on the basin floor overlie or are embayed by the basin-filling lavas. However, Dario's smooth floor suggests that it too became flooded by lavas, which also covered the floor of a 30 km crater that had formed on the southeast of Dario's floor.

It is what happened next that makes this area especially notable. Aneirin's basinfill was thrust westwards over the basin rim in the same manner as described for Sobkou and Beethoven, and the fault scarp continues across the floor not only of Dario but also of the 30 km crater within it. The fault scarp has to be younger than both those craters, and the most plausible explanation is that it is the surface expression of a thrust that took advantage of the underground interface between the basement to Aneirin and its lava-fill, despite the near-surface disruption caused by the Dario-forming impact.

4.4.4.6 Goethe

The high northern 320 km basin Goethe that was featured in Fig. 4.12 is worth revisiting in the context of tectonised basin-fill. If you look back at that figure, you will see that pretty much the whole of the basin edge is marked by either a lobate scarp or a wrinkle ridge, suggesting that the basin-fill has been thrust outwards over the basin-rim.

4.4.4.7 Smaller Flooded and Tectonised Basins

Outward thrusting of basin-fill continues down to smaller sizes. Figure 4.33 shows two adjacent approximately 280 km examples that lie 2,000 km north of

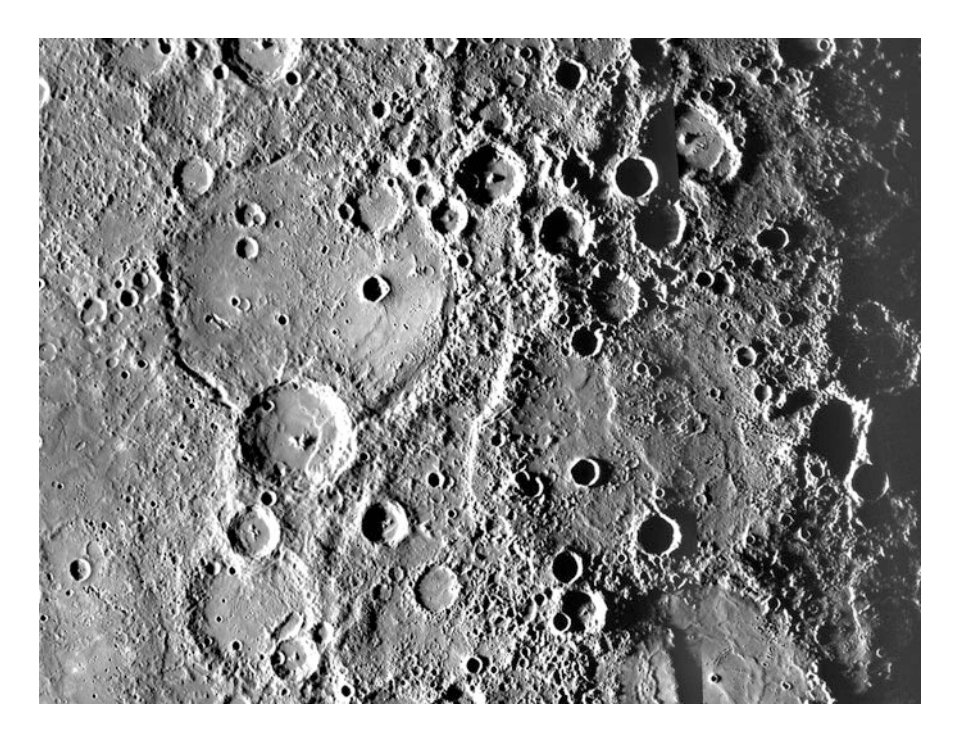


Fig. 4.33 MDIS mosaic based on fly-by images, including 280 km lava-filled and tectonised basins at upper left (Hafiz) and lower right (un-named). The area is 840 km wide, centred at 83° E, 18° N and is shown on a Transverse Mercator protection. The eastern edge of the image is a join between terminators, as in Fig. 4.26 (NASA/Johns Hopkins University Applied Physics Laboratory/Carnegie Institution of Washington)



Fig. 4.34 Sketch cross section (vertical scale exaggerated) showing how crustal compression could be expected to use the interface between basin-fill and basin-floor to localize faults. In this example, a westward-verging fault at depth reaches the basin floor and the displacement then propagates to the surface along a westward thrust and an eastward backthrust, localized at the interface between the two units

Rembrandt. The northwesterly of the two (named Hafiz after a Persian poet) to have an outward thrust fault following most of circumference the basin-fill, except were overprinted by later craters. Its un-named neighbour to the southeast is virtually brim-full with lava, and is discernable in Fig. 4.33 thanks only to the grazing incidence illumination. Along its western margin the basin-fill appears to have been thrust right over the basin rim. There is also a north–south lobate scarp crossing the centre of the basin that appears to be part of a 2,000 km long thrust belt of which Blossom Rupes (about 400 km south) is the only named component.

So, whereas some thrust systems such as the example in Fig. 4.33, Beagle Rupes (Fig. 4.22) and Enterprise Rupes (Fig. 4.26) cross basins, others are localized at the edges of basins. This may be because, as suggested in Fig. 4.34, the interface between the basin-fill lavas and the basin floor is a junction that acts to concentrate stresses so that a fault develops here rather than anywhere else.

4.4.4.8 Rachmaninioff

At 280 km diameter, Rachmaninoff is a peak-ring basin slightly bigger than Vivaldi (Fig. 2.4) and Michelangelo (Fig. 4.4). Between the peak-ring and the outer rim the terrain is mostly low reflectance material, rugged where the primary basin-floor is exposed and smooth where impact melt (of identical composition) has ponded. However inside the peak-ring the whole floor has been flooded by high reflectance red plains lava that breaches the peak-ring in the south and floods part of outer ring. The density of superimposed impact craters is low suggesting that although the basin is Calorian (perhaps 3.6 billion years in age), the flooding of the central region is considerably younger and may have occurred as recently as 1.0 billion years ago. This is in contrast to all previous examples of basin-filling plains, which are of Calorian age. The high-albedo region in the southeast of the outer ring is spectrally red, and is an example of a probable explosive eruption deposit of a widespread kind that will be discussed in Sect. 4.4.5.2.

The pattern of concentric fractures in the basin-fill of the inner ring cannot be well explained either by isostatic uplift of the basin floor or by subsidence due to lava loading. Instead they probably result from thermal contraction as the lava cooled (Fig. 4.35).

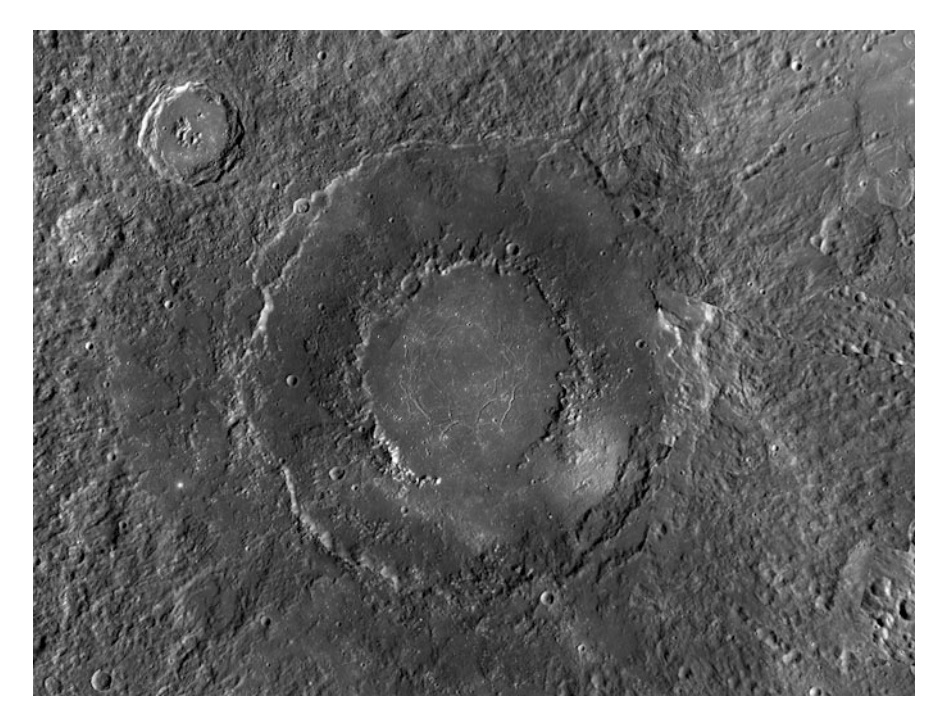


Fig. 4.35 MDIS orbital mosaic including Rachmaninoff. The area is 580 km wide, centred at 58° E, 26° N and is shown on a Transverse Mercator protection (NASA/Johns Hopkins University Applied Physics Laboratory/Carnegie Institution of Washington)

4.4.4.9 Raditladi

Raditladi (Fig. 4.36) is slightly smaller than Rachmaninoff, with a diameter of about 260 km. Concentric fractures form a similar pattern, suggesting a common origin. However, based on the low density of craters superimposed on its ejecta it formed much more recently, and a date as young as 1.3 billion years has been suggested. There was a much shorter time gap between formation and flooding in this case, because the high reflectance red plains lavas that flooded the floor within the peak-ring and also much of the outer annulus too seem to be only slightly younger than those at Rachmaninoff. Given the uncertainties in the crater-counting statistics, we cannot rule out the possibility that the red plains within Raditladi are impact melt rather than lava.

4.4.4.10 Final Words on Basins

Only a small subset of basins has been illustrated here. A survey of impact basins of Mercury published in 2012 listed twenty 'certain' basins in excess of 300 km diameter and 26 'possibles'. Most have lava-fill, and where it has been dated by

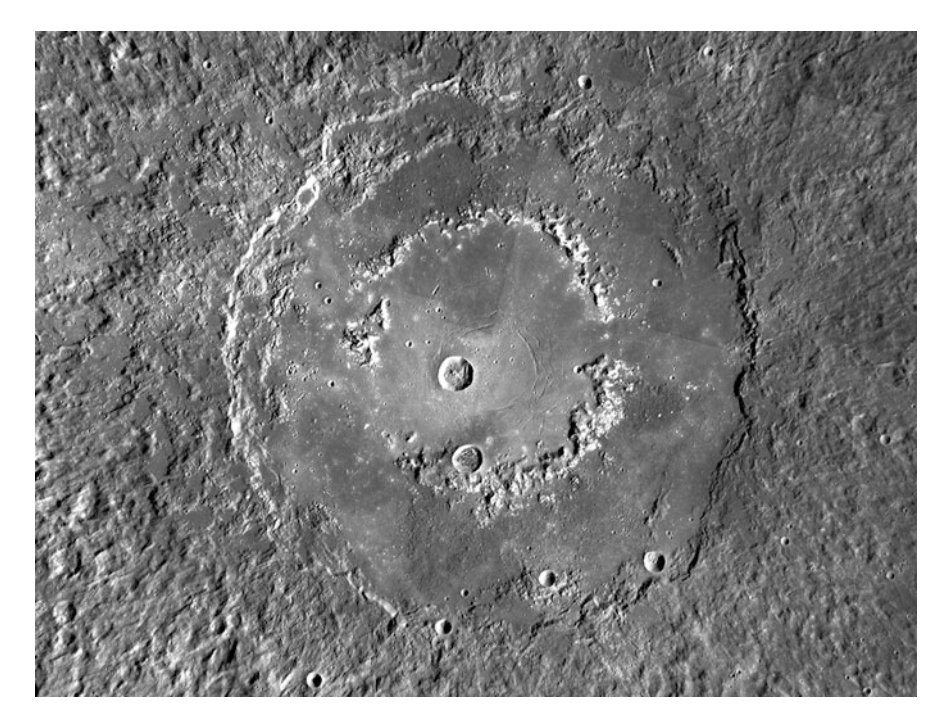


Fig. 4.36 MDIS orbital mosaic including Raditladi. The area is 440 km wide, centred at 119° E, 26° N and is shown on a Transverse Mercator protection (NASA/Johns Hopkins University Applied Physics Laboratory/Carnegie Institution of Washington)

crater-counting this is of Calorian age except in a few younger (and smaller) basins such as Rachmaninoff and Raditladi.

Basin-fill of Calorian age has been thrust towards, and sometimes over, the basin rim in several cases. Of 90 basins greater than 200 km in diameter about a third show signs of tectonism at the edges of their fill, whereas the proportion falls below 10 % for basins in the 100–200 km size range. In cases where it is possible to date the thrust movement, it seems to have happened no more than a couple of hundred million years after the plains emplacement. There are as yet no documented examples of basin-fill thrusting significantly younger than Calorian age, in contrast to those compressional tectonic features that are not related to basins where more recent (even possibly Kuiperian) examples are known (Sect. 4.4.3.5). This may simply reflect less thorough study rather than a real difference.

4.4.5 Volcanism

Revealing the extent, diversity and duration of volcanic activity was one of MESSENGER's most notable achievements – at least, from my perspective as a

volcanologist. Effusive volcanism (lava flows) was suspected but unproven on Mariner 10 images, whereas there was no previous evidence of explosive volcanism at all

4.4.5.1 Effusive Volcanism

As already described (Sect. 4.2), every extensive surface on Mercury that is not an impact crater or an impact ejecta blanket seems to have been emplaced as lava flows. You have already seen abundant evidence of this in the form of ghost craters and embayment of older units by younger. This plains-forming process has been going on episodically since as far back as we can trace (during the late heavy bombardment), continuing at lessening rates until as recently as about a billion years ago, for example the inner-ring plains of basins such as Rachmaninoff and (probably) Raditladi. We have also established (Sect. 4.3.2) that the lava composition is variable but essentially similar to various kinds of Mg-rich, Fe-poor basalt – a composition with low viscosity when molten.

Within plains, the vents responsible for the lava eruptions have not been identified. This is a property shared with the Moon, and is an understandable consequence of plains formation by low viscosity lavas that buried/flooded their own source vents, and whose final stages of growth could have been by inflation of a crusted lava from below. In contrast to the Moon where it is more often possible, individual lava flows can only rarely be made out, nor are there compelling candidates to be narrow channels analogous to lunar sinuous rilles that could be interpreted as collapsed lava tubes or narrow lava-eroded valleys. However there are places where broad valleys up to 30 km wide and a few hundred metres deep (Fig. 4.37) are prominent. These link expanses of smooth plains and their appearance, including midstream streamlined 'islands', is strongly suggestive of scouring by erosive lava as it spread from one plains region to the next. There are no comparable examples on the Moon, but similar braided channels are known on Mars and Venus.

These features were first recognised on Mercury on MESSENGER images, and in 2013 were allocated names on a newly-chosen theme of abandoned cities and settlements. At the same time, the only three named features previously catalogued as valles on the basis of Mariner 10 images were recognized to be chains of secondary craters, and redesignated as catenae.

Figure 4.37 is a good example of a MESSENGER-era vallis. Here lava seems to have flowed from flooded areas near the edge of the northern volcanic plains, travelling southeast along a 20 km wide valley named Angkor Vallis and flooding into (and beyond) a 136 km diameter peak-ring crater named Kofi. Streamlined 'islands' near the inlet and outlet of Angkor Vallis attest to the erosive power of the lava at the peak of its flow. If flow was turbulent, which is feasible for low viscosity lavas at high eruption rates, erosion would have been partly mechanical although thermal erosion was probably more important.

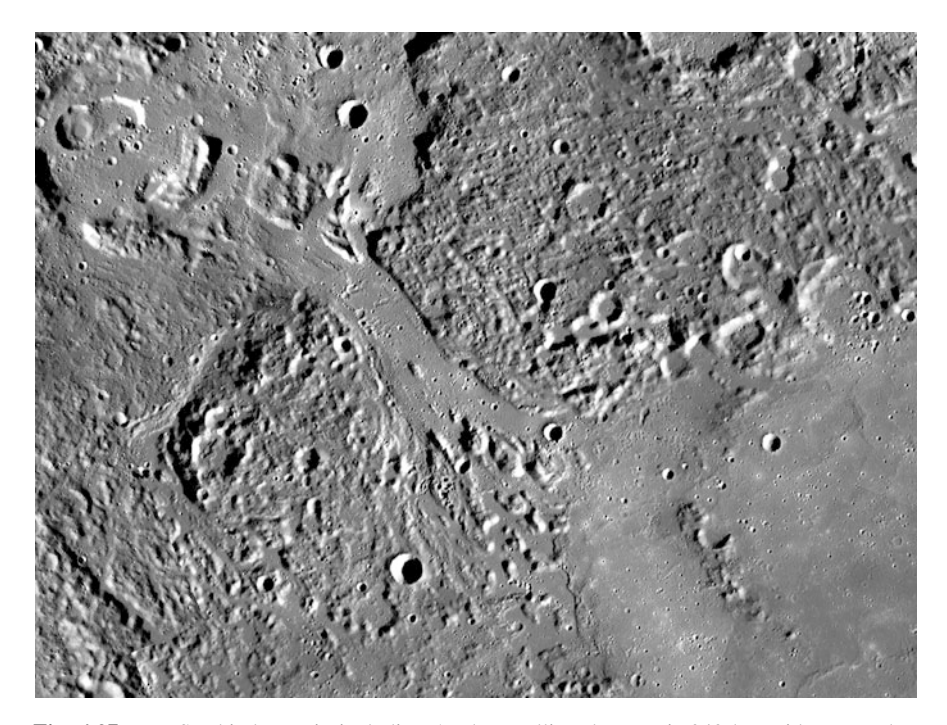


Fig. 4.37 MDIS orbital mosaic including Angkor Vallis. The area is 240 km wide, centred at 114° E, 58° N and is shown on a Transverse Mercator protection. The flooded peak-ring basin partly visible in the southeast is Kofi (NASA/Johns Hopkins University Applied Physics Laboratory/Carnegie Institution of Washington)

4.4.5.2 Explosive Volcanism and 'Red Spots'

Vents accepted as sites of explosive eruptions are more common and more prominent on Mercury than on the Moon. Well over three hundred have been identified. They consist of holes in the ground referred to in much of the literature as 'pits'. This is a useful term because it maintains a distinction on the one hand between pits (probable volcanic vents) and 'craters' (which are understood to be impact craters), and, on the other hand, a smaller-scale landform designated as 'hollows' that you will meet in the next section.

Mercury's pits are several km or a few tens of km in width and up to 4 km deep. Their perimeters are mostly smoothly curved but they are not circular nor even elliptical in shape, which distinguishes them clearly in most cases from impact craters. The surface surrounding the majority of examples is spectrally red out to a distance of as much as 130 km, which earned them the name of 'red spots' (Sect. 4.2.2) during the flyby phase of exploration. The outer edge of each red spot is diffuse, and so these were rapidly accepted as deposits made by explosive ('pyroclastic') eruptions originating at the central pit. Three examples occur in and around Rachmaninoff, as seen in Fig. 4.38. Of more than 300 pits identified, only

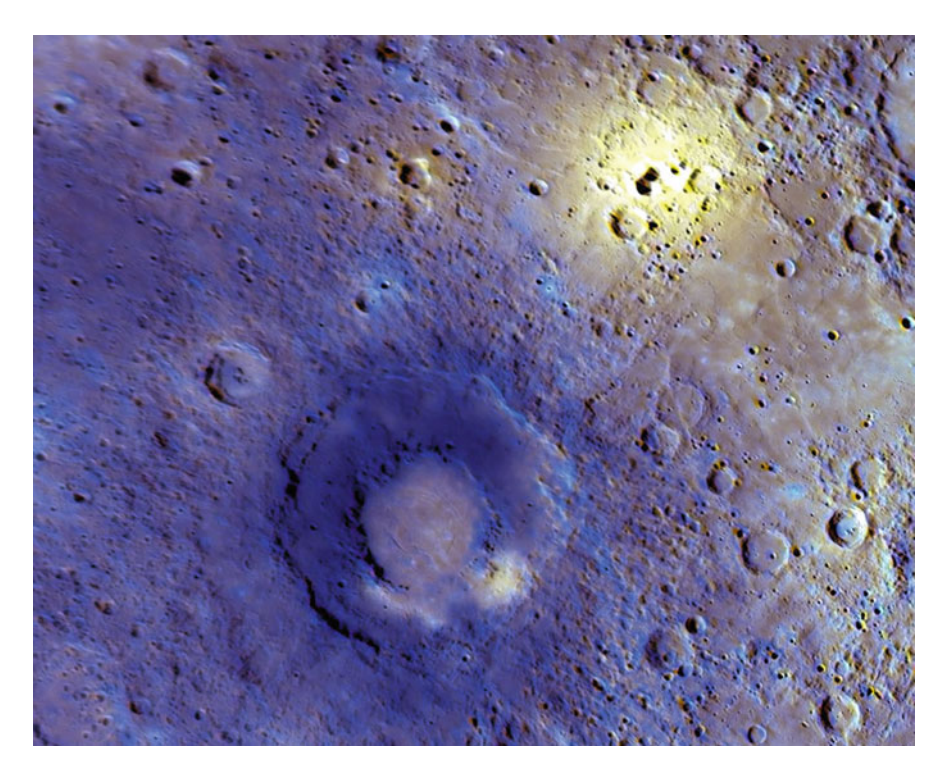


Fig. 4.38 910 km wide exaggerated WAC colour image of Rachmaninoff and the surrounding area (compare Fig. 4.35). There are three 'red spots', which appear yellow in this rendering. The largest lies to the northeast of the basin, and the shadow inside its non-circular 4 km deep central pit is prominent. This is the most extensive pyroclastic deposit on the planet (visible on Fig. 4.8), and is about 260 km across and at least 100 m thick close to the vent. A more subtle example surrounds a larger pit due north of the basin. A third occurs in the southeast part of Rachmaninoff's outer ring, no vent-pit being visible at this scale (NASA/Johns Hopkins University Applied Physics Laboratory/Carnegie Institution of Washington)

about 20% have no surrounding red deposit. Some of the latter may have a different origin, but in most cases the explanation is probably that the pyroclastic deposit was thin and has been degraded below the limit of visibility by the combined effects of space weathering and impact gardening.

An explosive eruption must be driven by the force of expanding gas within the volcanic conduit that leads to the surface. There are two ways for this to happen. One way is if the original magma contains sufficient dissolved volatiles that will come out of solution ('exsolve') to form gas bubbles during the magma's ascent towards the surface when progressively lower confining pressures are encountered. For such an eruption to be explosive, the bubbles must eventually expand with sufficient violence to shatter the magma into fragments. On Earth, the main magmatic volatiles are water, sulfur dioxide and carbon dioxide. The other way is for magma to encounter and mingle with volatiles just before it reaches the surface. On Earth, magma rising into water-saturated ground can erupt explosively because



Fig. 4.39 A 330 km high umbrella-shaped eruption plume on Io, imaged by New Horizons during it passage of the Jupiter system in 2007. This image was recorded in visible light, and is overexposed on the dayside to reveal features on the nightside (illuminated by light reflected from Jupiter) and also to show the plume to best effect. There is an incandescent spot at the source, which is a volcanic vent named Tvashtar (Credit: NASA/Johns Hopkins University Applied Physics Laboratory/Southwest Research Institute)

of the violent expansion of steam, in what is called a phreatic eruption. Depending on the source of the volatiles and on the nature of the vent through which the eruption takes place, material propelled upwards and outwards from the vent by the force of expanding gas can lie anywhere on a compositional spectrum ranging from entirely fragments of magma through to (in the extreme phreatic case) no magmatic content at all and entirely fragments of pre-existing rock blasted apart when the heat of the magma flashed the volatiles into gas without any magma being erupted at all.

The style of eruption in the airless conditions of Mercury would be like the eruption plumes seen on Jupiter's moon Io (Fig. 4.39) in which even dust-sized ejecta particles follow ballistic trajectories from vent to surface, rather than on Earth where air can be drawn in and heated, so that convection causes an eruption column to rise high above the vent. The scale of dispersal on Mercury would tend to be less than on Io because of Mercury's stronger gravity.

Io's eruptions have been observed in progress and analysed spectroscopically, so we know the main volatile phase to be S and/or SO_2 . On Mercury, we do not know what the volatile phase is. Candidates include S, Cl, C compounds such as CO, and H_2O . Any of these could be magmatic, but S and possibly Cl are also candidates for becoming incorporated just below the surface, in the hermean equivalent of a phreatic eruption.

Pyroclastic deposits on Mercury extend similar distances from vents as found for lunar examples, but Mercury's surface gravity is twice that on the Moon, so to propel material the same distance requires a higher volatile content on Mercury. Calculations for magmatic volatiles required to produce the most widely-dispersed explosive deposits seen on Mercury suggest about 20,000 ppm (parts per million) if the volatile is H₂O, about 30,000 ppm if it is S or CO, and nearly 70,000 ppm if it is SO₂. These values are about an order of magnitude higher than the volatile burdens found in terrestrial basalts in settings excluding island arcs (where volatiles are boosted by subduction and recycling), and are an important line of evidence that Mercury is rich in volatiles, to add to the XRS and GRS data in Sect. 4.3.1.

Mercury's red spots are generally too small for their elemental composition to be determined by MESSENGER instruments, but swiveling MESSENGER to allow its XRS to 'stare' at the largest example, northeast of Rachmaninoff (Fig. 4.38), as it

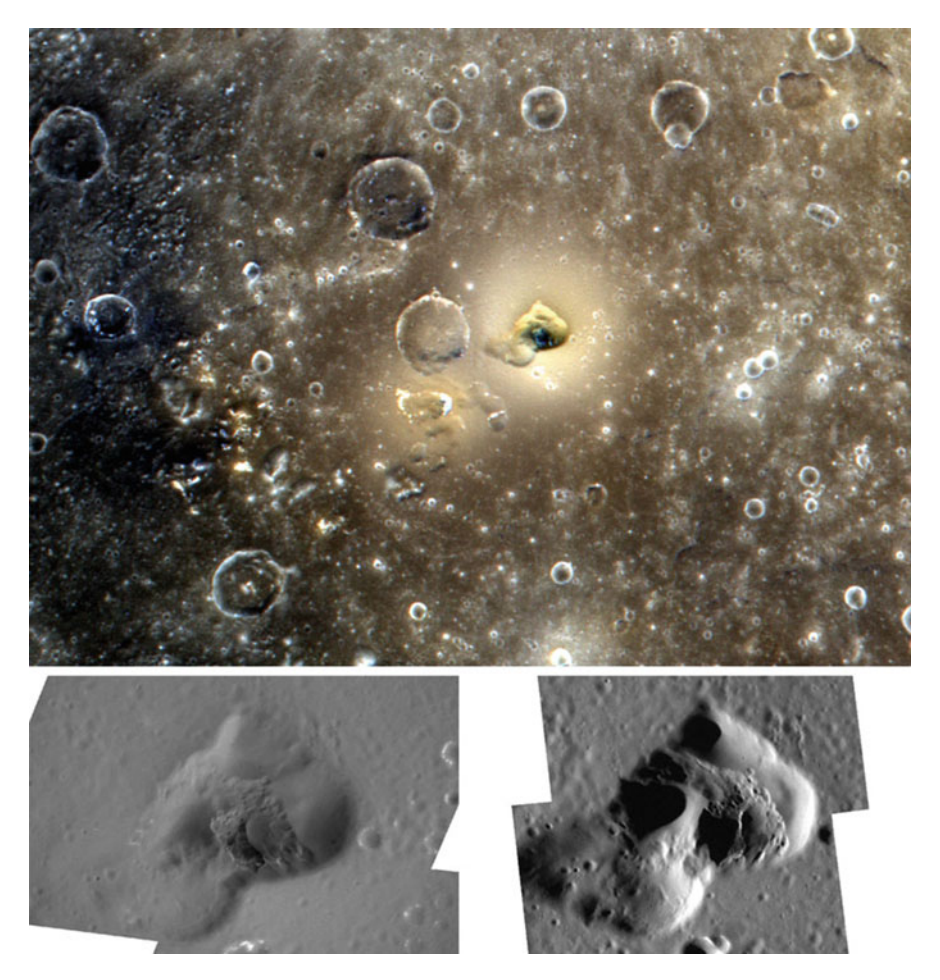


Fig. 4.40 *Main* image: 280 km wide MDIS WAC colour view (using the same channels as Fig. 4.31) of the 'RS3' area in the southwest of Caloris. Note the irregular shaped 'pit' near the centre, and its surrounding 'red' pyroclastic deposit (which is pale yellow in this rendering). The southwestern rim of the Caloris basin passes a little way inside the western edge of this view, and is marked by the colour change from high reflectance red plains inside the basin and low reflectance blue plains beyond. *Below*: two MDIS NAC images at 20–30 m per pixel, of the pit at different Sun angles, showing the multiple overlapping volcanic vents contained within it (NASA/Johns Hopkins University Applied Physics Laboratory/Carnegie Institution of Washington)

passed overhead has revealed that the deposit is significantly lower in sulfur than the local average. If the pre-eruption material was of similar composition, then it must have lost its sulfur during the eruption, though this does not prove that sulfur volatilization was the explosive driver. We will probably have to wait for BepiColombo before we can find out more.

One of the nicest examples of an explosive vent lies 100 km inwards of the southwest rim of the Caloris basin (Fig. 4.40) and was designated as 'Red Spot 3' or

'RS3' when it was discovered on images from the first flyby. The pit is about 25 km long and about 12 km wide, and is surrounded by a spectrally red deposit at least 50 km in diameter (there is a smaller 'red spot' surrounding a pit centred 38 km southwest).

The RS3 pit contains several pits within it, best revealed by the high Sun-angle NAC image in the lower right of Fig. 4.40. These are probably sites occupied by a volcanic vent that migrated within the periphery of the overall structure, making this what would be described in Earth as a 'compound volcano'. There are three vents in the western half, two in the east, and three or four smaller central vents. Cross-cutting relationships show that the central vents are younger than the vents to either side. They also have a particularly fine-scale internal texture, best seen in the low Sun-angle NAC image. This lack of smoothing by regolith-forming processes or mantling either by impact ejecta or pyroclastic deposits is consistent with a younger age, though the most recent activity in these vents could have been collapse into an evacuated conduit rather than explosive eruption.

Topographic mapping by MLA, backed up by shadow analyses, shows that the vent floors are 1–2 km below the brink of the overall pit. On the other hand, the brink of the compound vent is not at the summit of a volcano, as such. It is at most about 100 m above the surrounding plains, so that the volume of erupted material in this case could be less than the total volume of the resulting pit. This suggests magma withdrawal to undermine the pit. The vents have shallow-V-shaped profiles and lack the steep-sided, flat bottomed form typical of volcanic calderas formed by piston-subsidence along ring-faults, so subsidence was more likely by incremental collapse of the walls of the volcanic conduits.

The orientation of the elongated RS3 compound vent and alignments of some other vents in this part of Caloris suggest that the magma may have been supplied via radial dykes associated with the Pantheon Fossae system. As noted in Sect. 4.4.4.1, grabens that might overlie such dykes cannot be traced this far from the basin centre, though they might be too deep below the surface or too narrow to manifest themselves on the landscape. Whatever the magma supply route, it is clear that RS3 and nearly thirty other candidate vents around the edge of the Caloris plains cut through and so are younger than the plains-forming lavas.

Outside of Caloris (which itself is an impact crater, of course) the majority of vents are inside impact craters. Figure 4.41 shows two examples: an arcuate pit where we might expect part of a peak-ring to lie below crater-filling plains inside a 130 km crater named Picasso, and an arcuate put surrounding where a central peak might once have been inside a smaller crater. The shapes of these pits are probably controlled by faults and fractures that occurred during the impact that formed the host crater. Other examples are known where a pit wraps around, or even completely encircles, a surviving central peak. The spatial association with faults and fractures suggests that these provided the pathways for magma and/or volatile ascent, which elsewhere would have been made or difficult by the overall compressional tectonic regime caused be Mercury's global contraction.

The small extent of the pyroclastic deposits limits the reliability of dating them by crater counting, even for those thick enough to distinguish between partly-buried

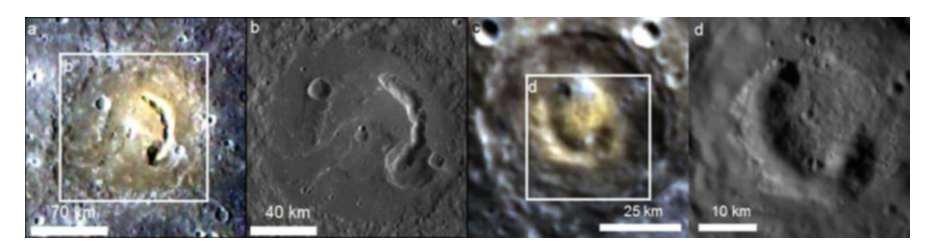


Fig. 4.41 (a) MDIS WAC colour view of Picasso $(50.1^{\circ} \text{ E}, 3.4^{\circ} \text{ N})$ using the same channels as Fig. 4.31. The outline traces the approximate limit of the pyroclastic deposit, and the *box* locates (b). (b) NAC view revealing details on the floor of Picasso. Apparent flow-fronts in lavas that probably pre-date the most recent explosive activity can be seen on the floor west of the actuate pit. (c, d): a similar pair of images of an arcuate pit inside an unnamed crater $(111.4^{\circ} \text{ E}, 40.1^{\circ} \text{ S})$ (NASA/Johns Hopkins University Applied Physics Laboratory/Carnegie Institution of Washington)

and superposed craters. All the examples illustrated above except the small deposit inside Rachmaninoff (Fig. 4.38) and the right-hand example in Fig. 4.41 have thick enough deposits and give ages for the bulk of each deposit in the range approximately 3.3–3.7 billion years, which is mid-Calorian until (at youngest) possibly early Mansurian. However later eruptions too thin to bury older craters cannot be ruled out for these, for example from the apparently young looking vents in the central part of the RS3 compound vent.

Fortunately, there is another way to determine the maximum age of a deposit when the vent occurs inside an impact crater, because the vent (and any deposits erupted from it) must be younger than the crater through which it punches. Figure 4.42 shows an example of relatively young explosive volcanism that occurred at a pit inside the crater Kuniyoshi. This crater has fresh-looking terraces and uncertain traces of rays, making it Kuiperian or late Mansurian in age, though a nearby crater of similar fresh morphology (Fig. 4.41c) has definite rays and is more clearly Kuiperian in age. The volcanism at the vent inside Kuniyoshi is therefore highly likely to have occurred within the past billion years, and this might apply also to the extensive field of pyroclastic deposits to its east, where one of the vents (Fig. 4.42d) is of a freshness comparable to youngest vents in RS3.

An interesting consequence of the widespread explosive volcanism apparent at the surface (and probably also in former times that have left no obvious evidence) is that Mercury's regolith in general must include a pyroclastic component, perhaps similar to the droplets of volcanic glass that are ubiquitous in the lunar regolith. Thanks to impact processes this will become dispersed from its original location, and may play a role in darkening and reddening the average spectrum over time.

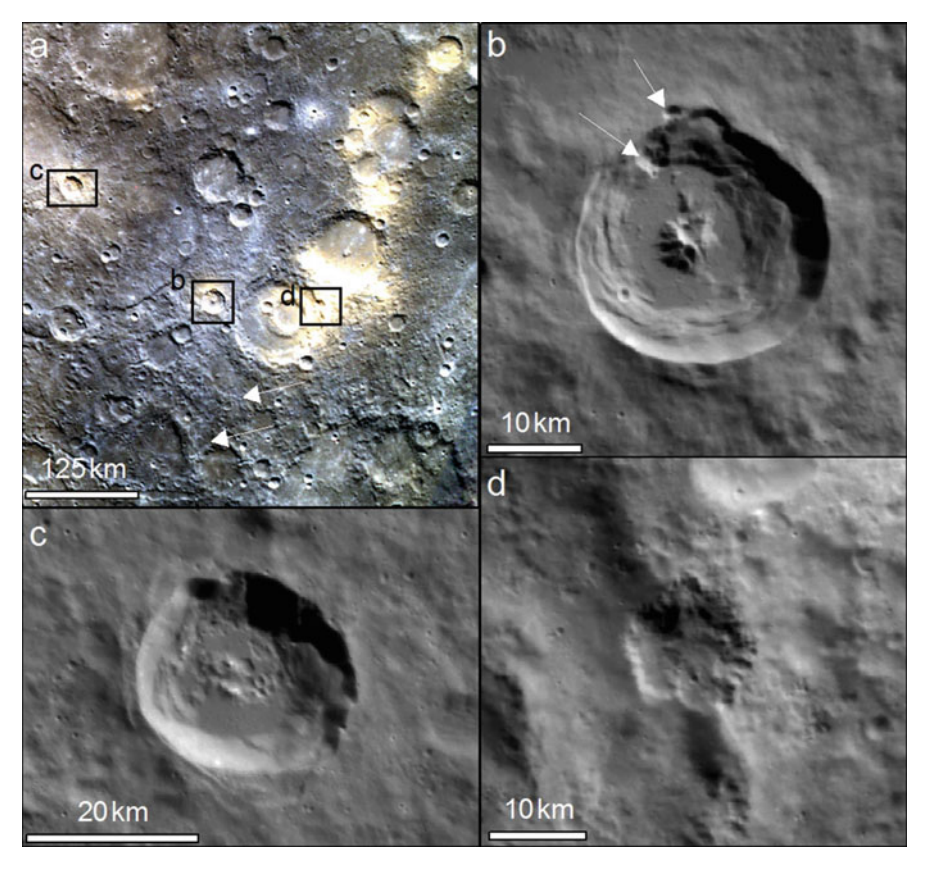


Fig. 4.42 (a) MDIS WAC colour view of the region surrounding Kuniyoshi (37.4° W, 57.8° S) using the same channels as Fig. 4.31. *Boxes* locate the other frames, *Arrows* indicate faint traces of rays that may originate from Kuniyoshi. (b) NAC image of Kuniyoshi. *White arrows* show two vents, one of which clearly punches through the terracing on the inner wall, and so must be younger than the crater. (c) NAC view of a nearby rayed crater, which by definition must be of Kuiperian age. (d) NAC view of a morphologically crisp compound vent in the red spot field to the east, which overlies Tolstojan to Mansurian craters (NASA/Johns Hopkins University Applied Physics Laboratory/Carnegie Institution of Washington)

4.4.6 Hollows

'Bright crater floor deposits' (BCFDs) were noted on Mariner 10 images, which showed them as high albedo patches inside a few craters, but they seem not to have aroused much curiosity at the time. They were more apparent in MESSENGER flyby images, which showed them be spectrally very blue as well as high albedo (Fig. 4.9). Higher resolution images from orbit (Fig. 4.43) reveal that these patches contain a landform now given the name 'hollows' that are individually up to tens of metres deep and several hundred metres across. Hollows have steep sides and flat bottoms. They are markedly smaller than pits, and also much shallower relative to

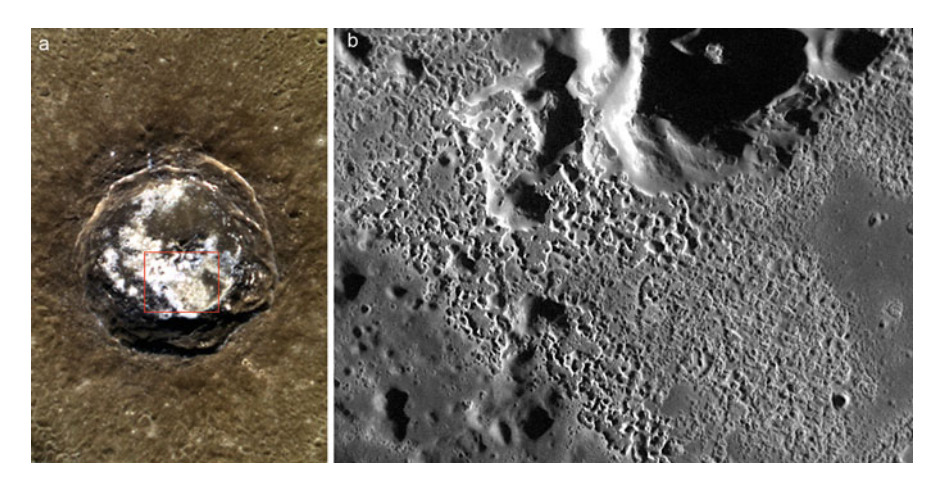


Fig. 4.43 (a) 70 km wide MDIS WAC colour view of Sander crater (114° E, 11° N) using the same channels as Fig. 4.31. The *box* outline locates (b). The bright crater floor deposit inside Sander that is white in this rendering is prominent as a cyan patch in the north of the Caloris basin in Fig. 4.9. (b) 14 km wide NAC image of the south end of Sander's central peak and the adjacent hollowed ground, recorded at 18 m per pixel, which corresponds to the BCFD in (a) (NASA/Johns Hopkins University Applied Physics Laboratory/Carnegie Institution of Washington)

their depth. They are morphologically fresh, and are arguably the youngest landscape class on the planet. Few, if any, impact craters can been seen superimposed upon them even in the highest resolution images.

As well as being distributed across crater floors, hollows also cluster around (Fig. 4.44a) and even upon (Fig. 4.44b) central peaks or on crater rims and terraces (Fig. 4.45b), and sometimes on the proximal ejecta of craters. The vast majority occur where the regional substrate is low reflectance material. Hollows are rare in smooth plains, and where they do occur in such a setting it is usually in a crater that has excavated into an underlying low reflectance substrate, as is the case for Sander (Fig. 4.43).

Hollows clearly represent the removal of about ten or more metres depth of material from Mercury's surface. Nothing about the landform suggests either explosive excavation or collapse into an underlying void. It looks very much as if the top layer has been stripped away, with progressive retreat of the scarp that bounds each hollow. With no wind to cause surface ablation, the only viable explanation would seem to be that this 'stripping away' has occurred through a component of the regolith turning to vapour (and then being either lost to space or redistributed).

For this to happen, the regolith must contain a volatile component that can be lost. Suggested mechanisms for volatile loss include simple sublimation (the substance undergoes a phase change from solid to vapour), thermal desorption (chemical bonds broken by heat, releasing atoms to space), photon stimulated desorption (a process thought to release alkalis to the exosphere), and sputtering caused by solar wind impact and/or micrometeorite bombardment (which vaporizes

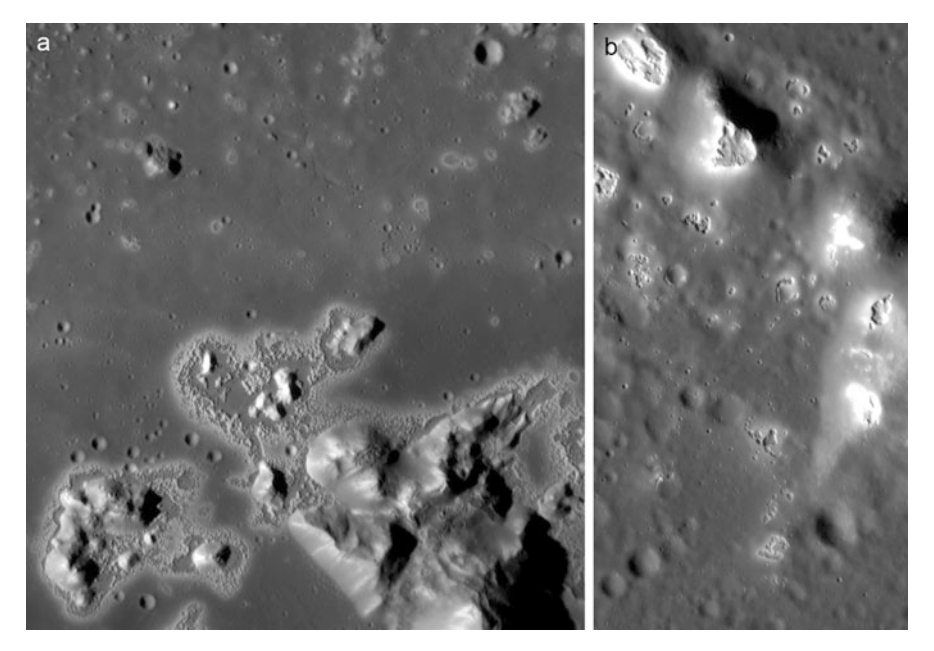


Fig. 4.44 (a) 30 km wide NAC view of an area including the central peaks of Eminescu crater (154° E, 42° N), recorded at 35 m per pixel. (b) 10 km wide NAC image of part of the peak-ring inside Velazquez (55° W, 37° N), recorded at 20 m per pixel (NASA/Johns Hopkins University Applied Physics Laboratory/Carnegie Institution of Washington)

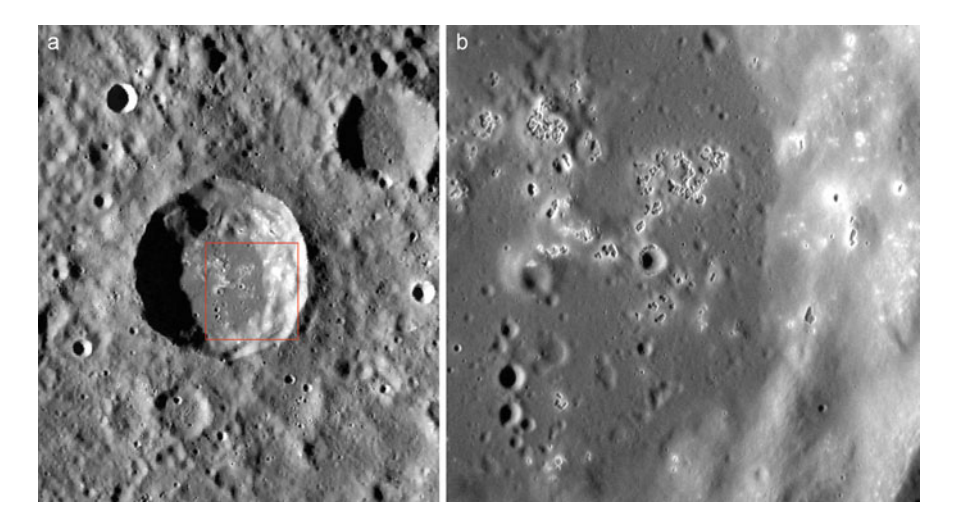


Fig. 4.45 (a) 80 km wide MDIS NAC mosaic centred on an unnamed 35 km crater (41.6° W, 46.5° N). The *box* outline locates (b). (b) 17 km wide NAC image of the crater floor and wall, recorded at 17 m per pixel. The terraced inner wall of the crater in the right of the image has several hollows, though there are more on the crater floor. Note also the 270° arc of tiny hollows on the rim of the 1 km crater in the centre of this view (NASA/Johns Hopkins University Applied Physics Laboratory/Carnegie Institution of Washington)

the target surface). The volatile component is unknown – maybe it is sulfides, or alkalis such as sodium and potassium – but whatever it is unlikely to make up the bulk of the regolith. If the volatile were to constitute 10 % by volume (recall that sulfur is up to 5 % by weight, though at the low spatial resolution of the MESSENGER XRS greater concentration on local scales cannot be ruled out), then a 10 m deep hollow would require loss of all the volatiles from 100 m thickness of regolith, with the accumulation of a 90 m volatile-free lag deposit at the floor of a 10 m deep hollow.

This seems all wrong. We would expect a lag deposit to 'armour' any underlying volatile-bearing material against volatile loss via the surface long before the lag deposit became tens of metres thick, so maybe the volatile substance is able to migrate upwards into the lag as it forms.

The closest planetary analogue to Mercury's hollows is the so-called 'Swiss Cheese' terrain observed on Mars's south polar cap (Fig. 4.46). The name derives from American-style slices of cheese with round holes, rather than a three-dimensional European cheese with bubbles. On Mars the volatile phase is known with certainty and the mechanism of volatile loss is well understood. A layer of pure (or perhaps slightly dusty) carbon dioxide ice sublimes during the warmth of summer. The scarps have been observed to retreat at a rate of about one to three metres per Mars year, and the somewhat cuspate outline of the hollows can be matched to the movement of the Sun as it tracks low across the horizon.

No such explanation for Mercury's hollows is apparent, and furthermore their geographic distribution is entirely different. Hollows on Mercury are confined almost entirely to within 60° of the equator. This applies even after allowing for the dominance of the far north by smooth plains (a surface type that lacks hollows at all latitudes) and for the poor spatial resolution of MESSENGER in the far south. The lack of hollows at high latitudes suggests that surface temperature or solar radiation may be a factor in causing hollows to form. Some support for this suggestion comes from mapping the distribution of hollows by longitude. There is an unexplained spike between 40 and 60° W where hollowed ground covers at least twice the area found in any other latitude bin, but, apart from that, hollowed ground is most abundant near the hot poles (0 and 180° E) and least near the cold poles. Additional support for solar influence comes from hollows on slopes. Over 90 % of hollows are either on flat ground or in a group that spreads across slopes of varied aspect, but fields of hollows in the northern hemisphere that are on a consistent slope have a very strong preference for south-facing slopes (there are too few southern hemisphere examples for a similar analysis).

Thus we are left with a rather frustrating picture. Hollows are strongly correlated with low reflectance material – so whatever the hollow-forming substance is, it seems to be concentrated in that substrate (until it is lost in the hollow-forming process). Hollows are mostly in craters, suggesting that the hollow-forming material is brought to the surface by the cratering process. The high albedo, spectrally blue, BCFD signature is probably an indication of the *absence* of the hollow-forming material, which has already been lost from the areas where hollows are abundant. However there are no MESSENGER data capable of determining what

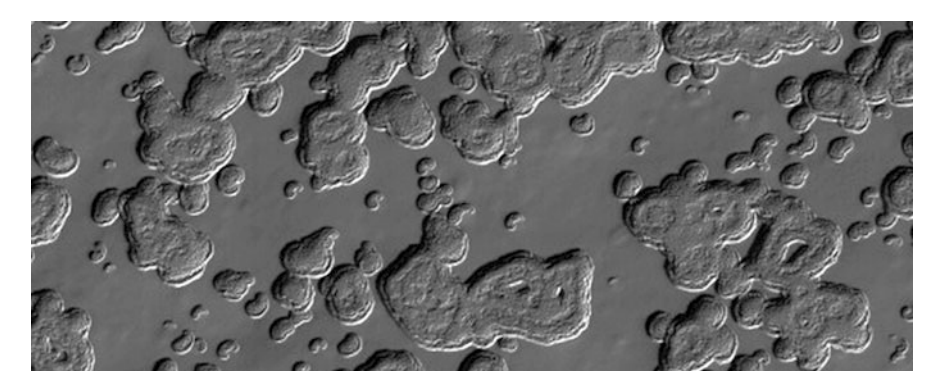


Fig. 4.46 HiRISE image of 'Swiss Cheese' terrain on the Martian south polar cap, recorded at 25 cm per pixel. This image is only 220 m across (Credit: NASA/JPL/University of Arizona)

the BCFD composition is, and we will probably have to wait for BepiColombo X-ray and visible and thermal spectroscopic data to give us a clearer idea.

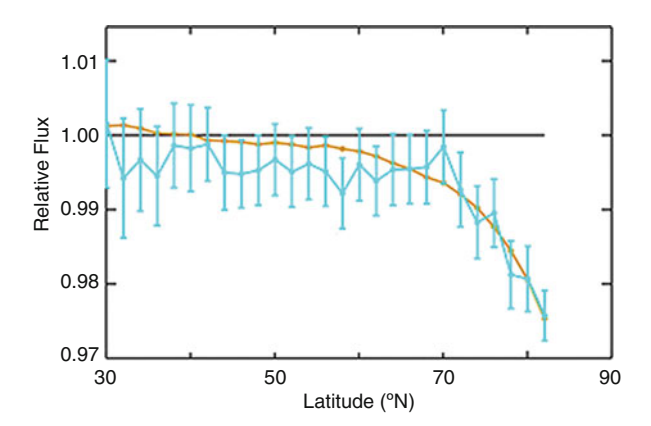
Then there is the issue of the ages of hollows. They all appear young, and occur with similar abundances in craters of all ages. That is perplexing, because if the hollow-forming material had been brought to the surface by the impact, then hollows should not have formed recently in very old craters, and older craters should have more hollows than younger craters. Perhaps we are seeing evidence of volatile migration through the crust, or at least through the regolith, originating in buried low reflectance material. This would allow hollows to continue to form at the present time (which could well be the case), and begs two questions: (1) does hollow formation go on continually, or is it an episodic process? and (2) why do we not recognize any old hollows?

Even if scarp retreat at the edges of any of Mercury's hollows is a rapid as the 3 m per year seen in parts of the Martian Swiss Cheese terrain (which few would regard as likely) it would be very challenging to detect this in MESSENGER images. Targeted high resolution NAC frames were planned for this purpose during the low altitude campaign, but re-imaging of MESSENGER frames more than a decade later by BepiColombo stands a better chance.

4.4.7 Polar Volatiles

MESSENGER's Neutron Spectrometer had as one of its primary goals the investigation of 'radar bright' material that had been detected in permanently-shadowed craters by ground-based radar (Fig. 2.20). The footprint of the neutron measurements was 300–900 km at high northern latitudes, and thus too large resolve individual craters, but the measured decrease in epithermal neutrons fitted very closely to what would be expected if all the radar-bright material were water-ice (Fig. 4.47).

Fig. 4.47 Epithermal neutron flux measured by MESSENGER's Neutron Spectrometer plotted against latitude. Blue line, the actual measurements (with error bars). Brown line, expected flux if radar bright regions were 100 % water-ice (Credit: NASA/Johns Hopkins Applied Physics Laboratory/Carnegie Institution of Washington)



Additional insight comes from mapping the flux of fast neutrons by latitude, which shows the expected poleward decrease though significantly less than would be the case if all the water-ice were at the surface. The best fit to the data is if, on average, the ice is buried by 10–30 cm of ice-poor (strictly, hydrogen-poor) regolith.

The Neutron Spectrometer findings were complemented by other MESSENGER data. Repeat imaging and topographic mapping confirmed the permanently-shadowed nature of the most striking ice-containing craters, and has allowed modelling of the expected surface temperature distribution. Surface reflectance measurements obtained from within permanent shadows by MLA (the laser altimeter) show an essentially bimodal surface: very strongly reflecting in the colder parts of the shadows (<100 K on average) and almost certainly representing exposed water-ice, and low reflectivity in the less-cold cold parts of shadow (100–210 K average), where the ice must be covered by a low albedo material. This is probably carbon rich organic material concentrated as a lag after ice has sublimed. This is consistent with models of the rate of sublimation of water-ice, which suggest that at 102 K a metre-thick layer of pure ice would sublime to space in a billion years, whereas cover by a 10–cm–thick lag deposit would suppress the rate to only a millimeter per billion years.

The reason for the range of temperature inside permanent shadows is because some light is diffusely reflected into them from sunlit crater walls. WAC images obtained through the 395–1,040 nm 'clear' filter are able to collect enough signal from the diffusely-illuminated surfaces inside shadows to show some details, from which counts of small craters may eventually yield age estimates for the deposits. Figure 4.48 shows a model for the water-ice and dark material inside permanent shadows. This is essentially the same as was tentatively concluded from ground-based radar alone, except that concentration of a dark lag at the top of the least-cold ice was not suspected.

Mercury's polar water-ice can be explained with confidence as having been delivered by comets. Thus, its detection adds no weight to the debate over the extent to which Mercury is intrinsically rich in volatiles, though it is possible that a tiny

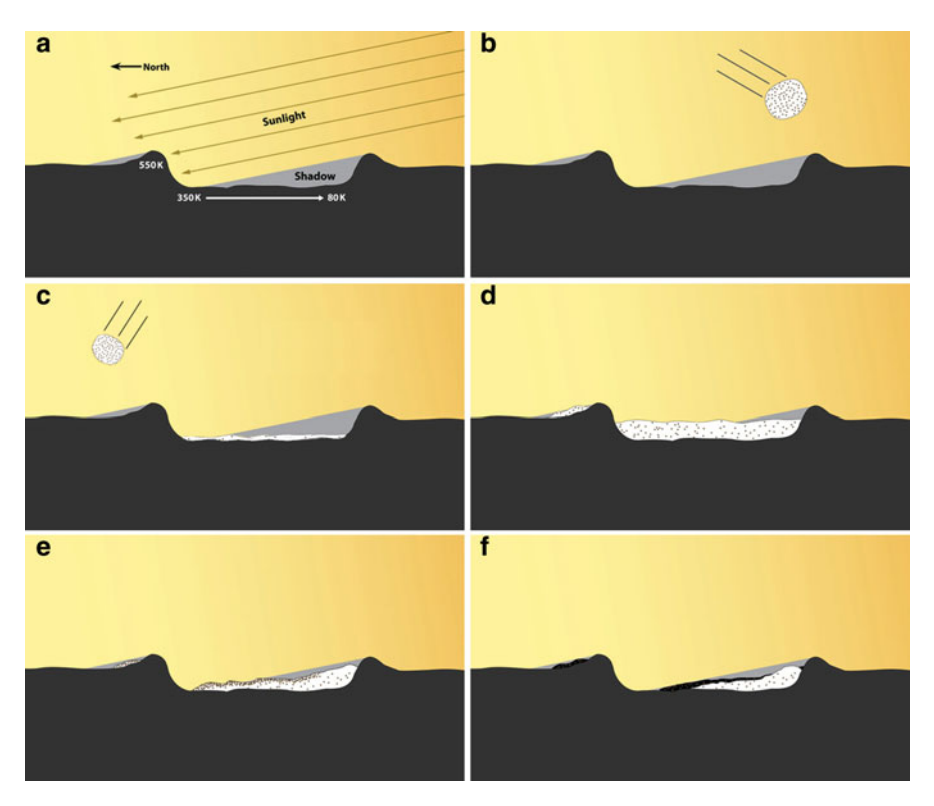


Fig. 4.48 A model for Mercury's polar ice deposits, in a time sequence running from **a** to **f**. (**a**) A permanently shadowed north polar crater, in cross-section. (**b**) A comet containing water-ice (*white*) and organics (*black*) strikes Mercury, hitting the surface anywhere on the globe. (**c**) A tiny fraction of the molecules of water and organics from the vaporized impacted comet ends up in the cold-trap within permanent shadows. Over time many other comets continue to strike the planet, each adding a contribution to the cold-trapped deposits. (**d**) Eventually (after billions of years) the mixed ice and organics build up to a substantial layer within the crater (thickness exaggerated here for clarity). (**e**) Ice sublimes in the warmer parts of shadow, and a lag of less-volatile organics becomes concentrated at the top (in reality, stages **c**-**e** will be concurrent). (**f**) Eventually, the organic lag is thick enough to prevent further sublimation of underlying ice (Credit: Modified after NASA/UCLA/Johns Hopkins Applied Physics Laboratory/Carnegie Institution of Washington)

fraction of the polar ice could have originated as water erupted through volcanoes. However, there are other volatiles on Mercury that seem to be intrinsic to the planet, and that are also concentrated at high (northern) latitudes. These are sodium, potassium and chlorine, all of which were mapped by GRS at inadequate spatial resolution to be sensitive to local variations. In the case of chlorine, its abundance north of 70° N is 0.36 ± 0.08 wt%, which is about three times greater than its northern hemisphere average. Potassium is perhaps even more strongly enriched in the north, whereas the sodium abundance north of 80° N is double the average. The jury is out as to whether these three elements have become concentrated towards the

pole as a result of some kind of thermal redistribution process via the exosphere (as will be discussed in Chap. 6) or became concentrated into the magmas that fed the northern volcanic plains. The picture should become clearer when we are able to use BepiColombo to measure the same elements in high southern latitudes, where extensive volcanic plains are absent.

4.4.8 Mysteries

This tour of Mercury may have left you with the impression that many aspects of Mercury's surface composition remain perplexing, whereas its surface features are better understood. However, it is entirely possible that some landform interpretations are mistaken. There are also various surface features with no accepted explanation, and this chapter concludes with a brief look at some of them.

4.4.8.1 The Sibelius 'Plateau'

One such mystery is what appears to be a plateau, immediately northeast of the 86 km smooth-floored crater Sibelius (Fig. 4.49). My first thought on noticing this was that it is an ancient lava-filled basin that has developed thrust faults around its margin, like an older version of Goethe (Sect. 4.4.4.6). However, the plateau measures about 360 km from southwest to northeast, but only about 265 km from northwest to southeast, so it is probably not sufficiently circular to be a basin. Another possibility is that it is some kind of constructional lava plateau, but if that were the case the plateau edges would be flow-fronts, and their height (several hundred metres) would imply much greater lava viscosity than has been observed elsewhere on Mercury.

Perhaps the answer comes from noticing how little of the feature's perimeter has survived being overprinted by impacts. Moving anticlockwise from Sibelius there is first an old 100 km crater and then an even older and degraded 210 km diameter peak-ring basin. That's about a quarter of the perimeter missing, and a case can be made for a fairly large portion of the northwestern perimeter being defined by overlapping impact craters too. In fact the plateau may be defined merely by the coincidental juxtaposition of a west-facing lobate scarp in the west and a northeast-facing lobate scarp in the northeast, with the intervening parts of the perimeter being nothing more than where impact crater rims cut into the landscape. The northeast-facing lobate scarp is certainly real, because the floors of 20 and 30 km craters superimposed on the northeast perimeter can be seen to be cut by it. Although it is bounded by scarps of one form or another, in the absence of topographic mapping it is not certain that the interior is all high ground. If there is an inward-facing dip-slope behind each of the two lobate scarps suggested above, then the feature as a whole is not even a plateau.

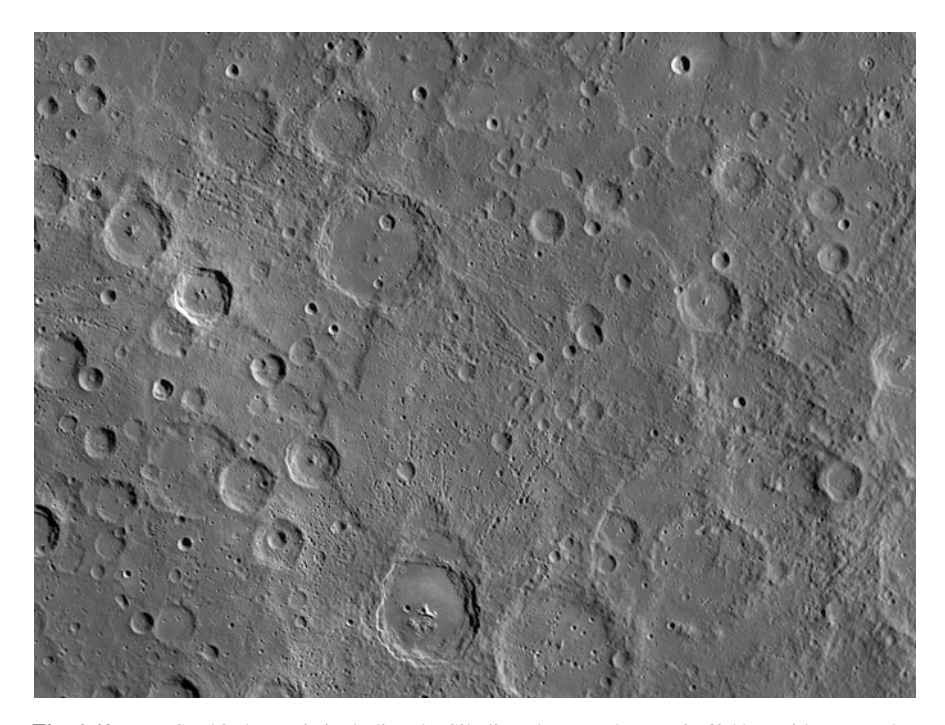


Fig. 4.49 MDIS orbital mosaic including the Sibelius plateau. The area is 685 km wide, centred at 140° W, 45° S and is shown on a Transverse Mercator protection. Silbelius is the central-peaked crater cutting the southern edge of the plateau, and responsible for chains of 3–5 km secondary craters that can be traced across the southern part of the plateau (NASA/Johns Hopkins University Applied Physics Laboratory/Carnegie Institution of Washington)

Sibelius itself is rather strange. Its perimeter is more polygonal than circular, and its northern rim is either double or it overprints a similar sized crater of the same age. Maybe the Sibelius impact was oblique and/or the impactor split into two pieces shortly before it hit.

4.4.8.2 'Catenae'

Uncertainties also abound when it comes to chains of craters, known by the IAU descriptor term 'catena' (Latin for 'chain'). In some cases there is little doubt that such features are caused by serial impact of secondary ejecta, for example Goldstone Catena (formerly Goldstone Vallis, see Sect. 4.4.5.1. This is a 100 km long trough radial to the 120 km crater Murasaki, which has Kuiper superimposed over its northwest rim (Fig. 4.13). Goldstone Catena is shown in more detail in Fig. 4.50a, where the matching outward curves on opposite walls show that it does indeed seem to be made from overlapping 6 km impact craters. There is a shorter, north—south unnamed catena, also radial to Murasaki, near the eastern edge

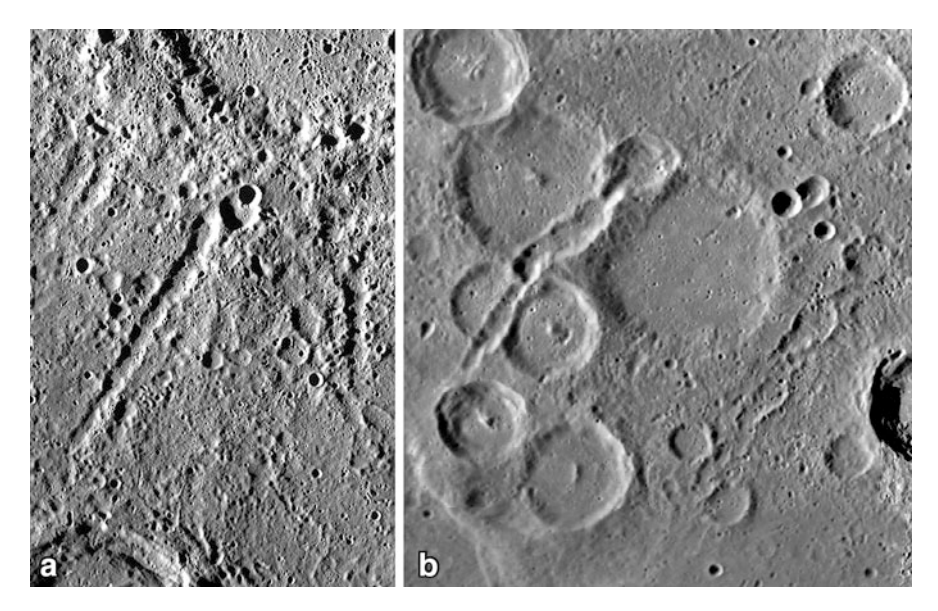


Fig. 4.50 (a) MDIS orbital mosaic including Goldstone Catena. Part of Murasaki crater, to which the catena is radial, is included in the upper right. The area is 140 km wide, centred at 31° W, 16° S and is shown on a Transverse Mercator protection. (b) MDIS orbital mosaic including two unnamed catenae. The area is 195 km wide, centred at 135° E, 11° S and is shown on a Transverse Mercator protection at the same scale as (a) (NASA/Johns Hopkins University Applied Physics Laboratory/Carnegie Institution of Washington)

of the view and a less clear example in the northwest. These are larger scale and more closely coalesced versions of the chains of secondary impact craters radial to Sibelius in Fig. 4.49.

Figure 4.50b shows two unnamed features that resemble catenae but whose origin is much less clear. These are 1,500 km southwest of the Caloris rim, but are not quite radial to it nor are they definitely of earliest Calorian age, which they would need to be were they formed by the Caloris impact. The southeastern of the pair is fairly cryptic, and has probably been largely flooded by lava. The northwestern one is plain to see, but rather than being completely straight its course is kinked to pass between some pre-existing craters in the 30–70 km size range. If this catena was formed by a string of ejecta, then control by local terrain features cannot be explained, so it may be some kind of volcanic or tectonic feature instead. There appears to be a landslide inside a 25 km wide Mansurian crater at its southern end, which may have been triggered by its formation. Several other equally perplexing 'catenae' occur elsewhere on the planet.

4.4.8.3 The Odin Formation

Hummocky plains immediately exterior to the Caloris Montes were mapped in the Mariner 10 era as the Odin Formation. MESSENGER revealed Odin-type plains extending a variable distance up to 500 km away from the basin rim around most of the basin, and showed a characteristic texture of numerous knobs projecting above a smoother surface. The most obvious interpretation is that the Caloris impact threw out lumps of ejecta and a sheet of impact melt. However, the crater-density on the Odin Formation is lower than that seen on Caloris Montes, and also marginally lower than on the interior plains and nearby exterior plains. If this relative dating is correct, then the Odin Formation has to be younger than the Caloris impact so and cannot be directly related to it. It now seems likely that only the knobs are impact-related and the plains that surround them are subsequent lava flows, but this remains contentious. The knobs become smaller away from the basin (which is consistent with their origin as ejecta) but their spatial density shows no outward decrease (which does not seem to fit the ejecta hypothesis).

Images recorded under gazing-incidence illumination (Fig. 4.51) exaggerate subtle features within the plains including possible flow-fronts and intriguing fine-scale fracture patterns.

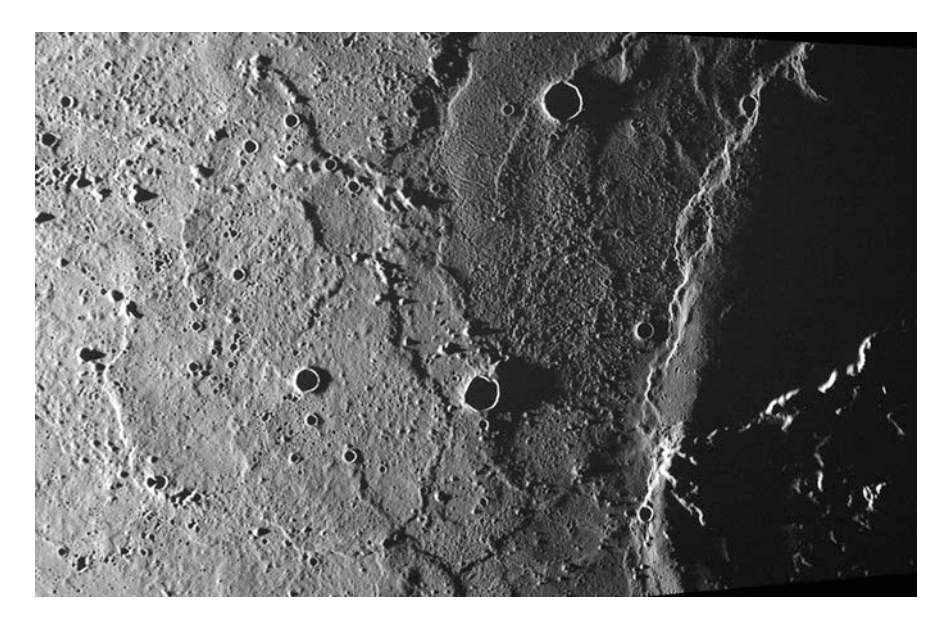


Fig. 4.51 400 km wide MDIS WAC image centred at 74.8° W, 24.8° N and covering part of the Odin Formation east of Caloris. This was recorded at extremely high incidence angle to exaggerate subtle topographic features. Note the 2 km size knobs in the west, the scarp of Schiaparelli Dorsum in the east, and a fine-scale hackly texture immediately west of the scarp which may in fact be widespread but apparent here only because of the grazing solar incidence (NASA/Johns Hopkins University Applied Physics Laboratory/Carnegie Institution of Washington)

4.4.8.4 Space Weathering and Surface Degradation Rates: The Age Old Controversy

In Chap. 2 we pointed out that the absolute ages on the timescale given in Table 2.3 could be considerably in error. We now know that they almost certainly are! MESSENGER has revealed that there are only about half the number of Kuiperian craters per unit area than there are craters of equivalent freshness (Copernican) on the Moon, whereas models for the near-Earth asteroid flux suggest that the impact rate on Mercury should be about 1.8–1.9 *higher* than on the Moon. Putting these two together, the observed number-density of Kuiperian relative to Copernican craters disagrees with the models by a factor of about four.

Comparison of MDIS colour images with similar images from the Lunar Reconnaissance Orbiter Camera suggests that the rate of optical maturation (essentially darkening and reddening) for Mercury surface materials is up to four times faster than for the Moon. Factors responsible for this are likely to include the greater and faster micrometeorite impact flux and the higher temperatures experienced on Mercury. Greater sputtering by solar wind protons striking the surface could also be a factor, depending on how the solar wind interacts with the magnetosphere during extreme events.

This faster rate of optical maturation on Mercury can account for the low number of Kuiperian craters on Mercury because the rays and bright ejecta haloes around young craters fade from visibility faster. It means therefore that the base of the Kuiperian could well be between half and a quarter the age assumed by equating it roughly with the base of lunar the Copernican system, placing it at 0.5–0.25 billion years rather than 1 billion years as in Table 2.3.

Similarly, the number density of Mansurian craters is on Mercury is about 1.2 times that of Eratosthenian craters on the Moon, whereas impact flux models would predict a ratio closer to 2, so the Mansurian period is probably somewhat shorter in duration than the Eratosthenian (and significantly younger given its late end implied by the late start to the Kuiperian). A shortening of the Mansurian makes sense if we consider that the faster rate of impacts on Mercury should also lead to faster degradation.

As our understanding develops we will probably develop models for cratering and space weathering that revise our age estimates, but the degree of trust to place in such models is always debatable. This means that absolute ages on Mercury will remain a matter of controversy at least until there has been a highly sophisticated lander or a series of sample return missions. However age estimates will probably become younger rather than older, so that (for example) the age of the youngest explosive volcanism (Sect. 4.4.5.2) will be pushed more firmly to within the past billion years.

Chapter 5 Mercury's Interior

5.1 Inside a Planet

As noted in Chap. 2, a generic terrestrial planet has a dense metallic core at its centre, surrounded by a less-dense silicate mantle that is overlain by a silicate crust of slightly lower density and slightly different composition. Prior to MESSENGER, the approximate size of Mercury's core had been inferred from the planet's density (though core size now appears to have been underestimated), and the presence of the core's liquid zone had been established from the magnetic field and the amount of libration (Sect. 2.5.4). However the thickness of the crust was unknown, and there were no data that could be used to infer the thickness of Mercury's outer mechanical layer, the lithosphere.

All of the properties mentioned above would be best defined if we could study how seismic waves are propagated through the interior and the depths at which seismic events ('earthquakes') of different types originate. However, until at least a few seismometers can be deployed on Mercury's surface we have to extract what information we can from data that can be obtained from orbit, which is a significant improvement on flyby data. In practice this means using latitudinal variations in gravity in conjunction with planetary parameters to derive Mercury's moment of inertia (explained below) as it spins, and mapping local spatial variations in Mercury's gravity field to probe how internal mass distribution varies with location.

5.2 The Core

5.2.1 The Core's Size

The second-degree (large scale) variations in gravity measured by MESSENGER's Radio Science (RS) experiment as deduced from accelerations experienced by the

148 5 Mercury's Interior

spacecraft were combined with ground-based radar determinations of Mercury's libration and the tilt of its axis (an almost negligible 2.04 ± 0.08 arc min) to derive Mercury's moment of inertia, C. This is a measure of a body's resistance to being spun up or spun down, and is defined by the torque necessary to achieve a given angular acceleration about the axis of rotation.

A sphere of uniform internal density has a value of C expressed by $C/MR^2 = 2/5$ (a value of exactly 0.4), where M and R are mass and radius respectively. The amount by which C/MR^2 of a planet is less than 0.4 tells you how strongly the mass is concentrated into denser internal zones. It could be greater than 0.4 only in the unrealistic case of a planet that was *less* dense on the inside than on the outside.

For Mercury, the new results show that $C/MR^2 = 0.346 \pm 0.014$ (M and R are very precisely known, so most of the uncertainty is in the value of C). For Earth, C/MR^2 is 0.3307, and the higher value for Mercury signifies that an internal zone of high density (its core) comes relatively closer to the surface than within the Earth – indeed it reaches about 200 km closer to the surface than previously thought. In the case of the Moon, C/MR^2 is 0.393, an even higher value than for Mercury, which is because the Moon has only a tiny core (if at all), so that the Moon comes close to having uniform internal density; virtually all its mass is composed of silicates, except for pressure-induced compression in the interior.

There is an infinite number of ways to arrange mass radially symmetrically within a sphere to end up with any given value of C/MR^2 . For a real planet the number of possible solutions is reduced first by allowing only those that are consistent with the bulk density of the planet, and then further reduced by choosing only realistic values for mantle and core densities given the likely compositions, temperatures and pressures of each. For Mercury an additional constraint comes from the ratio between the moment of inertia of the solid outer shell of the planet (everything outside of the liquid zone of the core), known as C_m , and its total moment of inertia, C. This ratio can be calculated from the amplitude of Mercury's libration and other rotational parameters. For Mercury C_m/C works out at 0.431 ± 0.025 , which requires the outer shell to be only about 410 km thick, as opposed to the approximately 600 km that had been the best-fit to the pre-MESSENGER models. Given the planetary radius of 2,440 km, this means a core radius of about 2.030 km.

To maintain the observed coplanar relationship between Mercury's spin axis, the normal to its orbit and the normal to the plane about which its orbit about the Sun precesses (so-called 'Cassini state 1'), it has been argued that there must be some relief on the core-mantle boundary. This would be most simply accounted for if the core is slightly more ellipsoidal in shape than the planet as a whole. Related arguments suggest that the spin axis of the core is displaced from the spin axis of the mantle by about 3.6 arc min.

5.2 The Core 149

5.2.2 The Core's Composition

The bulk of Mercury's core is surely iron, with possibly about 8 wt% nickel if this is present in its cosmic abundance (as in meteorites). However, pure iron (or pure nickel-iron) would be solid throughout the core at under all likely conditions. The well-attested liquid outer core requires one or more lighter elements mixed with the iron in the outer core to depress the melting temperature sufficiently for it to remain molten.

Geochemical arguments now come into play. Mercury's low surface iron content and the abundance of surface sulfur suggest that it formed under (and still experiences internally) conditions that are strongly chemically reducing, and which would encourage both S and Si to be scavenged along with Fe into the core. As the core cooled over time, Fe (plus Ni) would freeze onto a slowly-growing solid inner core but S and Si would tend to stay in the melt. Thus the outer core would become increasingly enriched in sulfur and silicon. Either of these would depress the melting temperature, and would help to keep the outer core liquid even as it cooled. Convection in the outer core would be driven not just by a thermal gradient but also by buoyancy differences as the denser metals accreted onto the solid inner core.

At the relatively low pressure prevailing near the top of the outer core, it is likely that the three main elements iron, sulfur and silicon would not be miscible, forcing iron sulfide to separate. This would have a lower density than the rest of the outer core, and would tend to rise and collect at the core-mantle boundary, leaving the bulk of the outer core to become progressively slightly enriched in Si. Sufficiently vigorous convection might continually stir and remix these components if they were all liquid. However, at the pressure prevailing at the top of the core, models suggest that any iron sulfide is likely to be solid, rather than liquid, so that it would accrete to form a solid roof to the liquid outer crust. This layer has become informally referred to as the 'anticrust'. If it exists, its present thickness may be as great as about 100 km, rivalling or even exceeding the thickness of the traditional surface crust. Growth of the anticrust would densify the molten material from which the sulfur had been extracted, so it would tend to sink, providing an additional impetus to convective motion in the outer core.

There is independent support for the anticrust from some libration and rotation analyses that derive a slightly higher value of C_m/C , which in turn requires a higher 'mantle' density. This can be accounted for by the contribution to average density from an iron sulfide anticrust, which would be at least 10 % denser than mantle silicates.

The radius of the inner core is not constrained by these arguments, but the north—south asymmetry of Mercury's magnetic field is easier to explain if the convecting molten outer core is a relatively thin layer, and it is generally supposed that the inner core makes up about three-quarters of the total core radius. The measured strength of the magnetic field is less than many models would predict, and this could be a result of shielding by the anticrust, because solid iron sulfide is an electrical conductor.

150 5 Mercury's Interior

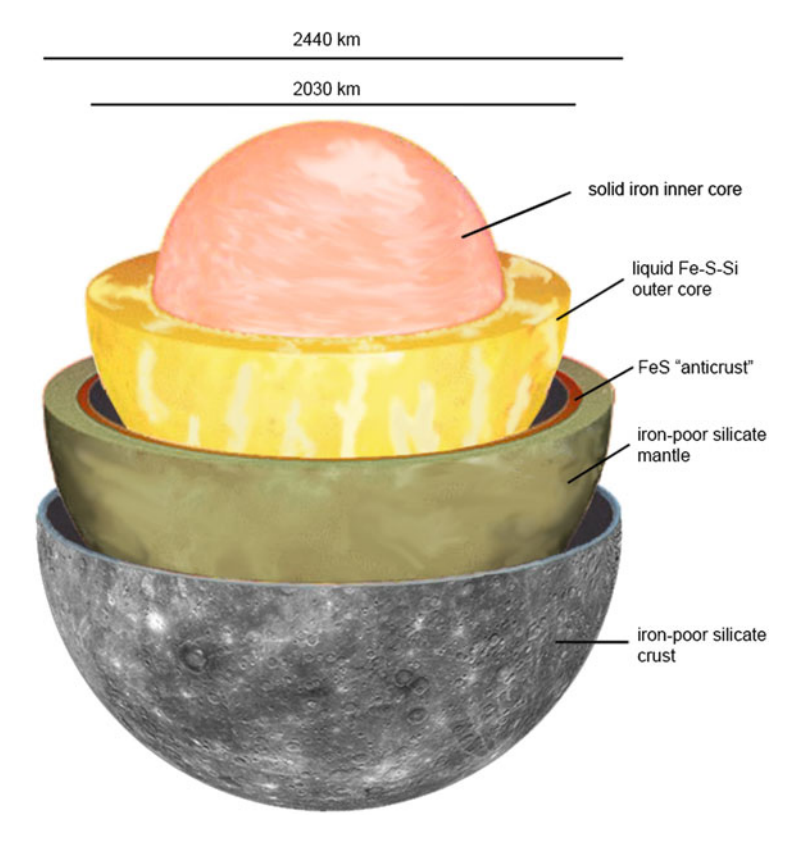


Fig. 5.1 Cut-away model of Mercury showing crust, mantle and inner and outer core to scale. Also shown is a hypothetical 'anticrust' of iron sulfide. The outer core is liquid and is convecting as indicated by the patterning (Modified from various sources)

Table 5.1 Geochemically feasible core models for Mercury that are consistent with bulk density and rotational parameters

Core model type	Core radius/km	Core density/kg m ⁻³	Mantle density/kg m ⁻³
Fe-S, S-poor	2,034	6,880	3,437
Fe-Si	2,022	6,976	3,390
Fe-S, S-rich	2,042	6,790	3,502
Fe-Si, FeS anticrust	2,023	6,982	3,379

Here 'core' is everything below the solid-liquid boundary, and 'mantle' is everything above – including the crust and, if present, the anticrust

Values from Hauck et al., J. Geophys. Res. v118, 2013

Figure 5.1 shows a cut-away model of Mercury showing a plausible internal structure that is consistent with the previous discussion. Table 5.1 shows some radii and densities for different iron:silicon:sulfur core compositions that are consistent with the measured C/MR^2 and C_m/C . In these models the core as a whole contains up to 36 wt% S and up to 17 wt% Si.

5.3 Crustal Thickness 151

5.3 Crustal Thickness

Crustal thickness can be mapped using spatial variations in the strength of gravity in conjunction with measurements of Mercury's exact shape, assuming reasonable crustal and mantle densities. Based on the crust's mafic-ultramafic nature (notably the high Mg, low Si composition derived from XRS) its density can be reasonably assumed to be only about 200 kg m⁻³ less than the mantle's density.

MESSENGER laser altimetry (MLA) was used to map the topography and hence the shape of the globe in the northern hemisphere. The north polar region is low lying (Fig. 4.18). This could merely reflect the random presence of the northern plains, unless the south polar region, which lacks any equivalent to the northern volcanic plains, is equally low lying. This could not be tested by MLA (for which high southern latitudes were out of range), but timing the occultations of MESSENGER's radio signal when it passed out of sight behind Mercury (or reappeared) as seen from Earth came to the rescue by showing that the radius from the centre to either pole is pretty much the same. It is between about 2.2 and 2.3 km less than the equatorial radius, and can be accepted as a true measure of Mercury's global flattening, or 'oblateness'. This flattening means that Mercury's gravity is slightly greater at lower latitudes would be the case for a spherical planet, and will cause the orbit of any spacecraft to evolve over time. The current degree of flattening may be inherited from the equilibrium shape when Mercury was spinning in about 100-200 h (as opposed to 1,408 h in its present 3:2 spin:orbit coupled state), depending on how much the shape has relaxed since that time.

Mercury's gravity field was mapped in detail by MESSENGER's Radio Science (RS) experiment that was able to measure accelerations experienced by the spacecraft. This technique allows spatial variations in a planet's gravity field to be mapped on a scale roughly equivalent to the orbiter's height, so was much more detailed in the north. However it became clear that there is a slight north–south asymmetry in Mercury's gravity field (its so-called J3 gravity field coefficient) whose effect on BepiColombo's MPO's periapsis and apoapsis over time had to be taken into account by BepiColombo mission planners (Sect. 3.4.1.2).

Figure 5.2 shows some derived data. The free-air gravity map displays the strength of gravity extrapolated to the reference spheroid (the flattened globe previously mentioned), and is shown as a positive (stronger than average) or negative (weaker than average) gravity anomaly. The geoid is Mercury's 'equipotential' surface, and is a map of the altitude relative to the mean shape of the planet, where gravity would be equal (another way to look at it would be that this would be sea-level if you were able to flood Mercury with water).

Crustal thickness variations can be mapped by comparing the geoid with the freeair gravity map and taking account of surface topography, if the crust and mantle are each assumed to be of uniform density. We know that this is not quite true for the crust, because we can see at the surface and the shallow depths revealed by impact excavation, that there is some variation represented by the low reflectance material, high-reflectance red plains and other colour units described in Sect. 4.2.2. However 152 5 Mercury's Interior

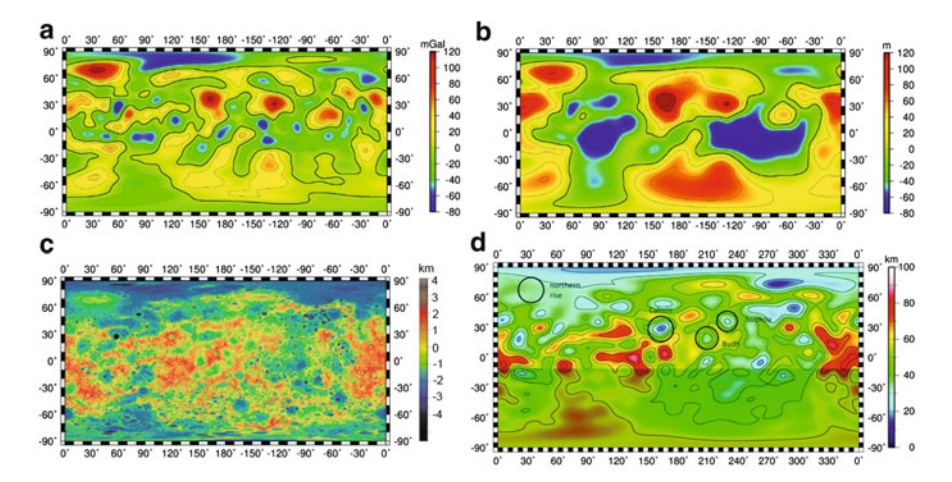


Fig. 5.2 Maps of Mercury showing (a) free-air gravity anomaly, (b) geoid anomaly, (c) topography based on MDIS stereo-mapping, and (d) crustal thickness (consistent with an assumed average thickness of 50 km), trustworthy only north of about 10° S. Circled named features are, from west to east, the northern rise, Caloris, Budh and Sobkou. The spatial resolution of (a) and (b) decreases greatly in the southern hemisphere, and crustal thickness variations south of 10° S are effectively unconstrained (a, b and d From Smith et al., 2012, *Science*, v336, reprinted with permission from AAAS, c from Becker et al., 2014, LPSC, courtesy of NASA/Johns Hopkins University Applied Physics Laboratory/Carnegie Institution of Washington/United States Geological Survey.)

density differences between units are probably small, and it is not unreasonable to assume that local variations are mostly negligible when averaged through the whole thickness of the crust. More problematic is the average crustal thickness, which is constrained only weakly by assumptions such as crust-mantle density difference and tectonic models about the depth to which faulting extends. About 50 km is a reasonable assumption, but the average could actually be anywhere in the range 30–100 km.

The crustal thickness map in Fig. 5.2d shows the distribution of crustal thickness derived from these assumptions, and is not valid south of about 10° S. It shows crust of less than 20 km in a part of the northern plains near 290° E that lies north of the high-magnesium region (Sect. 4.3.2) and a less dramatic low to its south that lies within the high-magnesium region. Crust appears thicker than 80 km beneath the quasi-linear rises south of about 30° N, that were noted in Sect. 4.4.1. The most notable tract of high ground that appears not to be supported by thick crust is circled as 'northern rise'. This is an otherwise unremarkable part of the northern plains whose surface elevation in the absence of a corresponding gravity-low seems to show that it cannot be explained by thick, low-density crust. Maybe it is supported dynamically, possibly by an upwelling zone in the mantle.

Other circled features on Fig. 5.2d pick out three areas of thin crust that coincide with three of Mercury's major basins that are officially mapped as planitiae: the relatively young Caloris, and the older Budh and Sobkou. The thin crust of Caloris

coincides with a positive free-air gravity anomaly on Fig. 5.2a and is a clear indication of the mantle being at a shallow depth below the surface. This is a classic 'mascon' (mass concentration) as exemplified by many of the lunar maria. Budh and Sobkou are mascons too; interpretation is trickier because of a topographic rise that passes between them, but essentially it seems that the crust below both of these basins is thin (as a result of basin excavation) and has not regained normal thickness despite flooding by lava, whereas the crust below the rise has been thickened by an unknown process.

5.4 The Lithosphere

When writing of a terrestrial planet other than the Earth, the term 'crust' is often misused casually in place of 'lithosphere' (Box 2.1). Strictly speaking, crust should be used only to refer to an outer layer of lower density (in the context of geophysical studies) or of chemically-evolved composition (in the context of derivation of the crust by partial melting of the mantle). Ideally, these two equate to the same thing.

Lithosphere means something different. It is an outer shell whose physical/mechanical properties distinguish it from the underlying region of a planet's mantle. Its base may not be far below the base of the crust, but there is no reason why the two should coincide, and in general a lithosphere includes the whole of crust plus the uppermost mantle.

A lithosphere can be defined mechanically as an elastic shell, below which the mantle (although solid) is able to flow plastically or even to convect. This is not as straightforward as it may sound, because the elastic shell of a planet will appear be a thicker in response to very rapid application of stress (such as in a major impact) than in response to slow processes such as global contraction. Lithosphere can instead be defined thermally, as the lid across which heat is transferred only by conduction (plus advection if igneous intrusions are able to form and rise), as opposed to the interior where a significant proportion of the outward movement of heat is accomplished by solid-state convective flow. The thermal and elastic lithospheres are similar, except that convective flow is slow so that a thermal lithosphere will be somewhat thinner than a mechanical lithosphere defined by the response to a major impact. A third definition, seismogenic lithosphere, is the layer in which rock will fracture rather than flow in response to global stresses, and hence where fracture-related earthquakes can occur. On all three definitions, it is to be expected that a planet's lithosphere will thicken over time, as its interior cools.

In the case of Mercury, the fracture patterns in Rachmaninoff (Fig. 4.35) and Mozart (Fig. 4.27) can satisfy models of an elastic lithosphere about 30 km thick in which subsidence resulted from flooding by lavas. This is very similar to possible local crustal thickness, but cannot be regarded as convincing proof of the local lithospheric thickness at the time, especially as it is mechanically plausible for faults to root at the base of the crust rather than at the base of the lithosphere.

5.5 Mantle Composition

MESSENGER established that the composition of Mercury's crust is essentially a Mg-rich, Fe-poor basalt (Sect. 4.3.2). However, if we wish to understand Mercury's bulk composition, it is important also to consider the composition of the mantle, which even though thin on Mercury compared to other terrestrial planets, probably contains several times more mass than the crust. During partial melting of mantle to produce magmas of the compositions represented by the crust, iron is scarcely fractionated – so the iron content of the crust probably reflects a similarly iron-impoverished mantle, perhaps about 2 wt% Fe. This is remarkably low, and it is possible that the lower mantle includes a reservoir of higher iron abundance that has not been tapped by partial melting.

In contrast to iron, during partial melting magnesium tends to be held within the solid residium (i.e., it stays in the mantle) with the amount escaping into the magma increasing with greater degrees of partial melting. Thus, the more the melting, the greater the magnesium abundance in the magma. The high-magnesium region mapped by MESSENGER XRS (Fig. 4.17) suggests up to about 20 wt% Mg in that area of crust, providing a lower limit to the mantle Mg content in the unlikely case that the mantle had been totally melted to supply these lavas. In reality the mantle is probably about 25 wt% Mg, comparable to the Earth's mantle and chondritic meteorites. Silicon is slightly fractionated into magma during partial melting and the other detected elements are more strongly fractionated into magma, so all these will be less abundant in the mantle than in the crust.

We currently lack a reliable way to decide whether the variations in Mg:Si ratio represent variations in the depth or the degree of partial melting in a mantle of uniform composition, or whether they reflect spatial heterogeneities in mantle composition. It can be argued that the northern volcanic plains have been derived by partial melting of mantle that was harzburgite in composition (olivine plus calcium-poor orthopyroxene), whereas intermediate terrain derives from partial melting of lherzolitic mantle (olivine, calcium-poor orthopyroxene, and calcium-rich clinopyroxene). However, the low spatial resolution of the elemental mapping and the possibility of mixed signals makes this less than convincing.

Mantle composition also bears on whether any primary crust would be able to form by flotation during crystallization of Mercury's hypothetical primordial magma ocean. At 2 wt% iron, the magma ocean would probably have been dense enough to allow plagioclase to float. Some models suggest that this could also have scavenged carbon (in the form of graphite) from the mantle, which would then be available as a possible darkening agent for later generations of crust. However, no candidate tracts of surviving exposed primary crust have been identified (unless this is the explanation for low-reflectance material). Carbon is not directly detectable with MESSENGER instruments, but there were hopes of using the neutron spectrometer to look for a change in the thermal/fast neutron ratio attributable to carbon, by examining data over regions of low-reflectance material during the low-altitude campaign during the final year of the mission.

5.6 Thermal Evolution 155

Questions of mantle composition and heterogeneity and the occurrence of primary crust will probably not be satisfactorily answered until more elements have been mapped at higher spatial resolution, so that competing petrologic models can be tested.

5.6 Thermal Evolution

The temperature history of Mercury's interior is even more speculative than its composition. The rate of internal heat production from radioactivity depends on the planet's burden of the main elements whose radioactive decay produces significant quantities of heat, which are uranium, thorium and potassium. MESSENGER GRS results suggest that their concentration averaged out over Mercury's silicate fraction is similar to other terrestrial planets, if the mantle contains about 20–50 % of the observed surface abundance of those elements. As already noted, the surface K:Th ratio is relatively high. It is possible that the strongly reducing conditions inside Mercury will have led to up to 10 % of its uranium and a lesser percentage of thorium having been partitioned into the core, so the amount and history of radiogenic heat production is poorly known.

The amount of primordial heat still held within the planet, and the rates of heat generation from phase changes and tidal stressing are model-dependent (though they are probably less important than radiogenic heating). The rate of heat loss depends on the thickness and thermal insulating abilities of the surface regolith and any more coarsely-fractured megaregolith below it. The planetary volume depends on the thermal history as controlled by these factors, convolved with thermal expansion of the mantle and core when internal temperatures were increasing and thermal contraction when temperatures were decreasing.

This makes for a very complicated story. The likeliest suites of models suggest planetary expansion for the first 1–1.5 billion years (i.e., lasting until 3.5–3 billion years ago), followed by contraction ever since with the core cooling at about $40–50^{\circ}$ per billion years. The modelled amount of radial contraction can be chosen to fit the 7 km determined from mapping the surface faults (Sect. 4.4.3).

These models also suggest that mantle convection, and with it the likelihood of volcanic eruptions fed by magma from decompression melting during convection, ceased between 2 and 0.3 billion years ago. If mantle convection has ceased, then Mercury's present-day thermal lithosphere extends right down to the top of the outer core.

Chapter 6 Mercury's Magnetic Field and Exosphere as Seen by MESSENGER

6.1 Above the Surface

To conclude our survey of Mercury as understood near the end of the MESSEN-GER era, we now look at Mercury's magnetic field, the magnetosphere that it dominates, and its interaction with the solar wind and Mercury's surface. Charged particles from the Sun (the solar wind) and ions arising from Mercury's surface are controlled by the magnetic field lines in Mercury's environment, whereas neutral atoms escaping from Mercury's surface belong to its exosphere and their motion is independent of magnetic fields. Clearly the magnetosphere and exosphere occupy overlapping domains. We will look at each in turn, and at their relationships with Mercury's surface.

6.2 The Magnetic Field

6.2.1 Strength and Asymmetry

MESSENGER was able to confirm that the axis of Mercury's magnetic field was aligned with its spin axis and was a magnetic dipole field not distinguishably different in strength or orientation from the field observed 40 years previously by Mariner 10. However, Mariner 10 had made only two magnetosphere crossings, so unsurprisingly MESSENGER was able to reveal much more information. One particular surprise, which became apparent only after the orbital campaign had begun to yield results, is a north–south asymmetry. Mercury's magnetic equator (where field lines are parallel to the field axis) is displaced northwards of the geographic equator by 480 km, which is nearly one-fifth of the planet's radius. In relative terms, this is five times larger than a similar offset in Saturn's magnetic field.

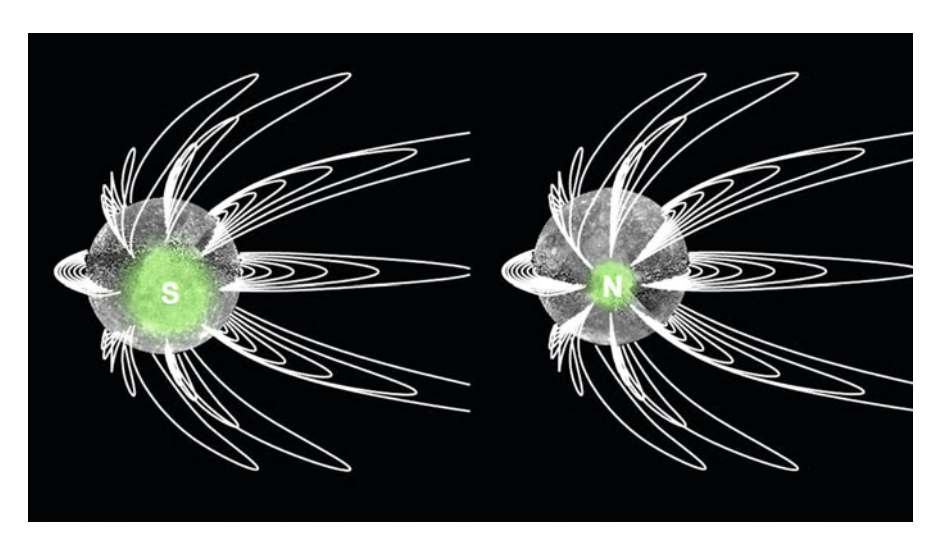


Fig. 6.1 The north–south asymmetry in Mercury's magnetic field, as discovered by MESSEN-GER from orbit. The two views show Mercury's magnetic field lines seen from the south and from the north. The zone in the south open to the solar wind is about four times larger than the equivalent in the north. The Sun is to the left in each case (Modified from NASA/Johns Hopkins University Applied Physics Laboratory/Carnegie Institution of Washington)

An important consequence of this is that the 'cusp' zone about the pole where open field lines reach the surface is broader around the south pole than around the north pole (Fig. 6.1). Charged particles, which must travel in spiral paths along magnetic field lines, can thus reach a wider latitude range about Mercury's south pole than in the north, with potentially important consequences for space weathering if the present-day field asymmetry is a sufficiently long-term situation. MESSENGER's Fast Imaging Plasma Spectrometer (FIPS) was able to measure the proton flux both into and reflected out of the northern cusp (the two populations being distinguished by different pitch angles). However, the spacecraft was always outside the magnetosphere when over the south polar region, so was not able to make comparable measurements of the proton flux affecting the southern cusp.

FIPS also found evidence of protons travelling along magnetic field lines linking low latitudes on the night-side. This suggests, even in the absence of measured cusp flux, that much of the southern hemisphere is continually bombarded by charged particles at night, contrary to the assumption that the magnetic field would normally protect most of the surface from the solar wind.

6.2.2 Dynamic Processes Related to the Magnetic Field

MESSENGER showed that Mercury's magnetic environment varies on a faster timescale than the Earth's. Only an author desperate for laughs would refer to it as

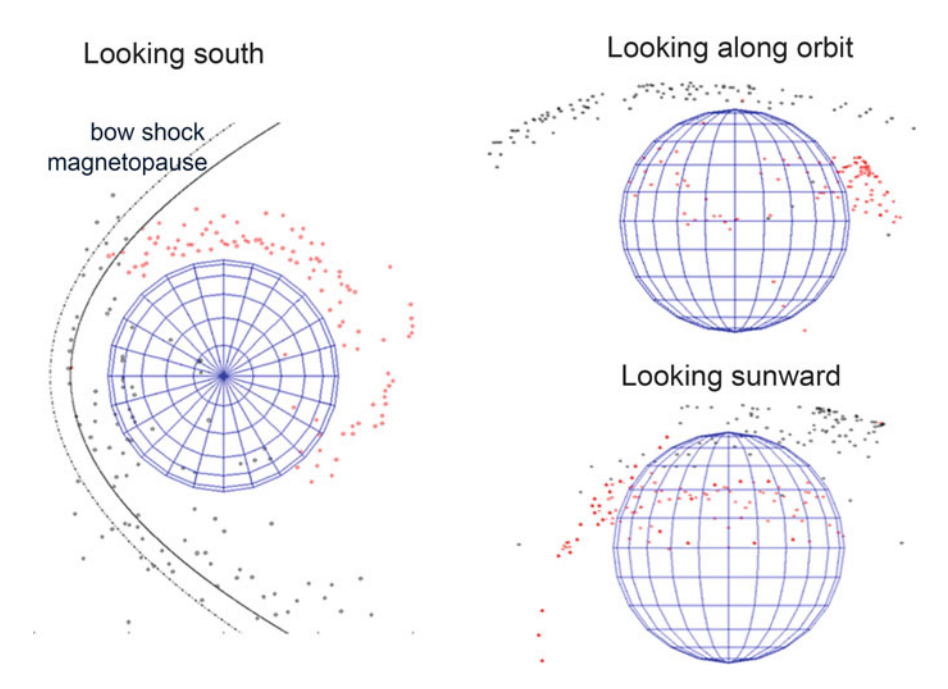


Fig. 6.2 Locations of high electron flux as determined by fluorescence of X-rays in the copper collimator of MESSENGER's XRS, plotted relative to Mercury as seen from three different vantage points. *Black points* are events experienced when inbound, *red points* are outbound events (Courtesy of the late George Fraser)

being in a state of flux. The following account draws mainly on interpretation of data from MESSENGER's magnetometer and the FIPS and EPS components of the Energetic Particle and Plasma Spectrometer. However it is informed by other data too, such as fluorescence of the copper collimator of the XRS attributed to a quasitrapped population of electrons inside the magnetopause (Fig. 6.2). The three-dimensional perspective obtained from this graphic does not show the full extent of the electron-rich region, because data-gathering was limited by the volume of space (relative to the planet) traversed by the spacecraft. The EPS showed that these electrons (which were also detected by the GRS) have energies up to 100–200 keV and arrive in bursts lasting seconds to minutes. In contrast to the Earth's Van Allen belts, the flux of these electrons varies wildly, and is not matched by energetic protons.

Many of the most important attributes of Mercury's magnetic environment, as deduced from multiple lines of evidence, are illustrated in Fig. 6.3. MESSENGER's orbit is shown here with a noon-time equator crossing, but the orbit was in a fixed plane so that as Mercury moved round the Sun the probe's orbit migrated to dusk equator crossings, then midnight, then dawn and back to noon. It thus sampled a volume of space relative to the planet that can be imagined by rotating MESSENGER's orbital ellipse out of the plane of the page. This enabled MESSENGER to determine that

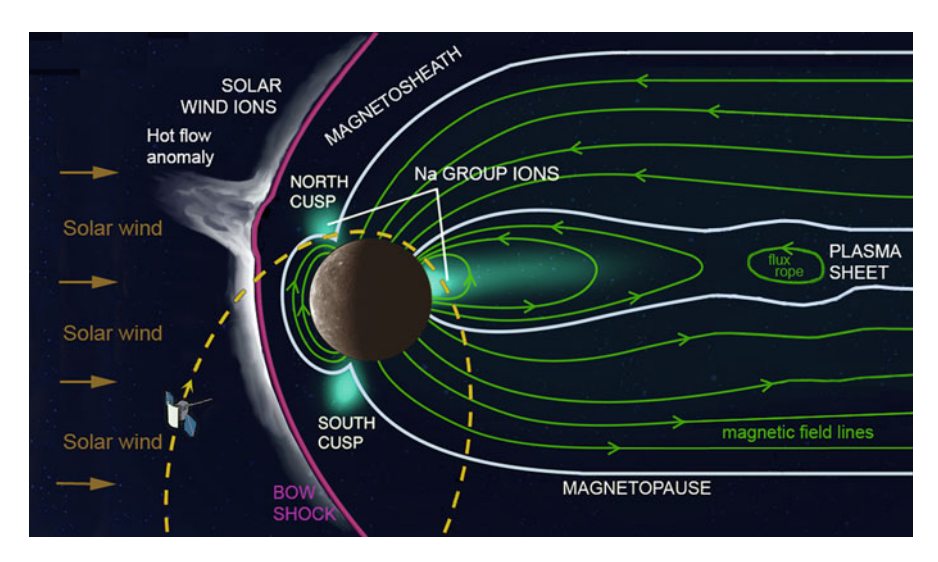


Fig. 6.3 Some important features associated with Mercury's magnetic field. The regions labelled 'Na group ions' correspond to the observed/inferred concentrations of ionized sodium, magnesium and silicon. Hot flow anomalies are transient and variable. The 'stand off' distance between bow shock and Mercury fluctuates with the intensity of the solar wind. MESSENGER is shown here approaching the bow shock from the up-Sun direction, but because the orientation of MESSENGER's orbit was fixed in space, during the course of a Mercury year its orbit sampled the magnetosphere from all directions. Flux ropes in the plasma sheet have been directly measured out to a distance of about three planetary radii when MESSENGER's periapsis was at noon (Adapted from multiple sources)

Mercury's magnetotail (the volume enclosed by the downstream portion of its magnetopause) becomes nearly cylindrical beyond about three Mercury radii downstream, with a radius of about 2.7 Mercury radii. In contrast, the Earth's magnetotail continues to widen much further downstream.

A diagram such as Fig. 6.3 cannot show the time-variable nature of the phenomena. This is very important at Mercury, whose proximity to the Sun means that its magnetosphere is strongly influenced by the extreme solar wind conditions. The solar wind speed at Mercury's orbit is about 400 km s⁻¹, similar to that experienced by the Earth, but solar wind density is about ten times greater. Furthermore, the interplanetary magnetic field (IMF) is about five times stronger than at Earth. IMF lines are not drawn in Fig. 6.3. They are sometimes described as 'frozen in' to the solar wind plasma, and are carried outwards from the Sun by the solar wind and distorted into a spiral by the Sun's rotation. At Mercury's distance from the Sun, IMF lines run either outwards or inwards from the Sun (with almost no up-down component and very little component out of the plane of Fig. 6.3) according to whether Mercury is currently north or south of the Sun's magnetic equator, which it crosses twice per orbit).

6.2.2.1 The Bow Shock and Hot Flow Anomalies

MESSENGER measured the location of the bow shock varying between about 1.9 and 2.3 Mercury radii upstream of Mercury's centre as the strength of the solar wind changed. The bow shock shape appeared not to change, in contrast to Earth's bow shock that becomes less curved when the solar wind strength decreases.

Magnetometer and FIPS data were also able to demonstrate the occurrence of a variety of 'space weather' called 'hot flow anomalies', an example of which is shown schematically in Fig. 6.3. These are transient events that happen when solar wind plasma is 'bounced' back from part of the bow shock, and heated and accelerated by interaction with the local electric and magnetic fields. Similar events are known at Earth and Saturn, and even at Venus and Mars where, lacking a magnetosphere, the obstacle to the solar wind is their ionosphere.

Mercury probably experiences thousands of these events per year. Their duration cannot be confirmed from individual passages made by MESSENGER, but each probably lasts for several minutes.

6.2.2.2 The Magnetopause and Magnetic Reconnection

MESSENGER located the magnetopause between 1.35 and 1.55 Mercury radii upstream of the planet's centre, varying according to solar wind pressure. It is possible that the magnetopause can be forced downwards very close to the planet's surface during intervals of excessive solar wind strength, which would occasionally expose all dayside latitudes to space weathering by charged particles, adding to the weathering caused by the fluxes into the north and south cusps and the night-time proton flux mentioned in Sect. 6.2.1. The 'gyro radius' of a solar wind proton (the radius of its spiral path about a magnetic field line) arriving at Mercury is about 20–50 km, which gives a measure of how close the magnetopause would need to be to the surface to expose it to space weathering by charged particles.

When crossing the dayside magnetopause, MESSENGER's magnetometer recorded numerous spikes in field intensity accompanied by wild excursions in direction, lasting for at most a few seconds. These are interpreted as 'flux transfer events', representing an occasion when a dayside closed magnetic field line is broken. One end splices into the IMF, a process often described as 'magnetic reconnection' and the other end is swept downstream to join the magnetotail. The lost closed magnetospheric field line would be replaced by outward migration of field lines from within the planet, thus maintaining the time-averaged steady-state field.

The 'snapping' of a field line releases a lot of energy, and turns out to be about ten times more intense at Mercury than an equivalent event in Earth's magnetosphere. During a flux transfer event 'shower', numerous events can occur within a few minutes. As a field line migrates into the IMF it twists into a vortex like magnetic flux tube, offering another pathway for solar wind plasma to break through Mercury's magnetic shield.

6.2.2.3 The Plasma Sheet and Flux Ropes

Reconnection can also occur in the downstream plasma sheet. This produces a feature known as a 'flux rope' containing plasma that will migrate either towards or away from the planet. An example is included in Fig. 6.3. Sometimes during 'hot seasons' when MESSENGER's periapsis was on the dayside (the opposite situation to that shown in Fig. 6.3) it was able to identify multiple such events during a single orbit, adding to the evidence that Mercury's magnetosphere is remarkably dynamic, in this case operating on a timescale about 40 times faster than the Earth's.

6.2.2.4 Planetary Ions

Mercury is accompanied by populations of ions that, rather than being captured from the solar wind appear to have originated from Mercury itself. These could be ions ejected directly as ions from the surface; sputtering caused by solar wind and micrometeorite impact usually releases neutral atoms as discussed in Sect. 6.3, but ions can be released by photoionization. Alternatively, neutral atoms could become ionized after release from the surface into the exosphere. Once a neutral atom becomes ionized its fate is controlled by the local magnetic field, and is no longer a component of the exosphere.

The ion population, especially in the cusps, fluctuates rapidly in association with the solar wind and magnetospheric dynamics, and there is also some variation correlated with local time (longitude east or west of local midnight).

Ions detected by FIPS are conveniently described in three groups. Those with a mass-to-charge ratio in the range $21{\text -}30$ include Na^+ , Mg^+ and Si^+ (singly ionized sodium, magnesium and silicon) and are dominated by sodium. These are called the Na group. Ions with a mass-to-charge ratio in the range $14{\text -}20$ include O^+ , H_3O^+ , OH^+ and H_2O^+ (singly ionized oxygen and various water-related ions), and are known as the O group. The third 'group' consists just of singly ionized helium, He^+ .

The Na group is strongly concentrated in the northern cusp (and presumably also in the unsampled southern cusp), and almost equally concentrated in the near-Mercury part of the plasma sheet, as labelled in Fig. 6.3. Beware that 'concentrated' may sound misleading: the cusp concentration of sodium group ions was rarely seen to exceed one ion per cubic centimetre. The O group shows a similar distribution, but is less abundant overall and also more weakly concentrated in the plasma sheet.

Helium ions are less abundant than the other groups, and are more evenly distributed. Solar wind helium is fully ionized (He²⁺) and it would be difficult to partly neutralize this back to He⁺, so Mercury's accompanying helium ions have probably been produced locally, by release from the surface (where it may originally have been implanted by the solar wind, and then neutralized). Upon release

from the surface by some kind of sputtering or thermal desorption process, helium atoms would then need to be ionized and accelerated to yield the observed energy distribution.

A substantial fraction of the population of heavier ions consists of ions with much more energy (travelling much faster) than would be expected for species originating from the surface, so they have presumably been accelerated by interactions with the magnetic field. Exospheric neutral atoms from the surface that are able to spread above the magnetopause before becoming ionized would then be accelerated by the solar wind (whereupon they would be described as 'pickup' ions) before being recaptured by Mercury. Some models suggest that flux transfer events would act so as to carry such ions into the cusps, possibly via the magnetosheath. For example, high energy sodium ions in the cusps could have been ionized close to the magnetopause before being swept into the cusps by flux transfer events, whereas low energy sodium ions, in the cusps and elsewhere, seem mostly to be upwelling from the surface.

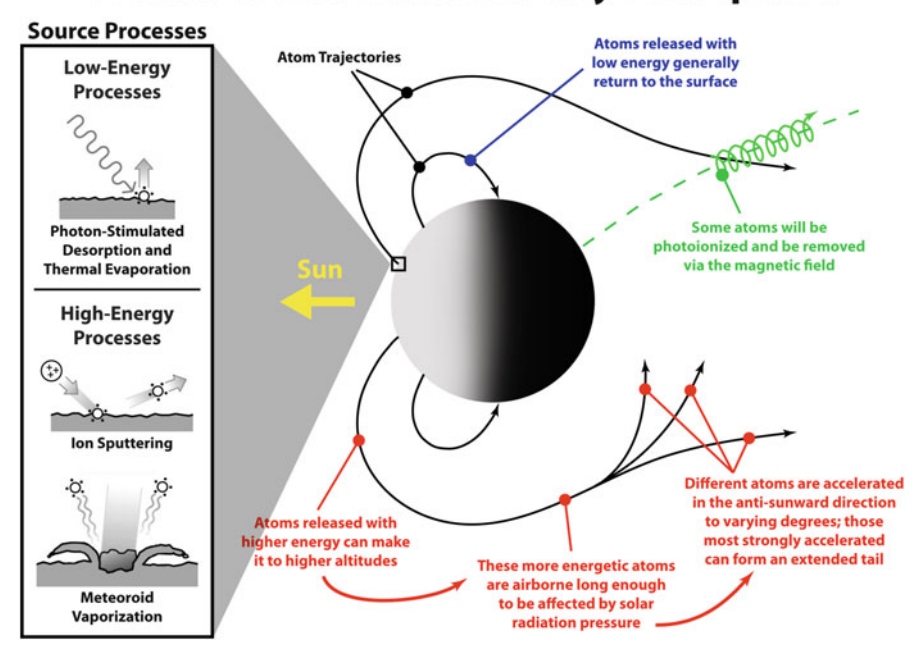
6.2.3 Field Generation

There is no doubt that Mercury's magnetic field is generated by dynamo processes in its liquid outer core. Despite the field's similarity to Earth's field (apart from the N-S offset), Mercury's field is three to five orders of magnitude weaker than a scaled down version of the Earth's (the range depends on the assumptions made during scaling). The field strength at Mercury's surface is probably about 260 nanoteslas, whereas at the Earth is it about 30,000 nanoteslas. Part of the reason for the field's weakness may be in the relative thinness of Mercury's outer core, restricting motion capable of contributing to the north–south dipole field to the part of the outer core lying outside an imaginary cylinder parallel to the spin axis and tangential to the inner core (this may also help to explain the north–south offset). An additional factor may be attenuation of the field strength by an electrically conducting iron sulfide anticrust, as suggested in Sect. 5.2.2.

6.3 The Exosphere

Figure 6.4 illustrates the possible processes that could operate to release a neutral atom from the surface into Mercury's exosphere, and the possible fates of such atoms.

Here we regard the exosphere as the neutral atoms surrounding Mercury, the distribution of which is not directly influenced by magnetic or electrical fields, though of course the volume of space occupied by the exosphere includes the ions discussed previously. The list of neutral species detected from ground-based



Processes at Work in Mercury's Exosphere

Fig. 6.4 Processes at work in Mercury's exosphere (Courtesy of Ron Vervack)

observations and MESSENGER now includes Ca, Na, Mg, K, O, H and He. Ground-based observations have also placed upper limits on Al, Fe and Si.

MESSENGER's main exospheric tool was the UVVS component of MASCS, which from orbit observed emission from the dayside exosphere by scanning above the limbs (Fig. 6.5), whereas nightside observations were made by rolling the spacecraft to achieve fantail scans that were allowed to intersect the planet's surface (Fig. 6.6).

Emission by helium was outside the range covered by UVVS, but the distribution of the more abundant metal species was quite well characterized by MESSENGER, in association with telescopic studies. There are some notable differences in the distribution patterns of each species. Ca is enhanced at dawn and declines towards dusk, Mg is more evenly distributed with a weaker dawn-dusk gradient, O peaks at noon, and Na is greatest near the poles (as can also be demonstrated by ground-based observations) and equatorially around noon.

Na, Ca and Mg all show seasonal variation, repeated with no significant differences for more than ten Mercury years. Each is most abundant soon after perihelion and least abundant soon after aphelion (Fig. 6.7). This looks like a solar influence, but such a correlation is not enough to show whether abundance changes are simply a thermal effect, or related to UV flux or to solar wind processes.

6.3 The Exosphere 165

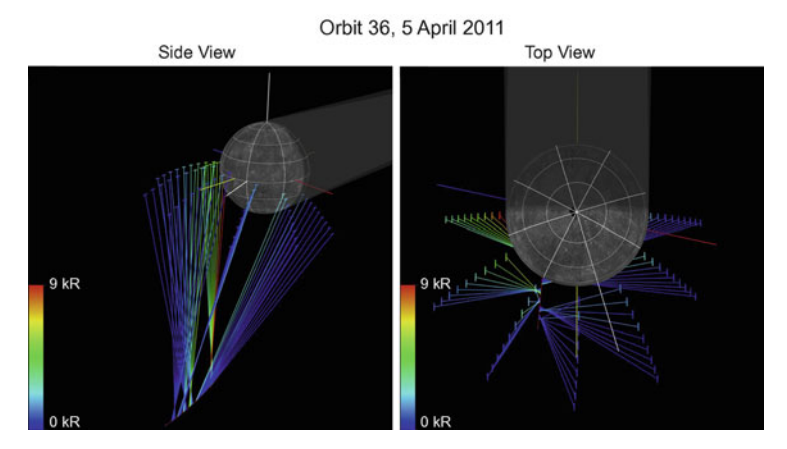


Fig. 6.5 Two perspective views of MESSENGER UVVS limb scan observations of calcium emission over Mercury's dayside on 5 April 2011. The orbital motion of the spacecraft is the fine red line at the origin of all the scans. The anti-sunward direction is indicated by Mercury's shadow. The colour scale is the total calcium radiance measured along the depth of the scan, in kilorayleighs (Reprinted by permission from Elsevier Ltd: *Icarus* v238, 51–58, M. H. Burger et al., 2014)

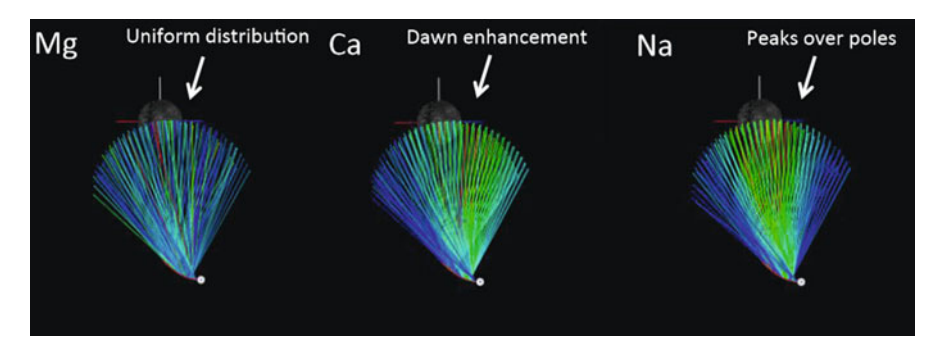


Fig. 6.6 Perspective view of MESSENGER UVVS fantail scans observations of magnesium, calcium and sodium emission over Mercury's nightside. Note the orbital motion of the spacecraft while these data were being acquired (Courtesy of Bill McClintock and the Hermean Environment Working Group)

Some clues to the source of the exospheric atoms come from their temperatures, which can be estimated independently by determining the emission line widths and by determining the scale height of the distribution of each species above the surface (the colder, less energetic, the molecules, the faster their concentration decreases with height). In the case of Na, the dayside equatorial Na consists of two populations: a 'warm' 1,200 °C population whose temperature is consistent with release by photon stimulated desorption and which shows consistent seasonal variation, and a 'hot' >5,000 °C population whose abundance varies on timescales measured in hours. Like the dayside equatorial Na, the sodium in Mercury's tail is

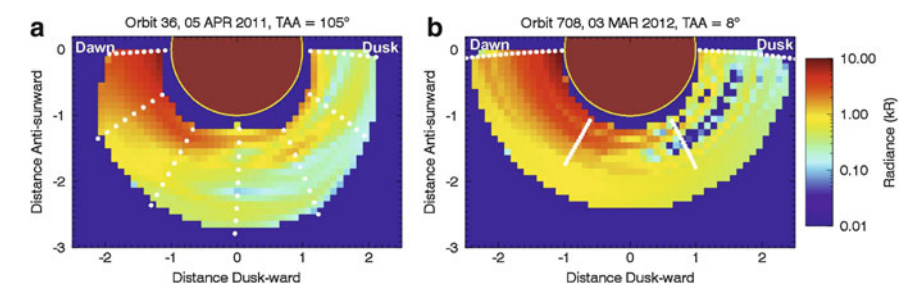


Fig. 6.7 (a) and (b) Synthetic images of calcium emission in Mercury's dayside equatorial plane at two epochs. TAA is true anomaly angle, which measures Mercury's position in its orbit round from perihelion. The colour scale is the interpolated calcium radiance. The *white dots* show the projections of line-of sight tangent points onto this plane (the actual lines of sight in (a) are shown in Fig. 6.5). The subsolar point is at the bottom (Reprinted by permission from Elsevier Ltd: *Icarus* v238, 51–58, M. H. Burger et al., 2014)

greatest near perihelion and has a temperature distribution that best matches release of sodium by photon stimulated desorption.

The distribution of Ca, which is around 400 times less abundant than Na, can be fitted by a single high temperature source near dawn, in the region of 30,000 °C. This is far too hot to be simple evaporation of Ca atoms that had condensed overnight, but could be from dissociation of Ca-bearing molecules released as vapour from micrometeorite impacts. Maybe this can be explained by Mercury's orbit near perihelion intersecting a train of dust from a comet, but if so the comet has not been identified and there is no match to comet Encke's current orbit.

Like Na, Ca and Mg are found in the tail, and UVVS observations showed a rapid decrease in neutral Ca accounted for by conversion to singly ionized Ca⁺ (also detected in the tail by UVVS) by photoionization.

Chapter 7 More Questions than Answers?

7.1 MESSENGER's Legacy

I write this with just a few months remaining before the end of the MESSENGER mission. The low altitude campaign has yet to bear its full fruits. These will include a wealth of NAC images at better than 10 m per pixel, some oblique upward UVVS scans from deep within the exosphere to study spatial enhancements of Ca and Mg, and a targeted search by GRNS for iron and carbon in areas surfaced by low reflectance material. Low altitude passages will also allow spatially smaller, and shallower, contributions to the gravitational field to be resolved, which may offer insights into the heterogeneity and/or thickness of the crust.

MESSENGER's forward speed at the instant of its March 2015 impact onto Mercury's surface will be about 3 km s⁻¹, less than a tenth the speed of most asteroidal or cometary impacts on Mercury. The resulting crater will probably be only about 5 m in diameter, but fresh ejecta may more than double the size of this new feature for BepiColombo to find. This is within the capability of BepiColombo's highest-resolution camera, HRIC, but if imaged it is unlikely to be distinguishable from other small, fresh craters. Plans have therefore been made for MESSENGER to image its likely crash site ahead of time, so that BepiColombo can spot the difference. Finding MESSENGER's grave will do more than merely satisfy our curiosity – it should also reveal whether any aspects of space weathering are sufficiently rapid to be noticeable over decadal timescales. This will be particularly handy, given that MESSENGER's limited highest resolution repeat imaging has not detected any new craters.

7.2 How Did Mercury Form?

Understanding Mercury's origin is a scientific goal worthy of pursuit on its own merits. It is a fascinating planet in its own right, and is an end-member example of our Solar System's family of four terrestrial planets. We will understand the Earth's origin better if we can also establish how its fellows formed.

Moreover, after a slow start in the 1990s, the recent dramatic increase in the rate of discovery of exoplanets has revealed numerous examples of 'hot Jupiters' and 'super-Earths' in close orbits about their stars. Earth-mass and perhaps even Mercury-mass examples will follow. Exoplanet data are crude but sufficiently numerous to allow the power of statistics to come into play, whereas Mercury data refer to a single example but are becoming increasingly sophisticated and detailed. Although pertaining to just a single example, they offer a 'reality check' and a counterbalance to exoplanet studies. Together, both fields are stronger than either would be in isolation. This applies not just to models of planetary origin, but to the compositions of enriched exospheres of exoplanets that might be detected spectroscopically.

Chapter 2 concluded by noting three types of post-Mariner 10 model that were invoked to account for Mercury's high density and large core:mantle ratio: selective accretion, post-accretion vaporization, and giant impact. There are problems in reconciling any of these with what we now know about Mercury's surface composition (particularly its richness in volatiles and deficiency in iron), except in the increasingly implausible scenario that the surface is wholly unrepresentative of the crust as a whole.

A weak consensus now seems to be emerging that can apparently reconcile models with reality. There are two main components to this: an origin for Mercury as a hit-and-run impactor, and scavenging of iron into the core as a result of strongly-reducing conditions. I present these below, as a plausible model for Mercury's origin that is consistent with such facts as we know.

7.2.1 Hit-and-Run

MESSENGER made the surprising revelation that Mercury is intrinsically rich in volatiles with a range of geochemical affinities. These include S, K and Cl, plus the unknown species providing the gas to drive explosive eruptions. The cold-trapped volatiles in polar craters, being late additions, are not relevant. All three of the previously-proposed models should leave Mercury less-rich in volatiles than its starting material, so unless Mercury accreted from some unknown exotic material inexplicably rich in volatiles to begin with (or its surface composition is totally misleading) these models are now untenable.

A new model that can be made to fit, has Mercury's parent body as a 'hit-andrun' impactor, that collides obliquely with a larger body (which might eventually

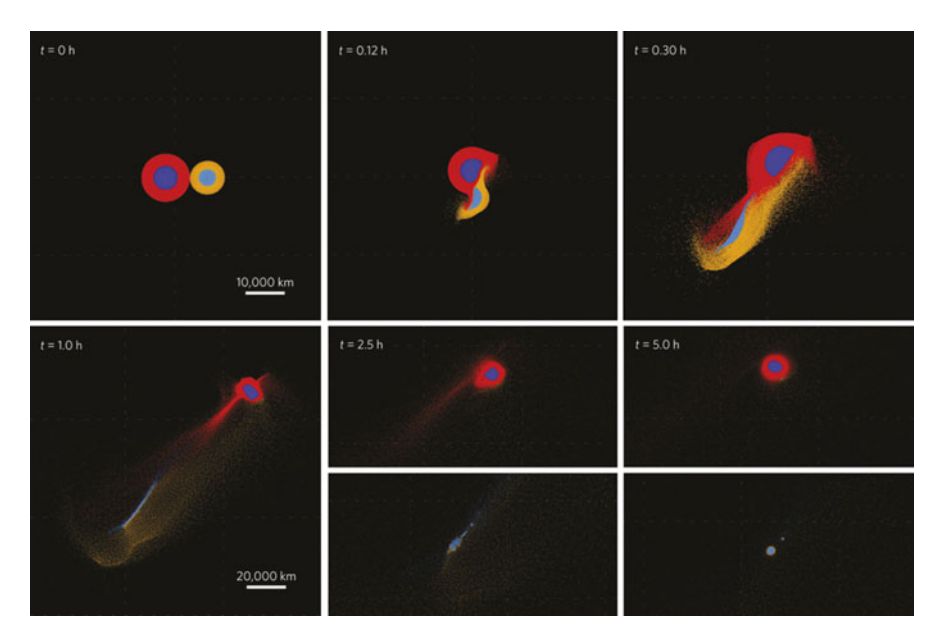


Fig. 7.1 Cross-sectional view of a possible hit-and-run origin for Mercury resulting from a grazing collision between two differentiated planetary embryos (cores and mantles distinguished by colour). The smaller one has a mass about 4.5 times greater than Mercury, and the larger is 3.4 times more massive (85 % the mass of the Earth). Note the scale change between top and bottom rows. After 50 h the surviving core of the smaller embryo is well on the way to becoming Mercury. The other body could eventually become Earth or Venus, probably after a few more giant impacts (Reprinted by permission from Nature Publishing Group: *Nature Geoscience* doi:10.1038/ngeo2189, E. Asphaug & A. Reufer, 2014)

become Earth or Venus) but avoids merger. Computationally intensive computer software that breaks a system down into a matrix of cells and calculates the forces affecting the material in each cell (known as hydrocode modelling) shows that it would be possible for a differentiated planetary embryo of several times Mercury's present mass to lose most of its mantle and part of its core as a result of a hit-and-run impact with a larger target. Figure 7.1 shows an example.

In such a hit-and-run scenario, the relative impact speed would be considerably less than in the giant impact model, in which the proto-Mercury was the target body. An important consequence of a hit-and-run incident is that the thin shell of mantle that Mercury would be able to re-accrete would not have become grossly depleted of its volatiles. It would be even easier to explain volatile retention if the mantle-stripping of the proto-Mercury occurred by a short series of about three less disastrous hit-and-run collisions, which could be achieved with an impact speed very close to the escape velocity.

To further reduce the constraints on the starting composition, it is worth noting that studies of exoplanet systems have made it clear that the orbits of planets can migrate inwards. It is possible, though perhaps unlikely, that Mercury formed further from the Sun than we now see it, in a region that was richer in volatiles. It

is less unlikely that the hit-and-run impactor was an interloper from further out, indeed this would seem to be necessary if the target body was Earth or Venus.

Thus Mercury's 'richness' in volatiles is not necessarily an enigma that defies explanation. It is more like an observed fact that helps to narrow down the ways in which Mercury is likely to have formed.

7.2.2 Iron Sequestration into the Core

The other major conundrum surrounding Mercury's composition is the low abundance of iron in its crust (and by implication its mantle too). This had previously been suspected, but was confirmed only when MESSENGER's XRS and GRS demonstrated that all forms of iron (in silicates, sulfides or metallic) total less than about 3 wt% at the surface.

Experimental petrology and theory show that an iron-poor mantle would be a consequence of chemically strongly reducing conditions (very low oxygen fugacity) in the mantle when the core was forming. This would make iron behave like a 'siderophile' element rather than a 'lithophile' element, so that it would preferentially mix with other iron, and sink to the core, rather than being taken up in silicate minerals. To explain the iron-poorness of Mercury's mantle, conditions would need to have been even more strongly-reducing than within the Earth.

The oxygen fugacities recorded in minerals found in meteorites span a wide range, so there is no problem in principle with accreting Mercury from a low-oxygen fugacity mixture. It has been suggested that lower oxygen fugacity represents conditions closer to the Sun, and that Mercury could have formed from the same source as enstatite chondrite meteorites. The extent to which such a low oxygen fugacity reflects a radial gradient within the solar nebula or a gradient in a direction out of the plane of the nebula need not concern us here, other than to note that it broadens the parameter space to allow the right sort of hit-and-run impactor to grow.

It is worth noting that similar conditions need not necessarily have prevailed throughout Mercury's growth. For example, it might have been sufficient for oxygen fugacity to have been very low during the growth of the hit-and-run impactor seen at the start of Fig. 7.1. It need not have been so low during and after the collision, because the re-accreting mantle would already be iron-poor.

7.2.3 Primary Crust

Mercury's oldest crust has not been identified. There are no extensive terrains equivalent to the lunar highlands, which are accepted as primary crust on the definition given in Table 2.1. Pretty much everything looks volcanic, and so is secondary crust (in the form of lava flows supplied by partial melting of the mantle),

with the possible exception of low reflectance material, at least some of which could be buried primary crust exhumed by impacts.

Reaccretion of silicates around Mercury's core after the hit-and-run event pictured in Fig. 7.1 would probably release sufficient energy to melt all or part of the new silicate shell into a magma ocean. Some models suggest that if the magma ocean had more than about 2 wt% FeO (which seems likely), then plagioclase ought to have floated. However no plagioclase-dominated terrains have been identified. Another suggestion is that that the carbon content of the magma ocean could have been sufficient to concentrate carbon (in the form of graphite) into the early crust. If the low reflectance material turns out to be darkened by carbon, then this will add weight to the argument that it is primary crust rather than impact melt.

7.3 Meteorites from Mercury?

With little prospect of a sample-return mission to Mercury for at least 20 years, what hopes have we of finding a meteorite from Mercury? Our understandings of Mars and the asteroid Vesta have both been enriched and informed by analysis of meteorites shown to have originated there. Even studies of the Moon, from which over 300 kg of samples have been returned, have benefitted from the wider diversity of rock types represented among lunar meteorites.

If we had a meteorite accepted to have originated from Mercury, studies of trace elements too low in abundance even for BepiColombo's MIXS would teach us about mantle melting processes, and fluid inclusions within crystals would record the cocktail of volatiles likely to have powered Mercury's explosive volcanism. Perhaps more importantly, ratios between stable isotopes would show the degree of affinity (or lack of it) between Mercury's source material and the Earth. It is even possible that clever use of hafnium-tungsten systematics might pin down the date when Mercury's core segregated. All of the above are feasible without knowing the exact provenance of a piece of Mercury, provided you are sure that it came from somewhere on the planet.

Dynamical arguments suggest that it is about a hundred times more difficult for a piece of ejecta from an impact on Mercury to find its way to the Earth than it is for a piece of ejecta from a lunar impact to get here. Related arguments suggest that it is about 25 times harder for ejecta to make the journey from Mercury to Earth than from Mars to Earth. In 2014, the number of known lunar meteorites rose above 200 and Mars meteorites to 70, so there is a reasonable chance that someone, somewhere, has an unrecognized meteorite from Mercury, or that one will be collected soon.

A feasible candidate collected soon after being seen to fall in southern Morocco in 2012, but not now widely accepted, is the meteorite known as NWA 7325, of which 35 fragments massing a third of a kg were collected. This is a crystalline igneous rock, consisting of intergrown calcium-rich plagioclase (55–60 %), calcium-bearing clinopyroxene (25–30 %) and olivine (10–15 %). The texture

matches that of a 'cumulate', formed by pyroxene and olivine crystallizing first (up to a mm in size) and plagioclase growing afterwards in the gaps. This doesn't look lava a lava flow, but would fit with a cumulate assemblage growing on the floor or sides of a shallow magma chamber, at a depth that could easily be excavated by a modest impact. The olivine and pyroxene are both Mg-rich and Fe-poor, providing a seductively good match to Mercury. However, the meteorite's sulfur content is way below that seen at Mercury's surface, and even more compellingly radiometric dating gives an age of 4.56 billion years. Nowhere on Mercury's surface seems to be that old; Sect. 4.4.1 suggests 4.1 billion years as the age of the oldest surfaces. Maybe this is a piece of one of Mercury's parent bodies, but it is unlikely to be from Mercury itself.

When a meteorite from Mercury does turn up, it is more likely to be a Mg-rich basalt, or a welded impact-breccia containing clasts of Mg-rich basalt, with at least 4 % S. It will be interesting to see if the sulfur is indeed in oldhamite, (Ca,Mg)S, as suspected for Mercury. Its age is most likely to fall in the range 4.1–3.5 billion years (Calorian and older), though an age as young as a billion years would not be a shock.

7.4 What Will BepiColombo Teach Us?

We currently can't answer even some quite basic questions, such as why hollows are high albedo and blue and why pyroclastic deposits are red.

The prognosis for BepiColombo is good. As described in detail in Chap. 3, it will have a diverse suite of instruments, many of them considerably more capable than their MESSENGER equivalents. MPO will have less-eccentric orbit, with a periapsis at low latitude enabling the southern hemisphere to be studied just as well as the northern. The MPO and MMO pairing will enable magnetospheric and exosphere dynamics to be observed in ways inaccessible to MESSENGER.

MESSENGER was blind in the thermal infrared, whereas BepiColombo's MERTIS will exploit this spectral region for studies of mineralogy and regolith properties. The X-ray spectrometer, MIXS, will have sensitivity and spatial resolution considerably improved on MESSENGER's XRS. BepiColombo's dust monitor, MDM, will be the first instrument at Mercury capable of detecting and measuring dust, whereas plasma and neutral particles will be more thoroughly analysed by other instruments.

More than likely, the most exciting results from BepiColombo will include revelations that no one expects. It is certainly well-equipped to find these.

MESSENGER has been a remarkable mission. As a member of the BepiColombo team I can only hope that our spacecraft works equally well and that our team will deliver so much good science in such a short time as the MESSENGER team did.

Appendix A

A.1 Previous Publications About Mercury

Books post-dating Mariner 10 but pre-dating MESSENGER include

Vilas F, Chapman CR and Matthews MS (eds) (1988) *Mercury*. University of Arizona Press, Tuscon. A thorough treatment of knowledge as it stood in the mid-1980s by specialist chapter authors.

Strom RG and Sprague AL (2003) *Exploring Mercury – The Iron Planet*. Springer/Praxis Publishing, Chichester.

Clark PE (2007) Dynamic Planet – Mercury in the Context of its Environment. Springer.

Antoniadi EM (translated by Moore P) *The Planet Mercury* (1974) Selsey Press, Selsey. Patrick Moore's English translation of Antoniadi's 1934 book *La Planète Mercure*, which can still be tracked down cheaply second hand online and is worth a read.

The MESSENGER website (see below) lists papers by MESSENGER team members. Other than that, I recommend Google Scholar as a search engine to locate papers on specific topics and/or including specific authors.

A.2 Mariner 10 Images

You can find a selection of Mariner 10 images on the Internet at http://photojournal.jpl.nasa.gov/ Click on Mercury, and then choose Mariner 10 in the 'Mission' window.

A virtually complete set of Mariner 10 images is provided on a CD-ROM included with Strom and Sprague's book listed above.

174 Appendix A

The full Mariner 10 data archive is available via NASA's PDS Planetary Data System http://pds-imaging.jpl.nasa.gov/portal/.

A.3 MESSENGER Data

The MESSENGER website is at http://messenger.jhuapl.edu/.

Here, you can find many MESSENGER images and some other data from the mission. The site also has a link to QuickMap, which allows you to zoom in and explore (and download if you wish) global image mosaics and terrain elevation maps. The Science Operations area includes a year-by-year list of MESSENGER publications by MESSENGER team members. This probably makes up about 95 % of the Mercury publications arising from the mission, and the most recent papers will give you an entrée to the whole field of Mercury literature.

A comprehensive archive of MESSENGER data is being added to at 6-monthly intervals at NASA's PDS Planetary Data System http://pds-imaging.jpl.nasa.gov/portal/.

A.4 BepiColombo Websites

There is an ESA BepiColombo website at http://www.cosmos.esa.int/web/bepicolombo.

A Japanese site focused on MMO is at http://www.stp.isas.jaxa.jp/mercury/.

A.5 Seeing Mercury for Yourself

If you want to spot the pale pink dot of Mercury for yourself, take note of the best times of year that I pointed out in Chap. 1. For specific dates, I suggest you use an Internet search engine to tell you whether or not Mercury is well placed or download an app for your smartphone.

Useful websites include

http://freestarcharts.com/index.php/the-planets-this-month http://www.nightskyinfo.com/ http://www.nakedeyeplanets.com/#findplanet

Finally, do not forget the 9 May 2016 transit of Mercury, ideally timed for viewing from western Europe and wholly or partly visible throughout the Americas too. There is some information at http://www.caglow.com/info/events/transit2016, and other websites are sure to spring up nearer the time.

If you missed that, there will be another on 11 November 2019, then no more until 13 November 2032. Please note the safety warnings that I gave in Chap. 1.

Index

A Agglutinates, 45–47	Bright crater floor deposits, 94, 95, 135, 136, 138–139
Albedo, 45, 47	Budh, 153
Aluminium, 101–102	2401, 100
Aneirin, 123–124	
Angkor Vallis, 128	С
Anticrust, 149–150, 163	Calcium, 48, 101–102, 164, 166
Antoniadi Dorsum, 110	Calorian, 40
Antoniadi, Eugène, 9–10, 12, 173	Caloris basin, 30, 32, 33, 35, 40, 85, 89, 95,
Aphelion, 3	105, 106, 117–120, 132, 152
Apollodorus, 118–119	radial sculpture, 33
Arecibo radiotelescope, 11, 49	Caloris Montes, 33, 117
Assyrians, 2, 5	Caloris Planitia, 117. See also Caloris basin
Asthenosphere, 44	Calvino, 98, 100
Atget, 107	Carbon, 103, 131, 154, 167, 171
Atmosphere, 6, 12	Carbon monoxide, 131
Axial tilt, 8, 12, 148	Catena, 30
	Catenae, 128, 143–144
	Cayley Formation, 33
В	Chlorine, 102, 131
Babylonians, 2	Chromium, 102
Basalt, 104, 128, 154	Cold traps, 50
Beagle Rupes, 110–112	Colombo, Giuseppe, 21, 54
Beethoven, 107, 121	Comets, 15, 20, 30, 50, 66, 83, 140–141, 166
Bello, 121	Conjunction, 5
BepiColombo, 54, 69–83, 103, 132, 139, 142, 151, 169, 171, 172	Contraction, 33, 38–39, 95, 108, 115, 125, 133, 153, 155
cost, 55	Convection, 43, 44, 109, 149, 153, 155
launch, 55	Cook, Captain James, 6, 36, 109
BepiColombo Laser Altimeter (BELA), 74	Copernicus, 1
Blossom Rupes, 125	Core, 16, 42, 44, 50, 147, 148, 155, 170, 171
Borealis Planitia, 30, 94	inner, 149
Bow shock, 41, 42, 82, 160, 161	outer, 42, 43, 149, 163

Core (cont.)	Endeavour Rupes, 109, 110, 114
spin axis, 148	Energetic Particle and Plasma Spectrometer
Core-mantle boundary, 148, 149	(EPPS), 68, 158, 159, 162
'Cornerstone' mission, 54	Energetic Particle Spectrometer (EPS). See
Crater-counting, 39, 107, 117, 126–127, 133	Energetic Particle and Plasma
Craters, 86	Spectrometer (EPPS)
naming convention, 29	Enterprise Rupes, 115
Crust, 16, 43, 44, 147, 151, 153	Equatorial bulge, 37–38
composition, 154	Eruption plumes, 131
density, 151	European Space Agency (ESA), 54, 55, 57
heterogeneity, 103	Exoplanets, 53, 168, 169
layered structure, 97, 98	Exosphere, 47–48, 80, 81, 136, 142, 157,
oldest, 170	163–166
primary, 44, 154, 170–171	seasonal variation, 164
secondary, 44, 170	temperature, 165
thickness, 151–153, 167	Extensional tectonics, 109
Cusps, 158, 161–163	
	F
D	Fast Imaging Plasma Spectrometer (FIPS).
Dario, 122-124	See Energetic Particle and Plasma
Darwin, Charles, 110	Spectrometer (EPPS)
Dawn-dusk asymmetry, 48	Feldspar, 104
Day-year relationship, 12	Flows (lava), 33, 128, 134, 142, 145
Debussy, 91	'Flux rope', 160, 162
Deep Space Network, 22, 62, 68	Flux transfer events, 161, 163
Degas, 120	Flybys, 53, 63, 70, 85–87, 94, 95, 103, 110,
Degradation states, 39	111, 115, 116, 129, 132, 135
Density, 15-16, 148	Fossa, 30, 118, 133
Derain, 91	Free-air gravity, 151
Discovery programme, 54, 55	
Discovery Rupes, 36, 37, 109, 111	
Dollfus, Audoin, 9–10	G
Dorsum, 30	Gamma-Ray and Neutron Spectrometer
Duyfken Rupes, 121	(GRNS), 64, 139–140, 154, 167
Dyce, Rolf, 11, 12	Gamma-ray spectrometer (GRS), 64,
Dykes, 119, 133	99–100, 155, 159
	malfunction, 64
	Gassendi, Pierre, 6
E	Geoid, 151
Earth, 15–16, 148, 160–162	Ghost craters, 96–99, 107, 113, 128
Eccentricity, 5, 15	Giant impact, 50, 168
Ecliptic, 3	Global contraction, 38, 108, 133
Egyptians, 2	Goethe, 96, 98, 124
Ejecta, impact, 94, 98	Gold, Tom, 11–12
Electron stimulated desorption, 48	Grabens, 119, 133
Elongation, 3, 5, 11, 12	Graphite. See carbon
Eminescu, 137	Gravitational slingshot manoeuvre.
Emitted Low-Energy Neutral Atoms	See Gravity-assist trajectory
(ELENA). See Probing the Hermean	Gravity, 105, 131, 147, 151
Exosphere by Ultraviolet Spectroscopy	Gravity-assist trajectory, 21, 54, 70
(PHEBUS)	Gravity field, 59, 147, 151
Encke, Johann, 15	Greeks, 2
Endeavour, HMS, 6	Green, Charles, 6

Index 177

GRNS. See Gamma-Ray and Neutron Spectrometer (GRNS) Ground-based observations, 19 GRS. See Gamma-ray spectrometer (GRS) 'Gyro radius', 161	J Janszoon, Willem, 121 Japan Space Exploration Agency (JAXA), 54 69–70
н	K Kepler, Johannes, 6 Kepler's third law, 5
Halley, Edmund, 114	Kofi, 128, 129
Heavily cratered terrain, 107	Komatiite, 104
Helium, 26, 28, 47, 162–164	Kuiper (crater), 30, 39, 99
Herschel, William, 8	Kuiper, Gerard, 30
High-magnesium region, 104, 152, 154 High-reflectance red plains, 92–94, 97, 118,	Kuiperian, 40, 94, 107, 146
120, 122, 126	Kuniyoshi, 134
High Spatial Resolution Imaging Channel	
(HRIC). See Spectrometers and Imagers	L
for MPO BepiColombo Integrated	Lag deposit, 138, 140-141
Observatory System (SIMBIO-SYS)	Lander, 54
'Hilly and lineated' terrain, 35	Late heavy bombardment, 33, 86, 107
Hit-and-run impact, 168–170	Lavas, 33, 123, 125, 126, 128
Hollows, 94, 129, 135–139	Le Verrier, Urbain, 7, 15
Hot flow anomalies, 161	Libration, 8, 42–43, 63, 66, 68, 147, 148, 149 Linked fault systems, 109, 112, 114
Hot poles, 13, 14, 30, 32, 59	Liszt, 122
Howard, William, 11 Hydrogen, 47	Lithosphere, 44, 147, 153, 155
Trydrogen, Tr	Lobate scarps, 36, 37, 108 ages, 115–117
•	Lowell, Percival, 9
I	Low-reflectance blue plains, 93, 98, 105
Ice, 49–50, 65, 139–140 Igneous intrusions, 43, 44, 99, 119, 153	Low-reflectance material, 94, 98, 99, 103,
IMF. See Interplanetary magnetic field (IMF)	122, 136, 138, 154, 167, 172
Impact basins, 117	Lunar cratering timescale, 39
Impact gardening, 39, 130	Lunar highland crust, 104 Lunar maria, 34
Impact melt, 88, 99, 122, 125, 126, 145	Lunai mana, 54
Impact vaporization, 48	
Implantation, 46	M
Inclination, 5	Magma ocean, 43, 50, 154, 171
Intercrater plains, 97, 104	Magnesium, 105, 154, 164
Intermediate plains, 93, 98, 99	Magnetic dipole, 42, 157
Intermediate terrain, 93, 97, 104, 154	Magnetic equator, 157
International Astronomical Union (IAU), 10–11, 28–30, 118, 143	Magnetic field, 27, 41–42, 149, 157, 163 asymmetry, 157, 163
Interplanetary magnetic field (IMF), 160	reconnection, 161–162
Io, 131 Ion drive. <i>See</i> Solar-electric propulsion	strength, 149, 163
Ion sputtering, 48	timescale, 158, 160, 162 Magnetometer (MAG), 65, 161
Iron, 45, 101–103, 149, 154, 170	Magnetopause, 42, 65, 161, 163
Iron, nanophase, 47	Magnetosheath, 41–42, 163
Isostasy, 105–106, 109, 119, 125	Magnetosheati, 41–42, 103 Magnetosphere, 41, 59, 70–71, 81, 157
Italian Spring Accelerometer (ISA), 76	Magnetotail, 42, 160
-	

Manganese, 102	Mercury plasma particle experiment
Mansur, 40	(MPPE), 82
Mansurian, 40, 107, 146	Mercury polar orbiter (MPO), 72
Mantle, 16, 43, 44, 147, 148, 154–155, 170	Mercury sodium atmospheric imager
composition, 154–155	(MSASI), 83
heterogeneity, 154–155	Mercury surface element (MSE), 55
Maps of Mercury, 8–10	Mercury thermal infrared spectrometer
Margot, Jean-Luc, 42	(MERTIS), 77, 103, 172
Mariner 10, 19, 50, 157	Mercury transfer module (MTM), 69, 72
cameras, 23	MERTIS. See Mercury thermal infrared
data transmission, 22–23	spectrometer (MERTIS)
global coverage, 23	MESSENGER, 55, 56, 58
magnetometers, 27	cost, 55
onboard tape recorder, 22	end of mission, 59-60, 167
payload, 23, 28	fly-bys, 57
trajectory, 20, 21	launch, 56
Mariner programme, 19	low altitude campaign, 59, 134, 139, 167
Mars, 19	mass, 60
Mascons, 153	orbit, 58–60, 159
Mass, 15–16	payload, 62
MDIS. See Mercury dual imaging system	propellant, 60
(MDIS)	thermal design, 61
Megaregolith, 155	Meteorites, 16, 149, 154, 170
Mercury, 1–3	enstatite chondrite, 170
names on, 10, 28, 29	Mercury, 171, 172
Mercury atmospheric and surface composition	NWA 7325, 171
spectrometer (MASCS), 66, 99–100,	Michelangelo, 88
103, 164, 167	Micrometeorites, 46, 48, 136, 146,
Mercury dual imaging system (MDIS), 62–63,	162, 166
99–100, 105	Microwave observations, 10
Mercury dust monitor (MDM), 83, 172	MIXS. See Mercury imaging X-ray
Mercury gamma-ray neutron spectrometer	spectrometer (MIXS)
(MGNS), 78, 139	MLA. See Mercury laser altimeter (MLA)
Mercury imaging X-ray spectrometer (MIXS),	Moment of inertia, 147, 148, 150
78, 81, 103, 171	Mons, 30
Mercury laser altimeter (MLA), 66, 76, 105, 151	Monteverdi, 95, 97
Mercury magnetospheric orbiter (MMO), 55, 72	Moon, 35, 53, 148
mass, 73, 74	Mozart, 118
orbit, 70	Mozart, 110
telecommunications, 73	
Mercury Magnetospheric Orbiter	N
Magnetometer, MMO/MGF	Narrow-angle camera (NAC). See Mercury
(MERMAG) (BepiColombo	Dual Imaging System (MDIS)
magnetometers), 76, 82, 83	National Aeronautics and Space
Mercury orbiter radio science experiment	Administration (NASA), 19, 54, 55, 59,
(MORE), 79	62, 68
Mercury Planetary Orbiter (MPO), 55, 69	Nepheline, 104–105
mass, 72, 74	Neutron spectrometer (NS), 64, 154
orbit, 71	Nickel, 149
telecommunications, 72	Northern plains, 67, 94, 97, 101, 105, 106, 142
thermal design, 73	151, 152
thruster burns, 70	Northern rise, 152

0	R
Oblateness, 151	Rachmaninoff, 104, 125, 128, 129, 131, 134, 153
Olivine, 104–105	Radar, 7, 11, 12, 19, 31, 42
Orbital capture, 54, 58, 70	Radar-bright material, 49-50, 65, 139-140
Orbital inclination, 5	Radar imaging, 49
Orbital resonance, 54	Radiation pressure, 47, 48
Orbital speed, 5	Radioactivity 47, 63, 64, 155
Orbit correction manoeuvre, 59	Radio science (RS) (MESSENGER
Origin, 17, 50–51, 53, 168	experiment), 68, 147, 151
Orthopyroxene, 104–105	Raditladi, 126, 128
Oxygen, 47, 103, 162, 164	Radius, 15
Oxygen fugacity, 170	Reconnection, magnetic, 82, 162
76 6 77	Red spots, 94, 129, 131
	Regolith, 32, 39, 45, 47, 77, 102, 103, 134, 139,
P	155
Pantheon Fossae, 30, 118, 133	Relativity, 7, 75, 76, 79
Paramour Rupes, 113, 114	Rembrandt, 92, 107, 115, 117
Partial melting, 104, 154	Rilles, sinuous, 128
Peak-ring basins, 88	Rock types, 103
Peale, Stan, 11–12	Romans, 2
Periapsis, 162	Rotation, 7, 8, 10, 11, 15
Peridotite, 43	Rotation period, 11
Perihelion, 3, 15	Rudaki
advance, 3, 6, 7	plains, 97
Pettengill, Gordon, 11, 12	Rupes, 30, 36
Phase angle, 45	114000, 20, 20
Photoionization, 48, 162, 166	_
Photon stimulated desorption (PSD), 46, 48,	S
136, 165–166	Sample return, 146, 171
Phreatic eruption, 130–131	Sander, 136
Picasso, 133	Sarmiento, 108
Pickup ions, 163	Sayat Noya, 121
Pits, 129–135	Schiaparelli, Giovanni, 8, 12
Plagioclase, 104–105, 154, 171–172	Schröter, Johann, 8
Plains, 33, 41	Search for exospheric refilling and emitted
Planetary ions, 162–166	natural abundances (SERENA), 80
Planetary Ion Camera (PICAM). See Probing	Seeing Mercury, 1, 3–5
the Hermean Exosphere by Ultraviolet	Seismic waves, 147
Spectroscopy (PHEBUS)	Selective accretion, 50, 168
Planitia, 30	Self compression, 16
Plasma sheet, 41, 42, 160, 162	Self-sustaining dynamo, 42
Plasma wave instrument (PWI), 82	Silicates, 16, 103
Post-accretion vaporisation, 50, 168	Silicon, 102
Potassium, 48, 102, 155	Smooth plains, 94, 97, 104
pre-Tolstojan, 41	Sobkou Planitia, 89, 90, 100, 123, 152
Principal components transformation, 90	Sodium, 48, 83, 102, 104–105, 164
Probing the hermean exosphere by ultraviolet	Sodium tail, 48, 57, 83, 165–166
spectroscopy (PHEBUS), 79	Solar eclipses, 7
Protons, 158, 161	Solar-electric propulsion, 72
110000, 100, 101	Solar intensity X-ray and particle spectrometer (SIXS), 81
Q	Solar wind, 42, 46–48, 68, 136, 157, 160–162
Quadrangles, 10, 28, 30	Space weathering, 46–47, 94, 129, 146, 158, 161, 167
Quartz, 104–105 Quasi-linear rises, 105–108, 152	Spectral diversity, 93
Quasi-illiear rises, 103–108, 132	Special diversity, 15

BepiColombo Integrated Observatory System (SIMBIO-SYS), 80–81, 103 Spectroscopy, 19 Spinel, 104–105 Spinorbit coupling, 12, 15, 23, 37, 151 Sputtering, 46–48, 136, 146, 162–163 Start from a Rotating Field Mass Spectrometer (STROFIO). See Probing the Hermean Exosphere by Ultraviolet Spectroscopy (PHEBUS) Stereo Channel (STC). See Spectrometers and Imagers for MPO BepiColombo Integrated Observatory System (SIMBIO-SYS) Sublimation, 136–141 Sulfides, 104–105, 138 Sulfur, 43, 50, 65, 101–102, 131, 132, 149 Sun angle, 23, 38 Surface composition, 45, 46, 99–105 Swiss Cheese terrain, 138–139 Synchronous rotation, 8–10, 12 Tectonisation of basin edges, 120, 121, 123, 124, 127 Telescopic observations, 7–8 Temperature, surface, 11, 14, 25–26, 47, 50, 77, 105, 138, 140, 146 Terrain units, 93 Thermal desorption, 48, 136 Thermal history, 155 Thorium, 102, 155 Thruster burns, 59 Thrust faults, 36 Tidal despinning, 38, 39, 109 Tidal forces, 8, 12, 15 Tidal despinning, 38, 39, 107 Tidal forces, 8, 12, 15 Timescale, 39–41 Titanium, 102 Tolstoj, 40, 89, 107, 122 Tolstojan, 40, 121, 122 Topography, 105, 151 Vallis, 30, 128 Velazquez, 137 Vents, 128, 129, 133 Vents, volcanic, 128 Vents, volcanic, 128 Vents, 16, 16, 19, 20 Victoria Rupes, 109, 110, 115 Visible and Infrared Spectrograph (VIRS). See Mercury Atmospheric and Surface Composition Spectrometer (MASCS) Visible and near-Infrared Hyperspectral Imaging (VIHI). See Spectrometers and Imagers for MPO BepiColombo Integrated Observatory System (SIMBIO-SYS) Visible and Infrared Spectrograph (VIRS). Vents, 128, 129, 133 Vents, 16, 16, 19, 20 Victoria Rupes, 109, 110, 115 Visible and Infrared Spectrograph (VIRS). Vents, volcanic, 128 Vents, 16, 16, 19, 20 Victoria Rupes, 109, 110, 115 Visible and Infrared Spectrograph (VIRS). Vents, 16, 16, 19, 20 Victoria Rupes, 109, 110, 115 Visible and Infrared Spectrograph (VIRS). Visible and Infrared Spectrograph (VIRS). Vents, 16, 16, 19, 20 Victoria Rupes, 109, 110, 115 Visible and Infrared Spectrometer (MASCS) Visible and near-Infrar
Spectroscopy, 19 Spinel, 104–105 Spin:orbit coupling, 12, 15, 23, 37, 151 Sputtering, 46–48, 136, 146, 162–163 Start from a Rotating Field Mass Spectrometer (STROFIO). See Probing the Hermean Exosphere by Ultraviolet Spectroscopy (PHEBUS) Stereo Channel (STC). See Spectrometers and Imagers for MPO BepiColombo Integrated Observatory System (SIMBIO-SYS) Sublimation, 136–141 Sulfides, 104–105, 138 Sulfur, 43, 50, 65, 101–102, 131, 132, 149 Sun angle, 23, 38 Surface composition, 45, 46, 99–105 Swiss Cheese terrain, 138–139 Synchronous rotation, 8–10, 12 Spectrometer, surface, 11, 14, 25–26, 47, 50, 77, 105, 138, 140, 146 Terrain units, 93 Thermal desorption, 48, 136 Thermal history, 155 Thorium, 102, 155 Tidal despinning, 38, 39, 109 Tidal forces, 8, 12, 15 Timescale, 39–41 Titanium, 102 Tolstoj, 40, 89, 107, 122 Tolstoj, 40, 40, 121, 122 Tolstoj, 40, 40, 121, 122 Tolstoj, 40, 40, 121, 122 Tolstoj, 40, 89, 107, 122 Tolstoj, 40, 89, 107, 122 Tolstoj, 40, 89, 107, 122 Tolstoj, 40, 40, 40, 121, 122 Tolstoj, 40, 89, 107, 122 Tolstoj, 40, 40, 121, 122 Tolstoj, 40, 89, 107, 122 Tolstoj, 40, 89, 107, 122 Tolstoj, 40, 89, 107, 122 Tolstoj, 40, 40, 121, 122 Tolstoj, 40, 40, 121, 122 Tolstoj, 40, 40, 121, 122 Tolstoj, 40, 40, 40, 40, 40, 40, 40, 40, 40, 40
Spinel, 104–105 Spinorbit coupling, 12, 15, 23, 37, 151 Sputtering, 46–48, 136, 146, 162–163 Start from a Rotating Field Mass Spectrometer (STROFIO). See Probing the Herman Exosphere by Ultraviolet Spectroscopy (PHEBUS) Stereo Channel (STC). See Spectrometers and Imagers for MPO BepiColombo Integrated Observatory System (SIMBIO-SYS) Sublimation, 136–141 Sulfides, 104–105, 138 Sulfur, 43, 50, 65, 101–102, 131, 132, 149 Sun angle, 23, 38 Surface composition, 45, 46, 99–105 Swiss Cheese terrain, 138–139 Synchronous rotation, 8–10, 12 T Tectonisation of basin edges, 120, 121, 123, 124, 127 Telescopic observations, 7–8 Temperature, surface, 11, 14, 25–26, 47, 50, 77, 105, 138, 140, 146 Terrain units, 93 Thermal desorption, 48, 136 Thermal history, 155 Thorium, 102, 155 Throitand despining, 38, 39, 109 Tidal forces, 8, 12, 15 Timescale, 39–41 Titanium, 102 Tolstoj, 40, 89, 107, 122 Tolstojan, 40, 121, 122
Spin:orbit coupling, 12, 15, 23, 37, 151 Sputtering, 46-48, 136, 146, 162-163 Start from a Rotating Field Mass Spectrometer (STROFIO). See Probing the Hermean Exosphere by Ultraviolet Spectroscopy (PHEBUS) Stereo Channel (STC). See Spectrometers and Imagers for MPO BepiColombo Integrated Observatory System (SIMBIO-SYS) Sublimation, 136-141 Sulfides, 104-105, 138 Sulfur, 43, 50, 65, 101-102, 131, 132, 149 Sun angle, 23, 38 Surface composition, 45, 46, 99-105 Swiss Cheese terrain, 138-139 Synchronous rotation, 8-10, 12 Tectonisation of basin edges, 120, 121, 123, 124, 127 Telescopic observations, 7-8 Temperature, surface, 11, 14, 25-26, 47, 50, 77, 105, 138, 140, 146 Terrain units, 93 Thermal desorption, 48, 136 Thermal history, 155 Thorium, 102, 155 Tidal despinning, 38, 39, 109 Tidal forces, 8, 12, 15 Tidal despinning, 38, 39, 109 Tidal forces, 8, 12, 15 Timescale, 39-41 Titanium, 102 Tolstoj, 40, 89, 107, 122 Tolstoj, 40, 80, 107, 122 Tolstoj, 40, 80, 107, 122 Tolstoj, 40, 80, 107, 122 To
Sputtering, 46-48, 136, 146, 162-163 Start from a Rotating Field Mass Spectrometer (STROFIO). See Probing the Herman Exosphere by Ultraviolet Spectroscopy (PHEBUS) Stereo Channel (STC). See Spectrometers and Imagers for MPO BepiColombo Integrated Observatory System (SIMBIO-SYS) Sublimation, 136-141 Sulfides, 104-105, 138 Sulfur, 43, 50, 65, 101-102, 131, 132, 149 Sun angle, 23, 38 Surface composition, 45, 46, 99-105 Swiss Cheese terrain, 138-139 Synchronous rotation, 8-10, 12 Volcanic glass, 134 Volcanism effusive, 128 explosive, 129, 130 von Oppolzer, Theodor, 7 Vulcan, 7 Vulcan
Venus, 1, 6, 16, 19, 20
Exosphere by Ultraviolet Spectroscopy (PHEBUS) Stereo Channel (STC). See Spectrometers and Imagers for MPO BepiColombo Integrated Observatory System (SIMBIO-SYS) Sublimation, 136–14 Sulfides, 104–105, 138 Sulfur, 43, 50, 65, 101–102, 131, 132, 149 Sun angle, 23, 38 Surface composition, 45, 46, 99–105 Swiss Cheese terrain, 138–139 Synchronous rotation, 8–10, 12 Tectonisation of basin edges, 120, 121, 123, 124, 127 Telescopic observations, 7–8 Temperature, surface, 11, 14, 25–26, 47, 50, 77, 105, 138, 140, 146 Terrain units, 93 Thermal desorption, 48, 136 Thermal history, 155 Throium, 102, 155 Thruster burns, 59 Thrust faults, 36 Tidal despinning, 38, 39, 109 Tidal forces, 8, 12, 15 Timescale, 39–41 Titanium, 102 Tolstoj, 40, 89, 107, 122 Tolstoj, 40, 89, 107, 122 Tolstoj, 40, 89, 107, 122 Tolstojan, 40, 121, 122
(PHEBUS) Stereo Channel (STC). See Spectrometers and Imagers for MPO BepiColombo Integrated Observatory System (SIMBIO-SYS) Sublimation, 136–141 Sulfides, 104–105, 138 Sulfur, 43, 50, 65, 101–102, 131, 132, 149 Sun angle, 23, 38 Surface composition, 45, 46, 99–105 Swiss Cheese terrain, 138–139 Synchronous rotation, 8–10, 12 Tectonisation of basin edges, 120, 121, 123, 124, 127 Telescopic observations, 7–8 Temperature, surface, 11, 14, 25–26, 47, 50, 77, 105, 138, 140, 146 Terrain units, 93 Thermal desorption, 48, 136 Thermal history, 155 Thorium, 102, 155 Thrust faults, 36 Tidal despinning, 38, 39, 109 Tidal forces, 8, 12, 15 Tidal despinning, 38, 39, 109 Tidal forces, 8, 12, 15 Timescale, 39–41 Titanium, 102 Tolstoj, 40, 89, 107, 122 Tolstojan, 40, 121, 122
Stereo Channel (STC). See Spectrometers and Imagers for MPO BepiColombo Integrated Observatory System (SIMBIO-SYS) Sublimation, 136–141 Sulfides, 104–105, 138 Sulfur, 43, 50, 65, 101–102, 131, 132, 149 Sun angle, 23, 38 Surface composition, 45, 46, 99–105 Swiss Cheese terrain, 138–139 Synchronous rotation, 8–10, 12 Volcanic glass, 134 Volcanism effusive, 128 explosive, 129, 130 von Oppolzer, Theodor, 7 Vulcanoids, 7
Imagers for MPO BepiColombo Integrated Observatory System (SIMBIO-SYS) Usible and near-Infrared Hyperspectral Imaging (VIHI). See Spectrometers and Imagers for MPO BepiColombo Integrated Observatory System (SIMBIO-SYS) Imaging (VIHI). See Spectrometers and Imagers for MPO BepiColombo Integrated Observatory System (SIMBIO-SYS) Vivaldi, 24, 88 Volatiles, 102, 103, 130, 131, 136–138, 140–141, 168, 170, 171 Volcanic glass, 134 Volcanism effusive, 128 explosive, 129, 130 von Oppolzer, Theodor, 7 Vulcan, 7 Vulcan, 7 Vulcanoids, 7 Vulcanoids
Integrated Observatory System (SIMBIO-SYS)
Imaging (VIHI). See Spectrometers and Imagers for MPO BepiColombo Integrated Observatory System (SIMBIO-SYS)
Sublimation, 136–141 Sulfides, 104–105, 138 Sulfur, 43, 50, 65, 101–102, 131, 132, 149 Sun angle, 23, 38 Surface composition, 45, 46, 99–105 Swiss Cheese terrain, 138–139 Synchronous rotation, 8–10, 12 Tectonisation of basin edges, 120, 121, 123, 124, 127 Telescopic observations, 7–8 Temperature, surface, 11, 14, 25–26, 47, 50, 77, 105, 138, 140, 146 Terrain units, 93 Thermal desorption, 48, 136 Thermal history, 155 Throium, 102, 155 Throium, 102, 155 Throium, 102, 155 Tidal bulges, 8, 15 Tidal despinning, 38, 39, 109 Tidal forces, 8, 12, 15 Timescale, 39–41 Titanium, 102 Tolstoj, 40, 89, 107, 122 Tolstojan, 40, 121, 122
Sulfides, 104–105, 138 Sulfur, 43, 50, 65, 101–102, 131, 132, 149 Sun angle, 23, 38 Surface composition, 45, 46, 99–105 Swiss Cheese terrain, 138–139 Synchronous rotation, 8–10, 12 Tectonisation of basin edges, 120, 121, 123, 124, 127 Telescopic observations, 7–8 Temperature, surface, 11, 14, 25–26, 47, 50, 77, 105, 138, 140, 146 Terrain units, 93 Thermal desorption, 48, 136 Thermal history, 155 Thorium, 102, 155 Throium, 102, 155 Throium, 102, 155 Tidal despinning, 38, 39, 109 Tidal forces, 8, 12, 15 Timescale, 39–41 Titanium, 102 Tolstoj, 40, 89, 107, 122 Tolstojan, 40, 121, 122
Sulfur, 43, 50, 65, 101–102, 131, 132, 149 Sun angle, 23, 38 Surface composition, 45, 46, 99–105 Swiss Cheese terrain, 138–139 Synchronous rotation, 8–10, 12 Tectonisation of basin edges, 120, 121, 123, 124, 127 Telescopic observations, 7–8 Temperature, surface, 11, 14, 25–26, 47, 50, 77, 105, 138, 140, 146 Terrain units, 93 Thermal desorption, 48, 136 Thermal history, 155 Thorium, 102, 155 Thruster burns, 59 Thrust faults, 36 Tidal bulges, 8, 15 Tidal despinning, 38, 39, 109 Tidal forces, 8, 12, 15 Timescale, 39–41 Timescale, 39–41 Tolstoj, 40, 89, 107, 122 Tolstojan, 40, 121, 122 Surface composition, 45, 46, 99–105 Vivaldi, 24, 88 Volatiles, 102, 103, 130, 131, 136–138, 140–141, 168, 170, 171 Volcanic glass, 134 Volcanism effusive, 128 explosive, 129, 130 von Oppolzer, Theodor, 7 Vulcan, 7 Vulcanoids, 7 W W W Warm poles, 14 Water, 64, 131 Wide-angle camera (WAC). See Mercury dual imaging system (MDIS) Wrinkle ridges, 96, 97, 108, 112, 118 X X-ray spectrometer (XRS), 64, 99–100, 131, 138, 151, 154, 159, 170
Sun angle, 23, 38 Surface composition, 45, 46, 99–105 Swiss Cheese terrain, 138–139 Synchronous rotation, 8–10, 12 Tectonisation of basin edges, 120, 121, 123, 124, 127 Telescopic observations, 7–8 Temperature, surface, 11, 14, 25–26, 47, 50, 77, 105, 138, 140, 146 Terrain units, 93 Thermal desorption, 48, 136 Thermal history, 155 Thorium, 102, 155 Thrust faults, 36 Tidal bulges, 8, 15 Tidal despinning, 38, 39, 109 Tidal forces, 8, 12, 15 Timescale, 39–41 Titanium, 102 Tolstoj, 40, 89, 107, 122 Tolstojan, 40, 121, 122
Surface composition, 45, 46, 99–105 Swiss Cheese terrain, 138–139 Synchronous rotation, 8–10, 12 Tectonisation of basin edges, 120, 121, 123, 124, 127 Telescopic observations, 7–8 Temperature, surface, 11, 14, 25–26, 47, 50, 77, 105, 138, 140, 146 Terrain units, 93 Thermal desorption, 48, 136 Thermal history, 155 Thorium, 102, 155 Thorium, 102, 155 Tidal bulges, 8, 15 Tidal bulges, 8, 15 Tidal forces, 8, 12, 15 Timescale, 39–41 Titanium, 102 Tolstoj, 40, 89, 107, 122 Tolstojan, 40, 121, 122 Volatiles, 102, 103, 130, 131, 136–138, 140–141, 168, 170, 171 Volcanic glass, 134 Volcanism effusive, 128 explosive, 129, 130 von Oppolzer, Theodor, 7 Vulcan, 7 Vulcanoids, 7 W Warm poles, 14 Water, 64, 131 Wide-angle camera (WAC). See Mercury dual imaging system (MDIS) Wrinkle ridges, 96, 97, 108, 112, 118 X X-ray spectrometer (XRS), 64, 99–100, 131, 138, 151, 154, 159, 170
Swiss Cheese terrain, 138–139 Synchronous rotation, 8–10, 12 Tectonisation of basin edges, 120, 121, 123, 124, 127 Telescopic observations, 7–8 Temperature, surface, 11, 14, 25–26, 47, 50, 77, 105, 138, 140, 146 Terrain units, 93 Thermal desorption, 48, 136 Thermal history, 155 Thorium, 102, 155 Tidal despinning, 38, 39, 109 Tidal forces, 8, 12, 15 Timescale, 39–41 Titanium, 102 Tolstoj, 40, 89, 107, 122 Tolstojan, 40, 121, 122
Volcanic glass, 134 Volcanism
Comparison of the compariso
T explosive, 129, 130 von Oppolzer, Theodor, 7 Vulcan, 7 Vulcan, 7 Vulcan, 7 Vulcanoids, 7 Telescopic observations, 7–8 Temperature, surface, 11, 14, 25–26, 47, 50, 77, 105, 138, 140, 146 Terrain units, 93 W Thermal desorption, 48, 136 Warm poles, 14 Water, 64, 131 Wide-angle camera (WAC). See Mercury dual imaging system (MDIS) Thrust faults, 36 Wrinkle ridges, 96, 97, 108, 112, 118 Tidal bulges, 8, 15 Tidal despinning, 38, 39, 109 Tidal forces, 8, 12, 15 X Timescale, 39–41 X-ray spectrometer (XRS), 64, 99–100, 131, 138, 151, 154, 159, 170 Tolstoj, 40, 89, 107, 122 Tolstojan, 40, 121, 122
Tectonisation of basin edges, 120, 121, 123, 124, 127 Telescopic observations, 7–8 Temperature, surface, 11, 14, 25–26, 47, 50, 77, 105, 138, 140, 146 Terrain units, 93 Thermal desorption, 48, 136 Thermal history, 155 Thorium, 102, 155 Tidal despinning, 38, 39, 109 Tidal forces, 8, 12, 15 Timescale, 39–41 Titanium, 102 Tolstoj, 40, 89, 107, 122 Tolstojan, 40, 121, 122 von Oppolzer, Theodor, 7 Vulcan, 7 Vulcanoids, 7 W Warm poles, 14 Water, 64, 131 Wide-angle camera (WAC). See Mercury dual imaging system (MDIS) Wrinkle ridges, 96, 97, 108, 112, 118 X X-ray spectrometer (XRS), 64, 99–100, 131, 138, 151, 154, 159, 170
124, 127 Telescopic observations, 7–8 Temperature, surface, 11, 14, 25–26, 47, 50, 77, 105, 138, 140, 146 Terrain units, 93 Thermal desorption, 48, 136 Thermal history, 155 Water, 64, 131 Wide-angle camera (WAC). See Mercury dual imaging system (MDIS) Thrust faults, 36 Tidal bulges, 8, 15 Tidal despinning, 38, 39, 109 Tidal forces, 8, 12, 15 Timescale, 39–41 Titanium, 102 Tolstoj, 40, 89, 107, 122 Tolstojan, 40, 121, 122
Telescopic observations, 7–8 Temperature, surface, 11, 14, 25–26, 47, 50, 77, 105, 138, 140, 146 Terrain units, 93 Thermal desorption, 48, 136 Thermal history, 155 Water, 64, 131 Wide-angle camera (WAC). See Mercury dual imaging system (MDIS) Thrust faults, 36 Tidal bulges, 8, 15 Tidal despinning, 38, 39, 109 Tidal forces, 8, 12, 15 Timescale, 39–41 Titanium, 102 Tolstoj, 40, 89, 107, 122 Tolstojan, 40, 121, 122 Vulcanoids, 7 W Warm poles, 14 Water, 64, 131 Wide-angle camera (WAC). See Mercury dual imaging system (MDIS) Wrinkle ridges, 96, 97, 108, 112, 118 X X-ray spectrometer (XRS), 64, 99–100, 131, 138, 151, 154, 159, 170
Temperature, surface, 11, 14, 25–26, 47, 50, 77, 105, 138, 140, 146 Terrain units, 93 Thermal desorption, 48, 136 Thermal history, 155 Thorium, 102, 155 Tidal despinning, 38, 39, 109 Tidal forces, 8, 12, 15 Timescale, 39–41 Titanium, 102 Tolstoj, 40, 89, 107, 122 Tolstojan, 40, 121, 122 Warm poles, 14 Warm poles, 14 Water, 64, 131 Wide-angle camera (WAC). See Mercury dual imaging system (MDIS) Wrinkle ridges, 96, 97, 108, 112, 118 X X-ray spectrometer (XRS), 64, 99–100, 131, 138, 151, 154, 159, 170
77, 105, 138, 140, 146 Terrain units, 93 W Thermal desorption, 48, 136 Thermal history, 155 Water, 64, 131 Wide-angle camera (WAC). See Mercury dual imaging system (MDIS) Thrust faults, 36 Tidal bulges, 8, 15 Tidal despinning, 38, 39, 109 Tidal forces, 8, 12, 15 Timescale, 39–41 X-ray spectrometer (XRS), 64, 99–100, 131, 138, 151, 154, 159, 170 Tolstoj, 40, 89, 107, 122 Tolstojan, 40, 121, 122
Thermal desorption, 48, 136 Thermal history, 155 Thorium, 102, 155 Thrust faults, 36 Tidal bulges, 8, 15 Tidal despinning, 38, 39, 109 Tidal forces, 8, 12, 15 Timescale, 39–41 Timescale, 39–41 Titanium, 102 Tolstoj, 40, 89, 107, 122 Tolstojan, 40, 121, 122 Water, 64, 131 Wide-angle camera (WAC). See Mercury dual imaging system (MDIS) Wrinkle ridges, 96, 97, 108, 112, 118 X X X-ray spectrometer (XRS), 64, 99–100, 131, 138, 151, 154, 159, 170
Thermal history, 155 Thorium, 102, 155 Thruster burns, 59 Thrust faults, 36 Tidal bulges, 8, 15 Tidal despinning, 38, 39, 109 Tidal forces, 8, 12, 15 Timescale, 39–41 Titanium, 102 Tolstoj, 40, 89, 107, 122 Tolstojan, 40, 121, 122 Water, 64, 131 Wide-angle camera (WAC). See Mercury dual imaging system (MDIS) Wrinkle ridges, 96, 97, 108, 112, 118 X X X X-ray spectrometer (XRS), 64, 99–100, 131, 138, 151, 154, 159, 170
Thorium, 102, 155 Thruster burns, 59 Thrust faults, 36 Tidal bulges, 8, 15 Tidal despinning, 38, 39, 109 Tidal forces, 8, 12, 15 Timescale, 39–41 Titanium, 102 Tolstoj, 40, 89, 107, 122 Tolstojan, 40, 121, 122 Wide-angle camera (WAC). See Mercury dual imaging system (MDIS) Wrinkle ridges, 96, 97, 108, 112, 118 X X X X-ray spectrometer (XRS), 64, 99–100, 131, 138, 151, 154, 159, 170
Thruster burns, 59 imaging system (MDIS) Thrust faults, 36 Wrinkle ridges, 96, 97, 108, 112, 118 Tidal bulges, 8, 15 Tidal despinning, 38, 39, 109 Tidal forces, 8, 12, 15 Timescale, 39–41 X-ray spectrometer (XRS), 64, 99–100, Titanium, 102 Tolstoj, 40, 89, 107, 122 Tolstojan, 40, 121, 122
Thrust faults, 36 Tidal bulges, 8, 15 Tidal despinning, 38, 39, 109 Tidal forces, 8, 12, 15 Timescale, 39–41 X-ray spectrometer (XRS), 64, 99–100, Titanium, 102 Tolstoj, 40, 89, 107, 122 Tolstojan, 40, 121, 122 Tolstojan, 40, 121, 122
Tidal bulges, 8, 15 Tidal despinning, 38, 39, 109 Tidal forces, 8, 12, 15 Timescale, 39–41 X-ray spectrometer (XRS), 64, 99–100, Titanium, 102 Tolstoj, 40, 89, 107, 122 Tolstojan, 40, 121, 122 X Tidal bulges, 8, 15 X Timescale, 39–41 X-ray spectrometer (XRS), 64, 99–100, 131, 138, 151, 154, 159, 170
Tidal despinning, 38, 39, 109 Tidal forces, 8, 12, 15 Timescale, 39–41 X-ray spectrometer (XRS), 64, 99–100, Titanium, 102 Tolstoj, 40, 89, 107, 122 Tolstojan, 40, 121, 122 X X X-ray spectrometer (XRS), 64, 99–100, 131, 138, 151, 154, 159, 170
Tidal forces, 8, 12, 15 Timescale, 39–41 X-ray spectrometer (XRS), 64, 99–100, Titanium, 102 Tolstoj, 40, 89, 107, 122 Tolstojan, 40, 121, 122 X X-ray spectrometer (XRS), 64, 99–100, 131, 138, 151, 154, 159, 170
Titanium, 102 Tolstoj, 40, 89, 107, 122 Tolstojan, 40, 121, 122
Tolstoj, 40, 89, 107, 122 Tolstojan, 40, 121, 122
Tolstojan, 40, 121, 122
1 opograpny, 105, 151 Y
Transits, 5–7, 174 Yen, Chen-wan, 54, 56, 70 Transpression, 111, 115
Transpression, 111, 113
Z
U Zupus, Giovanni, 7
Ultraviolet and Visible Spectrometer (UVVS).
See Mercury Atmospheric and Surface
Composition Spectrometer (MASCS)